December 1989 ANL-IFR-124

FIRST OVERPOWER TESTS OF METALLIC IFR FUEL IN TREAT: DATA AND ANALYSIS FROM TESTS M5, M6, AND M7

by

T. H. Bauer, W. R. Robinson, J. W. Holland, E. A. Rhodes, and A. E. Wright

Reactor Analysis and Safety Division
Argonne National Laboratory
9700 South Cass Avenue
Argonne, IL 60439

IFR TECHNICAL MEMORANDUM NO. 124

~~Results reported in~~ the IFR~~-TM series of memora~~nda
~~frequently are prel~~iminary a~~nd subject to revis~~ion.
~~Consequently they s~~hould not~~ be quoted or refere~~nced.

DISTRIBUTION OF THIS REPORT IS UNLIMITED David Hamrin OSTI 4/17/2017

~~APPLIED TECHNOLOGY~~

Any further distr~~ibution by any holder of this~~ document or data therein to third parties representing foreign interests, foreign governments, fore~~ign companies, and foreign~~ subsidiaries or foreign divisions of U.S. companies shall be approved by the Associate Deputy A~~ssistant Secretary for Reactor~~ Systems, Develop~~ment, and Technology~~, U.S. Depart~~ment of Energy. Fur~~ther, foreign ~~party release may re~~quire DOE app~~roval pursuant to Fe~~deral Regula~~tion 10 CFR Part 81~~0, and/or may ~~be subject to Secti~~on 127 of the Atomic Energy Act.

MASTER

RELEASED FOR ANNOUNCEMENT
~~IN ATF. DISTRIBUTION LIMITED TO~~
~~PARTICIPANTS IN THE IFR/TREAT~~
~~PROGRAM. OTHERS REQUEST FROM~~
[illegible]

TABLE OF CONTENTS

TABLE OF CONTENTS
(Contd.)

TABLE OF CONTENTS
(Contd.)

LIST OF FIGURES

LIST OF FIGURES
(Contd.)

LIST OF FIGURES
(Contd.)

LIST OF FIGURES
(Contd.)

LIST OF FIGURES
(Contd.)

LIST OF FIGURES
(Contd.)

LIST OF FIGURES
(Contd.)

LIST OF FIGURES
(Contd.)

LIST OF FIGURES
(Contd.)

LIST OF FIGURES
(Contd.)

LIST OF TABLES

FIRST OVERPOWER TESTS OF METALLIC IFR FUEL IN TREAT: DATA AND ANALYSIS FROM TESTS M5, M6, AND M7

by

T. H. Bauer, W. R. Robinson, J. W. Holland, E. A. Rhodes, and A. E. Wright

ABSTRACT

Results and analyses of margin to cladding failure and pre-failure axial expansion of metallic fuel are reported for TREAT in-pile transient overpower tests M5-M7. These are the first such tests on reference binary and ternary alloy fuel of the Integral Fast Reactor (IFR) concept with burnup ranging from 1 to 10 at.%. In all cases, test fuel was subjected to an exponential power rise on an 8 s period until either incipient or actual cladding failure was achieved. Objectives, designs and methods are described with emphasis on developments unique to metal fuel safety testing. The resulting database for cladding failure threshold and prefailure fuel expansion is presented. The nature of the observed cladding failure and resultant fuel dispersals is described. Simple models of cladding failures and pre-failure axial expansions are described and compared with experimental results. Reported results include: temperature, flow, and pressure data from test instrumentation; fuel motion diagnostic data principally from the fast neutron hodoscope; and test remains described from both destructive and non-destructive post-test examination.

EXECUTIVE SUMMARY

Transient Reactor Test Facility (TREAT) tests M5 through M7 were the first transient overpower (TOP) tests of safety related fuel performance of metallic fuel alloys designated for use in the Integral Fast Reactor (IFR) concept. Specific objectives addressed by these and all other M-series experiments were the identification of phenomena underlying pin failure and the verification of a wide margin to failure. In addition, prefailure axial expansion (a potentially significant pre-failure reactivity removal mechanism) was to be quantified, and the qualitative nature of post-failure dispersal events were to be assessed. Initial M-series tests, M2-M4 [1.1-1.5], used irradiated EBR-II Mark-II driver (U-5Fs) fuel that was available early on. The later tests, M5-M7 reported here, then used irradiated IFR ternary (U-19Pu-10Zr) and binary (U-10Zr) alloy fuel as appropriate samples became available.

Although the various metal-fuel types are similar in many respects, IFR reference alloys are typically irradiated at much higher temperatures than the U-5Fs alloy, and differ in physical structure, especially ternary alloys with high plutonium concentration. IFR alloys tested in M5-M7 also used advanced D9 and HT9 steels for cladding in contrast with the 316 SS used in the U-5Fs fuel tested previously. It is thus of interest to determine features of safety-related fuel performance which are fuel-specific and those which are common to all modern metal-fuel types.

Hardware design was guided by a need to test as many pins as possible in a single experiment while providing test conditions as independent as possible for each pin. The earlier M-series test train design accommodated three small diameter U-5Fs fuel pins in separately orificed flowtubes. The larger diameter of IFR concept fuel pins, however, required a new test train concept for M5-M7 that could accommodate only two pins. The new two-pin test train included significant hardware improvements in thermocouple mounting, pin support, and coolant flowrate measurement.

Choice of particular IFR concept fuel to test in M5-M7 was guided both by advanced core designs as well as general fuel characteristics that could potentially lead to adverse safety behavior. In general, pins of the highest available burnup available were tested: five ternary pins (containing 19% plutonium and 10% zirconium by weight) clad in D9 steel irradiated to peak burnups ranging from 0.8 to 9.8 at.% and one binary pin (containing no plutonium and 10% zirconium by weight) clad in HT9 irradiated to 2.9 at.%.

Estimating test fuel heating during overpower transients made use of specially performed calibration experiments with fresh fuel and flux monitor wires, supplemented by analyses to estimate neutronic effects of burnup and swelling. Overall coolant flow past the test pins was measured. Symmetry, separate hydraulic measurements, and "mini" flowmeters located on individual test pin flowtubes determined of coolant flow past individual pins in the test. Just prior to the overpower transient, a "heat balance" experiment was performed driving the test pins at constant power and coolant flow. Analyzing the coolant temperature rise past each pin during this heat balance enabled "in situ" calibration of the heating of each test pin relative to measured experimental power and flowrates as well as to nominal heating in a fast reactor. Because operating conditions of the heat balance and the ensuing overpower transient were in many respects identical, the heat balance

determination of test pin power coupling was used for "fine tuning" of the overpower transient and subsequent post-test analysis.

All test fuel in this series was subjected to similar overpower conditions: full coolant flow and an exponential power rise on an 8 s period. The 8 s period was chosen as the slowest transient possible that would commence from near-nominal power and carry through to cladding failure within the energy deposition limitations of the TREAT reactor. Baseline thermal conditions in the test fuel were referenced to nominal conditions in a fast reactor. These include a peak linear power rating of 40 kW/m (12 kW/ft), an inlet temperature of 630 K and a 150 K coolant temperature rise. The power rise was rapidly terminated upon detection of cladding breach or, by using previously measured failure thresholds, just prior to failure. Overpower levels achieved in each case were in the neighborhood of four times nominal and in one case as high as 4.8 times nominal. Pre-failure axial fuel expansion was measured in real time by the fast neutron hodoscope as well as by post-test radiography. Calculations indicated that at peak power approximately one-half of the total fuel inventory was molten. Of the six pins tested in M5-M7 only the two ternary pins of highest burnup were overheated to failure. In each case cladding breach was at the fuel top and very localized.

Post-test analysis of both thermal and fuel performance were performed with an extended version of the COBRA-PI code. Good agreement was achieved between measured and calculated coolant heatup. Calculated peak melt fractions also showed reasonable agreement with post-test microstructural examination, providing rough validation of the rather uncertain values for thermal conductivity of irradiated fuel used in the calculations. Fuel performance results were evaluated and analyzed with the help of models which had been developed in the course of earlier M-series tests.

Specifically, pre-failure axial expansion in IFR fuel was always positive and significant beyond thermal expansion, and expansions in the range of 2-4 % were typical of all burnups tested. Large expansions at low burnups, such as measured in U-5Fs fuel, were not measured in IFR fuel, however. Expansion of fission gas trapped in melting fuel provides a sound basis for modeling axial expansions, and differences in amounts of dissolved gas accounts for measured differences between fuel types. Failure threshold with the 8 s period overpower conditions tested is about four times nominal over a wide range of burnups and fuel types tested. Successful cladding failure models include effects of both overpressure and penetration of cladding by a low melting point eutectic. In all cases however, achieving overpower levels of four times nominal makes rapid eutectic penetration very likely. Because rapid cladding penetration also requires extensive fuel melting, failure due to rapid penetration might be delayed in a fuel with a high melting point, as illustrated by the survival of the IFR-binary pin tested in M7 to about 4.8 times nominal power.

In summary, simple models of pre-failure expansion and cladding failure developed during earlier tests on U-5Fs fuel were extended and validated by the M5-M7 database of IFR-type fuel. While safety-related fuel behavior of all fuel types tested is similar, post-test analyses highlight the fuel properties of fission gas retention and melting point as accounting for major differences observed between behavior of U-5Fs and IFR-type fuel.

Events following the two pin failures (M6 and M7) were generally benign. Because the coolant channel environment did not simulate a large pin bundle, however, only qualitative conclusions should be drawn. A sudden pressurization of the coolant channel (peak measured pressures about one order of magnitude less than the maximum pressure in the gas plenum of the failed pin) led to temporary reversal of coolant flow. Rapid ejection and sweepout of the pin's molten fuel inventory followed through a small breach at the top of the fuel. Coolant flow in the normal direction was rapidly restored.

Purely analytical studies with the cladding failure model indicate that for the fuel burnups and heating rates employed in M-series tests pins fail at or near the threshold point of rapid eutectic penetration. Although the same basic mechanisms of pressure and melting are believed to apply when significant cladding damage rates occur at lower temperatures, different modeling issues and questions arise. Moreover, fuel performance questions now raised in safety analyses of current reactor designs concern cladding damage at lower temperatures. A goal of TREAT M-series planning is to address these issues by extending the present fuel performance study to higher burnup fuel and/or to overheating conditions involving lower temperatures and longer times.

1.0 INTRODUCTION

The "M-series" program for a series of in-pile tests of modern metal fuel at the Transient Reactor Test Facility (TREAT) was initiated in 1984 to address key questions about metal fuel behavior during transient overpower (TOP) accidents. Although early safety assessments of the Integral Fast Reactor (IFR) concept indicated benign response of metallic fuel to most accident initiators, in-pile data on fuel cladding failure threshold and associated phenomena was also needed. Specifically, objectives of M-series TREAT tests were directed to:

1) Determination of margin to failure and identification of underlying mechanisms,

2) Assessment of pre-failure axial expansion as a potentially significant pre-failure reactivity removal mechanism, and

3) Preliminary assessment of post-failure events: behavior of disrupted fuel and coolant.

Overpower testing in the TREAT reactor has drawn upon more than 20 years of experience of transient safety testing in flowing sodium loops and allows for controlled transient overheating of test pins by fission in a near-prototypic thermal and hydraulic environment. Test fuel was to be subjected to simulated TOP accident conditions with attention centered on the time domain of cladding failure threshold. Particular requirements included stopping the power transient on the brink of failure, for some pins, and just after failure for others. Programmatic needs also entered test planning. It was important to test many pins quickly, despite limited availability of test hardware and of TREAT reactor time. Thus, the concept of testing two (or more) pins simultaneously, with separate and possibly different hydraulic environments for each pin was actively pursued.

M-series was intended to test various fuel and cladding combinations relevant to the IFR concept with as wide a range of fuel burnups as possible. Because of early availability of irradiated fuel and because it had been well-characterized, initial tests (M2-M4) in the series used (U-Fs) fuel. Later tests (M5-M7) used IFR type fuel which had been pre-irradiated in EBR-II, as appropriate test pins became available. All metal fuel of recent design features efficient heat transfer through high conductivity fuel and sodium thermal "bonding" to cladding. It is also fabricated to allow for both a high degree of fuel swelling and efficient release of fission gas to the pin plenum during normal operation. Until recently, EBR-II driver fuel had been a "binary" alloy of uranium and "fissium" (U-Fs). (Fissium is a mixture of metals representing an equilibrium composition of fission products after reprocessing.) Reference fuel for the IFR concept uses uranium, plutonium and zirconium in a ternary (U-Pu-Zr) and binary (U-Zr) composition.

All test fuel in this series was subjected to similar overpower conditions: full coolant flow and an exponential power rise on an 8 s period. In each case, the power transient was rapidly terminated upon detection of cladding breach or, by using previously measured failure thresholds, just prior to failure.

Results of the initial M-series tests, M2-M4, performed in 1985 and 1986 have been reported in Refs. 1.1-1.5. Nine pins were tested, three beyond cladding failure. Test results and analyses led to the development and validation of pin cladding failure and pre-failure fuel expansion models for U-Fs metallic fuel. For the overpower conditions tested, a high margin to failure of about four times nominal operating power in a fast reactor was observed. Cladding failures occurred in a localized region near the top of the fuel column and were consistent with combined effects of excessive plenum pressure and thinning by penetration of low-melting temperature fuel-steel alloy (eutectic). Pre-failure axial expansions were large (around 15-20 %) in low-burnup fuel but decreased rapidly with increasing fuel burnup. This observed axial expansion was consistent with fission gas retained in melting fuel expanding until reaching equilibrium with pressure in the pin plenum. Post-failure events were characterized by rapid ejection and dispersal of molten fuel, rapid coolant voiding, and partial flow blockage. In general, post-failure disruption was greater with fuel of higher burnup and was thus correlated to the amount of pin depressurization upon cladding failure.

This report describes results of the latter M-series tests, M5-M7 performed in 1986 and 1987. The prime objective of tests M5-M7 was continuation and extension of the studies begun in M2-M4 to metal fuel of different design and composition- and, in particular, to reference fuel of the IFR concept. It is of paramount importance to determine features of safety-related fuel performance which are fuel-specific and those which are common to all modern metal-fuel types. Although the various metal-fuel types are similar in many respects, certain features of IFR concept fuel have been identified which may well alter the safety related fuel behavior described above for U-Fs. These include:

1) Plutonium content--IFR reference fuels can contain high plutonium fractions. U-Pu-based fuels have the potential for being less compatible with cladding than are fuels based on uranium alone.

2) Thermal properties--IFR concept alloys have lower thermal conductivity than the U-Fs alloy previously tested. Melting inception of reference alloys varies greatly, depending upon particular composition. Both thermal conductivity and melting point decrease with increasing plutonium content.

3) Steady-state performance--IFR concept alloys are typically irradiated at much higher temperatures and have smaller grain size than the U-Fs pins tested previously. Both features tend to reduce the amount of fission gas retained by IFR type fuel during preirradiation in EBR-II. Additionally, steady-state irradiation of IFR ternary alloy leads to radial redistribution of constituents and the formation of distinct radial zones with different melting points and structure.

4) Fuel pin cladding--IFR concept alloys tested in M5-M7 were clad in D9 and HT9 steel as opposed to the type 316 stainless steel (316 SS) clad U-Fs tested previously. HT9 is an alloy which exhibits low swelling at high burnup but less creep resistant than either 316 SS or D9.

Preliminary reporting of test results from M5-M7 may be found in Refs. 1.6 and 1.7. Preliminary summaries of the overall M-series program may also be found in Refs. 1.8 and 1.9.

2.0 DESCRIPTION OF THE TEST FUEL

Choice of particular IFR concept fuel to test in M5-M7 was guided both by reference core designs and the general fuel characteristics that could potentially lead to adverse safety behavior. Indeed, high priority was given to tests of:

1) Fuel of the highest burnup fuel available,
2) Fuel with high plutonium content, and
3) Fuel clad in HT9 steel.

U-19Pu-10Zr ternary fuel (containing 19% plutonium and 10% zirconium by weight) clad in D9 steel was the first fuel of high plutonium content to be available for TREAT testing in the 1986-1987 time frame. In each test, the highest available burnup was included. The initial IFR fuel test, M5, included two ternary pins irradiated to peak burnups of 0.8 and 1.9 at.%. Subsequent test M6 included ternary pins irradiated to peak burnups of 1.9 and 5.3 at.%. Eventually, U-10Zr binary fuel (containing no plutonium and 10% zirconium by weight) clad in HT9 steel became available as well as higher burnup versions of the previously tested ternary pins. M7 tested both a ternary and a binary pin irradiated to peak burnups of 9.8 and 2.9 at.%, respectively.

All pins tested in M5-M7 were of common design and dimension intended for irradiation in EBR-II. Table 2.1 lists some design dimensions. More details of pin design may be found in Appendix A.

In all cases the preirradiation in EBR-II was to mimic temperatures and restructuring of full length (~1 meter long) fuel. Irradiation power levels in EBR-II were about 36-40 kW/m axial peak (ratio of average to peak was 0.92). Coolant temperature rose by about 100 K from a nominal 644 K inlet value. This power level is significantly higher than the (approximately) 25 kW/m axial peak power in the irradiation of the EBR-II driver fuel tested in M2-M4. Indeed, conditions of the irradiation compare favorably with the 40 kW/m peak power level, 630 K inlet temperature, and 150 K coolant temperature rise assumed throughout this report as nominal for an IFR-type reactor.

Table 2.1. Nominal Design Parameters Common to All M5-M7 Test Pins

Fuel	
length	343 mm
diameter of slug	4.32 mm
mass 78 g	
radial smear density (to cladding inner diameter)	72.5 %
Bond Sodium	
initial height above fuel	6.35 mm
total volume	2.0 cc
Gas Plenum	
length above sodium	246 mm
volume (initial)	5.0 cc
Cladding	
outside diameter	5.84 mm
inner diameter	5.08 mm
thickness	0.38 mm

A considerable amount of restructuring takes place during irradiation of all modern metal fuel which influences both fuel morphology and thermal properties. During the first at.% of burnup the fuel swells by as much as 50% of its original size until it makes contact with the cladding. The liquid sodium bond originally surrounding the fuel slug is displaced into the pin's gas plenum. Much of the fuel volume increase is comprised of gas-filled pores, but interconnection of pores leads to both release of fission gas to the plenum and infiltration of the porosity network by liquid bond sodium. Pressure in the plenum is influenced principally by fission gas release from fuel. After swelled fuel contacts the cladding there is little further swelling and total fuel volume remains approximately constant with increasing burnup. However, further burnup leads to the accumulation of solid and liquid fission products at an approximate rate of 1 vol % per at.% of burnup that tends to further reduce pore volumes filled with gas.

These characteristics are all of some significance for issues studied in M5-M7. Fuel swelling, infiltration of porosity by sodium, and accumulation of solid and liquid fission products strongly influence fuel thermal conductivity. Gas retention within the fuel supplies a potential driving mechanism for prefailure elongation, whereas, gas release from the fuel adds to an internal pin pressure which drives cladding failure.

Restructuring also differs significantly among various metal fuel types. Photographs in Fig. 2.1 show a sampling of cross-sections at several axial locations (relative to the fueled length) from irradiated fuel similar to those tested in M5-M7. In ternary fuel, migration of constituents and porosity leads to a three-zone radial structure including multiple irregularities, separations and cracks (Figs. 2.1a-d). Irregularities in fuel-cladding gap closure is also noted at low burnup (Fig. 2.1a). These zones include a skewing of both zirconium and porosity distributions toward the outside and some build-up of plutonium concentration mid-radius. Binary fuel, like the U-Fs fuel tested previously, restructured more uniformly (Fig. 2.1e).

Fission gas release from metallic fuel seems to depend chiefly upon fuel temperature during irradiation [2.1], emphasizing the importance of irradiation power level and fuel thermal conductivity. (Gas residing within large fuel pores is considered released from the fuel matrix.) Principally because of their higher irradiation power level, IFR-type test fuel typically retained a much smaller concentration of gas in the fuel matrix than did U-Fs test fuel.

For illustration, Table 2.2 lists some whole-pin average characteristics for the ternary and binary fuel tested, based on reported measurements of fuel swelling [2.2], sodium logging [2.3], and plenum pressurization [2.2, 2.3]. Characteristics of U-5Fs fuel tested previously are provided for comparison. Fuel melting points are handbook values [2.4]. The effect of restructuring on thermal conductivity is calculated by a model that estimates effects of both gas filled and sodium logged porosity and is described in Appendix G. Additional fuel characterization useful for post-test analysis is also included in Appendix G.

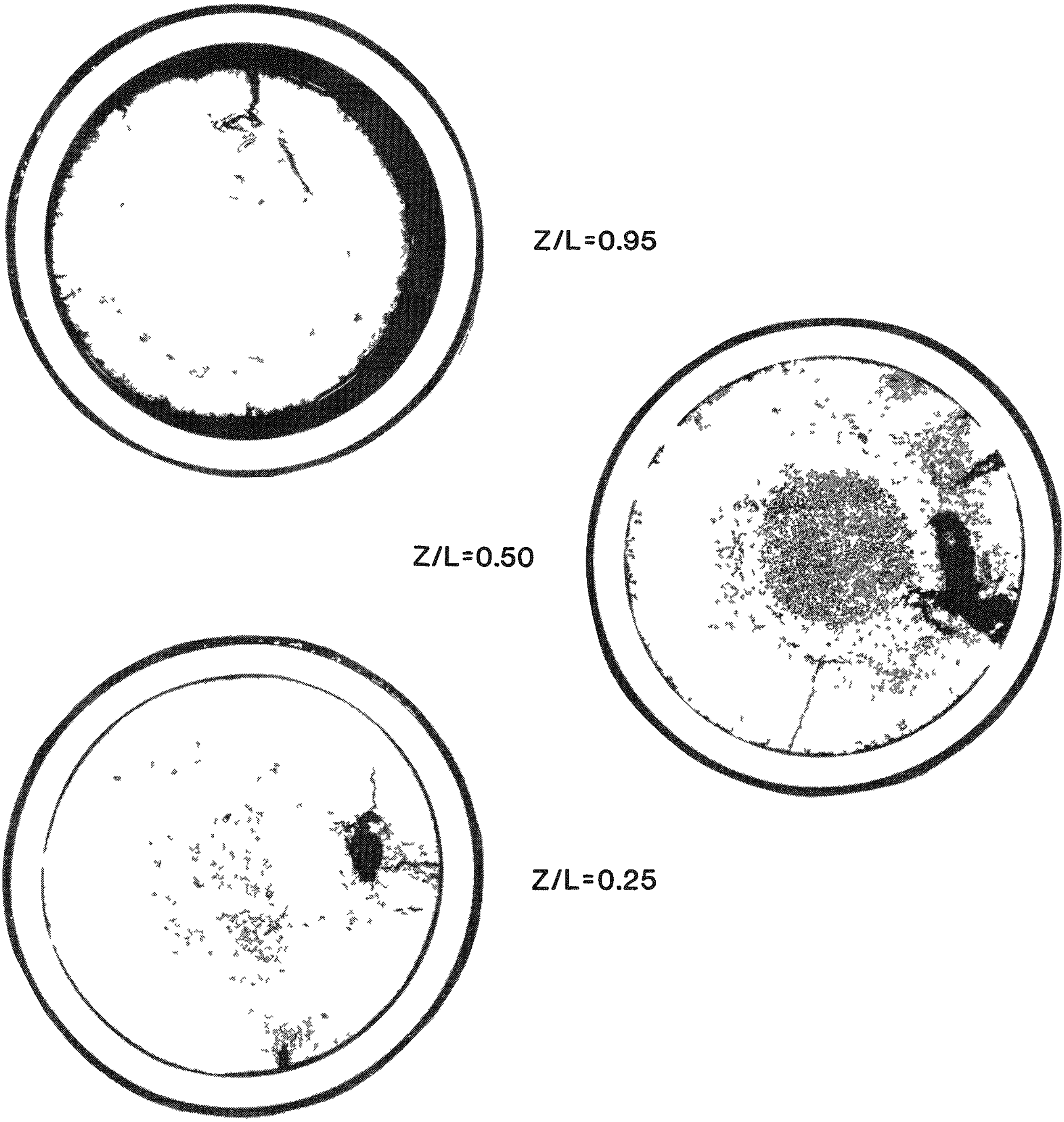

Fig. 2.1a. Untested Sibling to the 0.8 at.% Burnup (D9-Clad) U-19Pu-10Zr Fuel Pin Tested in TREAT Test M5

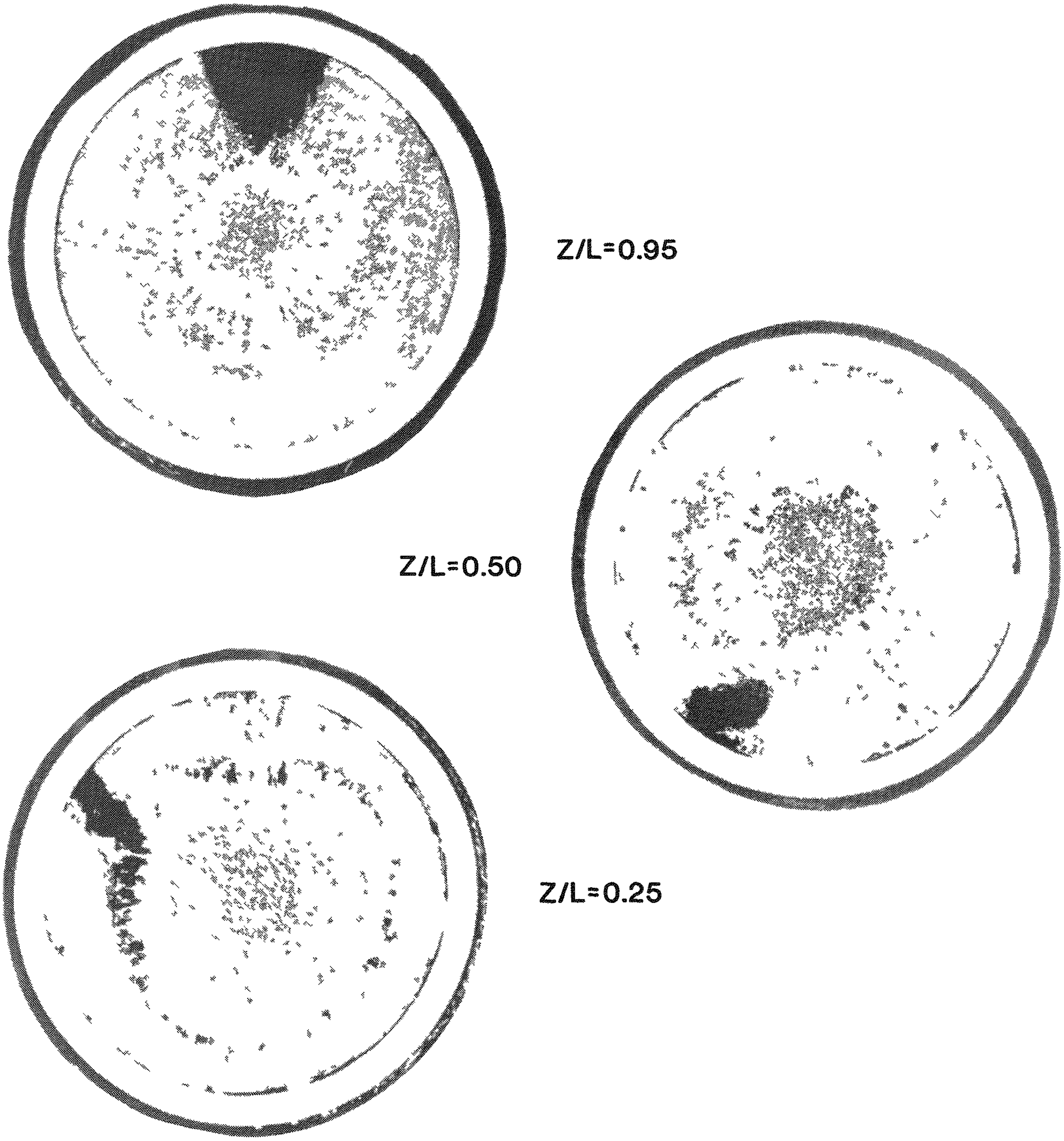

Fig. 2.1b. Untested Sibling to the 1.9 at.% Burnup (D9-Clad) U-19Pu-10Zr Fuel Pin Tested in TREAT Tests M5 and M6

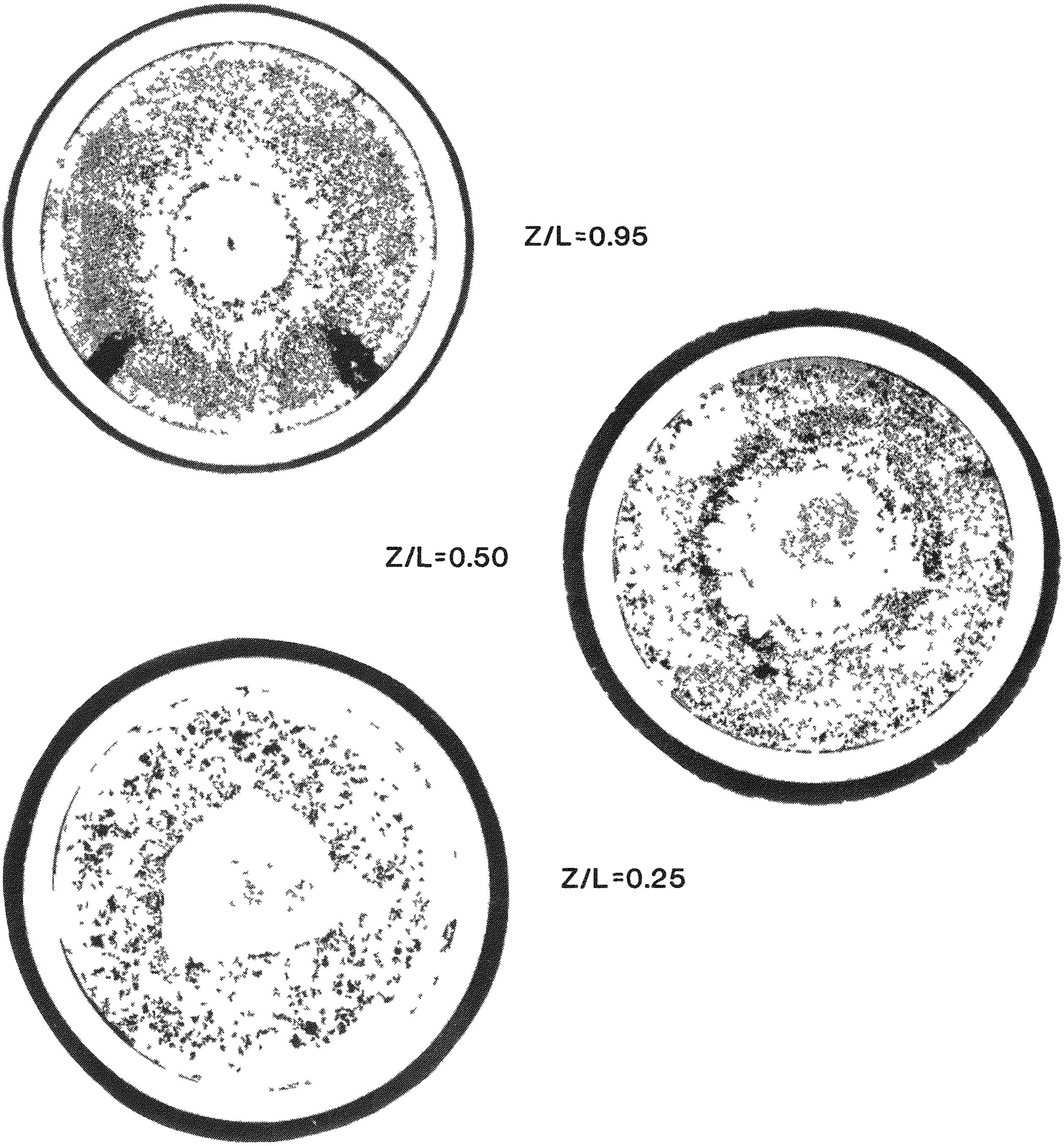

Fig. 2.1c. Untested Sibling to the 5.3 at.% Burnup (D9-Clad) U-19Pu-10Zr Fuel Pin Tested in TREAT Test M6

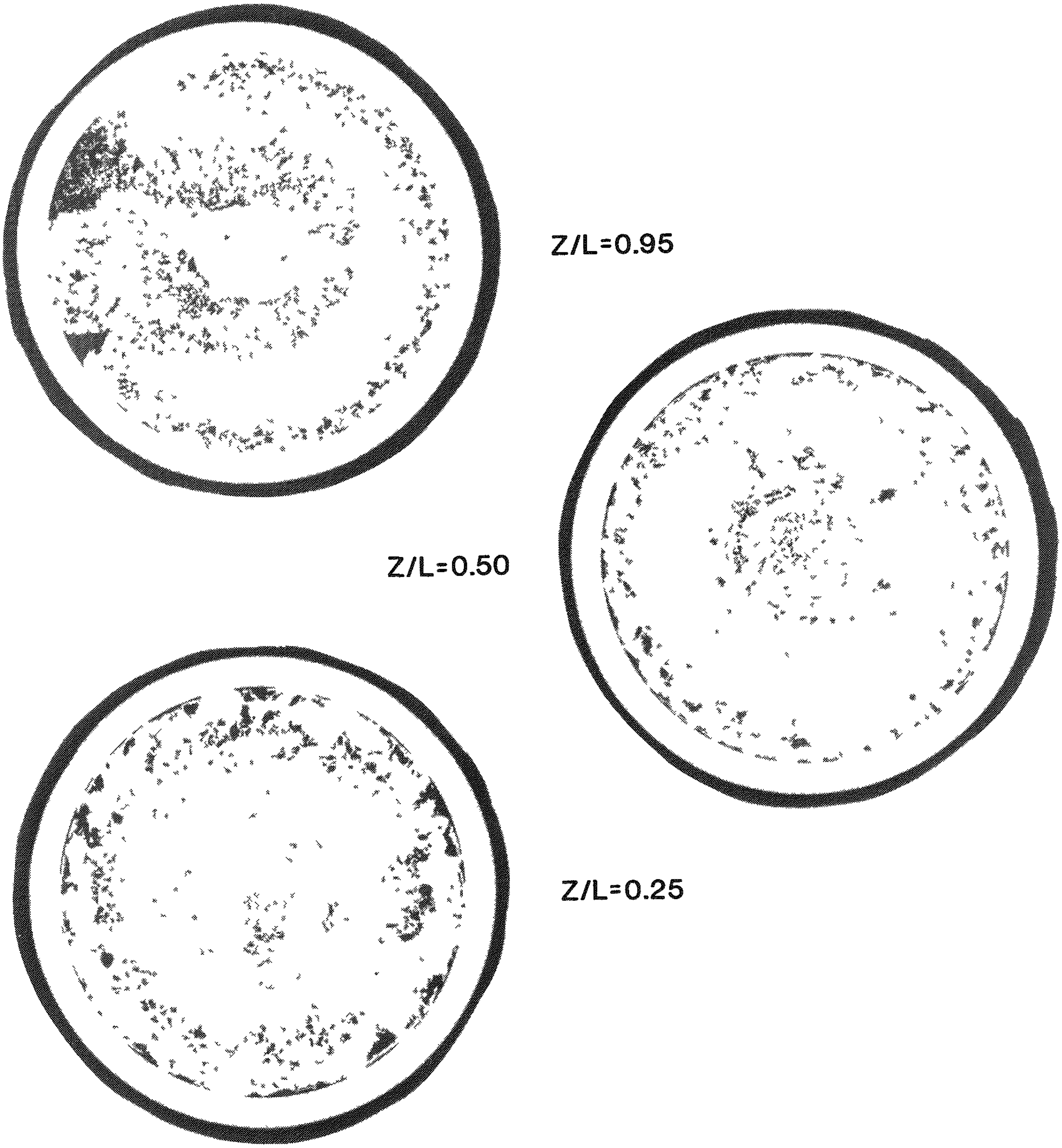

Fig. 2.1d. Untested Sibling to the 9.8 at.% Burnup (D9-Clad) U-19Pu-10Zr Fuel Pin Tested in TREAT Test M7

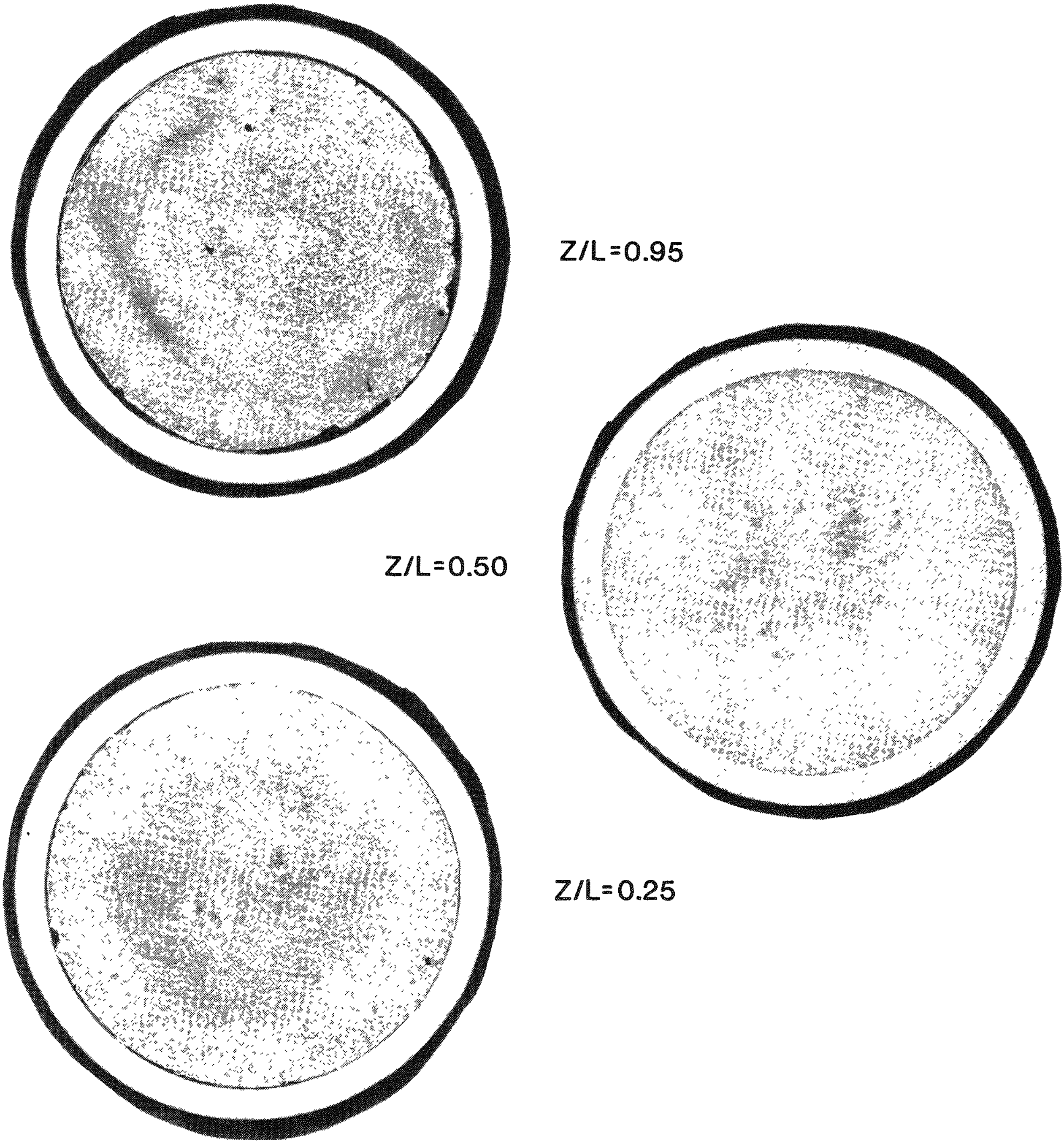

Fig. 2.1e. Untested Sibling to the 2.9 at.% Burnup (HT9-Clad) U-10Zr Fuel Pin Tested in TREAT Test M7

Table 2.2. Approximate Characteristics of Irradiated M-Series Fuel

Fuel Alloy	U-19Pu-10Zr	U-10Zr	U-5Fs
Peak Irradiation Power Level (kW/m)	38	38	25
Measured Gas Retention- as generated in the indicated burnup (at.%)	~0.5	~0.5	2
Burnup When Swelling Saturates (at.%)	1	1	2
Measured Axial Swelling (% of original height)	2-3	8-9	4-5
Swelled Fuel Volume (% of total fuel volume)	29	32	28
Measured Sodium Infiltration (% of total fuel volume)	8	13	6
Thermal Conductivity @ 1000 K (W/cm-K)			
avg. 0 at.% (fresh)	0.23	0.34	0.40
burnup 2 at.%	~0.15	~0.21	~0.20
10 at.%	~0.20	~0.30	~0.33
Melting Point (K)			
Solidus	1350	1508	1283
Liquidus	1515	1678	1373
Measured Gas Plenum Pressure at Room Temperature at the indicated peak burnups (MPa)			
peak 0 at.% (fresh)	0.10	0.10	0.10
burnup 5 at.%	2.3	2.3	2.5
10 at.%	5.1	5.1	6.0

3.0 FACILITIES AND TEST HARDWARE

3.1 Major Facilities

TREAT, located at ANL-West in the Idaho National Engineering Laboratory (INEL), is a uranium and graphite fueled reactor with a near-thermal neutron spectrum. A cutaway view is shown in Fig. 3.1. Its two pairs of fast-operating computer operated control rods provide capability of a wide range of power transients appropriate for reactor safety studies. A forced air cooling system provides a limited heat rejection capability at low power levels. However, in the high power transient mode most commonly used for safety testing, the reactor heats up nearly adiabatically. While adiabatic core heating contributes significantly to safe operation, it also results in limits to transient energy deposition due to both maximum allowable core temperatures and large negative reactivity feedback. In M-series, transient energy deposition in the test fuel was limited to the equivalent of several tens of seconds of full power operation.

Most experiments performed in TREAT require use of the fast neutron hodoscope, also shown in Fig. 3.1. The TREAT hodoscope is a diagnostic system that looks through a slot in the TREAT core to collimate and detect fast neutrons directly produced by fissions in the test fuel. Analysis of this data results in a history of test fuel motion in two dimensions. Fast neutrons from the test fuel can be generally distinguished from the dominant background of thermal neutrons from TREAT by their energy. In M-series, the hodoscope was used in conjunction with a full slotted core (core slots both in front of and behind the test hardware). Such a configuration reduces the maximum energy deposition, but minimizes background and provides the highest possible accuracy in fuel motion detection.

Many test support operations involving highly radioactive irradiated fuel pins and handling their remains need to be performed in a hot cell environment. In M-series such work was performed at hot cell facilities located both in ANL-West (Idaho) and ANL-East (Illinois). The Hot Fuel Examination Facility North (HFEF) at ANL-West provided in-cell facilities to assemble and disassemble experiments on irradiated fuel. In addition, non-destructive

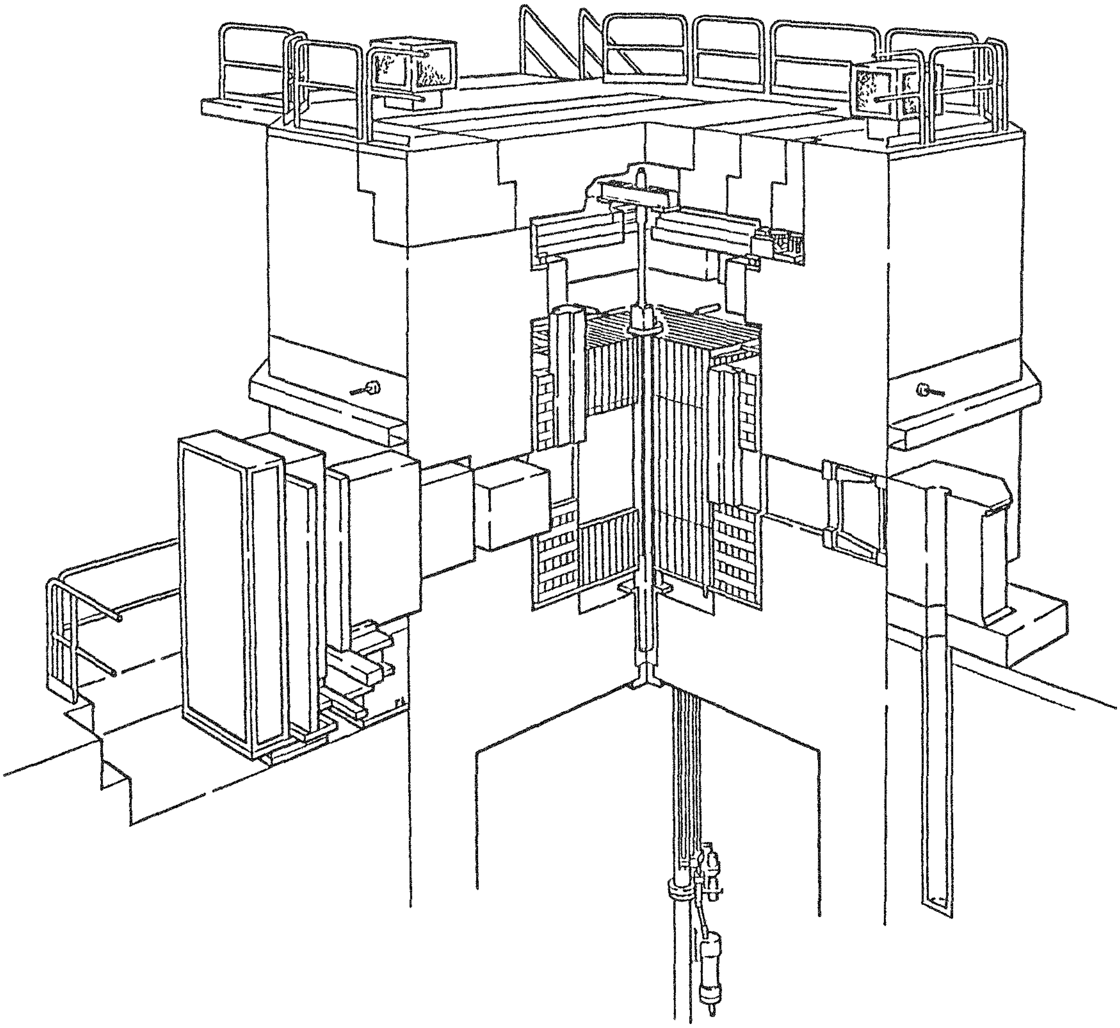

Fig. 3.1. TREAT Reactor "Cutaway" Showing Test Cavity at the Center and Hodoscope Slot and Detectors on the Left

radiography and profilometry of test fuel was also performed both pre- and post-test. Destructive examination of M-series remains, including both failed and unfailed pins was undertaken at the Alpha Gamma Hot Cell Facility (AGHCF) at ANL-East.

3.2 M-series Test Hardware

The sodium loop used in TREAT for Argonne's LMR safety experiments in recent years has been the Mark-III vehicle [3.1]. Figure 3.2 shows the Mark-III loop as configured for tests M5-M7. In essence it is an elongated loop of thick-walled stainless steel pipe through which liquid sodium is circulated by means of an electromagnetic pump. Two parallel legs of the loop are 3.5 m long with center-to-center separation of about 0.1 m. The entire system is housed in a long rectangular container of cross section dimensions 10 cm by 20 cm. designed to occupy the space of two TREAT fuel assemblies at the center of the reactor (see Fig. 3.1). The Mark-III vehicle is intended to be generic to a wide variety of test fuel types and bundles. A removable "test train" in one leg of the loop contains an instrumented test fuel configuration that addresses specific requirements of different programs. This "test leg" of the loop also includes an extension which serves as a gas plenum and provides the entrance through which the test train is inserted into the loop. The other leg of the loop includes a small annular linear induction pump to drive the sodium coolant. In operation, sodium flows upward past the test fuel. Thermal-hydraulic conditions in the loop are measured by three permanent magnet flowmeters, two pressure transducers, and numerous thermocouples.

Turning to the specific test train concepts used in M-series, axial lengths were guided by the fact that all test fuel in the program was preirradiated (or designed for irradiation) in EBR-II. The fueled length of all pins tested was therefore restricted to the EBR-II core-size of 34 cm. Each pin was located in a separate stainless steel flowtube, with the particular division of total loop sodium flow chosen to achieve the particular objectives for each pin. This division was achieved by properly sized orifices installed near the entrance to each flowtube. Lateral separation of test pins was as wide as possible to minimize the neutron shielding of one pin

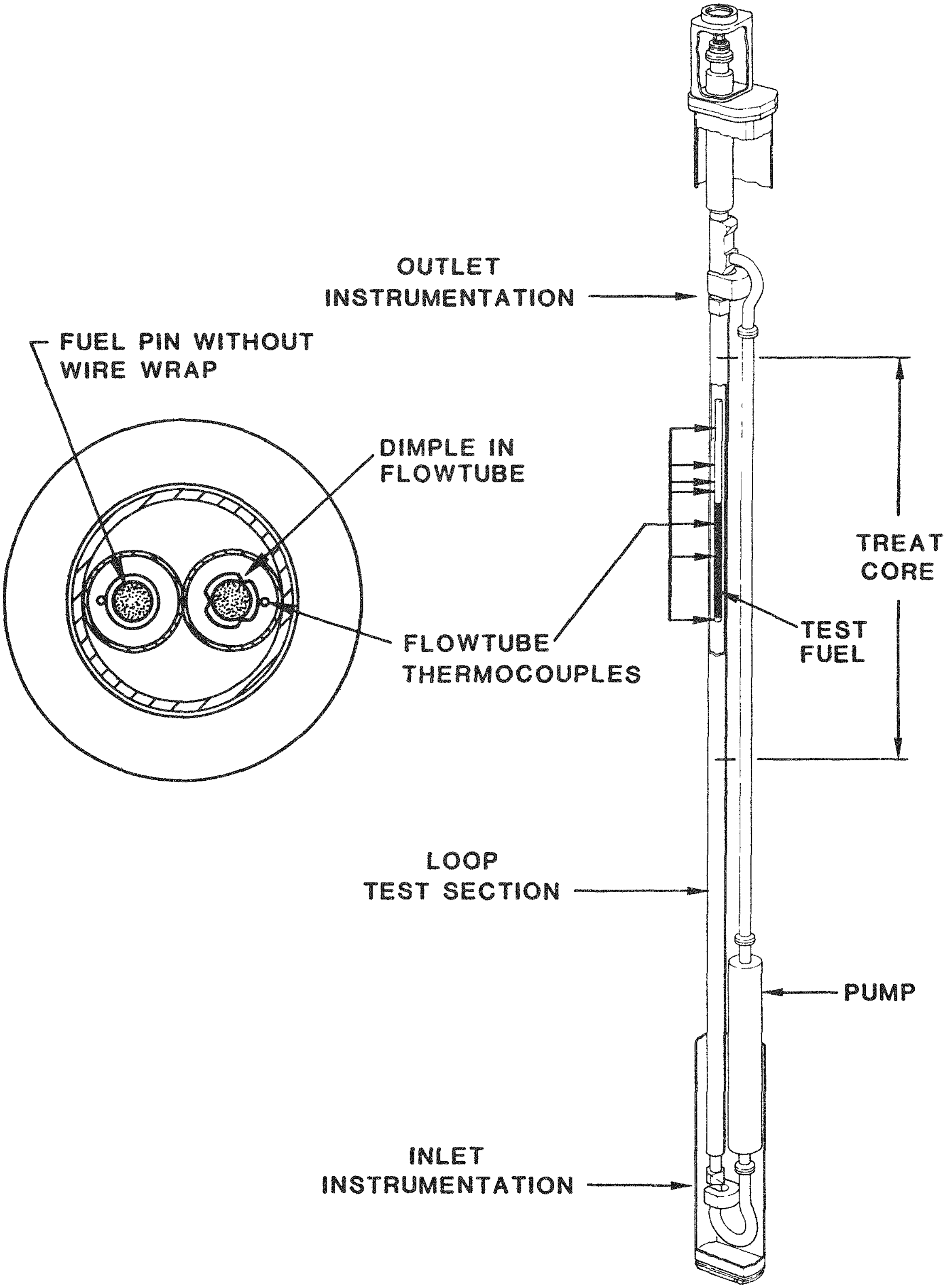

Fig. 3.2. Mark-III Integral Sodium Loop Configured with Two Fuel Pins as in Tests M5, M6, and M7

by another and to enhance the ability of the hodoscope to resolve individual test pins as individuals. The number of pins per test was determined principally by the bore diameter of the Mark-III sodium loop. Three of the smaller diameter U-Fs fuel pins could be accommodated per test, whereas only two IFR reference pins could be accommodated in M5-M7. Further details of the M5-M7 configuration are described in Appendix A.

Coolant temperatures at the outlet and along the fuel zone were measured using thermocouples attached intrinsically to the outer surface of each flowtube. (An illustration is shown later in Fig. 3.4.) Flowtubes were made as thin as possible (less than 0.5 mm) so that the test fuel and the flowtube-mounted thermocouples would be as closely coupled thermally as possible. Flowtubes were thermally isolated from each other and the rest of the test hardware by an additional "shield tube" placed around each flowtube with low-conductivity inert gas in between. The "shield tube" would also serve to prevent large amounts of debris released from one failed flowtube from damaging an adjacent flowtube. So far, these latter "protective" features of the shield tubes have not been needed in the four M-series tests performed where fuel pins failed. Flowtube breach occurred in only a single instance and was scarcely detectable.

The ability to reuse expensive and slow-to-build test hardware contributed to the timely performance of the test program. All six M-series experiments were performed in only two test loops. Test trains were reused following the two experiments where test fuel did not fail. However, because debris from failed fuel remained largely confined to the removable test train, it was practical to reuse loops even after pin failures. Hardware performance in every case demonstrated a high degree of reliability; however, some problems did occur in hydraulically "seating" test trains in loops which had been used several times. These problems were attributed to debris accumulation in loop sodium, but, in each case, seating difficulties were resolved in advance of experiment performance.

Although the principal instrument of nuclear diagnostics at TREAT is the fast neutron hodoscope, attempts have also been made to detect release and transport of fission products from failed fuel. During tests M5-M7 fission

---

products from failed fuel that were transported to the loop cover gas region were measured by the Fission Product Detection System (FPDS). These measurements detected gamma rays emitted by fission products Rb-89, Cs-138 and Xe-138 in the loop cover gas region that likely originated from the beta decay of Br-89 and I-138 expelled into sodium when fuel pins failed. A schematic of the FPDS is shown in Fig. 3.3. In this present arrangement, ability to detect radioactive fission products and delayed neutrons is very limited and, because of background, no measurements can be made until after the power transient is over. It is intended that measurements such as these will assist the development of more general source term diagnostic capability for the TREAT facility.

3.3 New Hardware Features Introduced in M5-M7

A new two-pin test train was used as depicted in the M-series hardware configuration shown in Fig. 3.2. This test train contained some new or enhanced hardware features in the areas of 1) thermocouple mounting, 2) pin support, and 3) coolant flowrate measurement which are briefly discussed here. Further details may be found in Appendix A.

In all M-series tests, thermocouples were intrinsically mounted on a vertical line on the outside of each flowtube along the active fueled length of the test pins. These thermocouples were used to determine coolant temperature rise with axial height. In M5-M7, improved accuracy of measured whole-pin coolant temperature rise was achieved by locating some thermocouples at several elevations above the active fuel to allow a maximum of thermal mixing in the coolant to be reflected in the temperature rise measurement.

Design improvements have also evolved in the area of test fuel support. In the earlier tests, M2-M4, wire-wrapped pins had been tested directly in smooth flowtubes. Metal fuel pins are mechanically weak at high temperature and a single wire-wrapped pin in a smooth flowtube provides poor support against distortion. It was believed that this method of support permitted pin bowing and flexing that caused both unexplained temperature oscillations at high temperature and hard-to-analyze irregularities and/or periodicities in the measured axial temperature rise at all temperatures [1.5]. To help

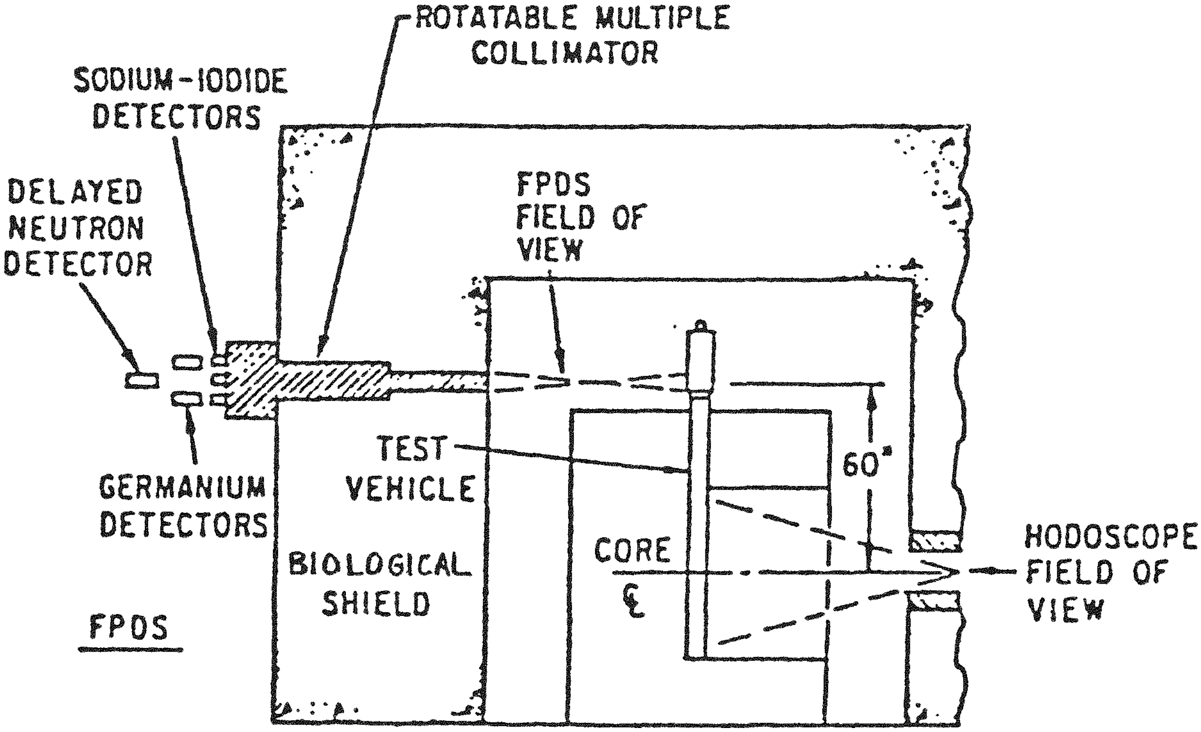

Fig. 3.3. Schematic Arrangement of Fission Product Detector System (FPDS) in TREAT

alleviate these problems in M5-M7, test pin wire-wraps, which had provided spacing and support during the EBR-II preirradiation, were removed. Pin support was provided, instead, by "dimples" in the flowtube spaced at ~10 cm axial and 120-deg azimuthal increments. While this new mounting scheme did not provide a coolant flow and contact pattern prototypic of a wire-wrapped pin in a large bundle, it was intended to provide the test fuel a commensurate level of resistance to warping and distortion. Improvements with this new mounting scheme were noted, but some irregularities and high-temperature oscillations remained in M5 and M6 data. These remaining problems were attributed to the fuel pins not being sufficiently centered. Consequently, in M7, the axial spacing between supporting dimples was decreased. Also, the dimple depth was increased to provide the greatest possible centering consistent with a minimal clearance needed to insert test pins within the tube. These modifications significantly reduced observed temperature anomalies in M7. By way of illustration, Fig. 3.4 shows the effect of improved pin-support methods on temperature measurements made along the test pin flowtube.

Additional attention was also given to reducing uncertainties in the measurement of coolant flow past each test pin. Combined sodium flowrate during a test is measured by calibrated permanent-magnet flowmeters at the inlet and outlet of the test section as well as in the pump leg of the loop. In the initial M-series tests flow division among test pins was inferred on the basis of symmetry and separate hydraulic measurements performed out-of-pile. However, beginning with M5, two "miniature" permanent-magnet flowmeters were also located near the inlet of each individual flowtube. Although the absolute sensitivities of these flowmeters were not determined, both were identical in design and layout so that the ratio of their output signals was used to determine the ratio of flowrates in the two tubes.

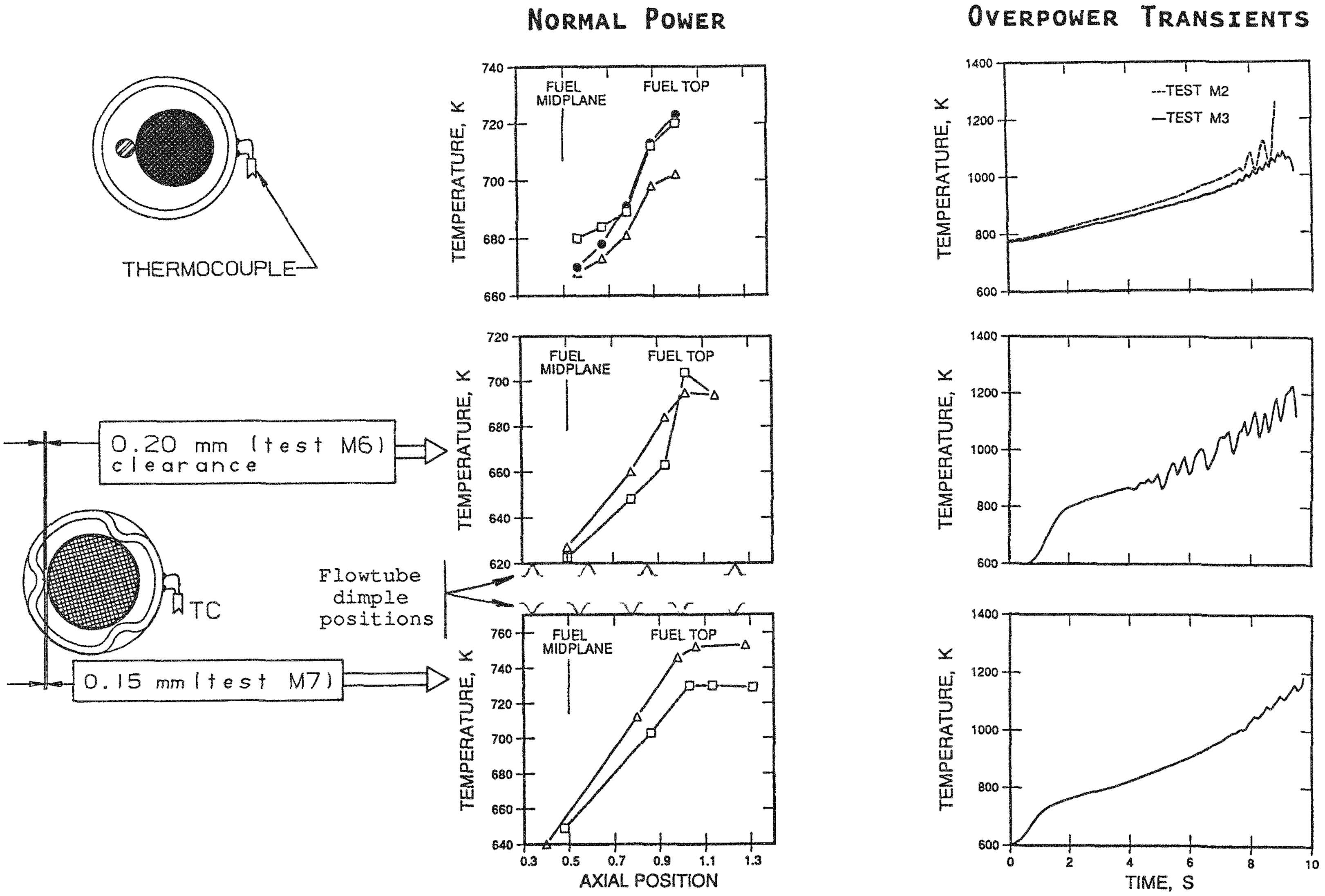

Fig. 3.4. Transient Temperature Measurement and Fuel Pin Support

4.0 TEST DESIGN AND TECHNIQUES

4.1 General Features

The design of all M-series tests included several general features that are discussed in this section. Low power, non-destructive operation verified equipment performance as well as the neutronic coupling of the test fuel to the TREAT reactor. The subsequent overpower transient was designed to generate thermal conditions in test fuel that mimic fuel overheated under fast reactor conditions. Finally, the overpower transient was terminated quickly enough to preserve conditions which existed at the peak of the overpower.

Heat balance transients run at constant power and flowrate were performed before each overpower transient to provide an integrated check of the thermal-hydraulic operation of the entire experiment system including the reactor, test fuel and sodium loop. However, a key measurement made during the heat balance was a coolant temperature rise from inlet to outlet under true steady-state conditions. This temperature rise provided a direct, in situ measurement of each test pin's "P/F" ratio of test fuel power (P) to coolant flowrate (F), bypassing uncertainties in reactor to test fuel power coupling, division of flow between flowtubes, etc.

For example, Fig. 4.1 shows the power history, total coolant flowrate and temperature rise past a ternary fuel pin measured at different axial elevations during an M7 heat balance. The results shown are typical of heat balances performed in the test series. The various thermocouples attached to the flowtube above the active fuel height ($X/L > 1$) agree closely and may be used to determine a whole-pin temperature rise midway through the power transient. In this example the temperature rise achieved was about 141 K (or P/F ratio of 0.94 times a nominal value of 150 K - see below) at a reactor power of ~46 MW at a total coolant flowrate of ~162 cc/s.

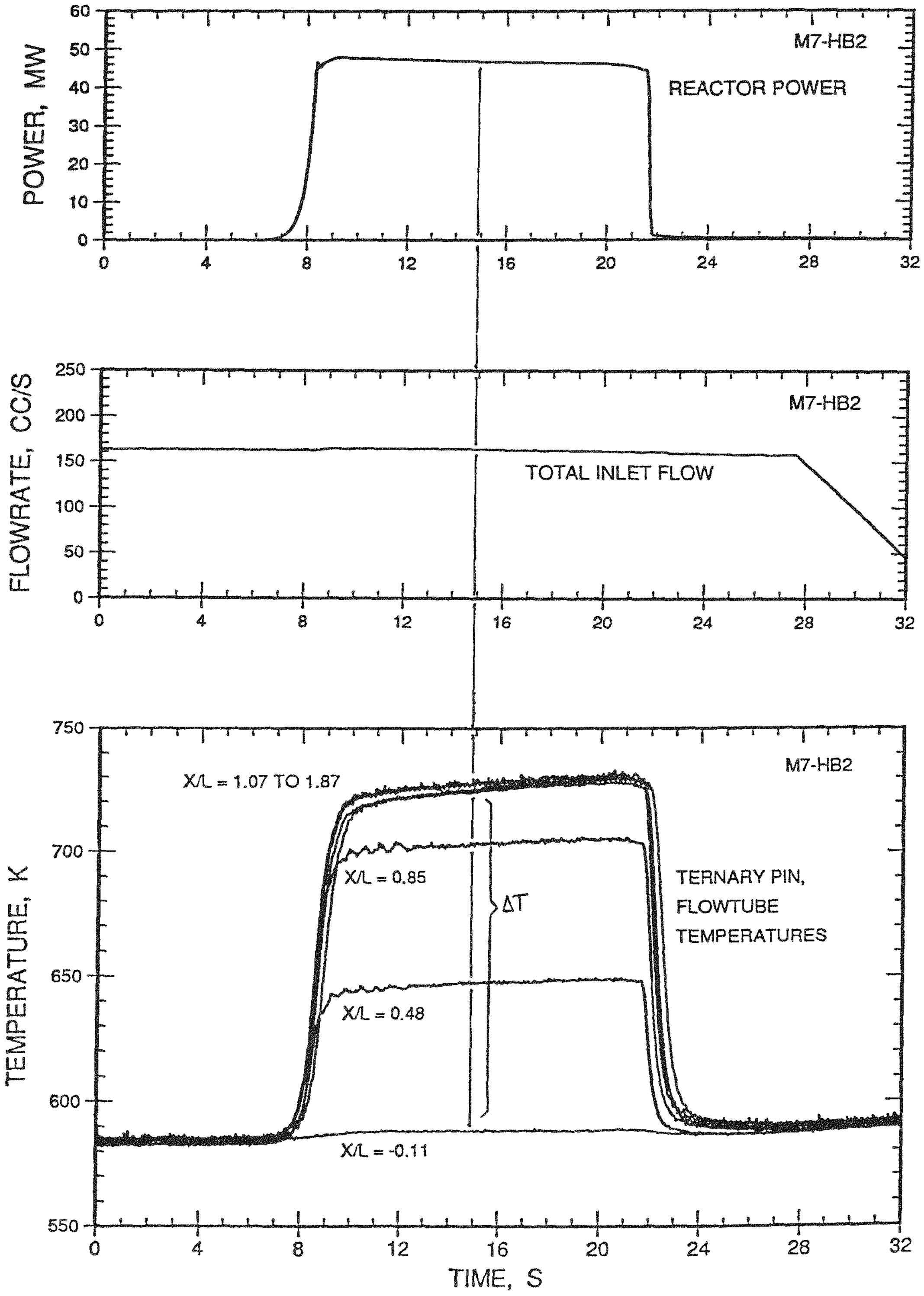

Fig. 4.1. Performance of a Typical M-series Heat Balance (M7); Measurement of Coolant Temperature Rise at Steady Power and Flow

In the analysis of M-series overpower transients the P/F ratio is probably the most important single parameter that can be used as a measure of severity. This follows basically because the key phenomena controlling safety issues (Sect. 6) are either driven by or closely correlated with peak coolant temperature, and the thermal response of a fuel pin is sufficiently fast that coolant temperatures are very close to steady-state values determined by P/F. Unfortunately, rapidly changing temperatures during overpower transients preclude direct measurements of P/F, as was described above for heat balances.

However, because operating conditions of the heat balance and ensuing overpower transient were in many respects identical a straightforward proportioning technique was employed to extrapolate P/F measurements made in a heat balance to P/F levels achieved during the subsequent overpower transient. Specifically, P/F (final) was obtained by multiplying the measured P/F ratio in the heat balance by the appropriate ratio of measured reactor power--(final to heat balance) and the appropriate ratio of measured flow--(heat balance to final).

All peak overpower levels given in this report were obtained in this manner and, based on consistency of measured temperature rises, are believed accurate to about the 3% level. This same technique also enabled the peak P/F values obtained in each overpower transient to be "fine tuned" just prior to the test by appropriate adjustment of the applied flowrate and/or reactor power transient. Finally, once the coolant flowrate past a test pin has been determined, the P/F measurement in the heat balance also determines the pin-average power coupling of the reactor to the test fuel (Sect. 4.2 below).

In performing the final overpower transients, all test fuel in this series was subjected to similar overpower conditions: full coolant flow and an exponential power rise on an 8 s period. The 8 s period was chosen as the slowest transient possible that would commence from near-nominal and carry through to cladding failure within the energy deposition limitations of the TREAT reactor. A "high" system pressure $\gtrsim 4$ atm prevented coolant boiling prior to cladding failure. Baseline thermal conditions in the test fuel were referenced to nominal conditions in a fast reactor. These include a peak linear power rating of 40 kW/m (12 kW/ft), an inlet temperature of 630 K and a

150 K coolant temperature rise. The power transient was rapidly terminated upon detection of cladding breach or, by using previously measured failure thresholds, just prior to failure.

In terminating the final overpower transient, "quenching" the fuel at incipient failure or immediately after failure was important to preserve the state of the fuel at that "instant" for post-test examination. Due to the high conductivity of the metal fuel such quenching occurred essentially upon reactor power shutdown.

By experience, sudden measurable changes in coolant flow have provided the fastest and most reliable indicators of pin failures. Therefore, a system was designed whereby a sudden and substantial decrease of the total sodium flowrate measured at the inlet (characteristic of coolant channel pressurization upon pin failure) induced an electronic device called the "shutdown signal generator" to output a signal triggering reactor shutdown. Figure 4.2 illustrates how the shutdown system worked using data from test M6 as an example. Note that the system was sufficiently sensitive to detect failure in only one flowtube. The "shutdown" signal was sent within ~10 ms of pin failure, and the reactor power began to decrease less than ~50 ms later. Further details of transient shutdown are found in Appendix F.

4.2 Power Calibration and Heat Balance Transients

Before the test conditions of any experiment can be set or any posttest analysis takes place, an accurate determination must be made of the coupling of the test fuel to the power generated by the TREAT reactor. Determinations must be made on a whole-pin basis as well as radial and axial distributions within a fuel pin. A complicating feature of M-series testing was a significant variation of power coupling among the various test pins due to differences in initial fissile content, wide ranges of test pin burnup, and significant morphological changes in the fuel with that burnup. A variety of techniques, both experimental and analytical, employing considerable redundancy and cross-checking were used to determine power couplings in M-series. Fundamental estimates made use of specially performed calibration experiments with fresh fuel and flux monitor wires, supplemented by analyses

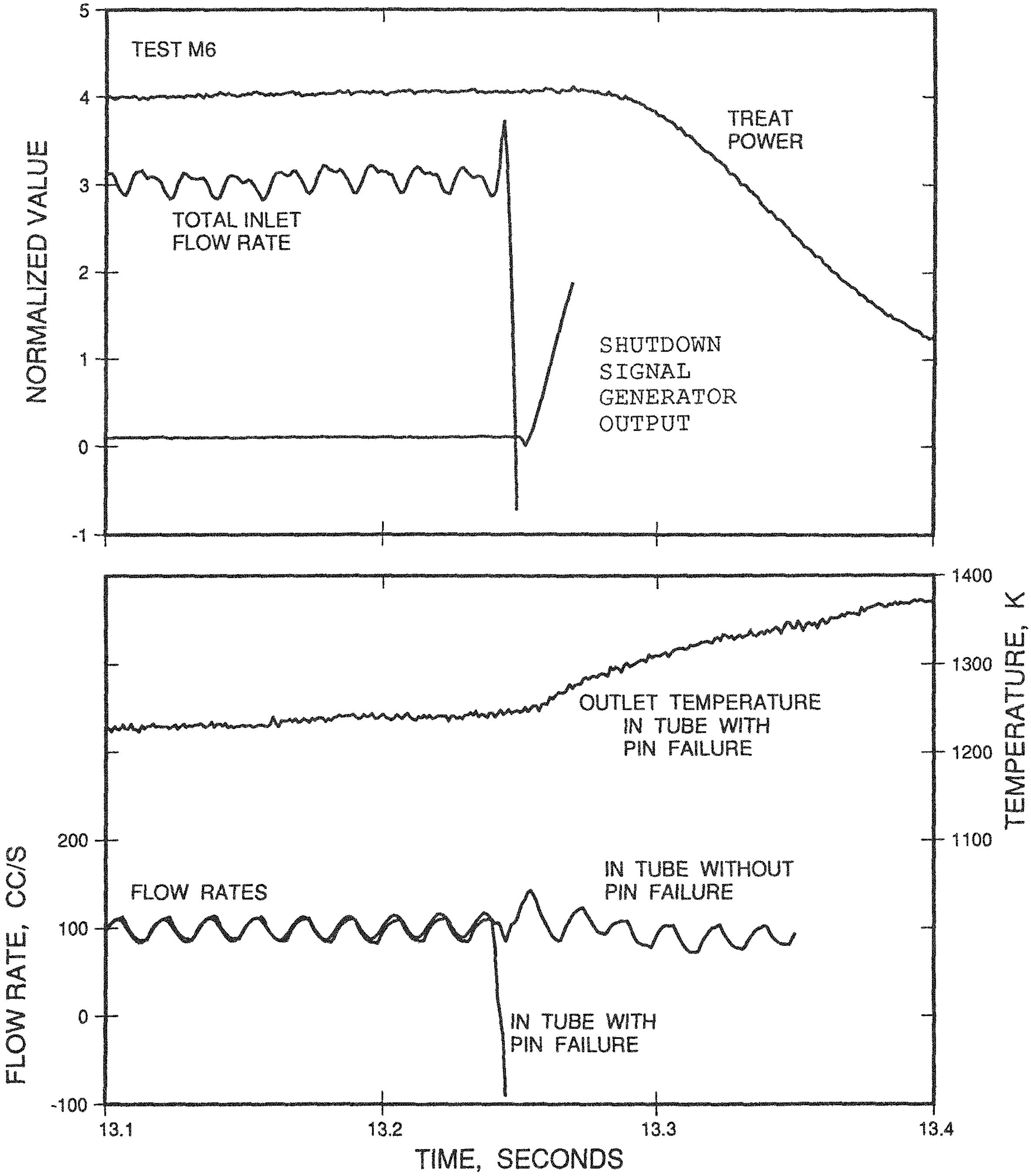

Fig. 4.2. Operation of the Shutdown Signal Generator During M6

to estimate radial distributions and neutronic effects of burnup and swelling. Independently, analysis of the measured coolant temperature rise during the heat balance produced an independent whole-pin power coupling estimate. Additional details may be found in Appendices B, C, and Ref. 4.1.

Fundamental calibration work commenced with special steady-state low-power in-pile calibration irradiations on fresh fuel performed in neutronic mockup hardware. Test fuel fissions were counted using nuclear chemistry and compared to the measured energy release in the reactor. Measured axial peak power coupling in fresh fuel tested in M5-M7 were 4.9 and 5.3 W/g per TREAT MW for ternary and binary fuel, respectively. The axial shape of the power coupling was controlled by a series of dysprosium flux shaping collars (Appendix A) designed to mimic a power shape appropriate to a fast reactor. This power shape was measured directly and found to have an axial peak to average of 1.095. In M-series, calculations were used to determine the radial dependence of test pin power with typical results described below in Sect. 4.3. Extrapolation from fresh to irradiated fuel required both neutronic analyses as well as accurate knowledge of morphological changes with burnup (Sect. 2). Fuel swelling, itself, leads to calculated increases of about 13%, whereas burnup of fissile isotopes lead to calculated decreases of about Bu/2 in percent, where Bu is fuel burnup in at.%.

Test transients in TREAT utilize power levels two and three orders of magnitude higher than those used in the special low power calibration measurements. Power coupling values measured at low power may require adjustment to be applicable to higher power irradiations. This is due to various differences in reactor operations at low and high power, including different control rod positions, different reactor power meters etc. Adjustment of measured results to high power was accomplished by irradiations of low enrichment flux monitor wires at both low power steady-state and in high power experiment transients, combined with the assumption that fuel fissions would be proportional to monitor wire fissions. In M5-M7, the measured correction factors for high power found in this manner (termed "transient correction factors" or TCF's) ranged from 0.89 to 0.92. There is no strong evidence that the in-pin axial power distribution measured at low power is significantly different at high power, and the adjustment is considered a normalizing factor applied to the fuel as a whole.

After building a sufficiently large data base of TCF's in high power transients it became possible to correlate the particular TCF value during each transient to the average control rod positions during that transient. The significant control rod motion that takes place during a power transient suggests that power coupling corrections are actually time dependent. Consequently, the correlation of TCF and average control rod position was used to calculate an instantaneous power coupling correction as a function of instantaneous TREAT transient rod position. Reported adjustments of the low-power coupling data to high-power situations were then done in two ways: first the average correction for a particular power transient (TCF) is reported as part of the test pin power coupling, and then a time dependent "rod shadowing factor" or RSF is included as a small (in this case several percent) correction to transient reactor power which averages to unity over the course of the entire transient.

Statistical errors due to the various measurements total around 4-5% in estimating a pin-average power coupling [4.1]. Calculated effects of burnup and restructuring on power coupling can be large and of opposite signs. The accuracy of such calculations depends chiefly on the accuracy of the irradiated pin characterization. Systematic errors are thus potentially large and difficult to estimate.

Independent power calibration measurement on actual test fuel in the actual test configuration, in situ is possible during the heat balance provided the coolant flowrate past each test pin is known. As described in the previous section (4.1),, performance of the heat balance transient is a central element of experiment design and test performance, acting as a reduced power version of the subsequent overpower transient. In the heat balance the measured temperature rise directly indicates each test pin's P/F ratio which results from application of a known reactor power and measured coolant flowrate. Multiplying the measured P/F by that known flowrate gives the total pin power. Dividing that pin power by the known reactor power then yields the whole-pin power coupling. Based on estimates of the precision of various factors needed in the calculation (Appendix B, Table B.2), the precision of this determination turns out to be similar to that of the more fundamental calibration work described above, roughly 5%, but with less potential for serious systematic errors.

For purposes of comparison with power couplings obtained from fundamental methods, axial peak values may be found by multiplying by the measured peak-to-average ratio. Also, values appropriate to final overpower transients are found by multiplying by the ratio of "heat balance to final" TCF's.

Table 4.1 compares axial peak values of the power coupling factor appropriate to the final overpower transient obtained from the fundamental methods with values obtained in situ from the heat balances. With a single exception, agreement between the two determinations is quite good and is within ~6%. It should be emphasized that these determinations are quite independent and their agreement provides good corroboration for the diverse methods involved. The single exception shows a heat balance determination ~20% below what was expected from fundamental considerations for a 9.8 at.% ternary pin in test M7. To provide an independent (also in situ) check in M7, scan data from the fast neutron hodoscope was used to determine relative power generation in the two M7 test pins. The ratio of binary to ternary pin power generation in M7 was measured to be ~1.31 corroborating the heat balance expectations of 1.34 but in disagreement with the estimate of 1.11 from the fundamental work. Further details may be found in Appendix B.

The underlying reason for the single large disagreement in Table 4.1 is not fully understood. However, there are strong indications when burnup is high, restructuring is such that the radial distribution of fissile uranium and plutonium are non-uniform and skewed toward the center of the pin. Non-uniform distributions such as this would have little effect in a fast reactor but could lower power coupling significantly in a thermal reactor like TREAT. Unfortunately, such distributions are difficult to quantify and were not taken into account in the Table 4.1 estimates.

For purposes of subsequent analysis both the pin-average power coupling and primary measurements of test pin P/F ratio are taken from temperature rise

Table 4.1. Axial Peak Test Fuel Power Coupling Factors

			Estimates of Power Coupling (W/g per mW TREAT)	
Fuel Type	Test	Burnup (at.%)	Fundamental	In Situ
U-19Pu-10Zr	M5	0.8	4.65-4.95*	4.95
	M5	1.9	4.92	4.91
	M6	1.9	4.98	4.96
	M6	5.3	4.93	4.94
	M7	9.8	5.12	3.97
U-10Zr	M7	2.9	5.66	5.31

*Reflects uncertainty in the amount of pin swelling.

measurements made during the heat balances. Referring to Table 4.1, in situ power coupling estimates are thus preferred over those derived from fundamental estimates. To summarize the reasons given above, the precision of the two methods is comparable and agreement between the two methods is generally good. However, fundamental estimates do involve large calculated extrapolations with potential for large systematic errors. In the one instance of a significant difference, fast neutron hodoscope scan measurements tended to support the heat balance measurement.

All other features of power coupling, such as high power transient correction factors, rod shadowing factors, and in-pin power distributions are taken from fundamental measurements and calculations. Because pin-average power coupling is based on heat balance determinations absolute TCF's are not significant, only the differences between heat balance and final overpower transients.

4.3 "Enhancement" of Power and Flowrate

Strong radial self-shielding of the TREAT thermal neutron flux by the test fuel causes a disproportionate fraction of power to be generated near the fuel surface with a surface-to-center ratio of about 3 to 1. By contrast, power generation in a fast reactor is spatially uniform over a radial cross section of a fuel pin. In order to generate radial temperature gradients during M-series TREAT transients prototypic of those that would be generated in a fast reactor, it becomes necessary to increase the net power generation of the TREAT test relative to that of the fast reactor reference. Under the quasi-steady-state conditions which characterize these transients, the TREAT power increase is an "enhancement" factor which depends on the details of the radial power dependence and test fuel thermal conductivity. For the test fuel used in M5-M7 this enhancement factor turns out to be ~1.40. However, it is also important to maintain a prototypic coolant temperature rise at any axial location, so coolant flowrate should be increased by precisely the same enhancement factor. Thus, a prototypic power-to-flow ratio is maintained. Finally, the additional heat (~40%) generated within the test fuel in TREAT causes a corresponding increase in the temperature gradient across the cladding. This temperature increase was compensated by a decrease in coolant inlet temperature (~50 K in M5-M7).

In practice, in a transient simulation where power rises steadily it was merely necessary to appropriately lower coolant inlet temperature and increase the coolant flowrate from fast reactor reference values by the appropriate enhancement factor. The benefits achieved by this technique are significant improvement in the prototypicality of computed fuel and cladding temperature of M-series tests. By way of illustration, Fig. 4.3 shows that with test condition "enhancements" calculations of peak test fuel melting (which are typical of all M-series tests) show close correspondence to a fast reactor prototype case. Without enhancement, such correspondence is only approximate.

4.4 Analysis Tools and Methods

Most of the phenomena under study in M-series are either directly driven or strongly influenced by transient thermal conditions produced in the tests. The rather few thermocouples on flowtube walls and at the ends of the test section necessitates significant analysis to fill in details of fuel, cladding and coolant temperatures. Thus, a primary focus of test analysis is thermal hydraulic with the aim of obtaining as accurate a thermal history of each test as possible on the basis of input power and coolant flow. The analyses reported here provide primary thermal input for further analyses of pre-failure fuel expansion and cladding damage and failure. Comparison of measured with calculated temperature along the flowtubes serves as a partial validation.

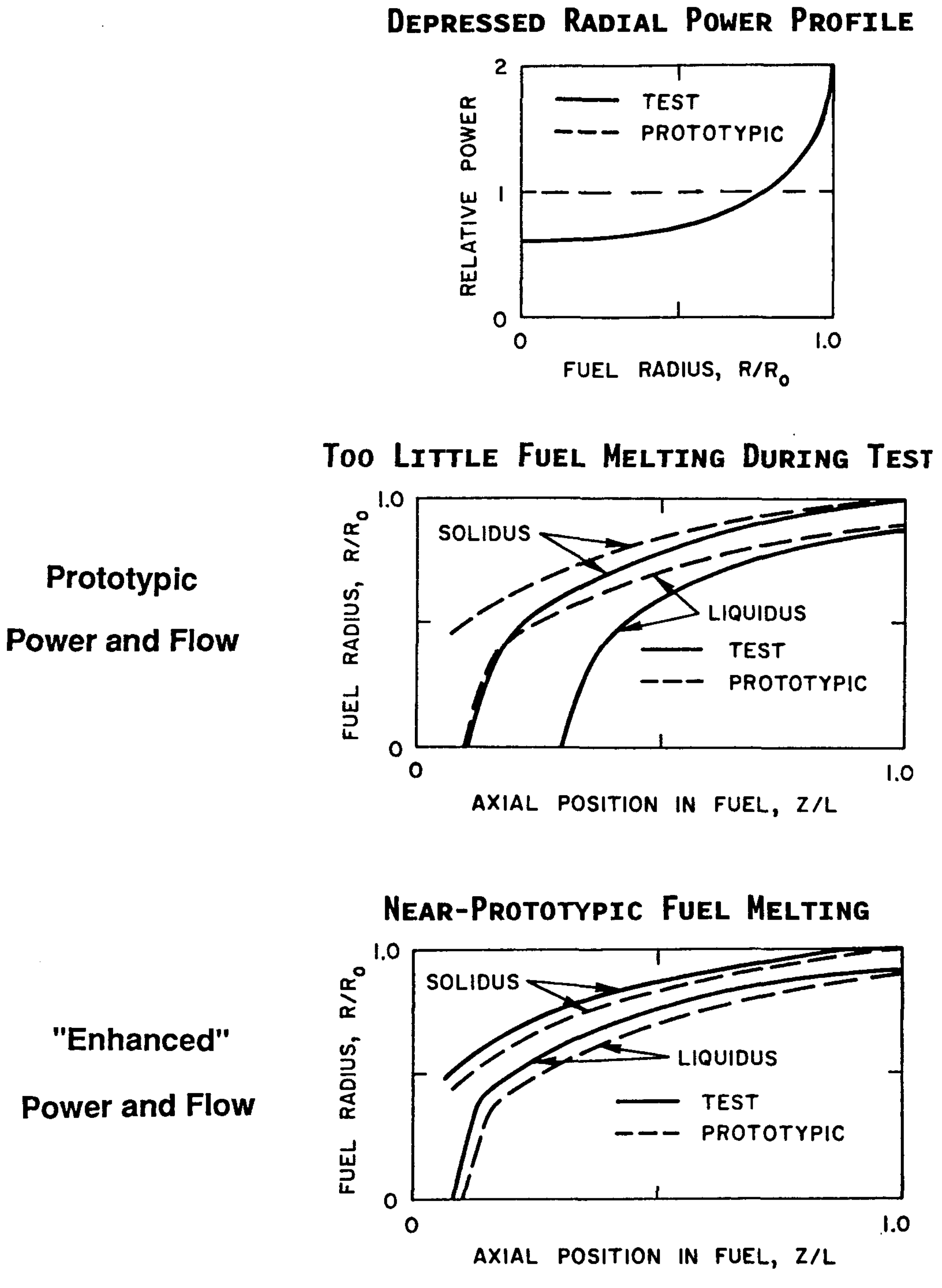

Fig. 4.3. Peak Fuel Melting Calculated With and Without "Enhancement" Compared to a Fast Reactor Prototype

Analyses presented in this report are chiefly intended to provide reasonable baseline estimates of thermal conditions achieved in the neighborhood of cladding failure threshold and, in addition, illustrative but quantitative estimates of the principal aspects of fuel performance observed in the experiments. Analyses reported here do not take account of coolant boiling or disruptive events following cladding failure.

The thermal hydraulic analyses of fuel pin thermal performance reported here used the COBRA-PI code [4.2]. Historically, COBRA-PI has been used extensively in analysis of TREAT in-pile experiments because of its ability to explicitly model pin bundle geometry in small-scale experiments. In this context its use has been limited, however, to intact (fixed) geometry and single phase coolant flow. For M-series the analysis incorporates detailed description of the fuel pin, flowing coolant and flowtube.

COBRA-PI's fuel pin model contains multiple radial and axial nodes. Azimuthal uniformity is assumed in the present M-series model. All thermal properties are temperature dependent with a melting transition computed in the fuel on the basis of input solidus and liquidus temperatures. Additionally, fuel properties, including melting temperatures, may also be input with radial dependence. Because of the fuel's sodium bonding, fuel and cladding are assumed in good thermal contact. The computed fuel-cladding interface temperature is used as a basis for assessing the formation of the low melting point eutectic. Formation of the low temperature molten phase under accident conditions at high temperatures is not reflected in this primary thermal analysis but is treated in a separate auxiliary calculation (below).

Axially, the M-series analysis extends the full length of a fuel pin, including both fuel and gas plenum region with multiple axial nodes. Coolant channel geometry is axially uniform, assumes a pin centered in the flowtube and models single radial nodes of turbulent flow thermally connected to both the pin cladding and a well-insulated flowtube. The "dimples" used to support the pin within the flowtube are not modeled.

Reported fuel performance calculations of pre-failure axial expansion and cladding failure were performed by a specially written routine, the EXP ("Extrusion and Penetration") model that is auxiliary to the COBRA-PI code. Development and application of the EXP routine was based on modeling concepts to be described in Sect. 6. Fuel expansion calculations envisions fission gas bubble growth and approach to pressure equilibrium in both solid and liquid fuel. The possibility of sodium bond vaporization is also considered. Cladding damage and failure calculations include cumulative effects of both pin plenum pressure and penetration by eutectic. Logical flow of the analysis is such that transient temperatures calculated by COBRA-PI provide driving input for EXP, but EXP calculations do not influence COBRA-PI. The combined program for metal fuel performance analysis is termed "COBRA/EXP".

Supporting thermal and hydraulic analysis of the Mark-III test loop as a whole has been performed by the SLOOP code [4.3]. SLOOP calculations provided detailed hydraulic analyses of both the actual test loop and train as well as analyses of supporting experiments testing actual and simulated hardware components in out-of-pile water and sodium loops. Integrating these calculations provided important verification of measured and anticipated flowrates. Details of these hydraulic analyses are found in Appendix D. Because COBRA-PI calculations included only the test fuel pin region, thermal analyses from SLOOP also permitted loop heatup during test transients to be anticipated and understood.

5.0 PERFORMANCE OF THE OVERPOWER TRANSIENTS

5.1 Test Performance and Event Sequence

Table 5.1 summarizes overpower testing of IFR fuel in TREAT to date. Six pins were tested, two to failure. General features of M-series test design and performance, nominal steady-state conditions for reference, and the ~8 s period power transient were described in Sect. 4.1. The first test, M5, was performed under an unusually stringent practical requirement that the test train hardware be reusable after the test. Since M5 was the first test of a new fuel type the power transient was terminated at a conservatively-low preset power level to avoid a pin failure. Initial results from this overpower transient indicated that the test fuel had not melted extensively or been brought near to failure threshold. The fuel was subsequently subjected to a second power transient with coolant flowrate reduced by 22%. Tests M6 and M7 were undertaken without any hardware reuse constraints and were performed in a more orthodox manner with the power transient terminated by experimental indications of a test pin failure. Tests M5 and M6 each tested two ternary fuel pins of different burnup, and nominal coolant flow was split equally between the test pins. Test M7, on the other hand, tested both a binary and a ternary pin; and to partially compensate for pre-test estimates of power coupling differences (Sect. 4.2) flow past the ternary pin in M7 was nominally about 10% less than the flow past the binary.

Table 5.1. Overpower Testing of IFR Fuel in TREAT

Test	Fuel (comp. wt.%)	Cladding	Burnup (at.%)	Date
M5	U-19Pu-10Zr	D9	0.8	8/86
	U-19Pu-10Zr	D9	1.9	
M6	U-19Pu-10Zr	D9	1.9	2/87
	U-19Pu-10Zr	D9	5.3-failed	
M7	U-19Pu-10Zr	D9	9.8-failed	10/87
	U-10Zr	HT9	2.9	

With the exception of the second overpower transient in M5, coolant flowrates were "enhanced" and inlet temperature was lowered from nominal values by amounts calculated to improve the matchup of test temperatures in TREAT to those generated by a fast reactor, as described in Sect. 4.3.

Results shown in Figs. 5.1 and 5.2 illustrate typical overpower test performance and event sequence when a pin failed. Figure 5.1 shows the axial-peak power densities applied to both test fuel pins, the resulting temperature transient measured on the outside of both flowtubes, and the flow perturbation generated by the failure of one of the test pins in M7. The efficient heat transfer in metal fuel systems causes flowtube temperatures to closely follow applied fission power with time delays of less than 1 s. Measured flowtube temperatures prior to failure closely followed adjacent coolant temperatures, and the indicated peak values (~1100-1200 K) were typical of these experiments and correspond closely to peak values of coolant temperatures. A sudden "jump" in flowtube temperature (to values indicative of coolant boiling at loop pressures of about 4 atm) coincident with the sudden reversal of inlet coolant flow marked the cladding failure of the ternary pin. The subsequent rapid power shutdown was pre-arranged and was triggered by the detection of sudden inlet flow reversal. The smooth response of the intact pin's flowtube temperature verifies that one pin's failure has a minimal influence on the other. Also coincident (but not shown in Fig. 5.1) are "spikes" in loop pressure transducer readings. Complete data from test instrumentation in M5-M7 is found in Appendix F.

"Transient hodographs" shown in Fig. 5.2 describe the above sequence of events from the viewpoint of fuel motion measured by the fast neutron hodoscope. Measured fuel density, averaged over the indicated time intervals, is displayed on the two-dimensional grid. (The scale is greatly expanded horizontally.) Note that the resolution is sufficient to easily distinguish the fuel columns of both M7 test pins. Prefailure axial expansion is seen in both test pins as an increase of fuel density near the top and above the fuel column. The eventual failure of the ternary pin is seen dramatically by sudden fuel gains extending to great distances above the original fuel column (with corresponding losses from the remainder of the pin). Timing of this event is in good agreement with other test instrumentation, such as shown in

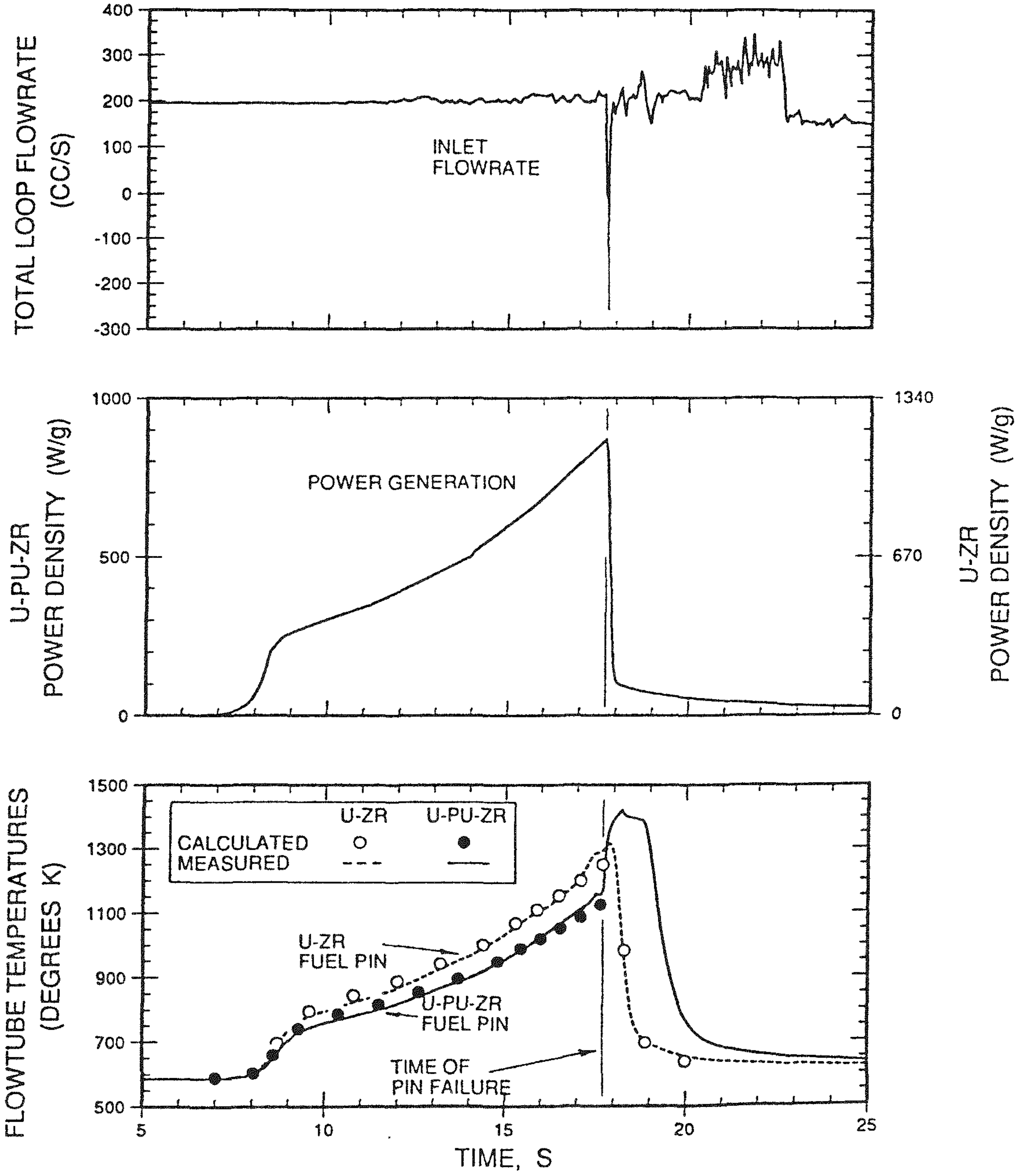

Fig. 5.1. Selected Test Results from M7

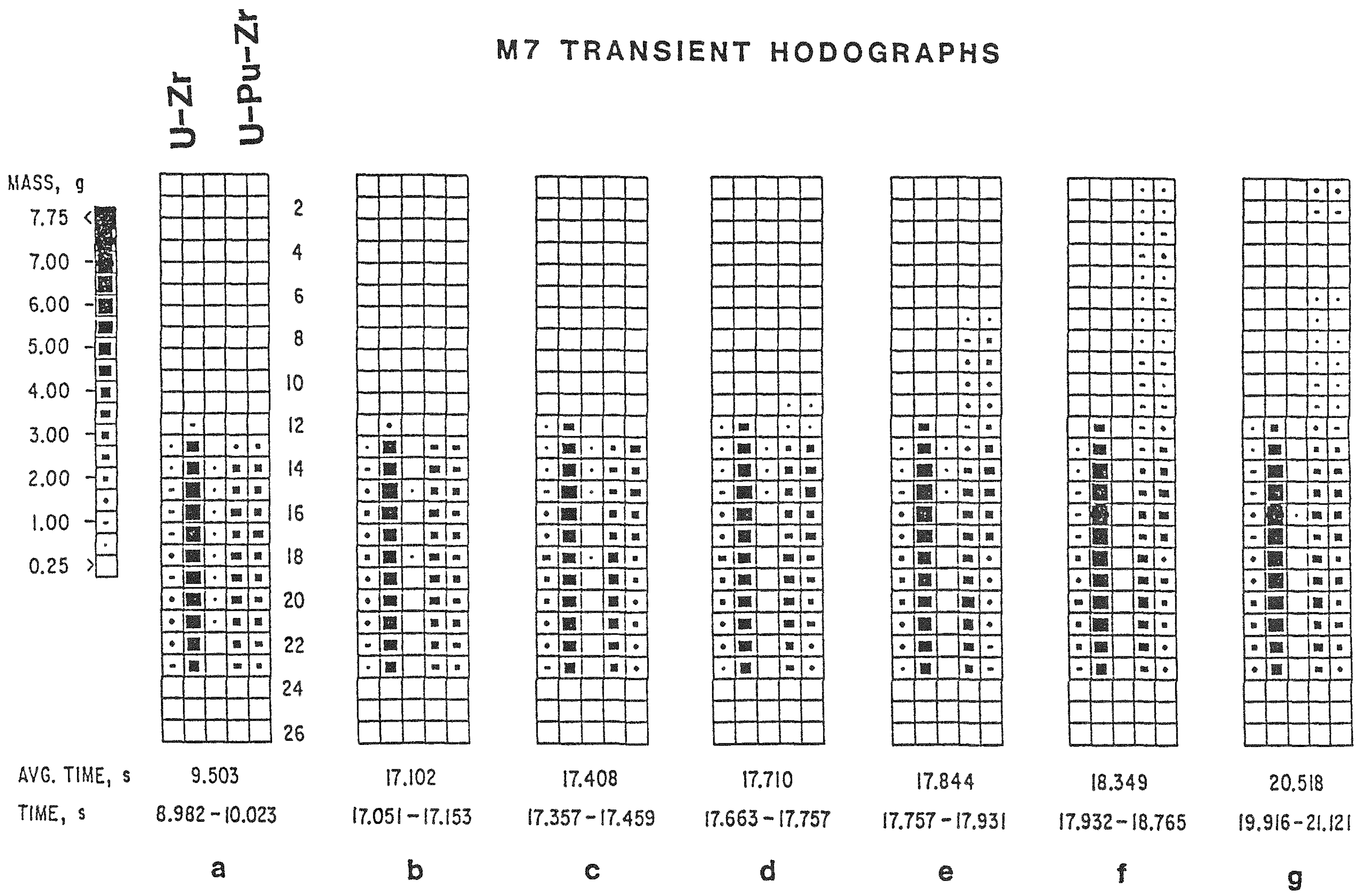

Fig. 5.2. Transient Fuel Motion Observed in M7

Fig. 5.1. A complete discussion of hodoscope results for M5-M7 is provided in Ref. 5.1.

5.2 Computed and Measured Heating

Comprehensive thermal-hydraulic analyses of all overpower experiments were performed with the COBRA-PI code as described in Sect. 4.4. Reactor power, measured flowrates, and measured inlet temperature were input to the computation. All such computations reported here assume intact geometry and are useful only prior to any significant fuel relocation or cladding failure. Analyses accounted for different pin-to-reactor power coupling, thermal conductivities, and melting points of different fuel types. Power couplings between test fuel and the reactor were obtained by the in situ method described in Sect. 4.2. Non-uniform radial distribution of fuel constituents were included for ternary fuel (but non-uniformity did not have a large effect on computed results). Characterization of the test fuel was made in Sect. 2. Appendix G includes details and parameters used specifically in these analyses.

5.2.1 Flowtube and Coolant Temperature Rise

Because of the high thermal conductivity of metal fuel and the relative slowness of the power transient, calculations indicate that the time dependence of the coolant temperature rise is very sensitive to the transient power generation within the test fuel. Also, since the flowtube is thin and surrounded by insulating low-conductivity gas, the coolant temperature closely matches the temperature measured on the outside of the adjacent flowtube. Thus, comparison of measurements with calculated temperatures at thermocouple locations on the outside surface of flowtubes provides assessment of calculated vs measured coolant temperature rise. Good agreement between measured and computed temperature rise along test pin flowtubes thus provides a measure of validation to the thermal-hydraulic analysis and thermal time response of the system as a whole.

Figure 5.1 shows such a comparison for thermocouple locations above the fuel in M7. Additionally, a fairly complete comparison of measured and calculated flowtube temperatures in all of the overpower transients is included in Appendix F. In all these comparisons calculations are compared to thermocouple measurements at "nearby" axial locations. As illustrated by Fig. 5.1, agreement is quite good when comparing a computed whole-pin temperature rise, with the several thermocouples located axially above the fuel. By design, thermocouples at these higher locations allow a maximum of time for the heat released by the test pin to be distributed radially and azimuthally within the coolant, thereby providing the most significant comparison with calculations. On the other hand, at elevations below the top of the fuel, calculated temperatures compare reasonably well with thermocouple measurements at elevations slightly above that of the nominal calculation (Appendix F). This small difference in elevation, corresponding to ~4-5 % of the fuel height, is consistent with an expected radial thermal mixing time of ~3 ms for the flowing sodium coolant in the flow channel annulus. Because such estimates of thermal mixing times in turbulent sodium are not very precise, the comparison below the top of the fuel should only be regarded as confirmatory.

5.2.2 Fuel Melting

All M-series overpower transients caused extensive melting in the test fuel amounting to about one-half the fuel inventory at peak power. The same thermal analyses that computed flowtube and coolant temperatures also computed fuel melting and temperature fields deep within the fuel pin. These internal temperatures were not accessible to direct measurement. However, experimental estimates of the maximum extent of melting were made during post-test examination from micro-examination of cross sections from each of the four intact pins at several axial locations. Indeed, the computed presence and amount of molten fuel provides key input to models describing pre-failure axial expansion and cladding failure, and agreement of calculated amounts of melting with measurements allows critical assessment of the actual role of fuel melting to be made.

In the experimental determination, the fraction of the fuel cross sectional area exhibiting some indication of melting was estimated. Figure 5.3 illustrates this measurement at the midplane of a ternary fuel pin tested

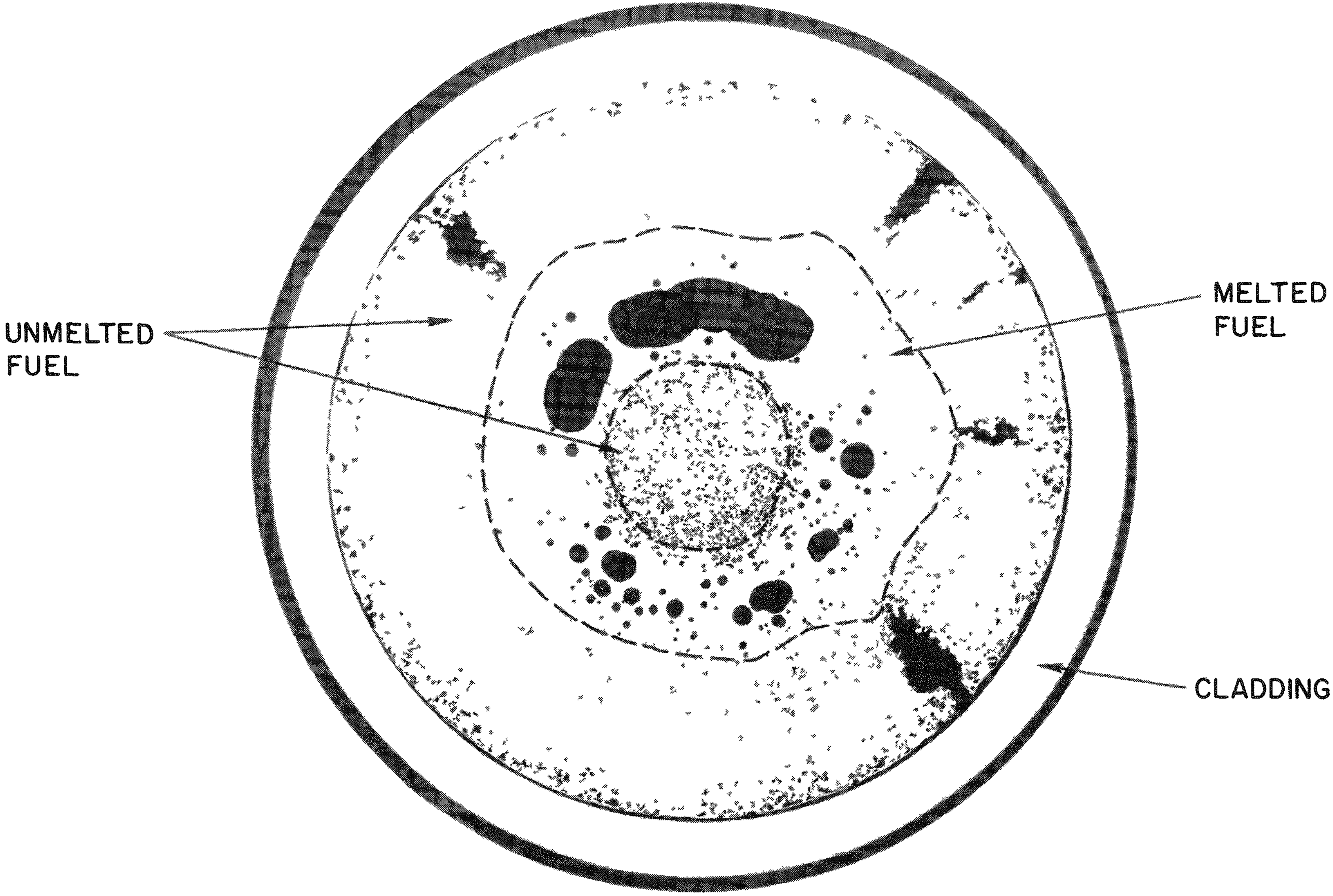

Fig. 5.3. Fuel Melting at the Midplane of the 1.9 at.% Burnup (D9-Clad) U-19Pu-10Zr Fuel Pin Tested in TREAT Test M5

in M5. In ternary fuel, the once-molten cross section shows obvious irregularities attributed to irregularities in thermal conductivity and melting points arising from previously identified inhomogeneities of constituents and morphology. These even include unmelted regions near the fuel centerline. For purposes of comparison with calculations, in each case a maximal once-molten area fraction was measured. (Unmelted regions were included when completely surrounded by melted areas.) The square-root of the maximal melted area fraction was then identified as the maximum relative radial extent of fuel melting (solidus radius) suitable for comparison with results of an azimuthally uniform calculation. Based on the uncertainty of distinguishing melted and never-melted fuel (e.g., Fig. 5.3), the precision of the experimental determination of relative solidus radius is around 5%.

Figures 5.4-5.6 show computed melt profiles at peak power for each of the M5-M7 test pins. Measured solidus radii are included on graphs for those pins which remained intact. As discussed below, accuracy of calculated solidus radii is quite sensistive to input values of thermal conductivity. Considering such uncertainties, agreement of measured and calculated solidus radii is quite good.

Agreement of measured and calculated solidus radii provides direct validation of fuel thermal conductivity estimates used in the analyses on a spatially averaged basis. Because of the large morphological changes which take place with fuel irradiation, including an assumed ingress of bond sodium into the fuel, fuel thermal conductivity is perhaps the least certain feature of the thermal hydraulic analysis. (The model used to estimate input thermal conductivity is described in Appendix G. Fuel characteristics assumed for the model are indicated in the figures.) Analytically, the depth of the solidus line into the fuel from its outer surface is directly proportional to the difference of fuel-solidus and fuel-surface temperature times the fuel thermal conductivity and inversely proportional to pin power. Since observed agreement between measured and calculated flowtube temperatures has already verified input pin power generation and computed temperature near the fuel surface, the additional agreement for maximum solidus radius then verifies input values of fuel thermal conductivity. Moreover, because the depth of the solidus line into the fuel is directly proportional to fuel thermal

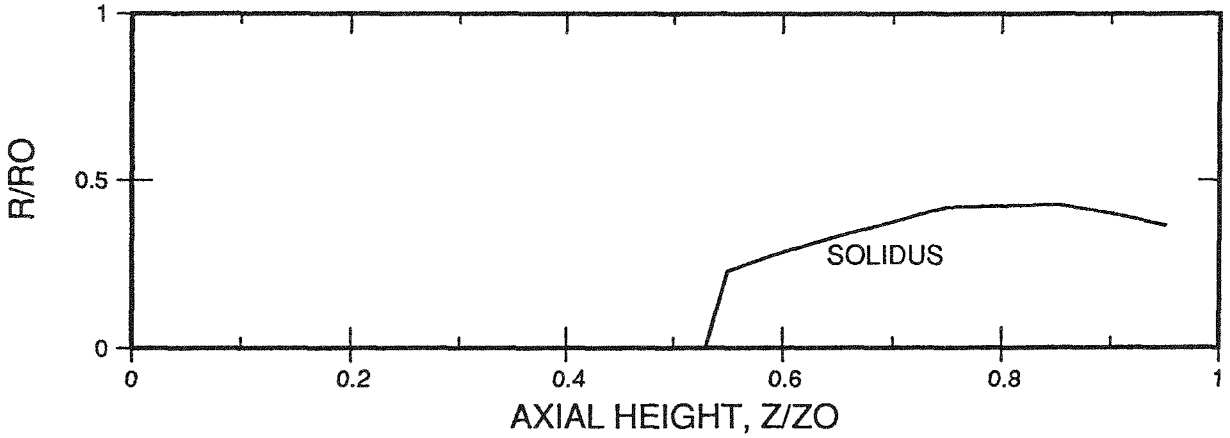

M5F1, 0.8 A/O BU, TERNARY PIN, 13.5% POROSITY, 0% NA LOGGING

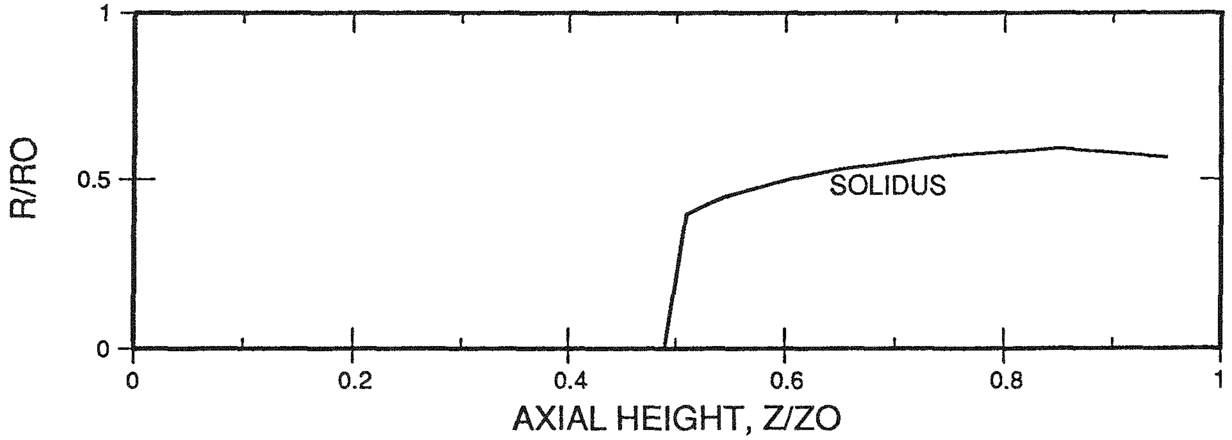

M5F1, 1.9 A/O BU TERNARY PIN, 27% POROSITY, AND 30% NA LOGGING

Fig. 5.4a. Calculated Melting in the First M5 Overpower Transient

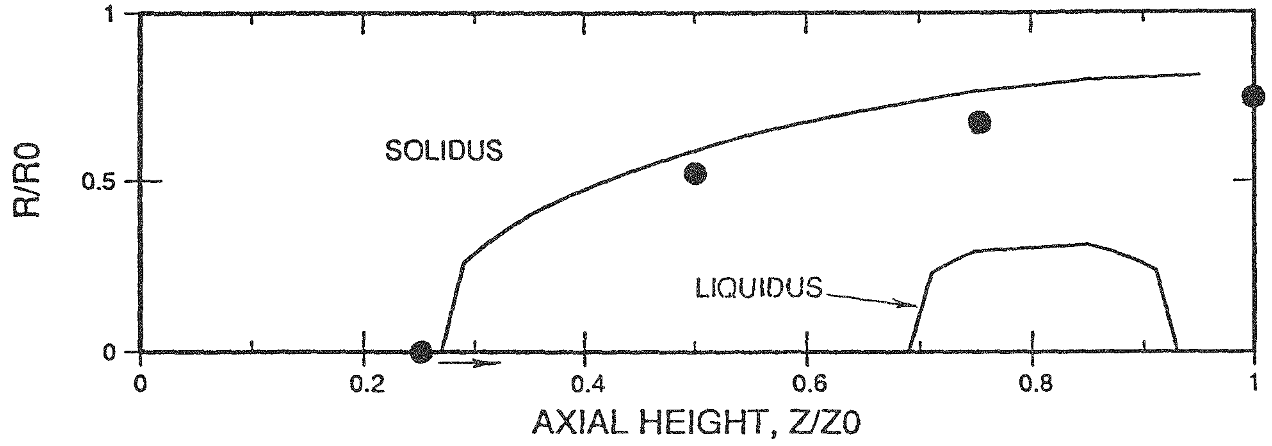

M5F2, 0.8 A/O BU, TERNARY PIN, 13.5% POROSITY, 0% NA LOGGING

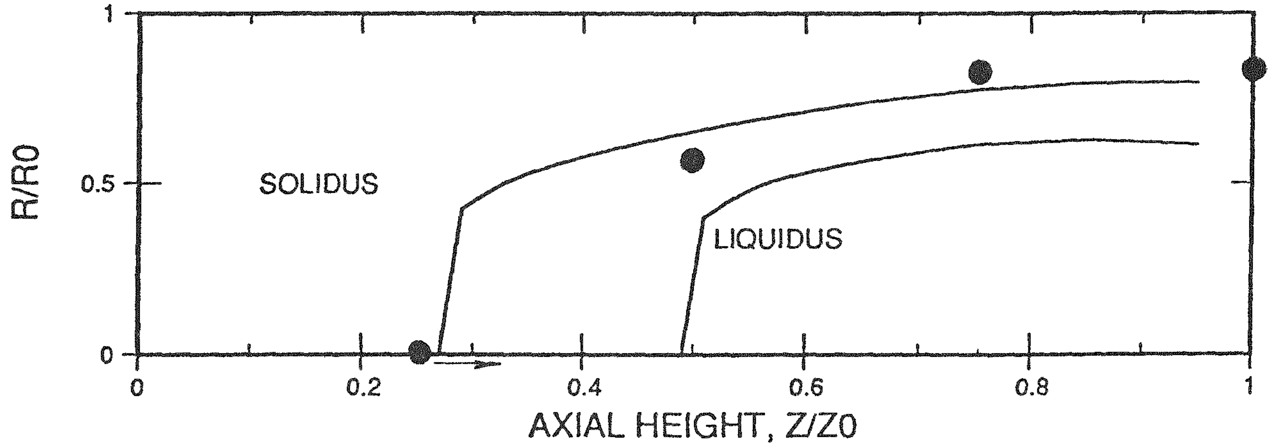

M5F'2, 1.9 A/O BU, TERNARY PIN, 27% POROSITY, AND 30% NA LOGGING

Notes:
1) Measurements denoted by (●).
2) The arrow associated with a measurement of zero melting indicates that the melt threshold itself, was not determined, but lies somewhere above.

Fig. 5.4b. Calculated Melting in the Second M5 Overpower Transient Compared with Measurements in the Intact Fuel Pins

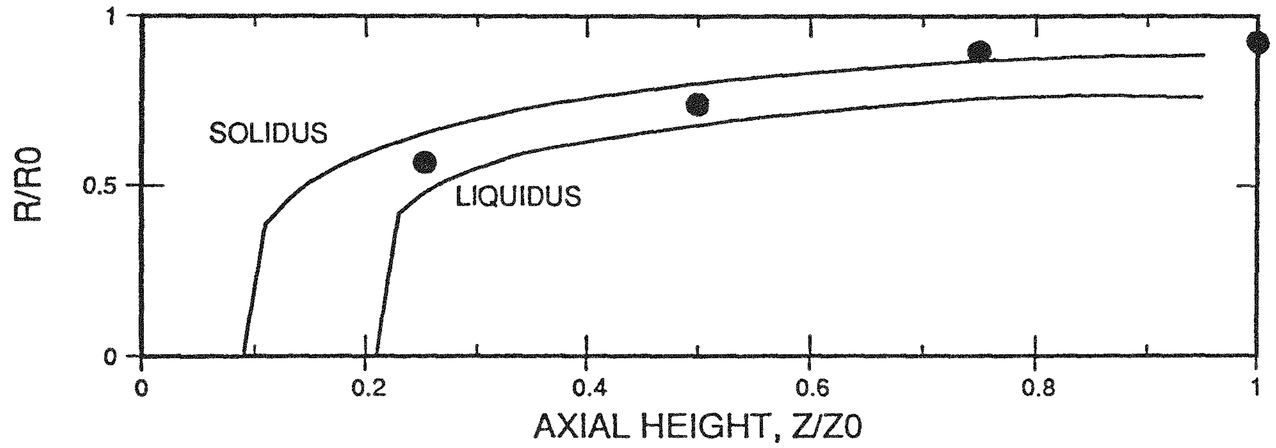

M6, 1.9 A/O BU, TERNARY PIN, 27% POROSITY, AND 30% NA LOGGING

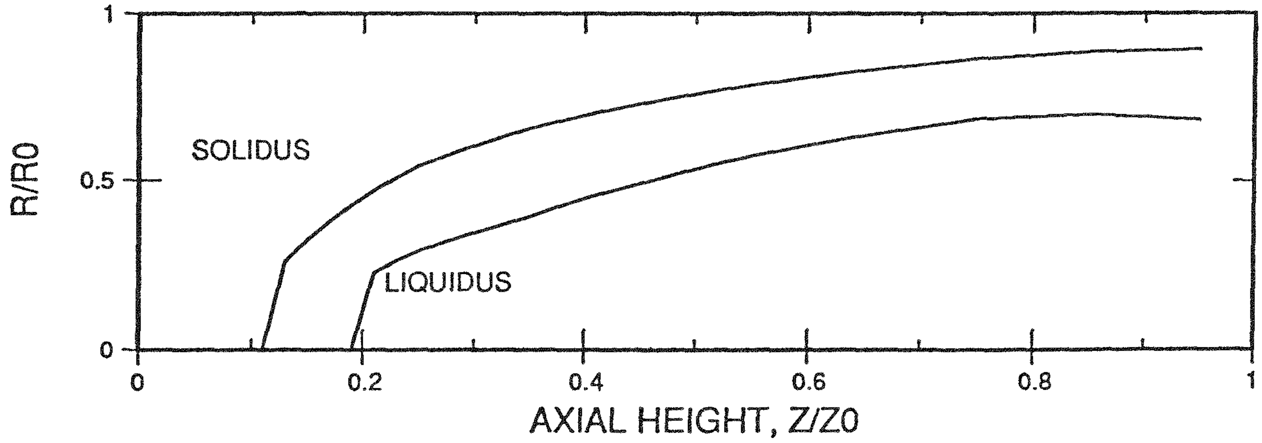

M6, 5.3 A/O BU, TERNARY PIN, 23% POROSITY, AND 35% NA LOGGING

Note: Measurements denoted by (●).

Fig. 5.5. Calculated Melting in the M6 Overpower Transient Compared to Measurements in the Intact Fuel Pin

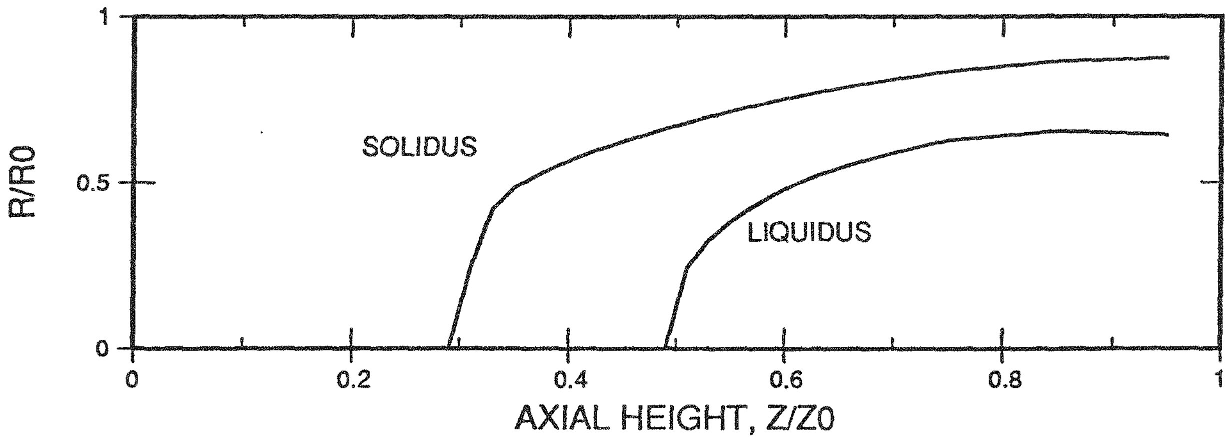

M7 TERNARY PIN WITH 19% POROSITY AND 42% SODIUM LOGGING

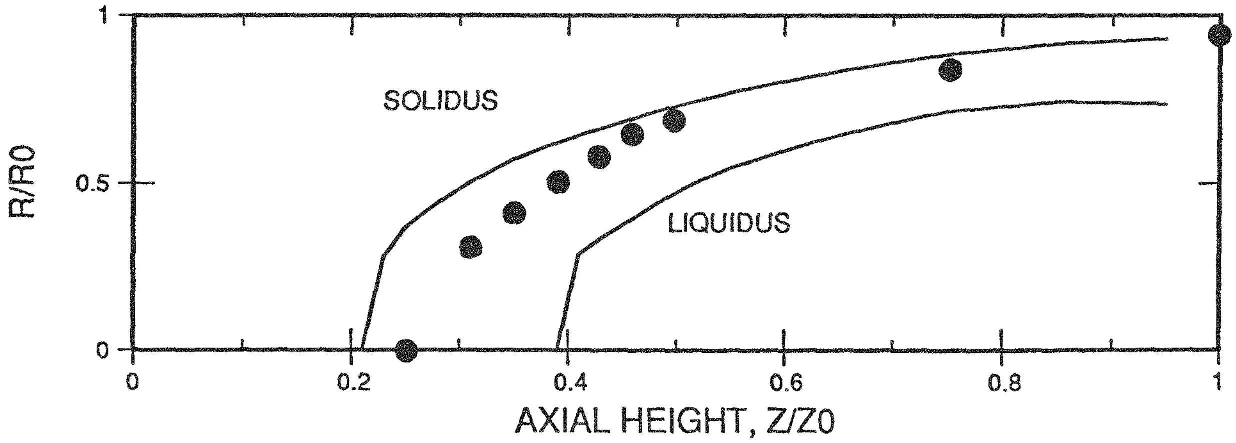

M7 BINARY PIN WITH 31% POROSITY AND 42% SODIUM LOGGING

Note: Measurements denoted by (●).

Fig. 5.6. Calculated Melting in the M7 Overpower Transient Compared to Measurements in the Intact Fuel Pin

conductivity, the relative "error" in the calculation's fuel thermal conductivity is numerically equal to simply the fractional difference between the calculated and measured depth of the solidus line. Accordingly, verification of thermal conductivity is most sensitive at axial locations at or just above the solidus threshold, where the measured depth in from the surface may be determined with greatest accuracy. Assuming that fuel thermal conductivity is the least certain element in the calculation of the solidus line (i.e., ignoring other possible sources of error), the comparisons of measured vs calculated solidus lines shown in Figs. 5.4-5.6 then suggest averaged input values of thermal conductivity are typically correct at the 20% level. Again, it should be cautioned that with ternary fuel this level of validation only applies on a spatially averaged basis, and significant local variations of thermal conductivity and melting point should be considered.

5.3 Peak Overpower Conditions and Fuel Performance Summary

A comprehensive summary of key overpower test results is given in Table 5.2. For comparison and completeness, results from earlier tests M2-M4 on U-5Fs fuel are included [1.5]. Peak overpower levels and summary indicators of fuel performance are reported. In every case some axial expansion of the test fuel was observed pre-failure with peak values shown in the table. However, at low burnup IFR-type fuel showed considerably less expansion than U-5Fs fuel tested earlier. Test pins were each subjected to overpower conditions exceeding four times nominal. In no case was pin failure observed significantly below this overpower level. Only two IFR pins failed, but calculations with a model designed to predict cladding failure (shown in the table) indicated that those pins that remained intact were nevertheless brought quite close to failure. Calculated values of peak pin pressures are also indicated.

Reported overpower levels are peak values of the P/F ratio obtained directly by extrapolation from the steady-state coolant temperature rises measured in heat balances, as outlined in Sect. 4.1. These carry an uncertainty of roughly 3%. In cases where test conditions were "enhanced" to compensate for the radial depression of neutron flux and power within TREAT-tested fuel pins, overpower levels reported accurately signify peak

Table 5.2. Peak Overpower Conditions and Fuel Performance Summary

Fuel/ Cladding	Axial Peak Burnup	Peak Overpower	Calc. Failure Threshold	Peak Pressure	Max. Axial Expansion
	(at. %)	(normalized)[c]		(MPa)	(%)
U-19Pu-10Zr/ D9 Steel	0.8[b]	(3.4) 4.3	(4.6) 5.1	(1) 1	(1) 1
	1.9[b]	(3.4) 4.3	(4.6) 5.1	(3) 3	(0.5) 2
	1.9	4.4	4.6	3	2-3
	5.3	4.4[a]	4.5	10	3
	9.8	4.0[a]	4.4	19	3
U-10Zr/ HT9 Steel	2.9	4.8	4.4	6	2-4
U-5% Fs/ 316 SS	fresh	3.8	4.3	0.6	4[d]
	0.3	4.1	4.7	0.6-0.8	16
	0.3	4.1	4.8	0.6-0.8	18
	2.4	4.1[a]	4.4	2-6	7
(Tests M2-M4)	4.4	4.2[a]	4.5	7-9	e
	4.4	4.0	4.4	7-9	4
	4.4	3.8	4.3	7-9	4
	7.9	4.1[a]	3.6-4.0	17-20	3
	7.9	3.4	3.6-4.0	17-23	4

[a] Indicates cladding failure occurred.
[b] Indicates M5 test pins; values in parentheses "( )" are from the first overpower transient.
[c] Relative to nominal conditions in a fast reactor: peak linear power of 40 kW/m, 630 K inlet, and 150 K coolant temperature rise.
[d] Expansion may have been caused by localized sodium bond boiling.
[e] Data ambiguous.

thermal conditions (temperatures, amount of melting, pressures, etc.) appropriate to a fast reactor. (In early tests M2 and M3 and in the second overpower transient in M5 enhancement was not performed; and application to fast reactor conditions is more approximate.) The considerable amount of fuel melting produced in these overpower transients has been shown in Figs. 5.4-5.6.

Maximum axial expansions are total expansions, pre-failure, relative to pretest measurements of the test fuel height. Reported measurements were based on transient data from the fast neutron hodoscope. In cases where pins remained intact, peak expansion was confirmed by post-test "scans" and neutron radiographs. Calculated cladding failure power levels shown in Table 5.2 are based on the model of cladding damage introduced in Sect. 4.4 whose physical basis is described in Sect. 6.2.

Additional fuel performance data is presented in Sect. 6, which emphasizes the underlying phenomena, mechanisms and ingredients needed for computational models. In particular, mechanisms and models of cladding failure threshold and pre-failure fuel expansion are proposed, described, and critically evaluated.

6.0 FUEL PERFORMANCE RESULTS AND ANALYSIS

6.1 Pre-Failure Fuel Expansion

Details of the fuel motion measurements in M5-M7 are reported in Ref. 5.1. Transient data from the hodoscope as well as comparison data from pre- and post-test static scans are included. In contrast with behavior of U-5Fs fuel, pre-failure expansion was typically less and did not show large burnup dependence. Because fuel density can be very non-uniform near the fuel top, there is uncertainty of ~1% in the peak expansions given in Table 5.2, a significant quantity when the expansion is small. However, there is no indication of any shrinkage, and measured expansions tend to be significant in excess of an approximate 1% that might be attributed to a purely thermal expansion. Good agreement between transient and post-test scan data implies that peak expansions persisted during cooldown. Expansions beyond pretest lengths are also evident in posttest radiographs of intact pins shown in Fig. 6.1.

It is also important to verify that measured expansions extend over a significant portion of the fuel and are not simply an "end effect" of local phenomena near the fuel top. Post-test density distribution measurements from an intact pin shown in Fig. 6.2 indicate fuel density reductions over the top half of the fuel, reflecting roughly the entire axial range where fuel melted during the transient. Perhaps the best single measure of the significance of this or any other measurement of extensive axial fuel movement is the net change in fuel "worth"; where "worth" is the integral of the measured axially-dependent fuel density, weighted by a curve of axial shape typical of reactivity worth in a full-scale reactor. A decrease in measured worth of a test pin during a transient, as determined from hodoscope data, reflects a net movement of fuel from axial locations of higher to lower "worth", and thus quantitatively estimates (in a generic way) the neutronic significance of the measured axial expansion. Table 6.1 indicates worth changes measured in tests M5-M7 [5.1], showing good agreement between transient data and post-test scan results. Measured worth decreases at the several percent level confirm the significance of the measured expansions.

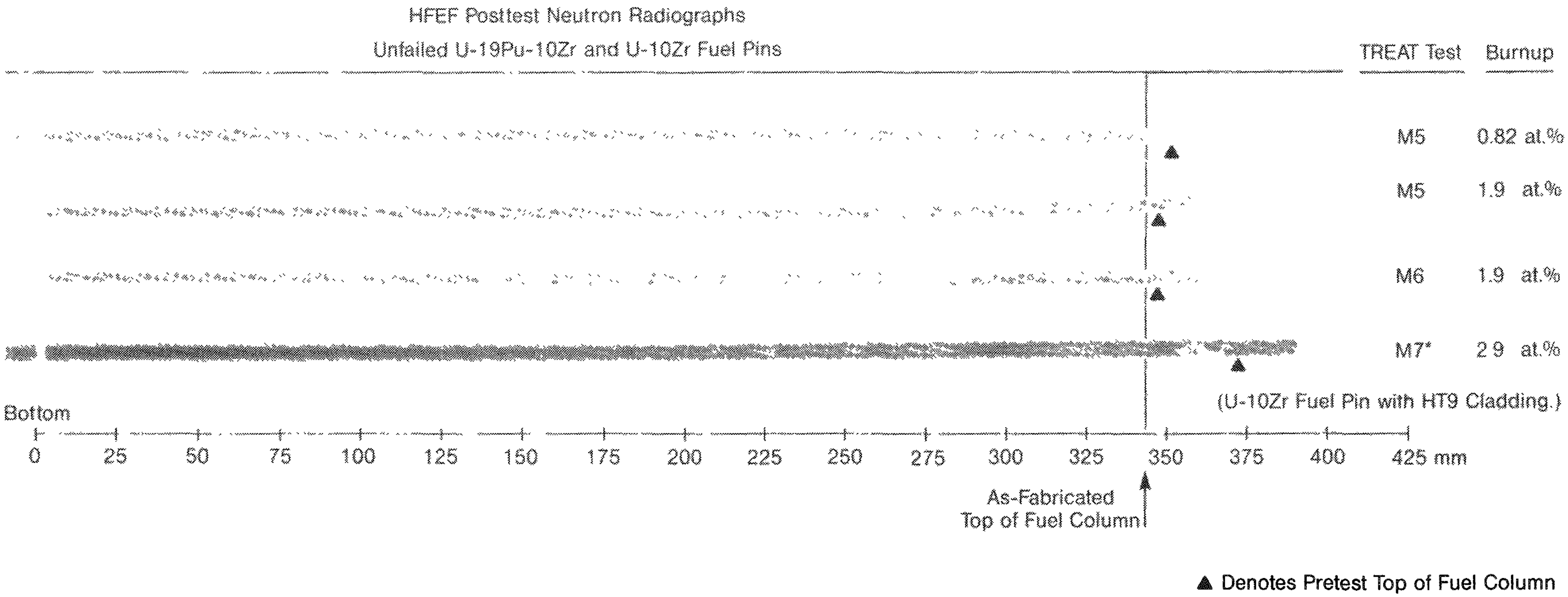

Fig. 6.1. Post-Test HFEF/NRAD Neutron Radiographs of Unfailed Pins from TREAT Tests M5, M6, and M7

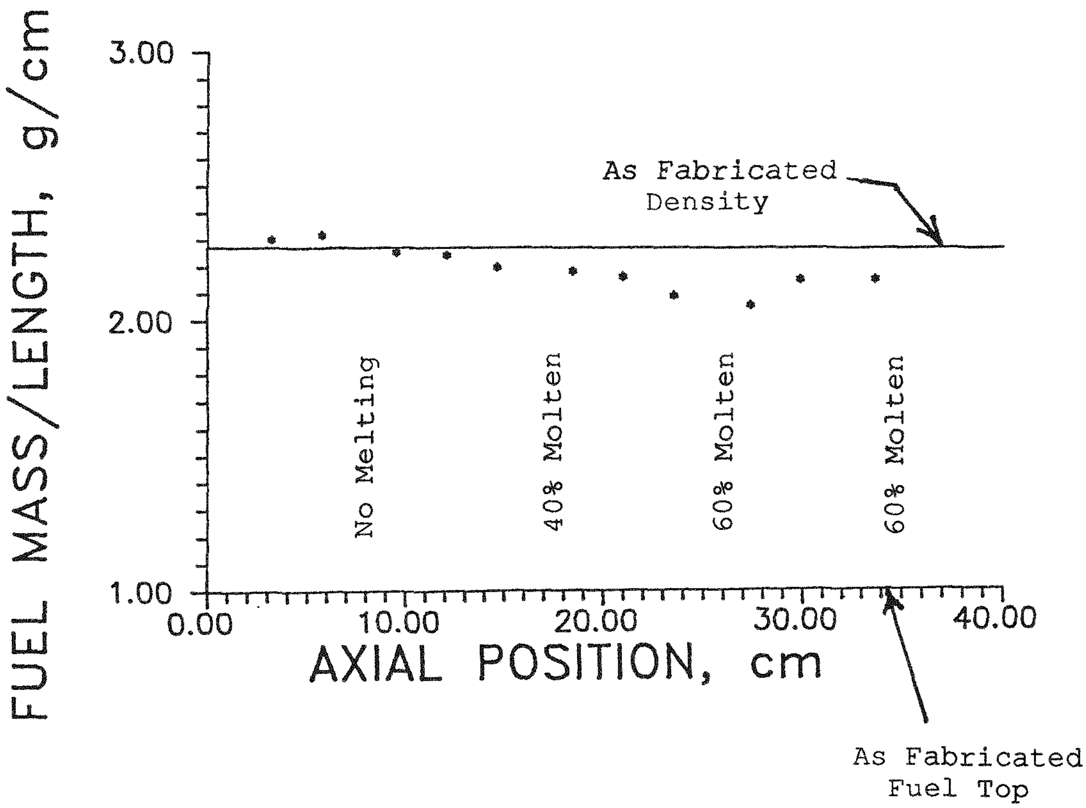

Fig. 6.2. Measured Axial Fuel Mass Distribution of the 1.9 at.% Burnup U-19Pu-10Zr Fuel Pin Tested in TREAT Test M5 Compared with As-Fabricated Density and Measured Areal Melt Fractions

Table 6.1. Maximum Pre-failure Worth Changes Measured in M5-M7

Fuel/ Cladding	Axial Peak Burnup (at. %)	Measured Worth Change[b] Transient (Max. %)	Post-Test Scan (%)
U-19Pu-10Zr/ D9 Steel	0.8[a]	(-1) -1	(-1) -1
	1.9[a]	(-1) -2	(-1) -2
	1.9	-2	-2
	5.3	-4	failed pin
	9.8	-4	failed pin
U-10Zr/ HT9 Steel	2.9	-2	-2

[a] Indicates M5 test pins; values in parentheses "( )" are from the first overpower transient

[b] Analyses assumed a "typical" worth curve with a cosine-squared axial dependence, peaked at the fuel midplane and a width (FWHM) of 0.81 of the nominal fissile fuel length [5.1].

In irradiated fuel, the mechanism underlying measured axial expansion is believed to be fission gas that is initially confined within solid fuel but freed to expand when fuel melts. (Expansion of the one "fresh" U-Fs pin tested, Table 5.2, may have resulted from boiling of bond sodium that had mixed in with molten fuel.) Post-test examination of test pins which remained intact all show large bubbles which are not typical of normal as-irradiated fuel but are indicative of extensive fuel melting, bubble coalescence and expansion at much higher temperatures. Two qualitatively different examples are shown in Figs. 6.3 and 6.4. Figure 6.3 shows a vertical section of a low-burnup U-5Fs pin where the fuel had expanded axially by nearly 20%. By contrast, Fig. 6.4 shows radial sections of an intact ternary pin (1.9 at.% burnup) which had been tested in M6 and expanded axially by only a few percent. Expanded fission gas bubbles shown in Fig. 6.4 are typical of those found in the M5-M7 test pins which remained intact: fewer bubbles than Fig. 6.3 but more than an untested sibling (Fig. 2.1). Further examples will be found later in Figs. 6.5, 6.6 and 6.10.

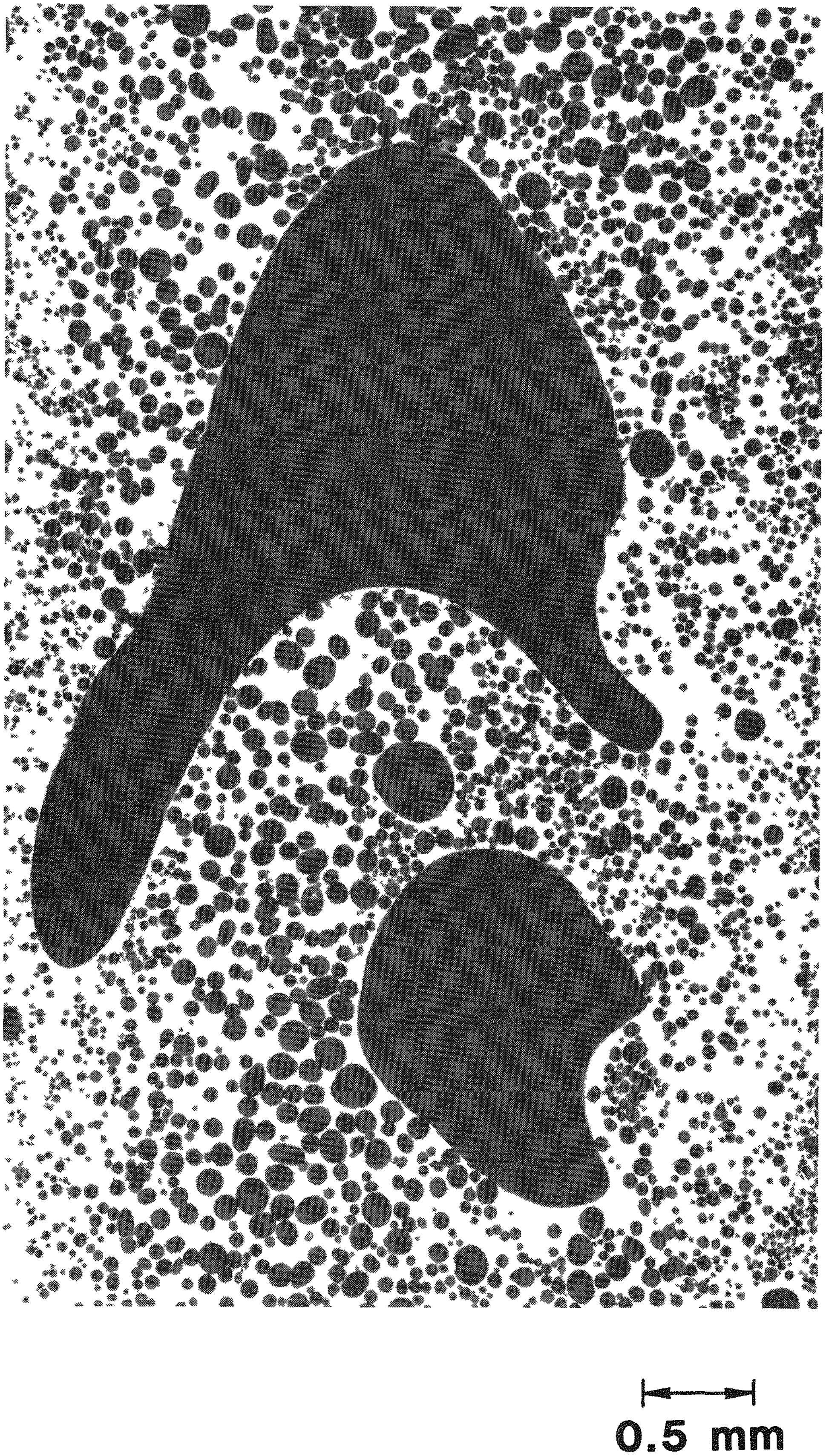

Fig. 6.3. Longitudinal Micrograph from the Top of the 0.35 at.% Burnup U-5Fs Fuel Pin Tested in TREAT Test M2 Illustrating Bubble Coalescence

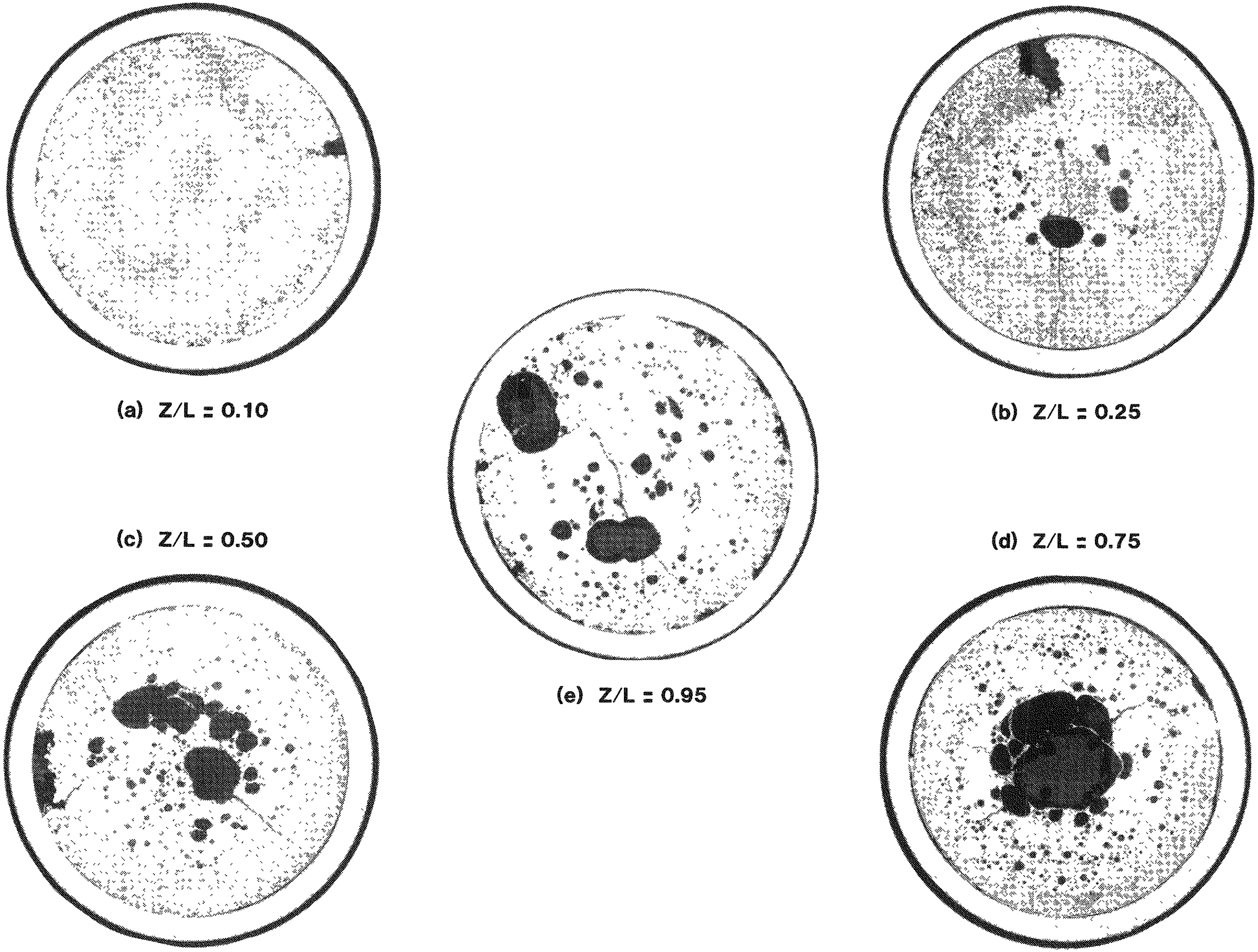

(a) Z/L = 0.10

(b) Z/L = 0.25

(c) Z/L = 0.50

(d) Z/L = 0.75

(e) Z/L = 0.95

Fig. 6.4. Transverse Micrograph at Various Elevations from the 1.9 at.% Burnup (D9-Clad) U-19Pu-10Zr Fuel Pin Tested in TREAT Test M6

Elements needed to compute the particular amount of axial expansion are:

1) the amount of molten fuel,
2) the concentration of gas made available to expand when fuel melts,
3) initial size of gas bubbles (initial surface tension effect), and
4) the magnitude of the pin plenum pressure resisting expansion.

Basically, axial expansion occurs when fission gas present in molten fuel expands until its pressure equals that of the pin plenum. The onset of fuel expansion coincides with significant fuel melting. Because of surface tension effects in the solid state, the initial volume occupied by fission gas depends on the initial bubble size. Small bubbles in the solid state indicate that gas is initially "dissolved" or packed within a very small volume, and held by surface tension. If bubbles in the solid state are initially large, surface tension plays no role and fission gas is in equilibrium with plenum pressure.

During transient fuel heatup, individual bubbles expand in an attempt to maintain equilibrium of internal pressure with pin plenum pressure and bubble surface tension. While fuel is solid, bubble expansion rates are severely limited by various diffusion and creep processes [6.1]. Bubble coalescence is also extremely slow. At heating rates typical of M-series, expansion of solid fuel is computed to be negligibly small. However, once fuel melts both expansion and coalescence are assumed to be sufficiently rapid that available fission gas expands instantly to equilibrium, regardless of initial bubble size (without any effect of surface tension). Thus, net expansion includes effects of both thermal expansion and, in the case of initially small bubbles, elimination of surface tension. Initially-small bubbles would lead to greater net expansion upon melting than would large bubbles.

Upon cooldown, at least part of the expansion in an intact pin will tend to be permanent. Because bubble coalescence is irreversible, expansion due to coalescence is permanent. Also, expansion of individual bubbles may be largely permanent since little contraction will occur in the solid state after refreezing. (However, large bubbles can migrate upward and eventually "escape" to the plenum if cooldown is not quick enough. The shapes of the largest bubbles in Fig. 6.3 show some such evidence of rising.)

Time-dependent computations of axial expansion in the tests were executed in the COBRA/EXP code module (Sect. 4.4) and made heavy use of the thermal analyses described above in Sects. 4 and 5. Thermal calculations estimated the amount of molten fuel at each axial node. Estimates of transient pin plenum gas pressure were based on sibling pin measurements at room temperature (Sect. 2) and simply scaled upward in accord with the calculated absolute temperature of the pin plenum. (Peak values were given in Table 5.2.) A concentration of fission gas at each axial node and a typical bubble size was explicitly input to the computation. Computed expansion was averaged over the radial cross section of each axial node. Upward bubble migration (rising) was not included in the computation.

The same basic modeling was used to calculate axial expansions in all M-series tests but with significantly different concentrations of available fission gas assumed for U-5Fs vs IFR fuel types. Interestingly, if the measured expansions (Table 5.2) are to be calculated with this model, the amount of fission gas "available" for producing axial expansion is always much less than the amount of fission gas retained in the pin as a whole (Table 2.2). This may be explained by the fact that local concentrations of dissolved gas decrease rapidly with irradiation temperature [2.1], and it is basically the fuel with the least dissolved gas that melts first and contributes most to axial expansion.

As reported previously [1.3-1.5], measured expansions in U-5Fs fuel were well predicted in timing, overall magnitude, axial distribution, and burnup dependence with the assumption of a fission gas concentration in small bubbles of 5 μ-moles/g-fuel (or equivalent to the total gas generated in about 0.5 at.% of burnup). This assumed concentration, equal to about one-fourth of the whole-pin average amount, corresponded closely to measured gas concentrations at hottest axial locations [6.2]. Permanence of the expansion upon cooldown was also predicted by the computation.

By contrast, IFR fuel test data requires rather different assumptions about fission gas availability. Assuming the same concentration of fission gas as employed successfully in the analysis of U-5Fs fuel leads to predictions of expansion magnitudes which are too large and a burnup dependence that is too strong (similar to U-5Fs fuel). It is noted, however, that the IFR fuel had smaller grain size and was irradiated at significantly higher linear power and temperature than the U-5Fs fuel (Table 2.2). Thus, the high temperature regions of IFR fuel which contribute most to axial expansion might contain little, if any, dissolved gas. In view of this, expansions in IFR fuel were instead calculated assuming a model where only gas trapped in large bubbles within the fuel porosity was available for expansion. Because this gas is initially in equilibrium with the pin plenum pressure, the density of gas present in the pin's porosity is itself proportional to the plenum pressure. Expansion then depends principally on the temperature difference between molten fuel and the pin gas plenum. Axial expansions computed with this simple model of fission gas concentration do indicate approximately the right magnitude and the weak dependence on burnup that is present in the reported data.

Table 6.2 shows some of the key input and results of axial expansion calculations for IFR fuel tested in M5-M7.

Table 6.2. Prefailure Axial Expansion Calculations for M5-M7: Key Input and Results

Fuel/ Cladding	Axial Peak Burnup (at. %)	Gas-Filled Porosity (%)	Plenum Pressure (MPa-cold)	Gas Conc. (μ-moles/g)	Peak Axial Expansion (%- calc.)
U-19% Pu/ D9 Steel	0.8[a]	13	0.27	1.2	(0.8) 2
	1.9[a]	19	0.65	4.5	(2) 3
	1.9	19	0.65	4.5	5
	5.3	15	2.3	12	4
	9.8	11	4.9	19	2
U-10% Zr/ HT9 Steel	2.9	18	1.4	9.1	4

[a] Indicates M5 test pins; values in parentheses "( )" are from the first overpower transient

6.2 Cladding Failure Threshold

Two principal mechanisms have been identified as causing cladding damage in metal fuel: overpressure and clad thinning [6.3, 6.4]. Because of the low mechanical strength of metal fuel, pin plenum pressure provides the primary source of pressure loading and stress on the cladding. Cladding stresses, however, reflect not only the pin plenum pressure but also thinning by formation of a low-temperature, iron-uranium eutectic.

Physical evidence exists from post-test remains to support and illustrate the two proposed mechanisms of cladding failure in metal fuel. These two mechanisms were readily identified in failed U-Fs pins from previous tests M2-M4 [6.5]. Representative micrographs from M5-M7 pins that remained intact are shown in Figs. 6.5 and 6.6. In addition to large bubbles of expanded fission gas previously illustrated in Fig. 6.4 (Sect. 6.1), Figs. 6.5 and 6.6 also illustrate an azimuthally non-uniform eutectic attack on the cladding. By contrast, M-series U-5Fs pins taken to comparable overpower levels, but short of failure, showed no evidence of eutectic attack.

Figures 6.5 and 6.6 also illustrate the multi-phase alloy formed as a result of this fuel-cladding interaction. In particular the "back scattered electron" (BSE) image shown in Fig. 6.6b provides direct information on the relative atomic number of the "layered" phases present in the microstructure; dark appearing phases in the figure are lower in atomic number than light phases. In addition, representative locations labeled A through F on Fig. 6.6b were subjected to X-ray analysis. In-depth analysis of these regions can be summarized as follows:

(a) Fuel that has not interacted with cladding containing large bubbles of expanded fission gas;

(b) Zirconium layer with little or no other constituents;

(c) A multi-phase zone with a high concentration of plutonium and lesser amounts of zirconium and uranium with trace amounts of cladding constituents;

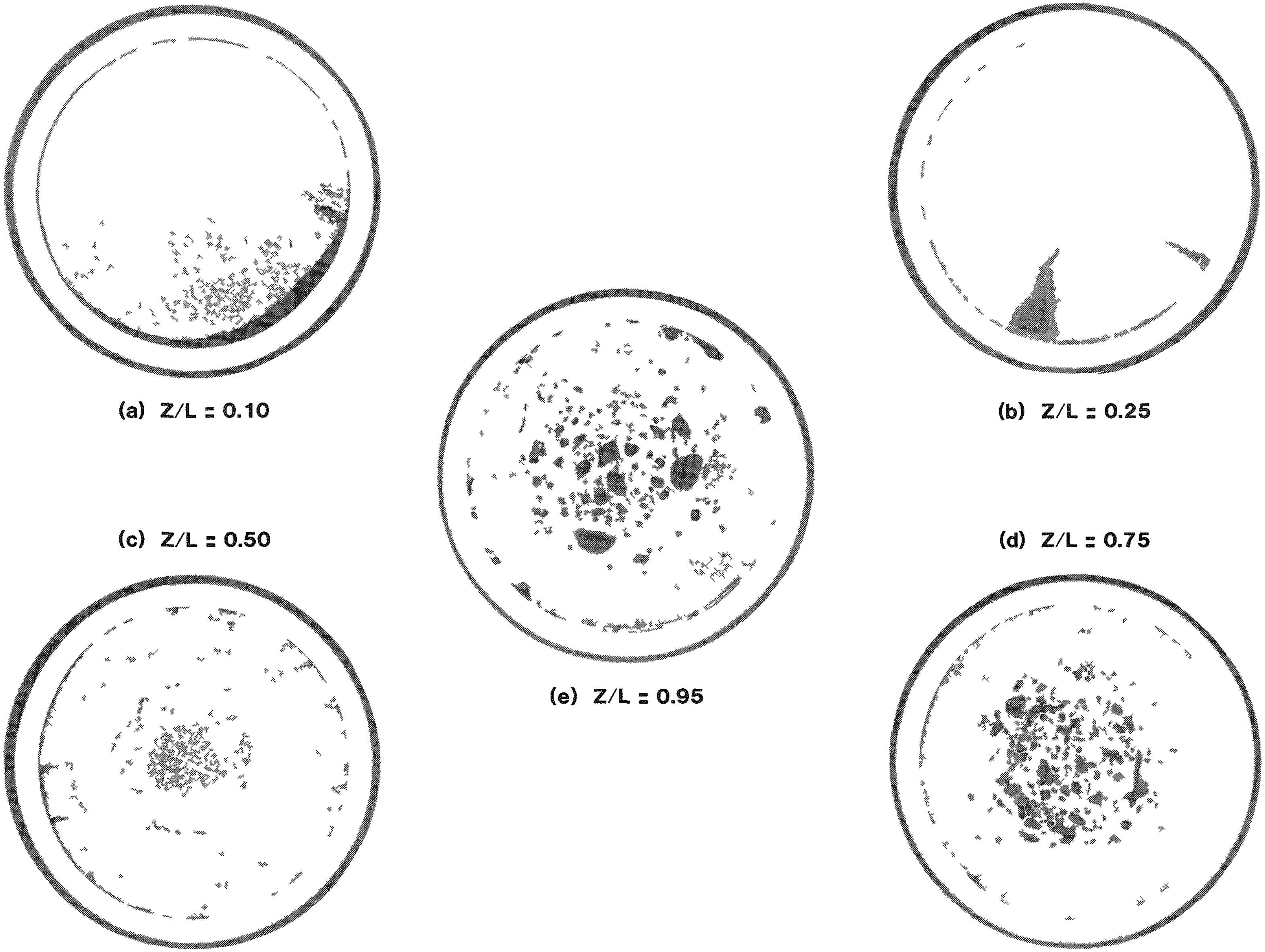

(a) Z/L = 0.10

(b) Z/L = 0.25

(c) Z/L = 0.50

(d) Z/L = 0.75

(e) Z/L = 0.95

Fig. 6.5a. Transverse Micrograph at Various Elevations from the 0.8 at.% Burnup (D9-Clad) U-19Pu-10Zr Fuel Pin Tested in TREAT Test M5 Showing Fuel-Cladding Interaction at Z/L = 0.75 and 0.95

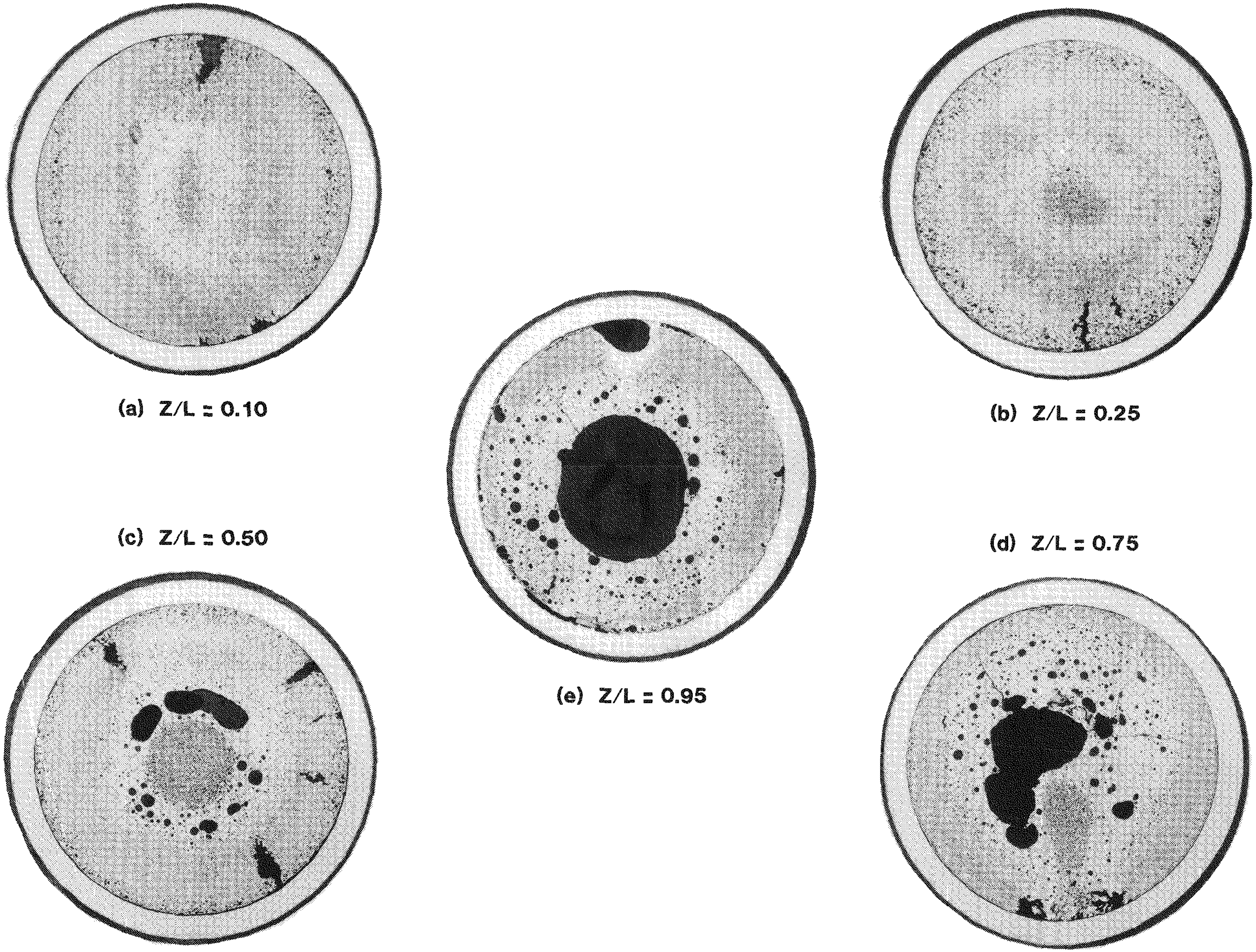

(a) Z/L = 0.10

(b) Z/L = 0.25

(c) Z/L = 0.50

(d) Z/L = 0.75

(e) Z/L = 0.95

Fig. 6.5b. Transverse Micrograph at Various Elevations from the 1.9 at.% Burnup (D9-Clad) U-19Pu-10Zr Fuel Pin Tested in TREAT Test M5 Showing Fuel-Cladding Interaction at Z/L = 0.75 and 0.95

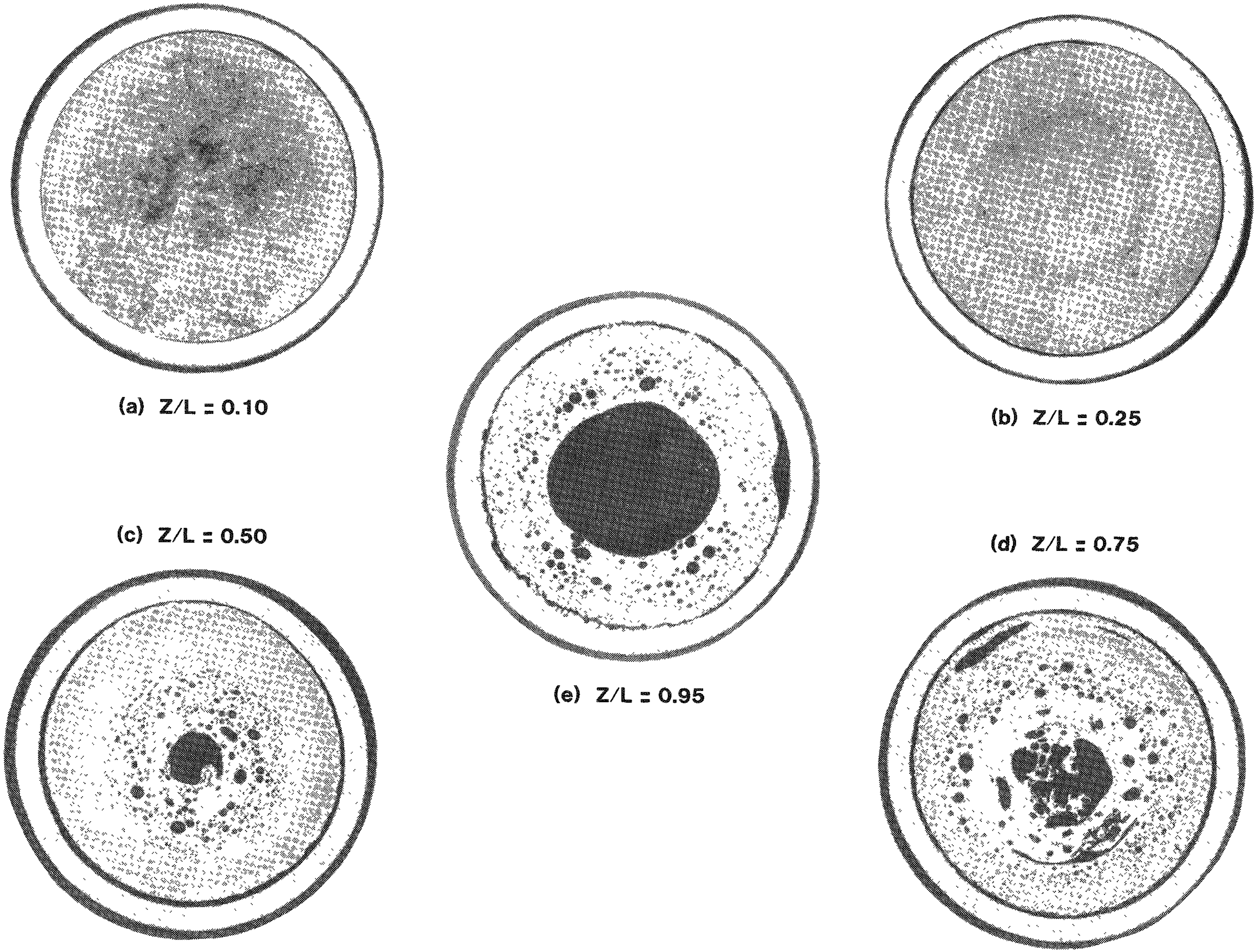

(a) Z/L = 0.10

(b) Z/L = 0.25

(c) Z/L = 0.50

(d) Z/L = 0.75

(e) Z/L = 0.95

Fig. 6.5c. Transverse Micrograph at Various Elevations from the 2.9 at.% Burnup (HT9-Clad) U-10Zr Fuel Pin Tested in TREAT Test M7 Showing Fuel-Cladding Interaction at Z/L = 0.95

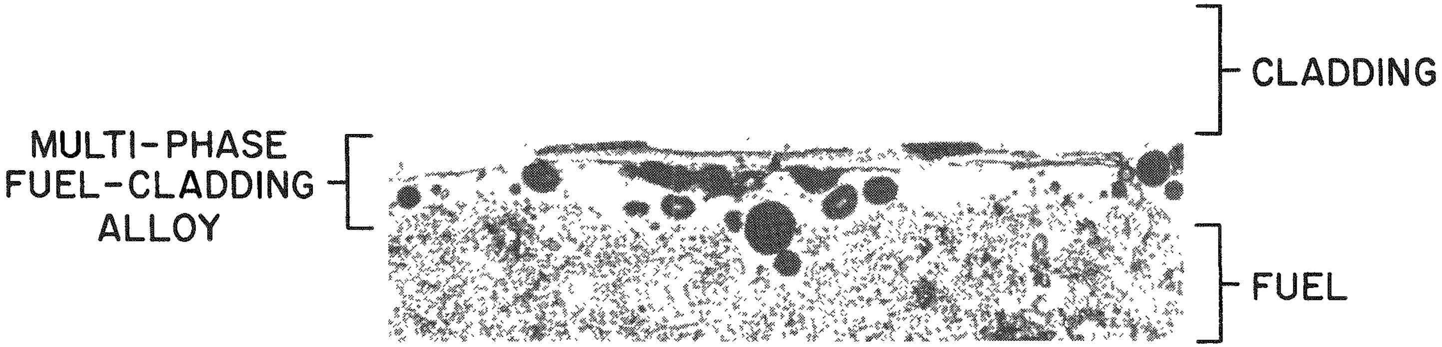

Fig. 6.5d. Medium-Power Micrograph Showing Fuel-Cladding Interaction in the 0.8 at.% Burnup (D9-Clad) U-19Pu-10Zr Fuel Pin Tested in TREAT Test M5

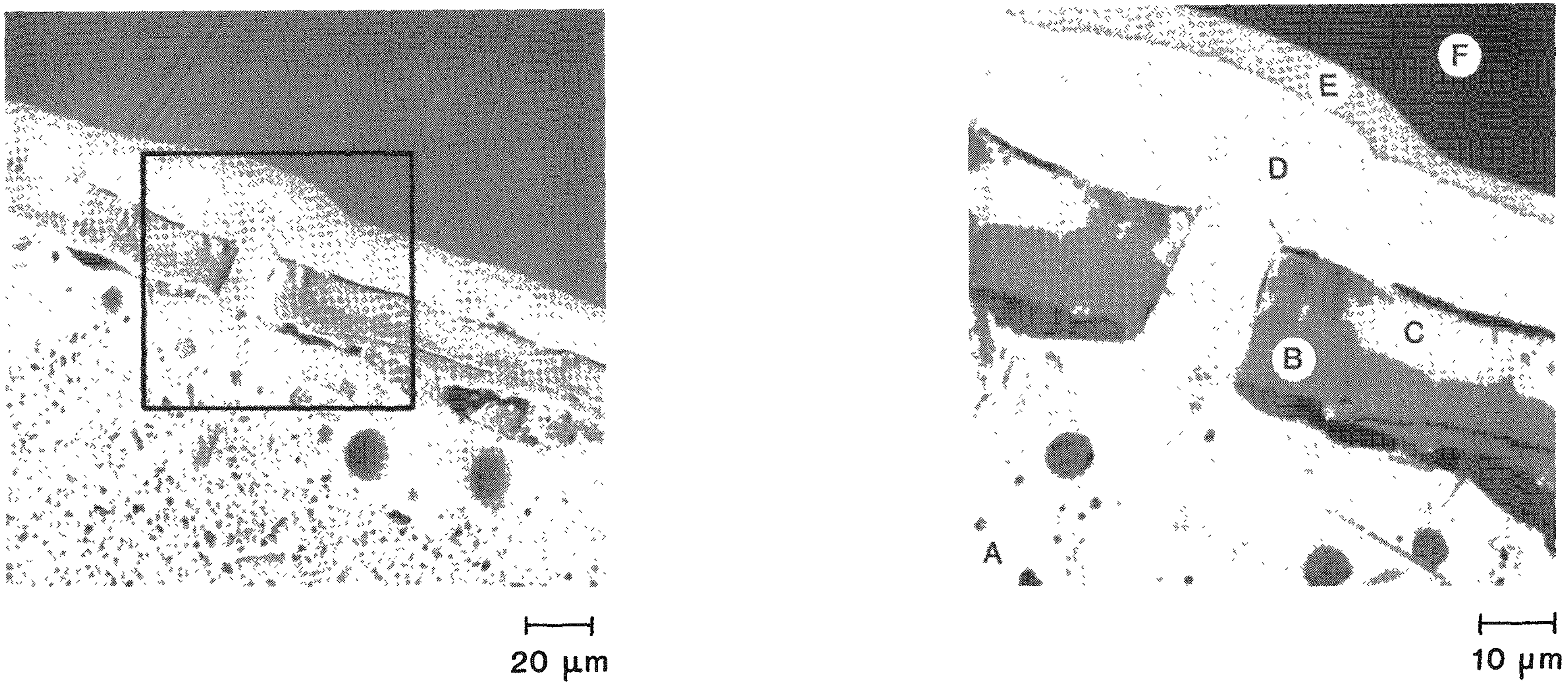

(a) SE

(b) BSE

Fig. 6.6. Scanning Electron Micrographs from the 0.8 at.% Burnup (D9-Clad) U-19Pu-10Zr Fuel Pin in TREAT Test M5. (a) Low Magnification Secondary Electron Image. (b) Back Scattered Electron Image Showing X-ray Analysis Sites.

(d) Major constituents uranium and plutonium with much lower but nearly equal concentrations of iron, chromium, nickel, and zirconium;

(e) A two-phase region containing approximately equal amounts of fuel and cladding; and

(f) Cladding that has not interacted with fuel.

It should be noted that regions C - D represent phases of very low melting point ~950-1000 K, and only region F retains mechanical strength associated with cladding.

Figures 6.7a and 6.7b show sections of failure sites of the two pins which failed in M6 and M7. Both failure sites occurred at the top of the fuel. In Fig. 6.7a the failure site of a medium (5.3 at%) burnup ternary pin shows strong evidence of cladding dissolution from the inside. (The attack evident on one outside surface was caused post-failure by molten fuel ejected from the pin.) The failure site of a higher (9.8 at.%) burnup ternary pin in Fig. 6.7b shows evidence of cladding bulging from pressure loading in addition to cladding dissolution from the inside.

Integrating these two damage mechanisms within a single analytical model to compute pin failure in metal fuel has been described in Ref. 6.3 under the assumption that both mechanisms act "independently". Cladding stress is first computed on the basis of computed gas plenum pressure and the remaining thickness of unreacted, load-bearing cladding (e.g., region F in Fig. 6.6b). Calculation of transient pin plenum gas pressure was described in Sect. 6.1. (Peak values for M-series were given in Table 5.2.) In the model, above an assumed threshold temperature of 1000 K, cladding thickness is assumed to be reduced at a temperature-dependent rate derived from out-of-pile measurements of iron dipped in molten uranium, shown in Fig. 6.8. A plastic strain rate is calculated from the computed cladding stress and temperature history using correlations derived from transient tube burst tests. On this same basis, cladding failure is inferred when computed plastic strain exceeds a preset amount (2% for D9 and 6% for HT9 steel). Detailed model calculations have been performed within the COBRA/EXP code module (Sect. 4.3) by linking this modeling scheme to the thermal hydraulic analysis.

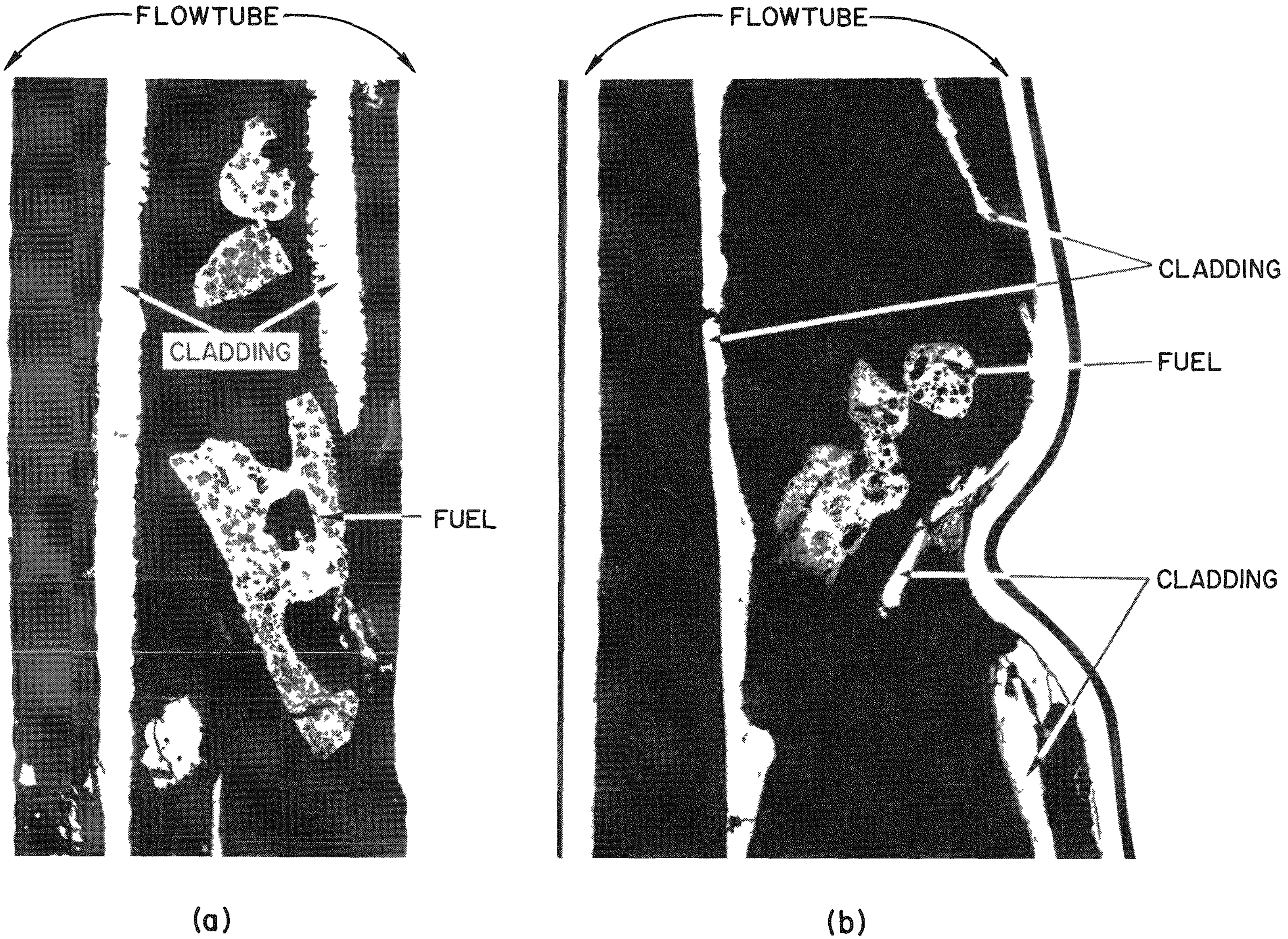

Fig. 6.7. Longitudinal Micrographs Showing Fuel Pin Failure Sites, Disrupted Fuel, and Fuel-Cladding Interaction. (a) 5.3 at.% Burnup D9-Clad Ternary Fuel Pin from TREAT Test M6. (b) 9.8 at.% Burnup D9-Clad Ternary Fuel Pin from TREAT Test M7.

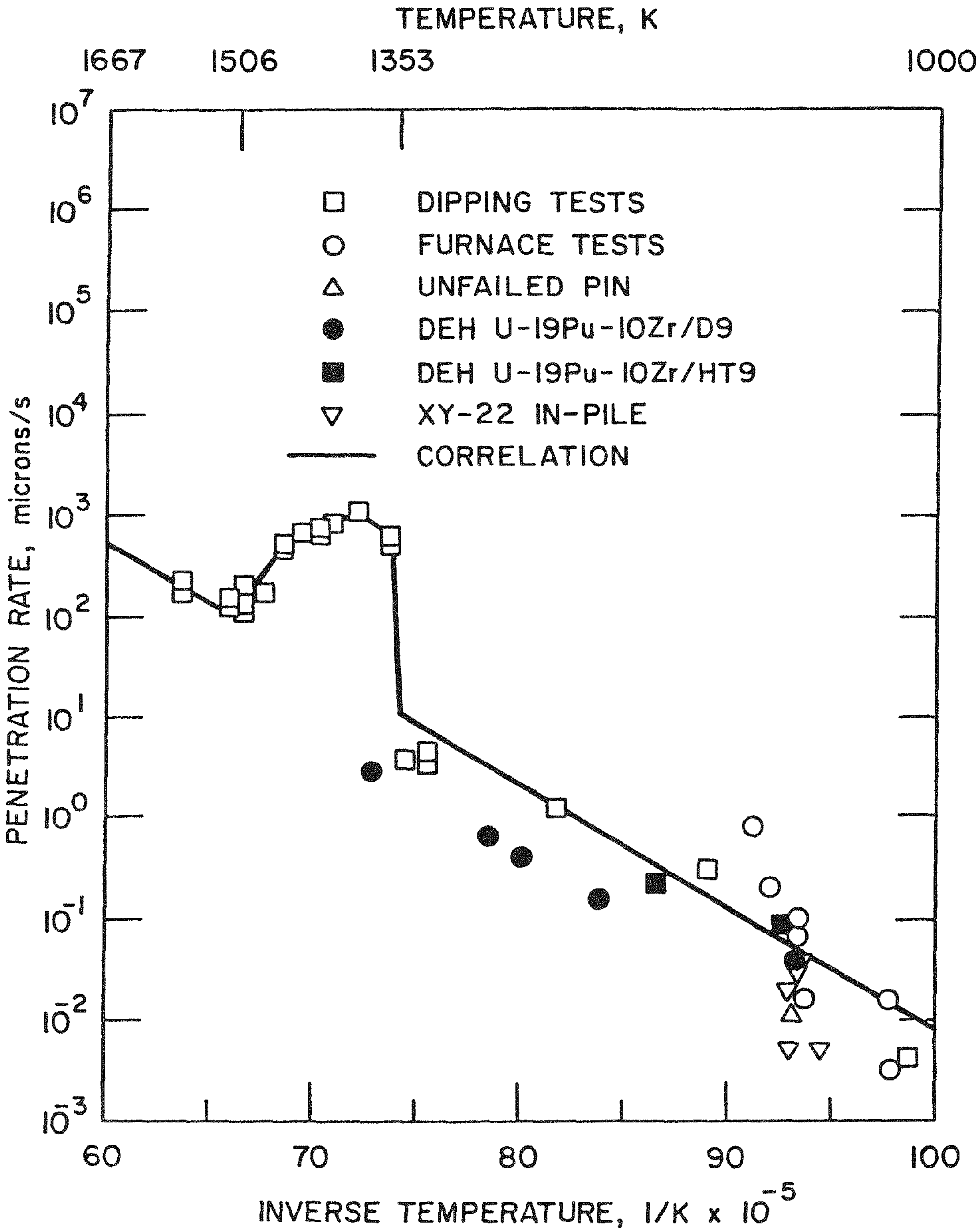

Fig. 6.8. Liquid Eutectic Penetration Rates from Various Tests [6.3]

These concepts may be easily applied to the present overpower test series in a "semi-quantitative" fashion. The high thermal conductivity of metal fuel assures peak cladding temperatures, hence likely failure sites, at the fuel top in agreement with observations. Temperatures key to the failure threshold analysis (pin plenum, peak cladding midwall and cladding inner-surface temperatures) are close to or easily derived from the measured whole-pin coolant temperature rise. The temperature rise is sufficiently rapid that, except at the highest possible burnups, failure would not be expected until the temperature of the fuel cladding interface exceeds a "threshold" value of 1350 K, the temperature at which Fig. 6.8 indicates eutectic penetration into the cladding becomes very rapid (associated with the melting of a protective solid iron-uranium compound). From thermal calculations, in most cases this temperature is reached at overpower levels of about four times nominal, in conjunction with cladding failure observations.

Calculated times of cladding failure are also reported in Table 5.2, expressed in terms of overpower level on the actual ~8 s period power transient (extended, if necessary). While these calculations are in no way definitive, the two observed cladding failures in IFR fuel were in reasonable agreement with expectations, and with the noticeable exception of the U-Zr pin tested, no failures were expected in the pins which actually remained intact. While agreement between measured and calculated pin failures has always been reasonable (neighborhood of 5%), earlier tests, M2-M4 showed some systematic tendency for observed failures to precede calculated. The possibility of hot spots generated locally around the cladding due to imperfect pin support is one physical mechanism that could induce failures earlier than anticipated, and improvements in pin mounting methods described in Sect. 3.3 may have helped alleviate this potential problem. The survival of the U-Zr pin, tested to about 4.8 times nominal power, was quite unexpected, not only because calculated failures have tended to lag behind observed cladding failures, but also because computed fuel-clad interface temperatures far exceeded the expected threshold for rapid eutectic penetration.

Figure 6.9 shows results of a post-test laser profilometry of the surviving U-Zr pin's cladding. The permanent cladding deformation shown at axial elevations at and just above the fuel top is indicative of severe

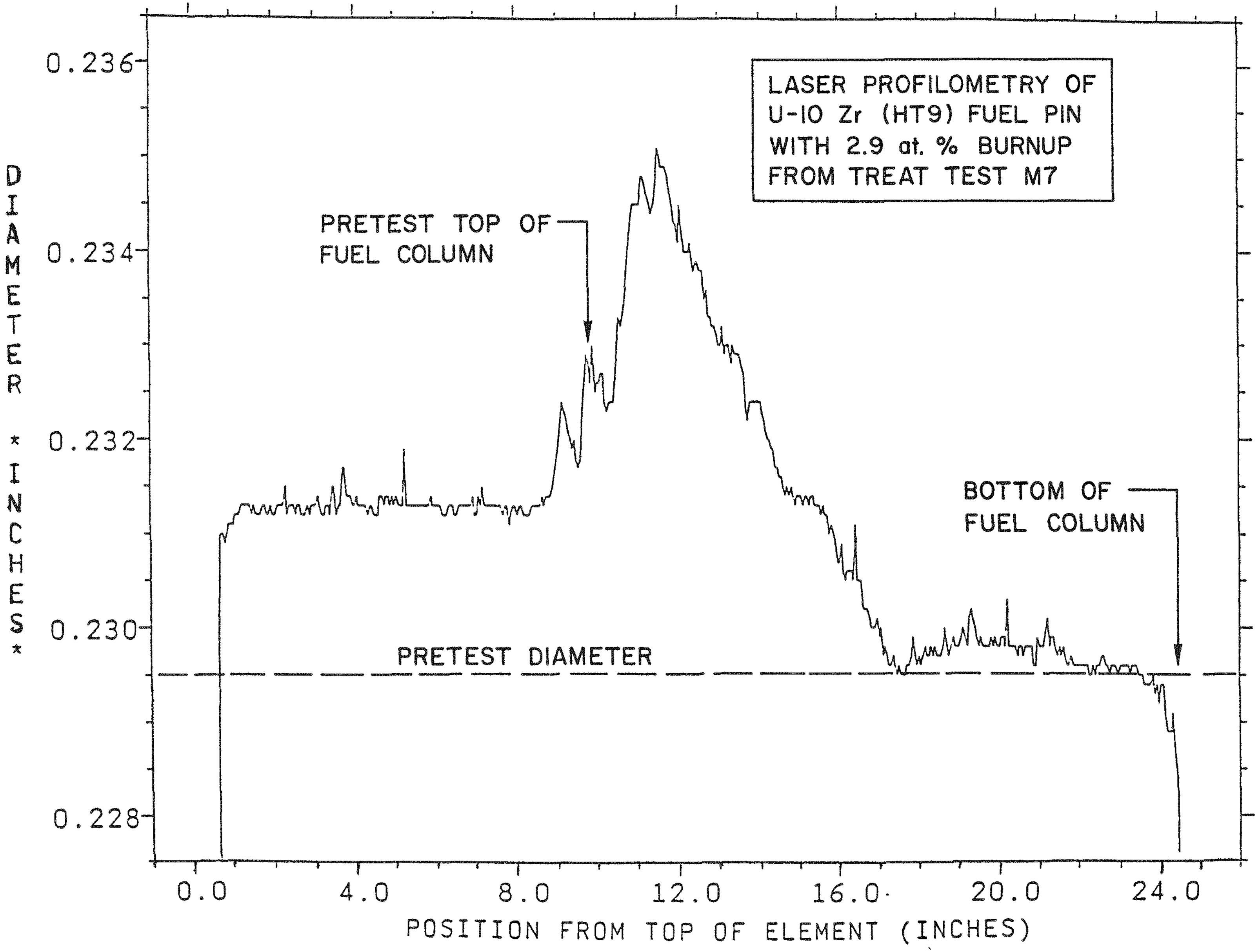

Fig. 6.9. Cladding Damage in the U-Zr Test Pin of M7

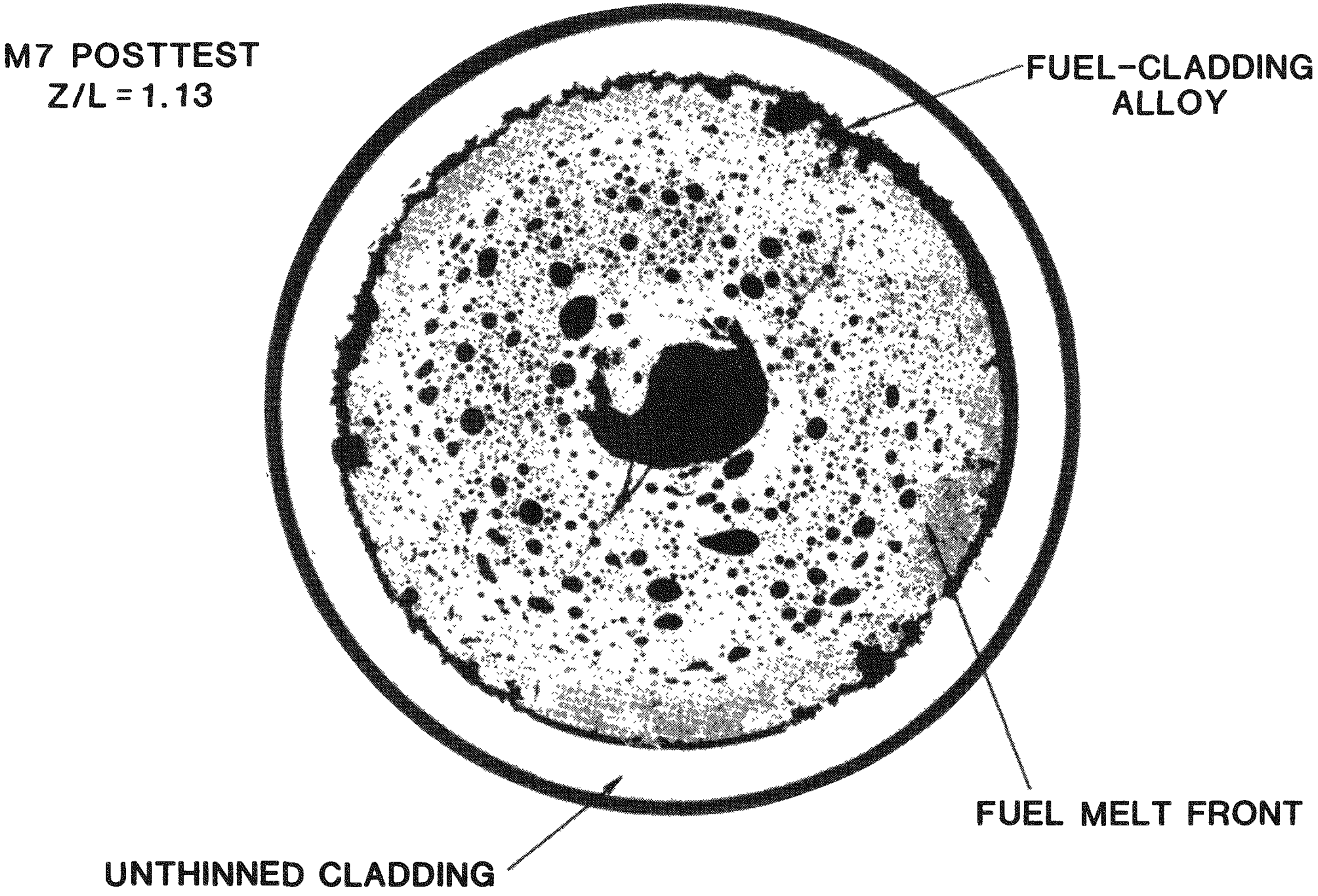

Fig. 6.10. Transverse Micrograph of 2.9 at.% Burnup (HT9-Clad) U-10Zr Fuel Pin Tested in TREAT Test M7 Illustrating Once Molten Fuel and Extensive Fuel-Cladding Interaction

cladding damage. Figure 6.10 shows the pin cross section at the elevation just above the top of the fuel (pretest) within the large deformation peak shown in Fig. 6.9. While there is evidence of a great deal of molten fuel around the center of the pin, Fig. 6.10 indicates cladding in contact with only a thin region of molten fuel and significant amounts of fuel never-molten. Cladding penetration shown is azimuthally non-uniform and extends to a maximum depth of about 30% of its original thickness. Based on the computed thermal history of the pin, this observed amount of penetration, while large, is about a factor of 10 less than expected from the correlation of Fig. 6.8. The key to understanding the unexpected survival of the U-Zr pin may be the observation that a significant amount of fuel near the cladding never melted. Proper application of the Fig. 6.8 melt-rate correlation requires a molten phase, rich in uranium, in contact with the cladding. For this to happen, melting at the interface must involve a much higher proportion of fuel volume than cladding volume (by a factor of ~5-15), but in Fig. 6.10 the volumes of fuel and cladding involved in the melt near the interface are approximately equal. Thus, any delay in melting fuel inward from the cladding would also be expected to slow the penetration into the cladding. In the U-Zr pin, such a delay might have been caused by the binary fuel's high solidus temperature of 1500 K. By contrast, in all other metal fuel tested thus far, lower solidus values insured an entire fuel cross section molten when the threshold for rapid eutectic penetration (~1350 K) was reached at the fuel-cladding interface.

General analytical studies with the cladding failure model indicate that by passing through low temperature quickly the cladding damage induced in tests M5-M7 was strongly weighted to high cladding temperatures in the neighborhood of 1350 K [6.6]. Typically, at M-series heating rates nearly total eutectic penetration would be required to fail cladding at low burnup, partial penetration would be required at midrange burnups, and almost no penetration would be required at high burnup. The abrupt rise of eutectic penetration rate at overpower levels near four times nominal was a dominating factor, and only calculations for the highest burnup (9.8 at.%) pin suggest a controlling role for pressure loading (although still at high temperature). In these tests margin to failure was not expected to depend strongly on the particular cladding type. At low temperatures, mechanical calculations do formally distinguish between properties of D9 and HT9 cladding (in both strain rates and plastic strain to failure), but, since most strain occurred at high temperature, computed differences were negligible. Future tests either with higher burnup fuel or with more slowly rising overpower transients could both induce cladding damage at lower temperatures and highlight differences in cladding type [6.6].

6.3 Post Failure Events

When cladding failed, similar post-failure events characterized the behavior of all fuel types tested. In each case about half of the fuel inventory, corresponding roughly to the fuel's melt fraction, was ejected rapidly through a small cladding breach at the fuel top. In all cases cladding failure was accompanied by a sudden, temporary reversal of inlet coolant flow and rapid coolant voiding. Measured pressure spikes were minor (less than 2 MPa) and were generally about one order of magnitude less than the plenum pressure of the failed pin. Fuel ejection from a failed pin could be driven by expansion of trapped fission gas and/or sudden boiling of the liquid sodium bond within the fuel. Ejected fuel then dispersed rapidly, combining with cladding and structural materials into a highly mobile low-melting point eutectic form and traveling upward with coolant to locations well downstream of the original fuel zone. Hodoscope data indicates this time period of significant disruption and removal to be around 100-200 ms [5.1]. This timing of disruption is also in agreement with pressured perturbations of pressure and flow. Afterwards, coolant flow past failed pins settled at about 2/3 of its pre-failure value indicating partial flow blockage. See Appendix F for details.

Figure 6.11 shows post-test radiographs of the two pins which failed in M5-M7. Figures 6.12 and 6.13 show cross sections at various axial locations of these failed pins indicating fuel losses and disruption of unmelted fuel. Quantitatively, for a given fuel type the amount of in-pin disruption of solid (primarily) fuel showed strong dependence on the amount of pin depressurization following failure. However, much more of the solid fuel remains stayed in place in failed IFR fuel than had been observed in previous tests with

---

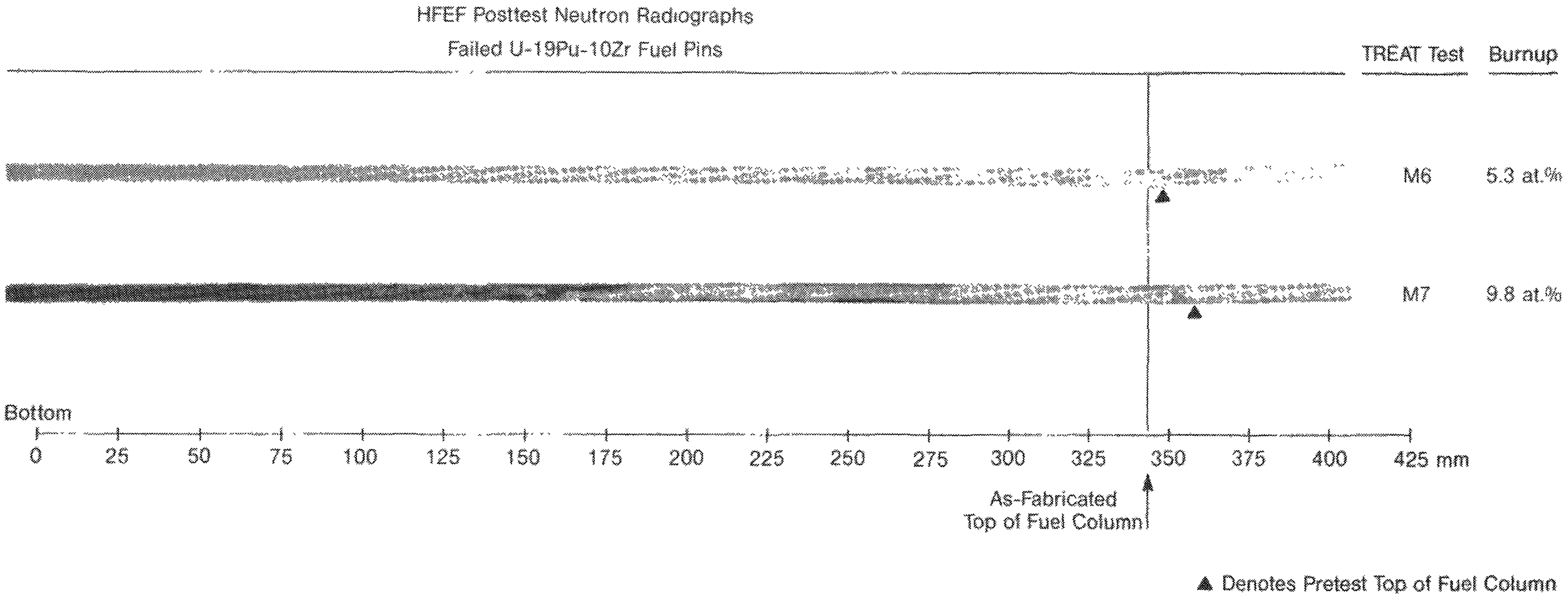

Fig. 6.11. Post-Test HFEF/NRAD Neutron Radiographs of Fuel Pins that Failed During TREAT Tests M6 and M7

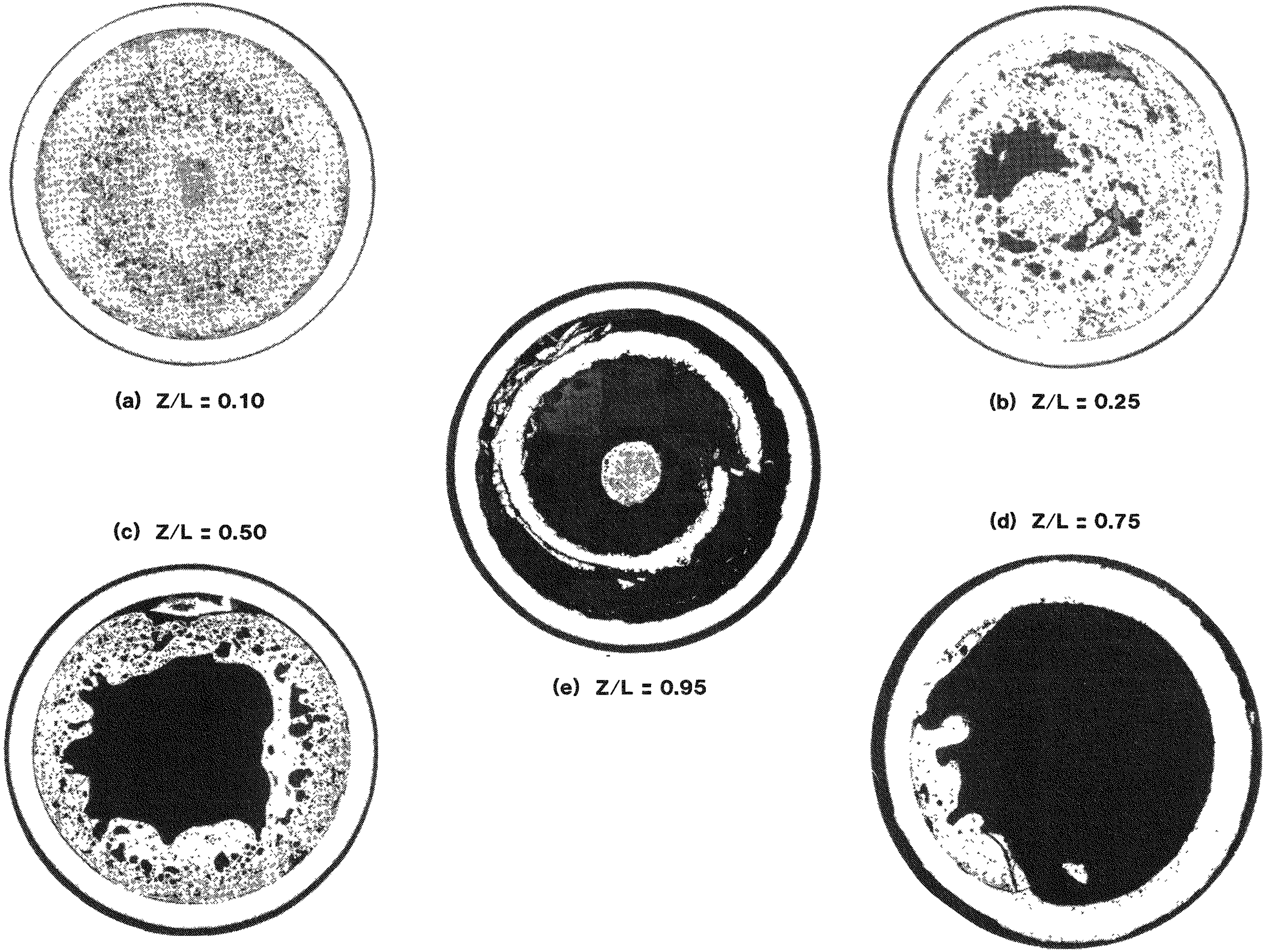

(a) Z/L = 0.10

(b) Z/L = 0.25

(c) Z/L = 0.50

(d) Z/L = 0.75

(e) Z/L = 0.95

Fig. 6.12. Transverse Micrographs at Various Elevations from the 5.3 at.% Burnup (D9-Clad) U-19Pu-10Zr Fuel Pin Tested in TREAT Test M6

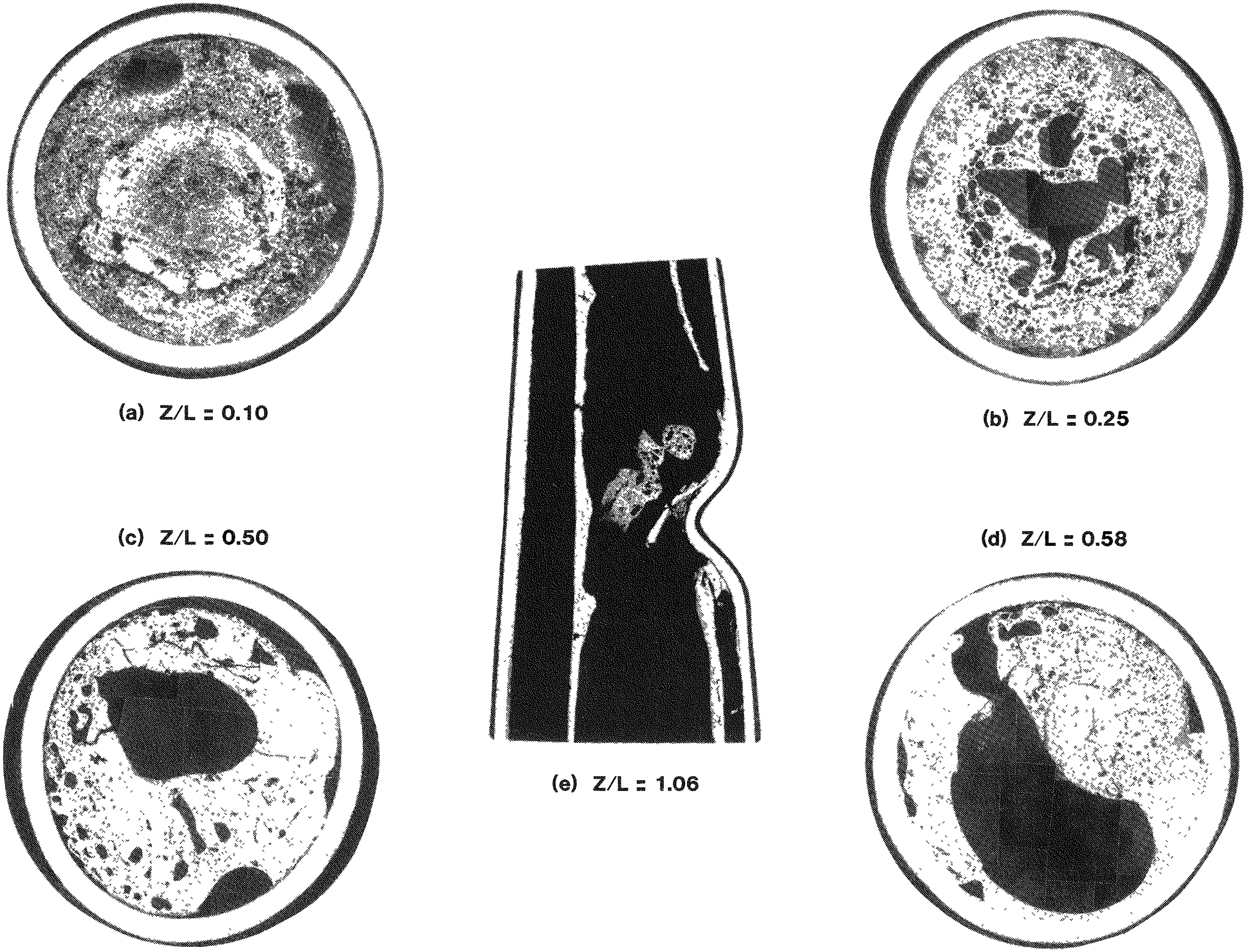

(a) Z/L = 0.10

(b) Z/L = 0.25

(c) Z/L = 0.50

(d) Z/L = 0.58

(e) Z/L = 1.06

Fig. 6.13. Transverse Micrographs at Various Elevations from the 9.8 at.% Burnup (D9-Clad) U-19Pu-10Zr Fuel Pin Tested in TREAT Test M7

U-5Fs fuel [6.5]. Figure 6.14 shows radiographs of failed U-5Fs pins for comparison with Fig. 6.11. Since IFR fuel contained significantly less dissolved gas than U-5Fs fuel, the difference suggests a gas-driven disruption mode for solid fuel.

After reactor power shutdown in tests M6 and M7, gamma rays characteristic of isotopes Rb-89, Cs-138, and Xe-138 were detected in the gas space above the loop plenum by the developmental Fission Product Detection System (FPDS). None were detected from M5 in which all pins remained intact. These observations are at present qualitative, but observed isotopes likely originated from the following chain of fission product release and transport:

1) Fission products Br-89 and I-138, which are soluble in sodium, were released from the fuel and transported efficiently in the coolant;

2) Br-89 and I-138 decayed into noble gasses, Kr-89 and Xe-138, which escaped into the gas plenum; and

3) Kr-89 and Xe-138 decayed into Rb-89 and Cs-138 which settled out on the loop wall.

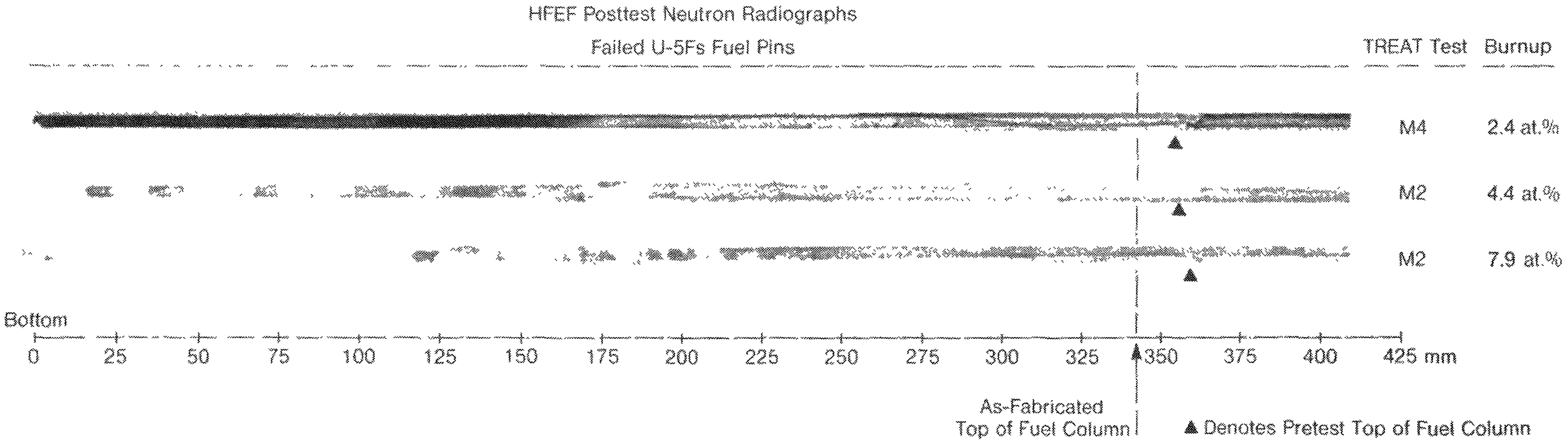

Fig. 6.14. Post-Test HFEF/NRAD Neutron Radiographs of U-5Fs Fuel Pins that Failed During TREAT Tests M2 and M4

7.0 CONCLUSIONS

Methods and techniques developed for multiple-pin overpower testing of failure threshold of metallic U-5Fs EBR-II Mark-II driver fuel have been extended to fuel types prototypic of the IFR concept. Hardware improvements in test pin mounting, flowrate measurement, and thermocouple placement have led to improved knowledge and control of each test pin's power and coolant flowrate during the overpower transient. Relatively simple adjustments or enhancements of test conditions have improved the simulation of prototypic fast reactor fuel temperatures. Calculated temperature rises were in reasonable agreement with measurements. Post-test measurements of maximum melting extent in intact test pins have helped confirm estimates of thermal conductivity for restructured metal fuel, including the impact of bond sodium, used in present analyses.

Simple models of pre-failure expansion and cladding failure developed during earlier tests on U-5Fs fuel have been extended and validated by the M5-M7 database of IFR-type fuel. Pre-failure axial expansion in IFR-type fuel was always positive and significantly beyond thermal expansion. Expansions in the range of 2-4% were typical of all burnups tested. Large expansions at low burnups, such as measured in U-5Fs fuel, were not measured in IFR-type fuel. Expansion of fission gas trapped in melting fuel provides a sound basis for modeling axial expansions, and differences in amounts of dissolved gas accounts for measured differences between fuel types. Failure threshold with the 8 s period overpower conditions tested is about four times nominal over a wide range of burnups and fuel types tested. Successful cladding failure models include effects of both overpressure and penetration of cladding by a low melting point eutectic. Because rapid cladding penetration by eutectic also requires extensive fuel melting, failure might be delayed somewhat in a fuel with a high melting point, such as IFR-binary U-10Zr tested in M7.

Studies with the cladding failure model indicates that, for the fuel burnups and heating rates employed in M-series tests, pins fail at or near the threshold point of rapid eutectic penetration. Different modeling issues and questions arise concerning slower cladding damage rates at lower temperatures.

Further model validation will require extention of the present fuel performance study to higher burnup fuel and/or overheating to lower temperatures for longer times.

Postfailure disruption in all fuel types tested involved a benign ejection of the failed pin's inventory of molten fuel through a small local breach at the top of the fuel. Extensive disruption of solid fuel remaining within failed pins is possible if a significant amount of fission gas is dissolved in that fuel. Once ejected, molten fuel was highly mobile in the coolant channel, showing little tendency to cause blockages. There is strong evidence from post-test remains that molten and mobile fuel in the coolant channel is in a low-melting-point eutectic form. Because the coolant channel environment in the tests was not optimized to simulate a large pin bundle, only qualitative conclusions should be drawn concerning dispersal of materials from failed pins.

While safety-related fuel behavior of all fuel types tested is similar, the above conclusions highlight the fuel properties of fission gas retention and melting point as accounting for major differences observed between behavior of U-5Fs and IFR type fuel.

8.0 ACKNOWLEDGMENTS

The following personnel were responsible for the numerous tasks related to performance of TREAT tests M5, M6, and M7 and the preparation of this report.

Management: A. J. Goldman, A. E. Klickman, L. J. Harrison, J. E. Herceg, A. DeVolpi, C. E. Dickerman, G. M. Teske, A. E. Wright, T. H. Bauer, N. J. Carson, and T. T. Anderson

General Guidance: R. H. Sevy

Design: R. J. Robertson and H. J. Myers

Experimenter: W. R. Robinson

Test Analyses: T. H. Bauer and W. R. Robinson

Hodoscope Analysis: G. S. Stanford, E. A. Rhodes, and J. P. Regis

Fission Product Detection System: T. H. Braid and R. C. Doerner

Safety Analysis: A. E. Wright

Test Engineer: D. A. Kraft

Machine Shop Planner and Instrument Maker: F. E. Van Hoegarden and Al Polowinczak

Machine Shop Liaison: F. J. Testa

Outfitting and Assembly: H. W. Helenberg assisted by R. R. Hopf, E. A. Pozzie, and T. Jackowski

Water Test Loop Measurements: E. E. Keppler
Electronics and Instrumtation: C. August and T. T. Anderson

Computer Programming and Graphics: P. H. Froehle, M. R. Kraimer, J. A. Morman, R. D. Baldwin, and R. Simms

TREAT Experiment Coordinators: W. W. Stevens, N. A. Kramer and, R. M. Bradford

TREAT Reactor Operations: R. L. McVean, R. H. Dodge, D. W. Krekel, L. Neuman, E. G. Rolle, and J. L. Stringham

TREAT Programming and Data Acquisition: G. R. Larsen, C. E. Bleak, R. C. Kontes, P. A. Cawley and, K. D. Crofts

TREAT Hodoscope Operations: D. M. Ray

HFEF Operations: G. M. Teske, K. T. Teraguchi, and J. F. Kerr

Radiochemistry: R. Villarreal, R. E. DeFelici, J. O. Young, and R. M. Coleman

Alpha Gamma Hot Cell Facility Examination: J. W. Holland

Typing: E. R. Brown and S. L. Swanson

9.0 REFERENCES

1.1. W. R. Robinson et al., "Integral Fast Reactor Safety Tests M2 and M3 in TREAT", Trans. Am. Nucl. Soc., 50, 352 (1985).

1.2. W. R. Robinson et al., "IFR Safety Tests M2 and M3 in TREAT: Data and Analysis," Argonne National Laboratory Report, ANL-IFR-18 (June 1985).

1.3. A. E. Wright, T. H. Bauer, R. K. Lo, W. R. Robinson, and R. G. Palm, "Recent Metal Fuel Safety Tests in TREAT", Proc. of the ANS/ENS Intl. Conf. of the Science and Technology of Fast Reactor Safety, CONF-86050, Guernsey, England, 1, 59 (May 12-16, 1986).

1.4. T. H. Bauer et al., "Behavior of Uranium-Fissium Fuel in TREAT Transient Overpower Tests", Trans. Am. Nucl. Soc., 53, 306 (1986).

1.5. T. H. Bauer et al., "Update of Safety Testing in TREAT on U-5Fs Fuel: Data from Test M4 and Combined Analysis of Tests M2, M3, and M4," Argonne National Laboratory Report, ANL-IFR-69 (May 1987).

1.6. W. R. Robinson et al., "First TREAT Transient Overpower Tests on U-Pu-Zr Fuel: M5 and M6", Trans. Am. Nucl. Soc., 55, 418 (1987).

1.7. A. E. Wright et al., "IFR Overpower Test M7 in TREAT," Trans. Am. Nucl. Soc., 56, 383 (1988).

1.8. A. E. Wright et. al., "Techniques of Metal Fuel Transient Testing in TREAT," Proc. of the Intl. Topical Meeting on Safety of Next Generation Power Reactors, ANS, 871, Seattle, WA (May 1988).

1.9. T. H. Bauer et al., "Behavior of Metallic Fuel in TREAT Transient Overpower Tests," Proc. of the Intl. Topical Meeting on Safety of Next Generation Power Reactors, ANS, 857, Seattle, WA (May 1988).

2.1. E. E. Gruber, "The Stars Model for Fission Gas Behavior: 1. Steady State Behavior," Argonne National Laboratory Report, ANL-IFR-58 (December 1986).

2.2. R. G. Pahl et al., "Postirradiation Examinations of U-Pu-Zr Fuel Elements from Subassemblies X419 and X419A," Argonne National Laboratory Report, ANL-IFR-55 (October 1986).

2.3. R. G. Pahl et al., "Lead IFR Subassemblies X419, X420, X421," IFR Fuels Performance and Fabrication Monthly Reports for 1987 (1988).

2.4. G. L. Hofman et al., "Metallic Fuels Handbook," Argonne National Laboratory Report, ANL-IFR-29 (November 1985).

3.1. A. E. Wright et al., "Mark-III Integral Sodium Loop for LMFBR Safety Experiments in TREAT," Proc. of the Conference on Fast, Thermal, and Fusion Reactor Experiments, I-174, Salt Lake City, UT, (April 1982).

4.1. W. R. Robinson and T. H. Bauer, "Power Coupling in TREAT M-Series: New Experimental Results from M7CAL and Updated Analyses," Argonne National Laboratory Report, ANL-IFR-86 (February 1988).

4.2. P. H. Froehle and T. H. Bauer, "COBRA-PI: An Extension of the COBRA-3M Code Dynamically Dimensioned to Accept Pin Bundles of Any Size", Advances in Reactor Computations, Proc. of the ANS Mathematics and Computation Division Topical Meeting, 211, Salt Lake City, UT (March 1983).

4.3. D. J. Dever and T. H. Bauer, "SLOOP: A Simulation of Thermal-Hydraulics for the MK-III Loop," Argone National Laboratory Report, ANL/RAS 83-31 PFR/TREAT (83) ANL-08 (August 1983).

5.1. E. A. Rhodes, G. S. Stanford, and J. P. Regis, "Fuel Motion In TREAT Tests M5F1, M5F2, M6, and M7: Preliminary Analysis of Hodoscope Data," Argonne National Laboratory Report, ANL-IFR-112 (July 1989).

6.1. E. E. Gruber and J. M. Kramer, "Gas-Bubble Growth Mechanisms in the Analysis of Metal Fuel Swelling," Argonne National Laboratory Report, ANL-IFR-27 (October 1985).

6.2. G. R. Fenske et al., "Fission Gas Retention and Axial Expansion of Irradiated Metallic Fuel," Argonne National Laboratory Report, ANL-IFR-45 (June 1986).

6.3. T. H. Bauer, G. R. Fenske, and J. M. Kramer, "Cladding Failure Margins for Metallic Fuel in the Integral Fast Reactor," Trans. of the 9th Intl. Conf. on Structural Mechanics in Reactor Technology, Lausanne, Switzerland, C, 31 (August 1987).

6.4. J. M. Kramer, T. H. Hughes, and E. E. Gruber, "Validation of Models for the Analysis of the Transient Behavior of Metallic Fast Reactor Fuel," Trans. of the 10th Intl. Conf. on Structural Mechanics in Reactor Technology, C, 65, Anaheim, CA (August 1989).

6.5. J. W. Holland, et al., "Posttest Examination Results of Recent TREAT Tests on Metal Fuel," Proc. of the Intl. Conf. on Reliable Fuels for Liquid metal Reactors, ANS, MST Div., 1, 6-164, Tuscon, AZ, (September 1986).

6.6. T. H. Bauer et al., "A Program to Resolve the Safety Implications of Fuel Damage in the Operation of Advanced Metal-Fueled Reactors," Argonne National Laboratory Report, ANL-IFR-103 (February 1989).

APPENDIX A

Details of the Experiment Hardware

Described in this Appendix are the fuel pins used, and the Mark-IIIC loop and test train in which the pins were tested.

A.1 Test Fuel

Of the six fuel pins tested in M5, M6, and M7, five were of U-19Pu-10Zr ternary fuel in D9 cladding and one was an HT-9 clad U-10Zr binary-fuel pin. All had been preirradiated in EBR-II. As-fabricated and as-irradiated fuel compositions, densities, dimensions, burnups, and plenum pressures are listed in Table A.1 for each pin. As-fabricated characteristics common to all six pins were shown in Table 2.1. A design drawing of the test pins is shown in Fig. A.1.

A.2 Sodium Test Loop

The same Mark-IIIC loop (serial number 010) was used in all three tests (M5, M6, and M7). It had been previously used in test M2. For completeness a schematic drawing of the loop previously shown in Fig. 3.2 is reproduced as Fig. A.2. Principally, the loop comprises two parallel pipes 3.5 m long with a centerline-to-centerline separation of about 0.1 m. The test section leg of the loop is 2.25 in. O.D. and 1.44 in. I.D. It has an extension that serves as a gas-filled plenum region above the sodium. This leg also provides a flanged entrance through which the test train can be inserted into the loop. A separate gas-line feedthrough and a high pressure valve provided access to the plenum when the test train is sealed in the loop. This allows the plenum to be pressurized pretest and the plenum gas to be sampled posttest to check for fission product activity.

The pump leg includes a small annular linear induction pump (ALIP). With the test train in place, sodium flows into the test train from the bottom, passes along the test fuel pins and flows from the train into the upper bend of the loop. The entire system is housed within a long secondary container,

Table A.1. Fuel Pin Characteristics (As-Irradiated and As-Fabricated)

	Test M5		Test M6		Test M7	
Jacket number:	T-280	T-154	T-186	T-102	T-131	T-427
Cladding	D9	D9	D9	D9	D9	HT9
As-Irradiated Fuel Characteristics						
EBR-II Irradiation Subassembly	X419A	X419	X419	X420	X421	X425
Grid Position in Subassembly	40	14	15	47	30	39
Burnup, at.%	0.8	1.9	1.9	5.3	9.8	2.9
Fissile Masses, grams						
U-235	31.04	30.90	30.67	?	?	?
Pu-239	13.65	13.48	13.41	12.21	11.48	0.09
Fuel Length(a), cm (in.)	35.1 (13.8)	34.8 (13.7)	34.7 (13.65)	34.7 (13.65)	35.8 (14.1)	37.3 (14.7)
Pin Plenum Pressure, psia (at room temperature)	39	94	94	332	706	205
Zone Structure (a)	---	---	---	(b)		none
As-Fabricated Fuel Characteristics						
Pu, wt.%	19	19	19	19	19	0
Fuel batch number (in EBR-II)	55	35	35	42	46	204
Total fuel mass, g	77.26	78.01	77.65	76.62	76.80	78.80
Wt.% U (mass in g)	70.93 (54.80)	71.66 (55.90)	71.66 (55.64)	71.77 (54.99)	71.77 (55.12)	89.66 (70.65)
Pu	18.99 (14.67)	18.93 (14.77)	18.93 (14.70)	18.49 (14.17)	18.84 (14.47)	-------------
Zr	10.34 (7.99)	10.17 (7.93)	9.41 (7.31)	9.74 (7.46)	9.49 (7.29)	9.70 (7.64)
Wt.% in uranium (mass in g)						
U-234	0.42 (0.23)	0.41 (0.23)	0.41 (0.23)	0.43 (0.24)	0.55 (0.30)	0.63 (0.45)
-235	57.43 (31.47)	57.09 (31.91)	57.09 (31.76)	57.28 (31.50)	56.99 (31.41)	68.50 (48.40)
-236	0.26 (0.14)	0.25 (0.14)	0.29 (0.16)	0.26 (0.14)	0.35 (0.19)	0.37 (0.26)
-238	41.88 (22.95)	42.23 (23.61)	42.23 (23.50)	42.03 (23.11)	42.10 (23.21)	30.50 (21.55)
Wt.% in plutonium (mass in g)						
Pu-238	0.03 (0.004)	0.03 (0.004)	0.03 (0.004)	0.03 (0.004)	0.03 (0.004)	-------------
-239	93.93 (13.78)	93.85 (13.86)	93.85 (13.80)	93.83 (13.29)	93.83 (13.58)	-------------
-240	5.61 (0.82)	5.70 (0.84)	5.70 (0.84)	5.70 (0.81)	5.72 (0.83)	-------------
-241	0.38 (0.06)	0.38 (0.06)	0.38 (0.05)	0.39 (0.05)	0.38 (0.05)	-------------
-242	0.07 (0.01)	0.07 (0.01)	0.07 (0.01)	0.07 (0.01)	0.07 (0.01)	-------------
Mass of Am-241 (g)	(0.002)	(0.002)	(0.002)	(0.002)	(0.002)	-------------
Density, g/cc	15.4	15.6	15.5	15.6	15.2	15.7
Smear density, %	72.4	72.0	72.1	70.1	72.3	72.3
Fuel length, mm (in.)	339.5 (13.365)	341.8 (13.458)	340.7 (13.412)	339.0 (13.348)	342.6 (13.490)	343.0 (13.518)
Diameter, mm (in.)	4.34(0.171)	4.32(0.170)	4.32(0.170)	4.29(0.169)	4.32(0.170)	4.32(0.170)

(a) From radiograph
(b) Axially uniform

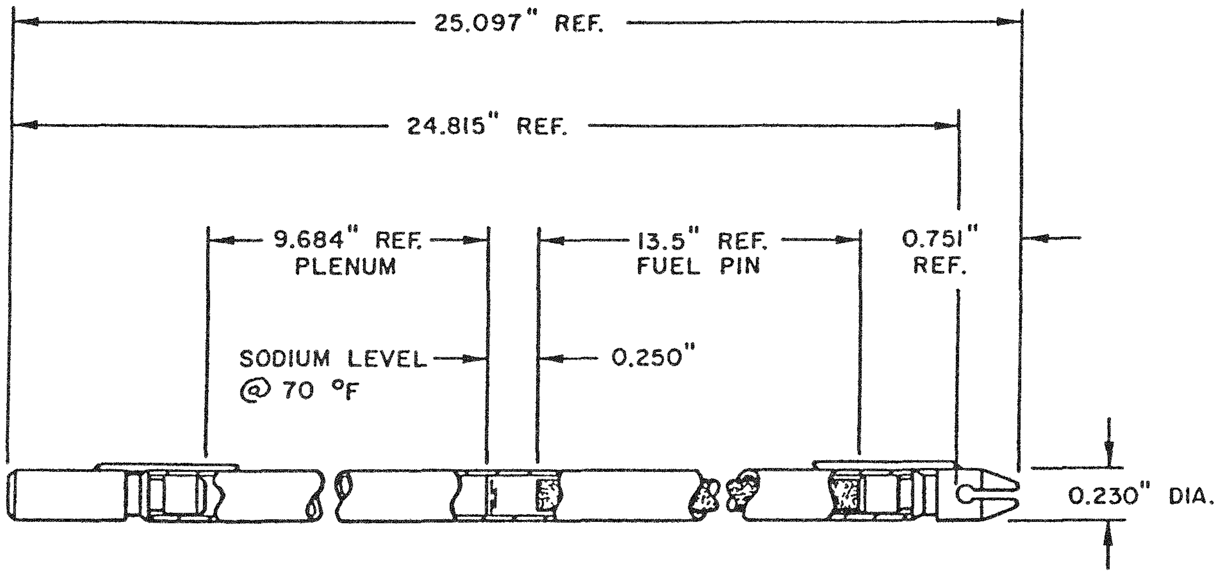

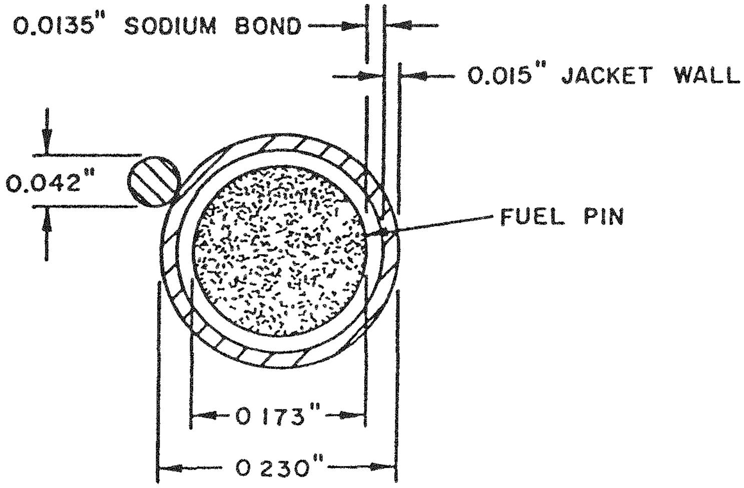

Note: Wire wrap removed after EBR-II irradiation

Fig. A.1. Design Drawing of the M5, M6, and M7 Test Fuel Pins

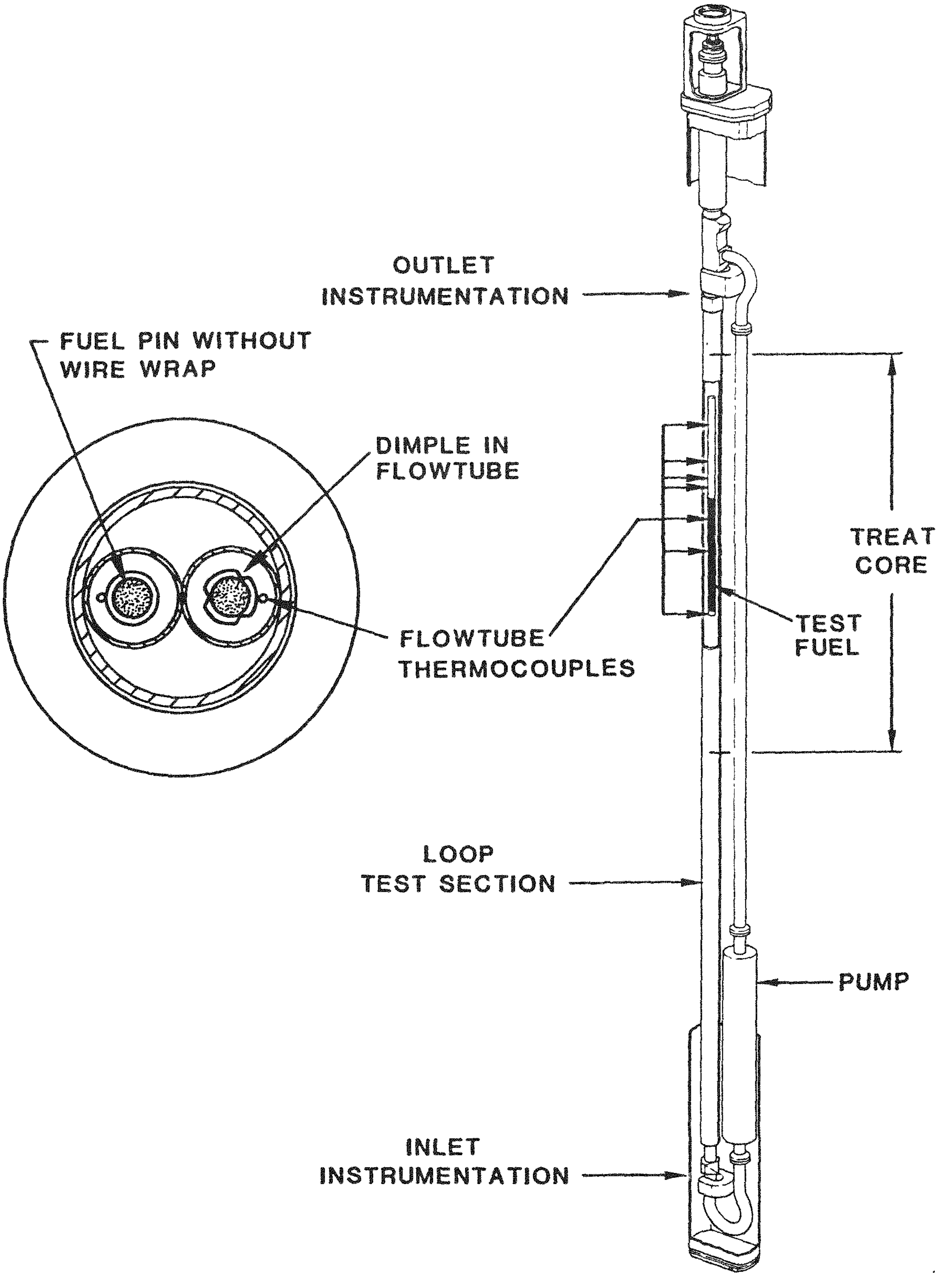

Fig. A.2. Schematic Drawing of the Test Vehicle and Cross Section Through the Loop and Test Train of cross section dimensions 4 in. (10.2 cm) x 8 in. (20.4 cm), which is designed to replace two TREAT reactor fuel assemblies. The secondary containment is capable of containing sodium or fission gases released from the primary containment. A gas system is provided for purging the secondary containment through a connection at the top plate of the loop.

Electrical heaters are attached around the test section leg of the loop to melt the sodium and to provide the desired pretransient sodium temperature. Wire-wrapped trace heaters are used to heat the pump leg and the upper and lower bends of the loop.

In each test, the midplane of the active test fuel column was located at the midplane of the TREAT core. An asymmetric configuration of dysprosium neutron-shaping collars (Fig. A.3) was used to achieve the desired axial power profile in the test fuel. Except for these shaping collars, the loop was unfiltered.

Loop instrumentation is described in Sect. A.4.

A.3 Test Train

The test train is a long cylindrical structure designed to be inserted into the loop test section. It serves to (a) support two fuel pins in the loop test section, (b) provide for temperature measurements in the vicinity of the test fuel, (c) provide a mating gas-tight seal with the loop top closure flange, and (d) provide sodium bypass flow in the sodium annulus between the test train and test section walls. The same test train was used for tests M5 and M6. A new, slightly modified version of the M5/M6 train was used for M7.

Each fuel pin was located in a separate flowtube. Lateral separation of the flowtubes was as wide as possible (0.625 in. centerline-to-centerline) in order to minimize the azimuthal power gradient in the test fuel due to neutron shielding of one fuel pin by another. Connected to the bottom of each fuel pin was a solid-rod extender (approximately 4 ft long) which was anchored to the test train structure near the test train bottom and fabricated to the same diameter as the fuel pin. The flowtubes along the test fuel length were

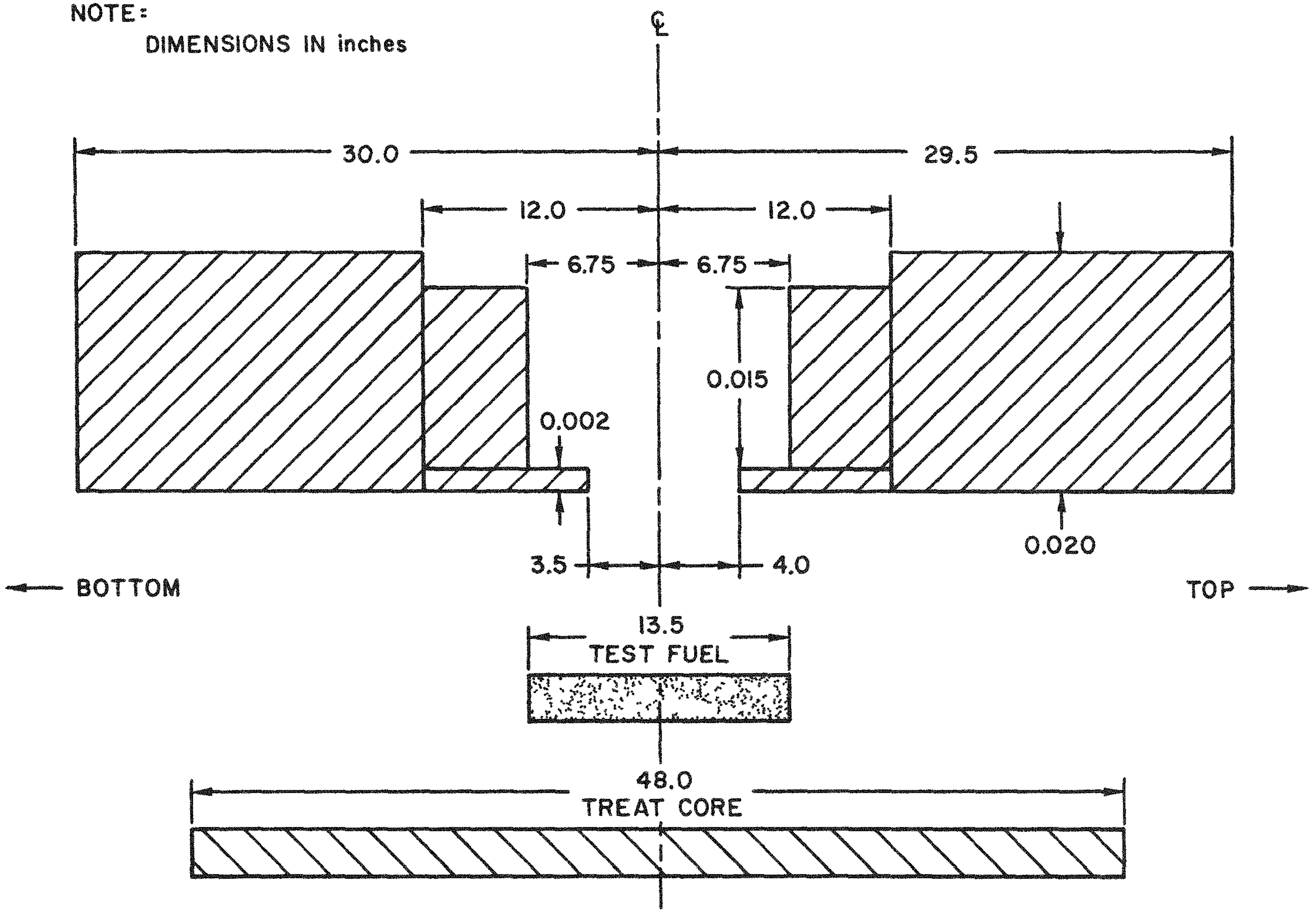

Fig. A.3. Configuration of Dysprosium Axial-flux-shaping Collars on the Loop Test Section of 0.348 in. (8.84 mm) O.D. and 0.311 in. (7.90 mm) I.D. Sodium flowed upward between the fuel pin and the flowtube in a flow area of 0.222 cm^2. Along the pin extender the flowtubes were 0.437 in. (11.10 mm) O.D. and 0.367 in. (9.32 mm) I.D. The enlarged region diminished the pressure drop and allowed passage of the connector that joined the fuel pin to the pin extender. Except for the flowmeter magnets, the test train was made of stainless steel.

To avoid the thermal-hydraulic effects of the wire-wrap spacing on single pins within flowtubes which was experienced in earlier tests, the wire wraps were removed from the pins, and lateral support of the pins was provided by three hemispherical dimples in the flowtubes at each of several axial elevations. At each elevation the three dimples were separated azimuthally by 120°. In the M5/M6 test train the dimples were indented to a depth which resulted in a local flowtube I.D. of 0.246 in. (0.625 cm). This restricted the pin-to-flowtube separation to be greater than half the separation that exists when the pin is perfectly centered within the tube. To reduce pin oscillations relative to the flowtube in the M7 test train, the dimples were made slightly deeper such that the local flowtube I.D. was 0.242 in. (0.615 cm). In the M5/M6 train, at each elevation the triad of dimples were located at 0, 120, and 240°. In the M7 train, to provide further support to the pin, alternate triads were displaced 60°, i.e., with dimples located at 60, 180, and 300°, as indicated in Table A.2.

The test trains were designed to accommodate orifice plates near the inlet of each flowtube, as shown in Fig. A.4. This would allow control over the relative split of the flow into the two flowtubes. In the M5 and M6 tests, no orifices were necessary. In test M7, a single orifice was used, of 0.170 in. (4.32 mm) diameter placed in flowtube 1 (9.8 at. % burnup ternary fuel pin). The orifice was installed at the Hot Fuels Examination Facility (HFEF) shortly before the fuel pins were loaded into the test train. The effect of the orifice on the flow distribution among the two flowtubes was estimated by calculations based on measurements in flowing water and later checked by means of a heat-balance transient with the fueled loop in TREAT.

Table A.2. Location of Flowtube Dimples and Thermocouples

M5/M6 Test Train				M7 Test Train		
Dimple Angles (a) (degrees)	Dimple Elevations (b) (in.)	TC Elevations (b) (in.)		Dimple Angles (a) (degrees)	Dimple Elevations (b) (in.)	TC Elevations (b) (in.)
		+11.75				+11.75
0,+/-120	+8.0			+/-60,180	+9.0	
				0,+/-120	+6.0	
		+ 4.0				+ 4.0
0,+/-120	+3.0			+/-60,180	+3.0	
		+ 2.0				+ 2.0
		+ 1.0				+ 1.0
			(Fuel top)	0,+/-120	0.0	
		- 1.0				
0,+/-120	-2.0					- 2.0
		- 3.0		+/-60,180	-3.0	
0,+/-120	-5.5					
				0,+/120	-6.0	
		- 6.75	(Midplane)			- 7.0
0,+/-120	-9.0			+/-60,180	-9.0	
0,+/-120	-12.5			0,+/120	-12.0	
			(Bottom)			
	-14.0					-15.0

(a) Relative to the vector with origin on the flowtube axis and pointing to the test train axis. (clockwise looking down)

(b) Relative to an elevation 13.5 in. (34.3 cm) above the bottom of the active fuel column.

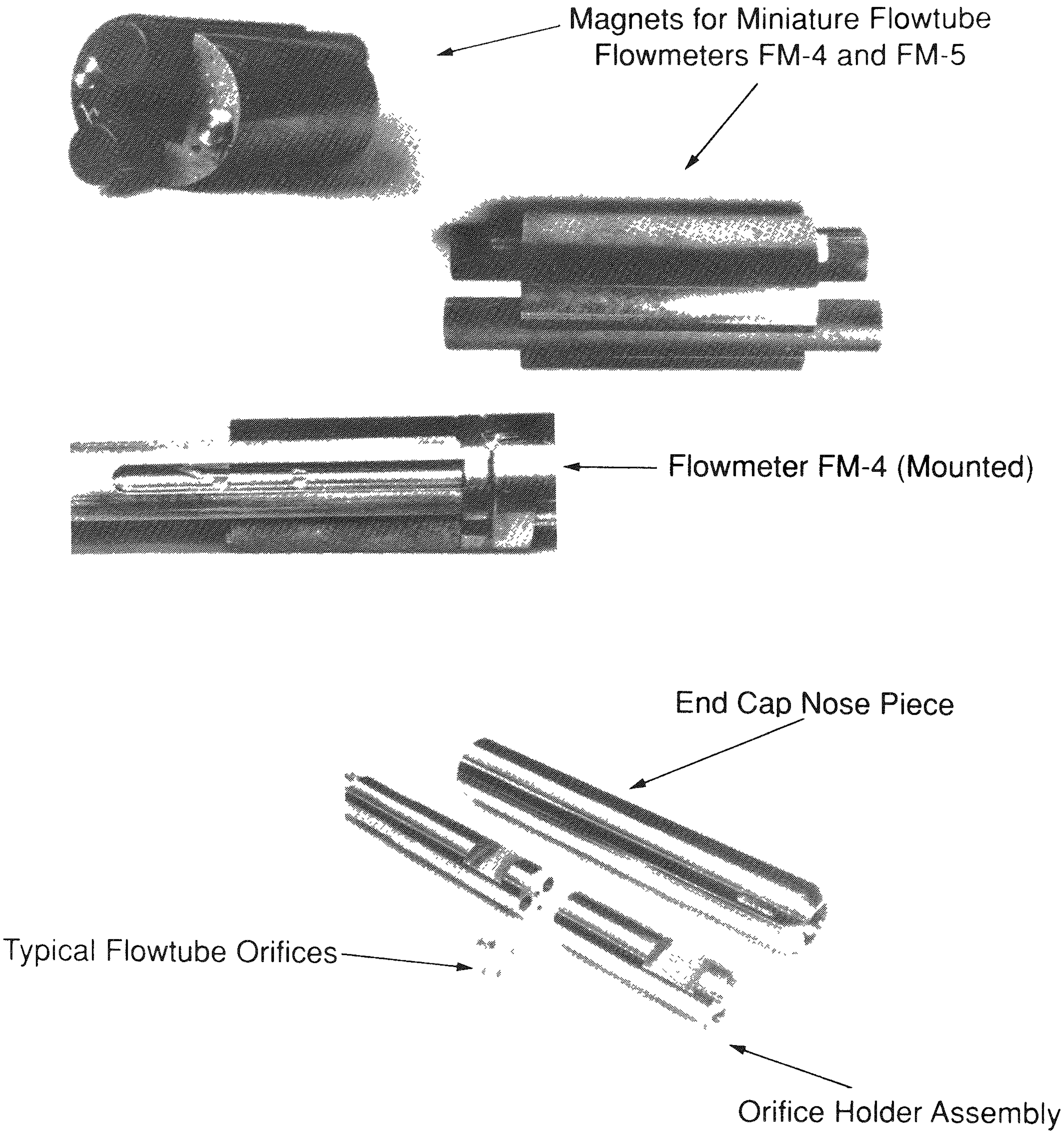

Fig. A.4. Photographs of the Mini-flowmeters and Orifice Assembly of the M5/M6 Test Train

Because of the potential for flowtube meltthrough due to the formation of a low-melting point fuel-steel alloy, a shield tube of 0.625 in. (15.88 mm) O.D. and 0.020 in. (0.51 mm) wall was located around each flowtube over most of the flowtube length. The shield tubes were intended to limit radial fuel motion after pin failure should the flowtubes be penetrated by fuel. Spaces between the flowtubes and the shield tubes and between the shield tubes and the outer test train wall were filled with an Ar-He gas mixture and pressurized to four atmospheres (absolute).

At the top of each flowtube was a 3.1 in. (78 mm) long bellows assembly located at the elevation of the top of the TREAT core. The bellows accommodated differential thermal expansion between the flowtubes and test train outer tube. Above the bellows assemblies, the two sodium flow channels discharged into a small manifold.

In the M5/M6 test train a set of three perforated baffles were installed in the manifold to trap fuel debris. Trapping the fuel increases the probability of being able to remove the test train from the loop and reduces the amount of fuel particulate remaining in the loop, thus allowing the loop to be reused in subsequent tests. The lower baffle contained seven holes of 0.25 in. (6.4 mm) diameter, the middle baffle contained seven holes of 0.187 in. (4.7 mm) diameter and the top baffle 19 holes of 0.125 in. (3.2 mm) diameter. For the M7 train, the fuel trap design was modified to include extensive coolant mixing and decrease the amount of structure in the manifold that would affect the measurement of the mixed-mean outlet sodium temperature by TC-16. The two designs are shown in Fig. A.5.

A stainless-steel reference marker 0.25 in. (0.635 cm) in diameter and 0.375 in. (0.953 cm) long was affixed to flowtube 1 on each of the two test trains (M5/M6 and M7) to aid in identifying that particular flow channel in neutron radiographs. The top of the marker was 4 in. (10.16 cm) below the active fuel column midplane.

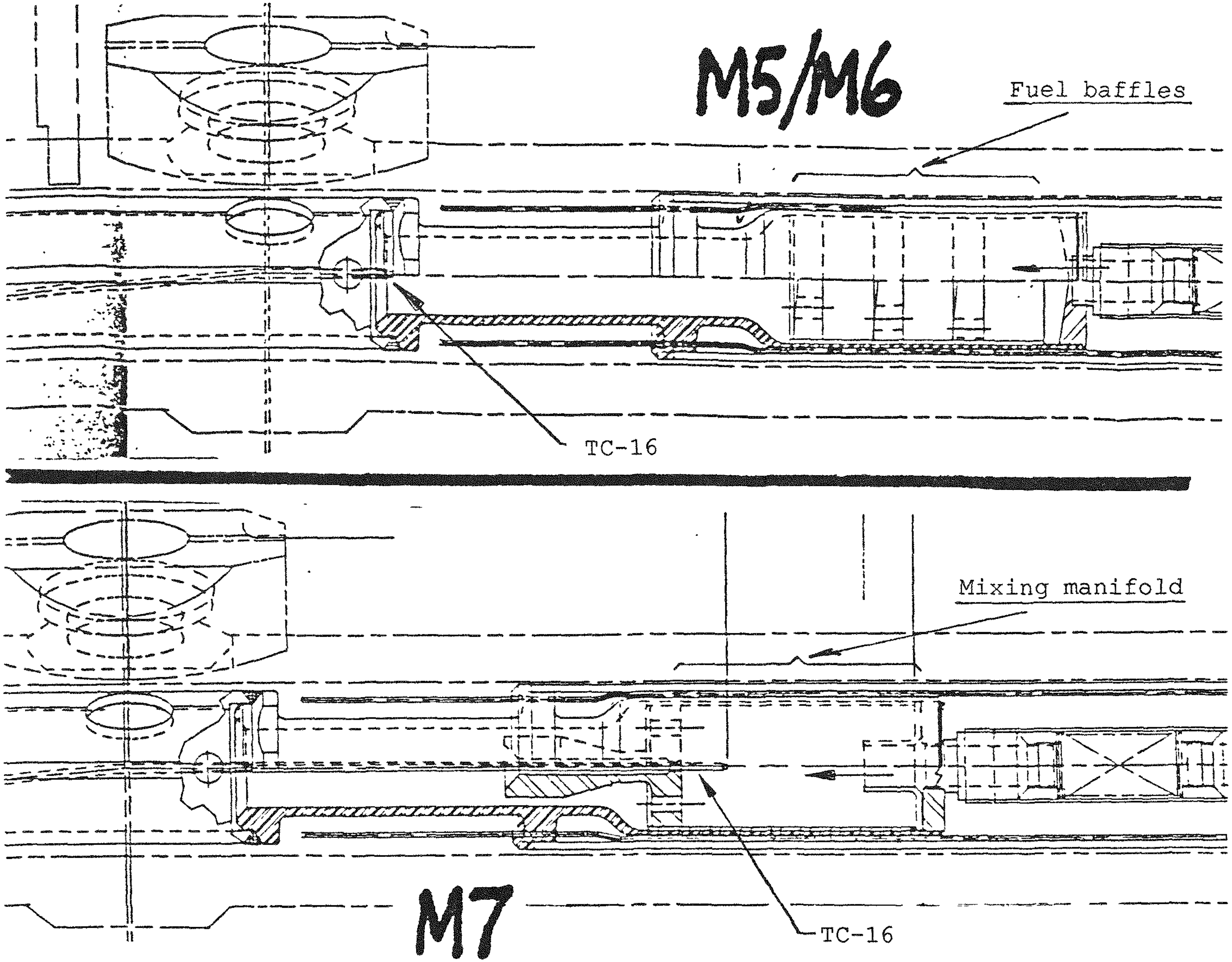

Fig. A.5. Outlet Regions of the Test Trains

A.4 Instrumentation

Figure A.6 schematically shows the locations of the flowmeters, thermocouples, and pressure transducers used in the tests.

A.4.1 Flowmeters

Total loop coolant flowrates were measured by three permanent magnet flowmeters which were mounted on the loop piping: flowmeters FM-1 (at the bottom of the test-section leg) and FM-3 (at the top of the pump leg) measured the inlet flow rate. Flowmeter FM-2 (at the top of the test section leg) measured the outlet flow rate. The response time of the flowmeters is better than 1 ms. The flow rate in each flowtube was measured by two permanent-magnet miniature flowmeters, FM-4 and FM-5, mounted one on each flowtube near the bottom of the test train. Figure A.4 shows a photograph of the "miniflowmeters".

Test M5 was the first test to use the miniature flowmeters. The magnets of the miniflowmeters consisted of two identical pieces, each roughly semicircular, having a pole face on each end, arching between the flowtubes on a plane perpendicular to the tubes, and providing a field strength of about 0.08 tesla. An important feature of the flowmeter design was that, because both flowmeters were of identical design and shared the two halves of the magnet, the field strengths and hence the sensitivities of the flowmeters were essentially identical. Thus, even without being calibrated, they could be used to accurately indicate the ratio of flowrates in the two tubes. At TREAT the combined flow rate indicated by the pair of miniflowmeters was calibrated relative to the measured total loop flow rate.

The loop flowmeters were calibrated at ANL-E against a previously-calibrated sharp-edged orifice and were later cross-calibrated relative to one another at TREAT both in the neutron radiograph stand and again in the reactor prior to each heat balance and final transient. During the cross calibrations at TREAT, FM-3 was chosen as the reference flowmeter since (a) unlike the outlet flowmeter (FM-2) the calibration of FM-3 is independent of which train is in place in the test section, whether it is the actual fuel-bearing test

TESTS M5 and M6

		Flowtube 1 West	Flowtube 2 East
Fuel Pins	M5	T-280 0.8 at.% BU U-19Pu-10Zr D9 clad	T-154 1.9 at.% BU U-19Pu-10Zr D9 clad
	M6	T-186 1.9 at.% BU U-19Pu-10Zr D9 clad	T-102 5.3 at.% BU U-19Pu-10Zr D9 clad
TC Locations	(Z/L)= 1.87	--	TC15
	1.30	TC14	TC7
	1.15	TC13	TC6
	1.07	TC12	TC5
	0.93	TC11	TC4
	0.78	TC10	TC3
	0.50	TC9	TC2
	-0.04	TC8	TC1
Flowmeters		FM5	FM4

TEST M7

		Flowtube 1 West	Flowtube 2 East
Fuel Pins		T-131 9.8 at.% BU U-19Pu-10Zr D9 clad	T-427 2.9 at.% BU U-10Zr HT9 clad
TC Locations	(Z/L)= 1.87	TC15	TC8
	1.30	TC14	TC7
	1.15	TC13	TC6
	1.07	TC12	TC5
	0.85	TC11	TC4
	0.48	TC10	TC3
	0.26	--	TC2
	-0.11	TC9	TC1
Flowmeters		FM4	FM5

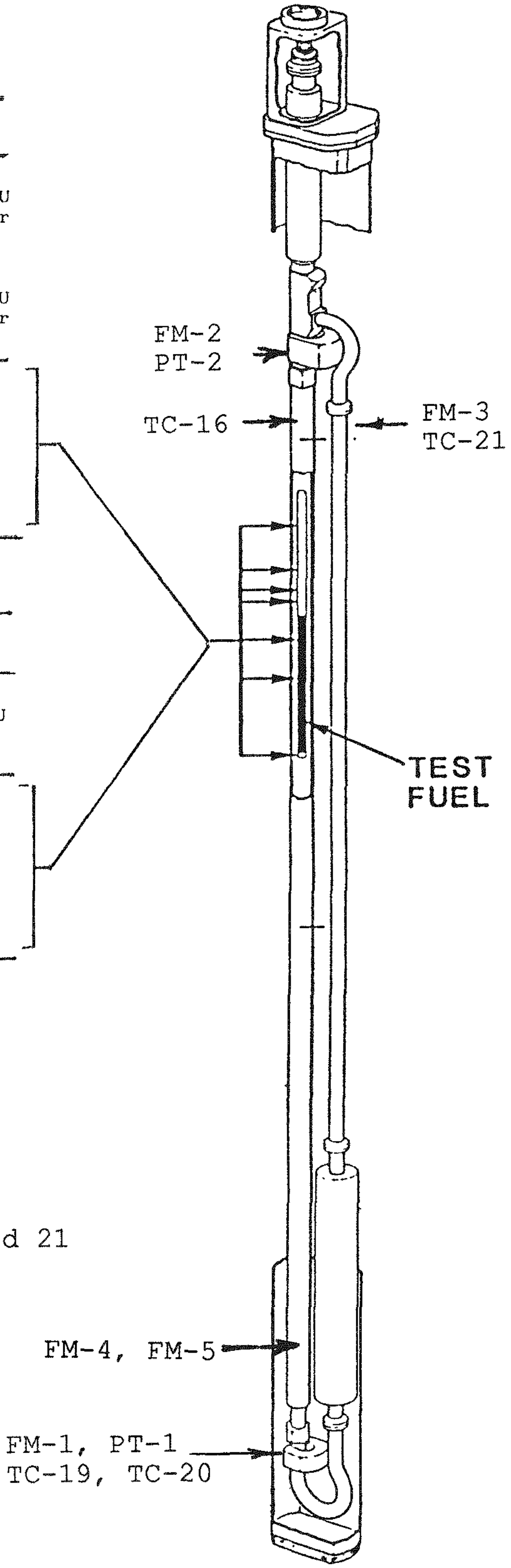

Note: TCs-16, 19, 20, and 21
are in-sodium TCs

Fig. A.6. Principal Test Vehicle Instrumentation train (as when the loop is in the TREAT reactor core) or whether it is the calibration orifice train used during the ANL-E flowmeter calibrations, and (b) unlike FM-1 the calibration of FM-3 is not affected by the presence of carbon steel in the TREAT biological shield near the lower portion of the test loop.

During M6 preheat operations, even through the loop flowmeters (FM-1, FM-2, and FM-3) almost always agreed with one another and even though the two miniature flowmeters were also a consistent pair, on a day-to-day basis a significant change in the ratio of pump current to flowmeter output was noted. The change in the flowmeter output for constant ALIP current changed by up to 50% for FM-3 and about 20% for FM-5. The reason for the changing ratio is believed to be poor seating of the test train due to accumulating debris in test loops subjected to multiple use. The pump/flowmeter output ratio stablized toward the end of the M6 test but was again present during preheat operations for the M7 test. Reversing the flow of sodium in the loop just prior to the M7 heat balance transient dramatically eliminated the pump/flow instability. Once stability was attained flowmeter output and applied ALIP current agreed reasonably with expectations of hydraulic analyses (Appendix D).

Calibration factors to reduce the mV flowmeter output test data to cc/s are given in Table A.3. During M5, calibration factors for FM-1 and FM-2 were obtained by averaging several sets of cross-calibration data. Calibration factors for the test train miniflowmeters for M5 and for all flowmeters for M6 and M7 are the individual flowmeter measurements obtained during cross calibrations taken on the particular day of the heat balance or final transient. Cross-calibration data were always taken at the initial operating coolant temperature (580 K).

It is recognized that the flowmeter calibration is slightly dependent on both the sodium temperature and the temperature of the flowmeter magnet. Measurements of these effects were not taken during the M5-M7 calibration; however, an estimate of their effect is given in Ref. A.1.

The wetting time for sodium to stainless steel is inversely proportional to the temperature of the sodium (Ref. A.2). The loop was operated well above the minimum time considered necessary to thoroughly wet the flowtubes. (For example, during preparations for M7, the loop was operated for 17 hours at temperatures at or greater than 650 F).

A.4.2 Thermocouples

Coolant temperatures at the outlet and along the fuel zone were measured by 15 (TC-1 to TC-15) MgO insulated chromel-alumel type K thermocouples attached to the outer surface of each flowtube. The TCs contained conductors of approximately 0.006 in. (0.15 mm) diameter. Each conductor was separately welded to the 0.0185 in. (0.47 mm) thick flowtube wall to form an "intrinsic" junction. It was advantageous to use thin walled flowtubes so that the measurements of coolant transient heating would not be limited by the time response of heat transfer through the flowtube. The molten metal fuel at the time of cladding failure would not be expected to greatly exceed the melting point of the flowtubes.

The TCs were stainless-steel sheathed with an outside diameter of 0.040 in. (1.02 mm). Axial locations of the TCs in tests M5-M7 are shown in Fig. A.3. The flowtube thermocouple locations, different from those in earlier tests, were chosen to provide more definitive indications of in-pin axial elongation during the transients. In addition, the axial locations were chosen to be as far removed from the flowtube dimples as possible with the TCs positioned in vertical lines.

One test train thermocouple (TC-16) was installed in the sodium flow. In tests M5 and M6, this TC was downstream of the flow-baffle arrangement. In M7, TC-16 was located inside the fuel trap outlet manifold (see Fig. A.6). Three additional in-sodium TCs penetrated the loop primary containment at the following locations: TC-19 and TC-20 at the test section inlet, and TC-21 closely adjacent to flowmeter FM-3 at the top of the pump leg. TC-22 and 23 penetrated the loop primary in the gas plenum region of the test vehicle and provided evidence, in all three tests, that they were slightly above the sodium level at the loop pretest temperature setpoints.

The loop also included a number of auxiliary thermocouples, some of which are indicated in Fig. A.7. Two TCs were attached to the magnet of each of the three loop flowmeters: TC-24 and 25 to FM-1, TC-26 and 27 to FM-2 and TC-28 and 29 to FM-3. Data from five of the loop-wall TCs were also collected; TC-30 and 31 at the location of test-section main loop heaters number 2 and 3, TC-32 and 33 at the location of the upper pump leg heater and TC-34 at the location of the lower pump leg heater.

All TCs were useful up to their melting point of approximately 1700 K and all TCs had a specified accuracy of +/- 3/4% of the difference between the indicated temperature and the reference-junction temperature of 338 K.

A.4.3 Pressure Transducers

Coolant pressures were measured by Statham PG732TC-1M-350 pressure transducers of 0-1000 psi (6.9 MPa) range on NaK-filled standoff assemblies that are coupled to the sodium by thin bellows. One such pressure transducer assembly (PT-1) was connected to the bottom (inlet) of the loop and the other (PT-2) to the top (outlet) of the test section leg above the fuel pins. According to the manufacturer's specifications, the accuracy of the pressure transducers is +/- 0.75% of full scale, i.e. +/- 7.5 psi or +/- 0.05 MPa. The manufacturer's calibration factors for the pressure transducers are 64 psi/mV (0.44 MPa/mV) for PT-1 and 63 psi/mV (0.43 MPa/mV) for PT-2.

A.5 Abnormal Instrumentation Performance

The instruments functioned properly during all three tests, with the following exceptions.

Loop Instrumentation:

As described above, during the preparations for M5-M7 significant changes in the ratio of pump current to flowmeter output was noted. The three loop flowmeters were almost always consistent with each other, and the two miniflowmeters were also a consistent pair but indicating a different flowrate than the loop flowmeters. An analytical hydraulic model of the M5/M6 test

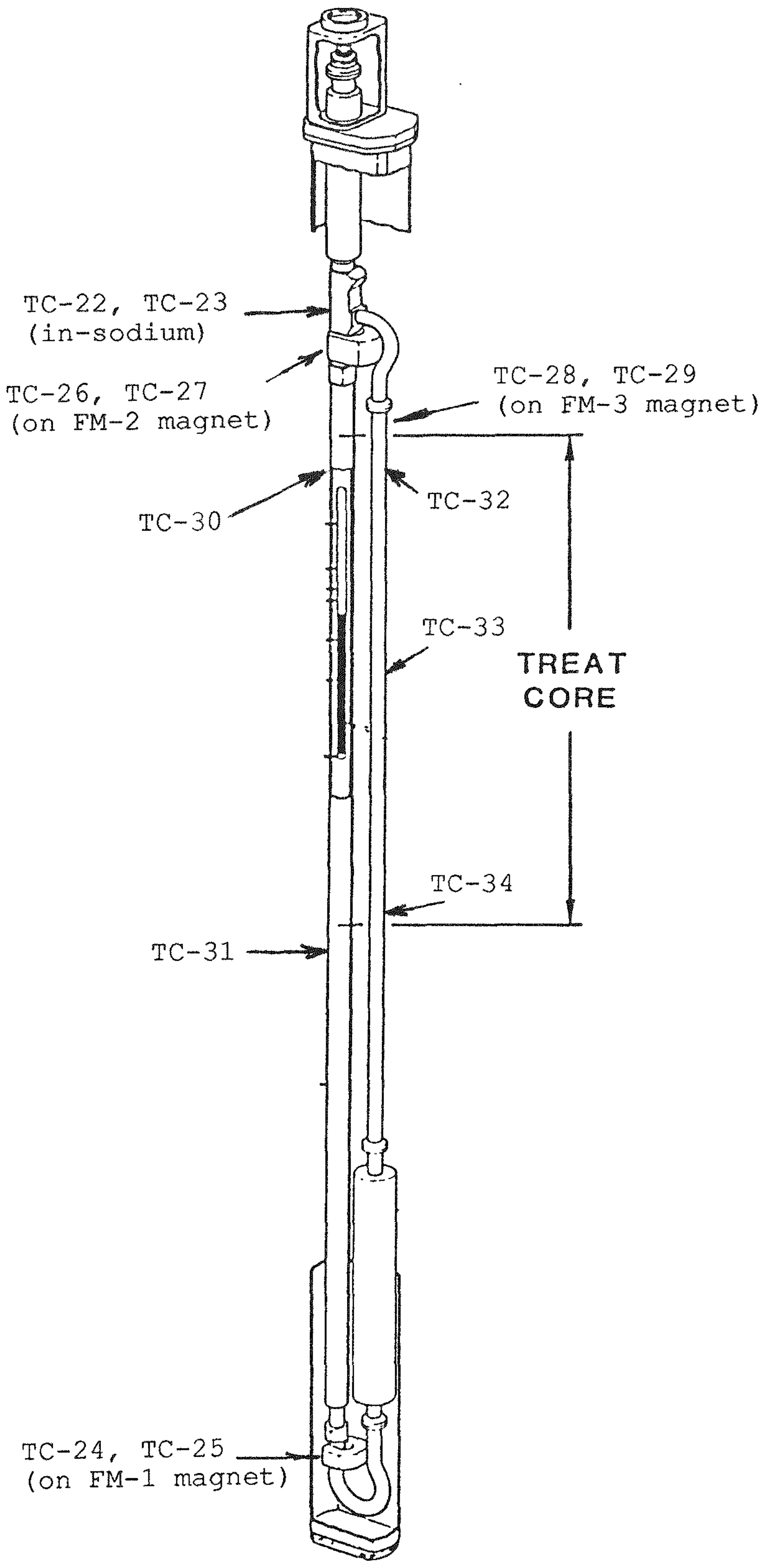

Fig. A.7. Auxiliary Test Loop Instrumentation section, loop, and electromagnetic pump (ALIP) was developed (Appendix D) to help resolve these inconsistencies. The independent hydraulic calibration data taken at ANL-E prior to M5 were used to validate the model. Validation of the ALIP characteristics involved the use of pretest data taken with the M5/M6 loop containing a specifically-calibrated orifice assembly. Once stability was achieved the analyses verified that the data used in final M6 test planning were correct.

Pressure transducer PT-2 was inoperable during test M7. Thermocouple TC-20 was disconnected during M5-HB1, M5-F1, and M5-HB2 due to suspect response. TC-31 was not operational during any of the M5 transients, and TC-34 was not operational for M5-HB2.

Test Train Instrumentation:

On the M7 test train, TC-7 was not operational for M7-HB1, and TC-3 was not operataional for M7-HB2.

References

A.1. W. R. Robinson et al., "Preliminary Data and Data Analysis Report for PRF/TREAT Test L07", ANL-RAS 84-13, Argonne National Laboratory Report (June 1984).

A.2. C. August, Argonne National Laboratory, unpublished information, (August 1987).

APPENDIX B

Test Fuel-to-Reactor Power Coupling

In every TREAT experiment the key power parameter is the quotient of power generated in the test fuel to that generated by the reactor as indicated by an instrument at the core edge. This quotient, called the power coupling factor, depends on numerous parameters including the test vehicle design, reactor core configuration, test fuel composition and density, and positions of the reactor control rods. To support the analysis and planning of M-series experiments on metallic fuel a number of independent experiments and neutronic calculations were performed to estimate the power coupling factors.

Measurements included separate "calibration experiments" on fresh fuel and monitor wires at low power levels as well as high-power transient irradiations of monitor wires performed at the time of the transient experiment, itself. Calibration results from M7CAL (the M7 Power Calibration Experiment) using U-Zr and U-Pu-Zr fuel and from M2CAL (the M2 Power Calibration Experiment) using U-Fs fuel have been reported in Refs. B.1 and B.2. Neutronic analyses have been used to account for test fuel burnup including corrections for isotopic depletion and fuel swelling.

During a calibration experiment, fuel can only be irradiated at low power levels, but U/Zr monitor wires can be irradiated at both high and low power levels. Extending measurements to high power transient irradiations is accomplished by comparing measured "high-power" and "low-power" U/Zr monitor wires power couplings. In applying this method careful measurements of the ratio of test fuel to monitor wire fissions were made under low-power (LLSS) conditions, and representative high-power transient irradiations of U/Zr flux monitor wires were performed at the time of each M-series experiment.

While many such features of power coupling depend principally on the characteristics of the test fuel, there is in addition, explicit dependence on the variables which define the TREAT reactor performance, especially during high-power transients. Basic experimental information concerning such changes of the measured power coupling during high power TREAT transients was obtained from monitor wire irradiations at both low power and during trial transient simulations.

A full-slotted TREAT core has been used throughout the M-series testing. The full-slotted core was chosen to enhance the hodoscope results. The full-slotted core lowers the neutron background behind the test vehicle and increases the hodoscope signal-to-noise ratio.

Power coupling factors for the M-series tests were obtained by first measuring the peak axial, LLSS power coupling factor with fresh fuel and then applying measured and calculated corection factors. Table B.1 lists the fresh fuel coupling factors and the measured and calculated correction factors that were used to obtain the power coupling factors for the test fuel in tests M5, M6, and M7.

B.1 Results of Calibration Experiments

B.1.1 Peak Axial, Low-level Steady-state (LLSS), Fresh Fuel Power Coupling Factors

For each fuel type, the peak axial, absolute fissions/gram per MJ value was multiplied by the appropriate Joules/fission conversion factor (Ref. B.3 taking into account the fuel composition) to obtain 4.91 and 5.27 J/g-TREAT MJ for U/Pu/Zr and U/Zr fuel, respectively.

An additional 0.03 J/g-MW was added due to gamma-heating making the total peak axial, LLSS, fresh fuel power coupling factors 4.94 and 5.30 J/g-TREAT MW.

B.1.2 Measured Transient Correction Factors

Because the test fuel and TREAT ex-core reactor power meters are physically far removed from one another some dependence of power coupling on rod motion and core temperature is to be anticipated. The transient correction factor (TCF) relates the averaged power coupling of test fuel during a power transient to that which applies at a low-level, steady-state

Table B.1. Power Coupling Factors for Tests M5, M6, and M7

Test	Fuel Type (wt. %)	Fuel Pin Burnup (at.%)	Peak Axial, Fresh Fuel, LLSS Coupling Factor (W/g-MW) (approx. +/-4%)	Calculated Burnup Correction Factor	Calculated Fuel Density Change Correction Factor	Peak Axial, LLSS Coupling Factors (a) (W/g-MW)	Measured Transient Correction Factor (b)
M5	U-19Pu-10Zr	0.8	4.94 (c)	0.996	1.06	5.22	0.89
	U-19Pu-10Zr	1.9	4.94	0.991	1.13	5.53	0.89
M6	U-19Pu-10Zr	1.9	4.94	0.991	1.13	5.53	0.90
	U-19Pu-10Zr	5.3	4.94	0.973	1.14	5.48	0.90
M7	U-10Zr	2.9	5.30 (d)	0.983	1.12	5.84	0.92
	U-19Pu-10Zr	9.8	4.94	0.946	1.13	5.28	0.92

a) Corrected for isotopic depletion and fuel restructuring due to fuel burnup.

b) TCF-Fit value from Table V corresponding to the energy release in the final test transient. This multiplicative factor corrects the LLSS coupling factor to that appropriate for the final test transient conditions.

c) {(105.8E12 fissions/g)(27.5 pJ/fission)/(592 MJ)} + 0.03 W/g-MW = 4.94 W/g-MW

d) {(114.8E12 fissions/g)(27.2 pJ/fission)/(592 MJ)} + 0.03 W/g-MW = 5.30 W/g-MW

(LLSS) power condition in TREAT. Data for determining TCF's are obtained from U/Zr monitor wire irradiations both with low power and trial transients. The TCF value is found by dividing (a) the coupling of U/Zr monitor wire fissions to reactor energy observed in high power transients by (b) the corresponding coupling for a LLSS irradiation.

The transients used in the M-series TCF database span a wide range of control rod motion and reactor energy. All transients in the database were performed with the same core loading (with full north-south slot) and the same test vehicle (M2CAL test vehicle). The database spans about three years with many intermediate core changes between the M-series tests along with changes in the instrument calibrations.

The axial peak absolute wire activity and coupling to reactor energy was obtained by the following procedure:

1) Dividing each of three wire segment determinations of the absolute number of fissions per gram by their respective normalized relative gamma activity and averaging the three ratios.

2) Determining the axial peak relative activity by means of a polynomial fit to the relative gamma activity measurements within the central 7.5-in. (19.1 cm) high non-filtered axial region. Excluded from these fits were data from the axial location where a gap was inadvertently left in the neutron filter that was placed on the wire holder (See Appendix C).

3) Multiplying the results from item one by the results from item 2). Little axial dependence of the TCF has been noted in past measurements and none is assumed in this report.

Reference B.1 lists four LLSS wire irradiations in the full-slotted core configuration: 9/17/84, 1/21/87, 3/31/87 and 9/28/87. The axial peak fissions/gram/TREAT MJ values from these four irradiations were 1.67xE10, 1.59xE10, 1.63xE10 and 1.67xE10, respectively. Their consistency attests to the general consistency of LLSS data. Since it is assumed that the ratio of wire fissions to fuel fissions is invariant, to compute a TCF that minimizes effects of meter drift or re-calibration it is optimal to use the LLSS value obtained at the same time as the calibration of fuel and the high-power trial transient obtained at the same time as the appropriate experiment. Measured TCF's from M5, M6, and M7 were determined from the 3/31/87 M7CAL LLSS value (1.63xE10 fissions/gram/MJ).

Fitted TCF's were calculated from a linear correlation of measured TCF's to the average (power-weighted) positions of rod pairs T-1, and T-2 and the outer pneumatic rod bank (RB). The inner pneumatic rod bank is always fully withdrawn. Since the transient energy increases as control rods are withdrawn, dependence on reactor energy or core temperature is implicit. The correlation procedure is described in greater detail in Ref. B.4, but the fit reported here includes the entire database of M-series monitor wire transients from M2-M7. The calculated standard deviation of an individual, measured TCF from the fit is about 2%, and the random standard error in "TCF-fit" is estimated to be about 1%. If the effect of transient power meter recalibration between M6 and M7 is taken into account,* these fits demonstrate an excellent consistency of data.

Fitted TCF values corresponding to the energy release in the final test transient are shown in Table B.1. As long as the fits to the database are good, the fitting process minimizes random error and effectively interpolates within the trial transient database.

B.1.3 Calculated Effect of Isotopic Depletion on Power Coupling

Power coupling is effected by isotopic depletions due to fuel burnup. Calculated corrections were made to account for this effect (Ref. B.5). The corrections were made on the basis of depleting fissile isotopes U-235 and Pu-239 by equal amounts until the specified heavy metal loss fraction was

---

*Identical transients (identical in rod motion, core temperature rise, and measured monitor wire fissions) performed both during the M6 and M7 time frames recorded 7% less reactor energy deposition during M7. Between M6 and M7, a transient meter re-calibration of this magnitude and sign was reported. A 7% increase was, therefore, made to calculated M7 TCFs .

achieved. This simple prescription has been verified subsequently by more sophisticated analysis (Ref. B.6). Because of significant radial neutron flux depression in TREAT's thermal neutron flux, assumptions concerning fuel density and radial distribution of materials are important to these analyses. However, a uniform distribution of isotopes is assumed throughout.

Interpolated isotopic depletion correction factors from the tables of Ref. B.5 are listed in Table B.1 for the specific test fuel pins of M5-M7. Estimated relative uncertainties in these estimates are +/- 0.1% for fuel burnups less than 10 at. % and +/- 1% for fuel burnups greater than 10 at. % (Ref. B.7). These calculations indicate, as a good approximation, for every 1 at. % burnup, the power coupling is calculated to decrease by 0.5%.

B.1.4 Calculated Effect of Fuel Density and Radius on Power Coupling

Strong radial self-shielding of the TREAT thermal neutron flux by the test fuel causes a flux depression in the fuel and causes fissions in the test fuel to occur predominately near the fuel surface. Changes in the fuel surface area therefore tend to affect the power coupling factor. High-swelling IFR metal fuels undergo significant physical change in the first few at. % burnup as fuel expands outward to the inner cladding radius. Even if no axial elongation takes place, fuel surface area increases by about 16% and density decreases by about 28% (for fuel initial diameters of 0.170 in. (0.43 cm) as in tests M5-M7). Significant power coupling increases (up to about 9%) occur with fuel swelling. Therefore, calculated correction factors were obtained as a function of fuel density and radius (Ref. B.8). The tables of Ref. B.6 were used to obtain the calculated correction factors for the specific test fuel pins used in tests M5, M6, and M7. Two key assumptions were made in these estimates:

1) Fuel density and distribution of fissile isotopes are both uniform.

2) Axial swelling was ignored because the net effect on whole-pin coupling might be small. It has been estimated that any coupling factor increase from fuel density being further reduced would be offset by

losses due to heavy shielding of any fuel above the nominal fuel height. The correction factors are listed in Table B.1. Uncertainties in these calculated correction factors are difficult to estimate because of the idealized nature of assumptions 1) and 2), above.

B.2 Results from the Heat Balance Transients

Power couplings were determined from the midpoint of the heat balance transient; i.e., at the halfway point of energy deposition. The axial peak power coupling factor (PCF) was computed from the following relationship:

$$\text{PCF (HB)} = \text{(temp. rise)} \times \text{(coolant mass flow)} \times \text{(sodium specific heat)/(pin mass)} \times \text{(reactor power)} \times \text{(axial avg.-to-peak ratio)} \qquad \text{(B.1a)}$$

Measurement of the ratio of axial average to peak power is reported in Appendix C. Transient correction factors (TCF's) are used to adjust these power couplings to "final transient" conditions:

$$\text{PCF (Final)} = \text{PCF (HB)} \times \text{TCF-final/TCF-HB} \qquad \text{(B.1b)}$$

The measured coolant temperature rise used in the analysis averaged several thermocouples above the top of the test fuel on each flowtube and subtracted averages of thermocouple measurements of coolant inlet temperature. In every case "suspect" thermocouples or individual measurements which were noticeably different from the norm were excluded. Appendix E shows all of the relevant thermocouple and flowrate data.

Key assumptions in this analysis of M5-M7 heat balances were:

1) In tests M5 and M6 an equal division of flow between flowtubes was assumed in accord with nominal symmetry. In M7, where the two flowtubes were orificed differently, measurements from the mini-flowmeters experimentally determined flow division.

2) Power couplings from the two M5 heat balances were inconsistent. Only the first heat balance was used to determine power couplings for later use. The second heat balance was performed after the first overpower

transient, and the idealized geometry that is assumed in simple heat balance analysis was likely corrupted.

3) At the time of the M6 heat balance, validity of the total measured flowrate was questionable. The M5 power coupling measurement of a 1.9 at. % burnup pin common to both tests was assumed equally appropriate for M6 (adjusted only for TCF's). Thus, the reported total flowrate for M6 heat balance was then calculated on the basis of an assumed PCF and the other measurements.

4) In M7, results of the two heat balances were consistent. Results from the second heat balance involving the larger temperature rises are recommended here for use in further analyses.

Table B.2 summarizes the input and results of calculations used to determine power coupling factors.

B.3 Results from Hodoscope Scans

A small amount of direct experimental information on relative power coupling factors is available from TREAT fast neutron hodoscope measurements. Prior to each test, hodoscope scans were taken with the test vehicle in place in the reactor. After background is subtracted, the relative signal from each test fuel pin should be proportional to its power coupling.

Reference 5.1 provides the results of hodoscope scan data to obtain the ratio of fission neutron emission from the two M7 test pins when irradiated in TREAT. The ratio of the total fission neutron emission from the binary pin to that from the ternary pin was measured at 1.21 +/- 0.02. The calculated ratio of relative neutron emission per fission for the binary alloy to that for the ternary alloy is 0.926. (Effects of burnup upon fissile composition were included). The estimated relative power from the two pins is therefore:

$$\frac{\text{Binary pin power}}{\text{Ternary pin power}} = \frac{1.21}{0.926} = 1.31$$

and this ratio may be compared to the measured M7 heat balance power ratio of 1.37.

Table B.2. Summary of Heat Balance Power Coupling Analyses

Transient	M5-HB1	M5-HB2	M6-HB	M7-HB1	M7-HB2
TREAT Power (MW) *(at transient midpoint)* rod shadowing incl.	38	40	48	47	44
Transient Corr. Factor (TCF)					
heat balance	0.88	0.88	0.88	0.92	0.92
final transient	0.89	0.89	0.90	0.97	0.97
Total Flowrate (g/s) (at transient midpoint)	187	181	(216)	193	145
Fuel (Burnup, at. %)					
flowtube #1	0.8	0.8	1.9	9.8	9.8
flowtube #2	1.9	1.9	5.3	2.9	2.9
Fuel Mass (g)					
flowtube #1	77	77	78	77	77
flowtube #2	78	78	77	79	79
Flowsplit (%)					
flowtube #1	(50)	(50)	(50)	48	46
flowtube #2	(50)	(50)	(50)	52	54
Temperature Rise (K) (at transient midpoint)					
flowtube #1	112	92	122	106	141
flowtube #2	112	109	120	131	164
Power Coupling Factor (W/g-mWT) (adjusted to final transient)					
flowtube #1	(4.95)	[3.94]	(4.96)	[4.15]	(3.97)
flowtube #2	(4.91)	[4.63]	(4.94)	[5.44]	(5.31)

Assumed or calculated values are shown in parentheses "( )".

Calculated power couplings shown for interest but not recommended for further analyses are shown in square brackets "[ ]".

Estimated uncertainties are about 2% in the TREAT power and total flowrate and 3% in the flowsplit and temperature rise leading to an approximate 5% combined uncertainty in the computed power coupling factor.

References

B.1. W. R. Robinson and T. H. Bauer, "Power Coupling in TREAT M-Series: New Experimental Results from M7CAL and Updated Analyses", Argonne National Laboratory Report, ANL-IFR-86 (February 1988).

B.2. W. R. Robinson, "Power Calibration Experiment for TREAT Test M2", ANL-IFR-8 (April 1985).

B.3. T. H. Bauer, Argonne National Laboratory, unpublished information, (March 1980).

B.4. T. H. Bauer et al, "Update of Safety Testing in TREAT on U-5Fs Fuel: Data from Test M4 and Combined Analyses of Tests M2, M3 and M4", ANL-IFR-69 (May 1987).

B.5. R. W. Swanson and G. Klotzkin, Argonne National Laboratory, unpublished information (August 1985).

B.6. R. W. Swanson, Argonne National Laboratory, unpublished information, (November 1987).

B.7. R. W. Swanson, Argonne National Laboratory, private communication, (1987).

B.8. R. W. Swanson, Argonne National Laboratory, unpublished information, (July 1987).

APPENDIX C

Power Distribution Within the Test Fuel

C.1 Axial Power Profiles

Axial power profiles were obtained by gamma counting the relative fission product activity from two segmented flux monitor wires, two segmented U-Zr fuel pins and two segmented U-Pu-Zr fuel pins from the M7CAL experiment (Ref. B.1). The fuel slugs from the four fuel pins were removed from the cladding, sheared into approximately half-inch long segments and weighed. The count rate per gram of segment was determined for each segment, and the values were normalized to unity at the axial peak of a polynomial fit performed over the central 7.5 in. (19.05 cm) high non-dysprosium filtered region. This normalization allows for better intercomparison of axial shapes as well as more accurate determinations of power coupling at the axial peak. Three segments from each fuel pin were dissolved and counted to determine the absolute number of fissions per gram (Ref. C.1).

The wires were removed from their stainless-steel sheaths and cut into approximately half-inch long lengths. Each segment was weighed and gamma counted to determine its relative activity. Three segments for each wire were dissolved and counted for absolute fissions. In the wire distributions one or two abnormally high points were observed just below the midplane of the distribution. Radiographs of the monitor wire holder within the calibration vehicle showed an approximate 0.13 in. (0.31 cm) thick gap in the 0.015 in. (0.032 cm) thick axial dysprosium filter at about the same axial location (Ref. B.2). The gap evidently allowed a local neutron flux peak.

The axial distributions from the two different fuel types and the wires are consistent within a 3% scatter of the data as shown by Figs. C.1 and C.2. Figure C.1 shows the measured normalized axial distributions for U-Fs, U-Zr, and U-Pu-Zr fuel in the full-slotted core configuration. The solid curve represents a least squares fit through all the data. The U-Fs data is from the M2CAL experiment (Ref. B.2) and the U-Zr and U-Pu-Zr data is from the M7CAL experiment. Figure C.2 compares the same fitted curve to the four LLSS

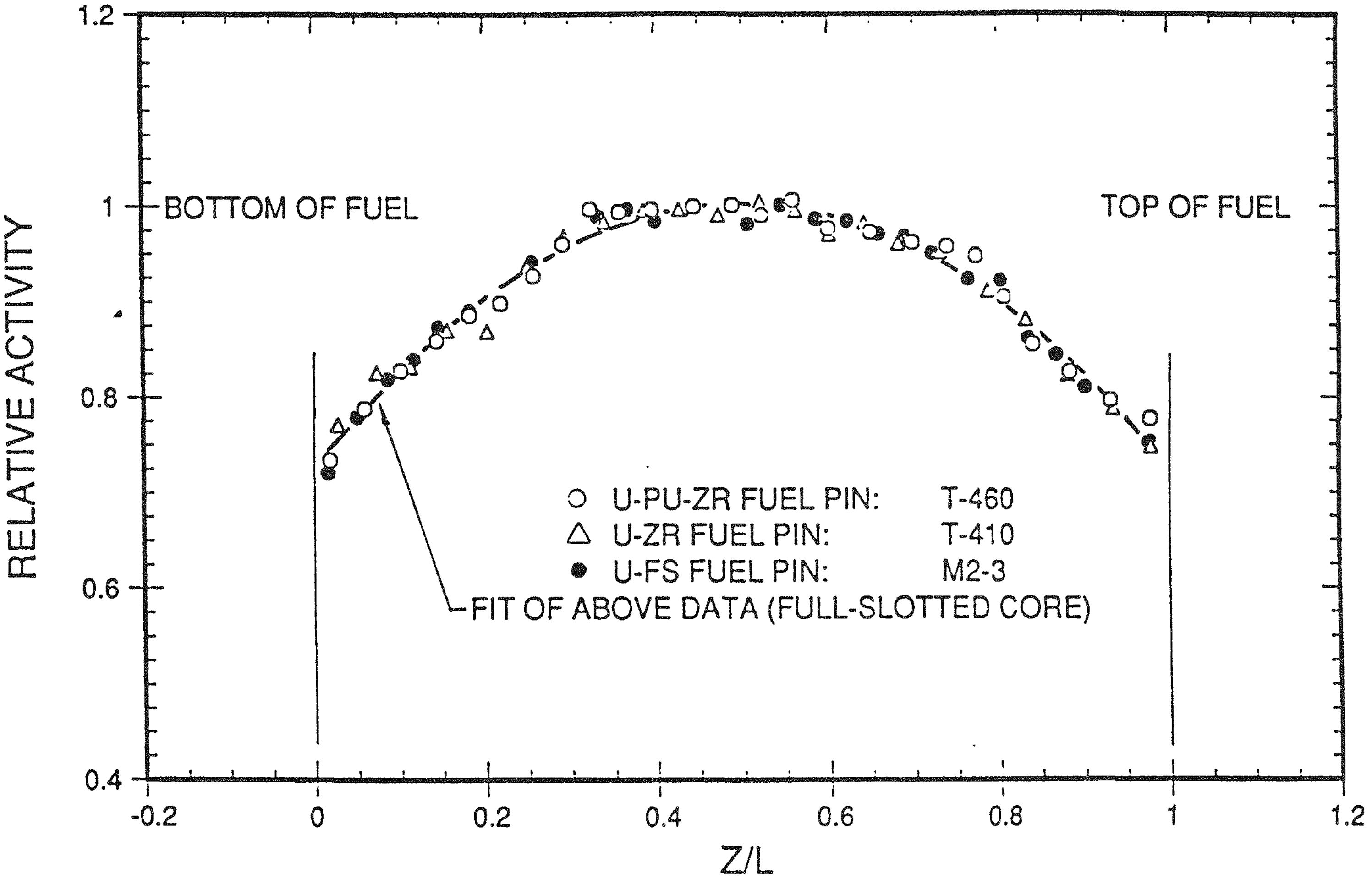

Fig. C.1. Measured Axial Power Profiles in the Full-slotted TREAT Core from U-Fs, U-Pu-Zr and U-Zr Fuel Pins

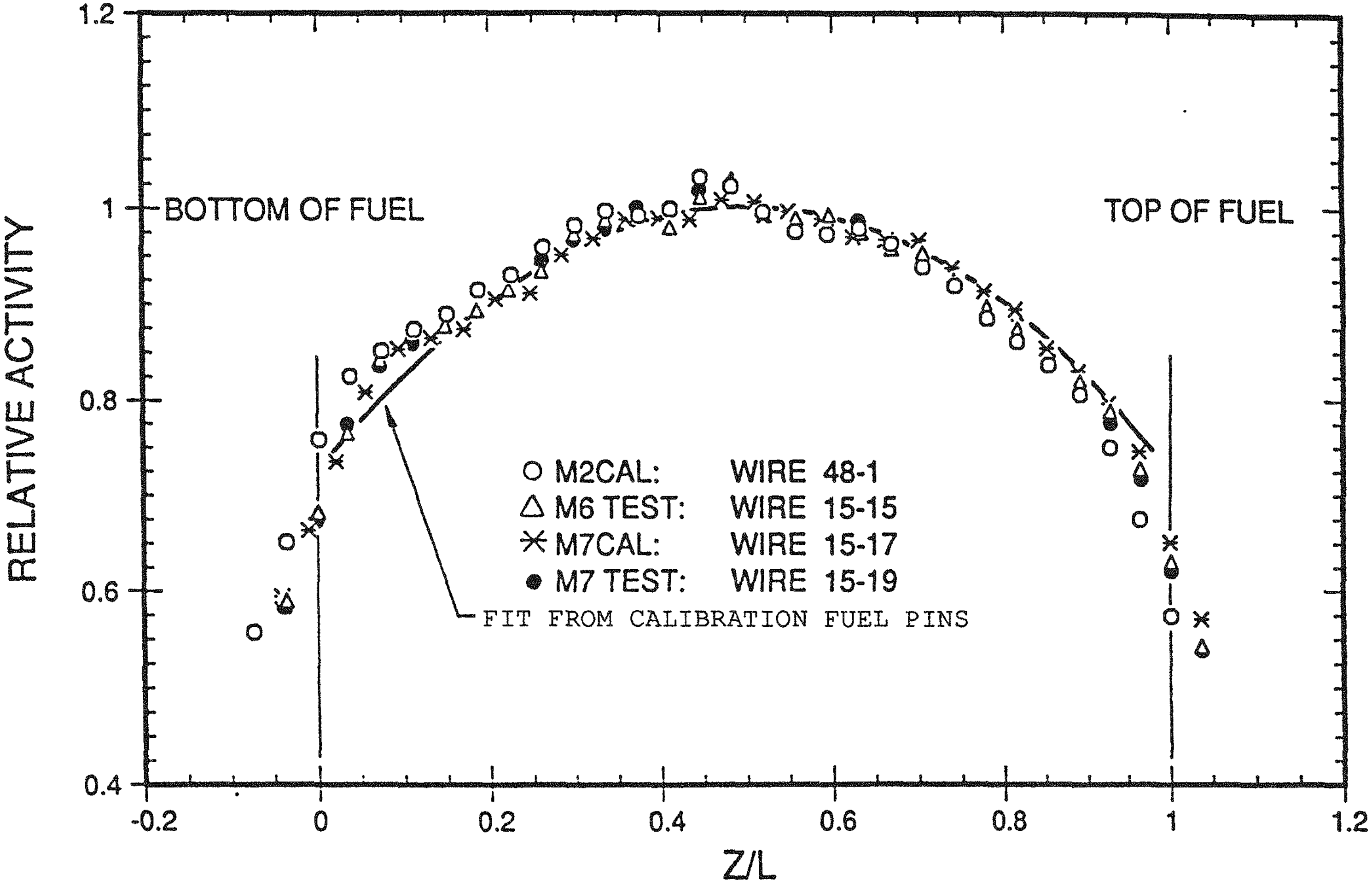

Fig. C.2. Measured Axial Power Profiles in the Full-slotted TREAT Core from Monitor Wires and Fuel Pins monitor wire distributions in the full-slotted core configuration (from M2CAL, M6, M7CAL and the M7 Test). The ratio of axial peak to axial average is 1.095 for the fitted curve shown in Figs. C.1 and C.2.

C.2 Radial Power Profiles

For completeness, the calculated test fuel radial power profiles from Ref. B.5 for both U-Zr and U-Pu-Zr fuel are shown in Fig. C.3. The profiles were determined by one-dimensional transport theory using the assumption that the two pins were sufficiently separated so that a single pin analysis would be adaquate.

Reference

C.1. J. O. Young, R. E. DiFelici, and J. F. Berg, Argonne National Laboratory, unpublished information, (May 1987).

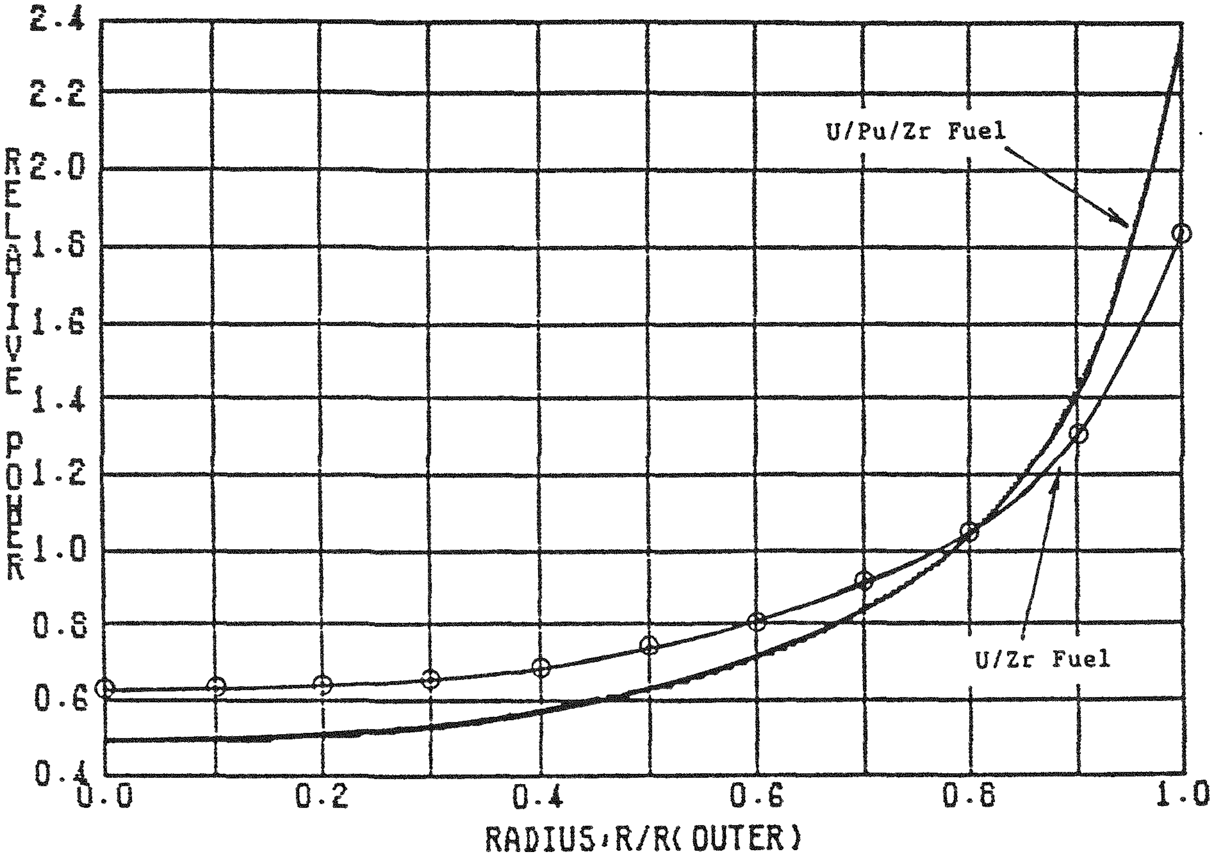

Fig. C.3. Calculated Radial Power Profile for Fresh U-Zr and U-Pu-Zr Fuel

APPENDIX D

Steady-State Hydraulic Model and Analysis

A series of hydraulic analyses (Ref. D.1) were performed for the M5-M7 test geometry to help resolve inconsistencies among hydraulic parameters and between measured and expected flowrates. The series consisted of the following:

1) Constructing a model which consisted of a fuel pin and its extender in a single M5/M6 flowtube in the ANL-E water loop.

2) Constructing a second model consisting of the actual two-pin M5/M6 test train in the water loop.

These first two models were calibrated by adjusting the hydraulic loss to the experimental flow data.

3) Constructing a third model consisting of an orifice and an annular linear induction pump (ALIP) in a sodium loop. This model was used to find the pump current output to be used in the fourth and final model.

4) The fourth model was constructed using the hydraulic simulation feature of SLOOP (Ref. 4.3) as applied to the hydraulics of the M5/M6 loop. A set of six ALIP currents from a test run of the loop were then input to the SLOOP model and produced flow rates within 2-7% of the measured flow rates.

D.1 Model of a Single M5/M6 Flow Tube in the Water Loop

Water loop measurements were first taken to ascertain the pressure drop characteristics of a single flowtube plus pin. This model consisted of a number of pipe elements between the pressure transducers of the water test loop. Hydraulic pipe elements in the SLOOP model simulate the friction losses in the actual test loop. In the model a dummy was added to the system for the sole purpose of fitting the resulting SLOOP flow rates with those measured in the test.

The first set of experimental flow data consisted of 15 pressure drops measured in the water loop with a dummy fuel pin attached to a pin extender. An orifice was not included. The data was input to the SLOOP model and the SLOOP results were fitted to the measured flow rates by increasing the nominal pressure drop by 16.6% (by assigning a loss coefficient to the dummy pipe).

The above friction loss was then carried over to a second set of experimental data which included an orifice. In the SLOOP calculation the orifice was considered simply as a sudden expansion from the vena contracta. The resulting SLOOP flow rates agreed well with the measurements and indicated both the correctness of the general SLOOP model for the water loop and the correct consideration of the orifice loss as one of sudden expansion.

D.2 Model of the Actual M5/M6 Test Train in the Water Loop

Later water loop measurements characterized the pressure drop of the actual test train. Starting from the model used above, the SLOOP calculation flow rate was brought into agreement with the measured flow rates for the single flow tube without an orifice. The second flow tube of the dual set is assumed identical to the first and is therefore represented by the same SLOOP model.

The pipes new to this model are pipes which represent the lower, middle, and upper flow baffles, and the remaining length of test train between the last baffle and the upper pressure transducer. The SLOOP model therefore consists of three flow paths and a junction. In SLOOP, the measured upper and lower pressure transducer values are input and the junction pressure is determined by the code as well as the flow in each of the three flow paths.

The pipe lengths representing the baffles in the upper portion of the test train were adjusted until the friction losses resulted in flow rates for SLOOP equal to the measured rates from a set of experimental data with the actual M5/M6 test train in the water loop.

D.3 Model of the Orifice Test Train in the Sodium Loop

The orifice test train in the sodium loop calibrates loop flowmeters and determines ALIP performance on the basis of known flowrates through calibrated orifices. The model for a special orifice test train consisted of hydraulic pipe elements and an ALIP element within a sodium loop. This model provided the normalization factor for the output head of the M5/M6 ALIP. Experimental data were provided using different orifice sizes and different sodium temperatures. The loss due to the orifice was adjusted where necessary to agree with measured pressure drops.

The experimental data were input to the SLOOP code and the normalization factor for the ALIP element of SLOOP was varied until the flow rates and pressure drops of SLOOP matched closely those measured.

D.4 Model of the M5/M6 Test Train in the Sodium Loop

Using parameters from each of the three above models it was now possible to construct a model for the hydraulics of the M5/M6 test train in a sodium loop. These were compared to in-situ flow characteristics measured during stable phases of operation.

Six ALIP currents were input to this final SLOOP model and produced flow rates within 2-7% of the measured flow rates during a stable portion of operation. A calibration factor of 201.5 cc/s/mV was assumed for FM3.

D.5 Conclusion

The conclusion drawn from these SLOOP calculations is that during the stable phases of loop operation with the actual test train, flowrates measured by loop flowmeters and applied ALIP currents are consistent with our best understanding of the hydraulics of the Mark-III loop and test train. In particular, there is strong support for the accuracy of measured flowrates. Pressure drops are consistent with that of the full test train and there is no evidence of bypass flow.

Reference

D.1. D. J. Dever, Argonne National Laboratory, unpublished information, (May 1987).

APPENDIX E

Details of the Heat Balance Transients

Low-power heat balance transients were included as integral parts of the experiments; two in M5, one in M6, and two in M7.

E.1 Heat Balance Transient Summaries

Table E.1 summarizes information about the test conditions during the five heat balance transients. For the M5 transients (M5-HB1 and M5-HB2) the reactor operated at a near-constant power level of 40 MW for about 17 sec, for the M6 transient (M6-HB) 48 MW for about 14 sec and for the M7 transients (M7-HB1 and M7-HB2) 47 MW for 13 sec (see Fig. E.1). These values include small corrections for the "rod-shadowing" effects described in Sect. 4.2.

The sodium flowrate was nominally constant during the transients, but the coolant temperatures measured at the bottom of the fuel may have risen several degrees K by the time of power shutdown. The measured flowtube temperature rises near the top of the active fuel column, during the three heat balances which were used to determine power couplings, are shown in Fig. E.8. The temperature rise of the mixed mean outlet temperature as measured by TC-16 which was positioned above the outlets of the two flowtubes is shown in Fig. E.9.

With the few exceptions noted in Sect. A.5, all loop and test train instrumentation, as well as the readout and recording systems, functioned properly during the five heat balance transients. Section A.5 describes the omission of a few test sensors during the transients. Factors for converting the flowmeter and pressure transducer mV data to units of cc/s and MPa (absolute) are given in Table A.3 and in Sect. A.4.3, respectively.

TABLE E.1. Heat Balance Transient Test Conditions

	M5-HB1	M5-HB2	M6-HB	M7-HB1	M7-HB2
TREAT transient number	2711	2713	2733	2773	2774
Date of performance	8/6/86	8/14/86	2/2/87	10/9/87	10/13/87
Total flowrate at midpoint of flattop, cc/s	213	207	242	220	165
g/s	187	181	216	193	145
Flowsplit, %					
Flowtube 1	50	50	50	48	46
Flowtube 2	50	50	50	52	54
Initial temperature, K	581	579	588	585	586
Initial ALIP current, A	24.4	21.6	24.0	22.2	16.0
Initial pressure drop, MPA (*)	0.23	0.21	0.38	0.19	0.13
TREAT power at midpoint of flattop, MW (+)	38	40	48	47	44
Total TREAT energy, MJ	623	659	664	638	635
Transient correction factor (from trial transients)	0.88	0.88	0.88	0.92	0.92
Flowtube 1:					
Fuel pin identification	T-280		T-186	T-131	
Fuel pin composition	U-Pu-Zr		U-Pu-Zr	U-Pu-Zr	
Burnup, at.%	0.8		1.9	9.8	
Thermocouples	8-14	8-14	8-14	9-15	9-15
Axial temperature gradient across active fuel column, K	112	92	122	106	141
Flowmeter identification	FM-5	FM-5	FM-5	FM-4	FM-4
Flowtube 2:					
Fuel pin identification	T-154		T-102	T-427	
Fuel pin composition	U-Pu-Zr		U-Pu-Zr	U-Zr	
Burnup, at.%	1.9		5.3	2.8	
Thermocouples	1-7,15	1-7,15	1-7,15	1-8	1-8
Axial temperature gradient across active fuel column, K	112	109	120	130	164
Flowmeter identification	FM-4	FM-4	FM-4	FM-5	FM-5

* Measured using PT-1 and PT-2, the latter reading esentially the loop plenum pressure at which it had been zeroed. The error in the measurement is probably a large fraction of the value given. See Section A.4.3.

\+ Including "rod shadowing" effects.

E.2 Graphical Data from M5-HB1, M6-HB, and M7-HB2

Graphical data from the three heat balances which were used to determine power couplings and P/F ratios in the final overpower transients (Sect. 4 and Appendix B) is reported in Figs. E.1 to E.18.

E.3 Graphical Data from M5-HB2 and M7-HB1

Graphical data from the two remaining heat balances (M5-HB2 and M7-HB1) is shown in Figs. E.19 to E.35.

M5-HB2 was performed after the initial M5 overpower transient, M5-F1, to verify overall system performance before the performance of M5-F2. Power and flow imposed on the test fuel were nominally identical to M5-HB1. Measured temperature rises were not, however, identical, very likely because of changes in the test fuel, e.g., bending or distortion, wrought by the first overpower transient.

M7-HB1 was the first heat balance transient performed in M7, and its results are considered reliable. However, for purposes of determining power couplings, M7-HB1 was repeated with reduced coolant flow to induce larger temperature rises (M7-HB2).

E.4 Tabulated and Graphical Data

Tabulation of the data from all five heat balance transients is presented on microfiche and is included in the pocket on the back cover of this report. Table E.2 gives the order of the test sensor listings, the sensor designation and the units of each sensor. The listings consist of 1 ms data averaged over 50 ms intervals from 0 to 25 s for all but a few of the test sensors. A separate microfiche is provided for M5, M6, and M7.

The following graphs show 1-ms data averaged over 50-ms intervals.

Table E.2. Order of Test Sensor Listings, Designations, and Units

Test Sensor	Identification	Unit
SAF1	Safety instrument 1 -- reactor power meter	MW
INT1	Integrator instrument 1 -- reactor energy meter	MJ
SFIC	Safety instrument 1 -- (corrected to correspond to IN1C)	MW
IN1C	Integrator instrument 1 -- (corrected for zero shift)	MJ
ROD1	Transient rod pair 1	cm
ROD2	Transient rod pair 2	cm
RSF	Rod shadowing factor - (energy normalized)	—
PRSF	Product of SF1C and RSF	MW
ERSF	Product of IN1C and RSF	MJ
FM-1	Inlet (lower) flowmeter	mV
FM-2	Outlet (upper) flowmeter	mV
FM-3	Pump leg flowmeter	mV
FM-4	Individual flowtube flowmeter	mV
FM-5	Individual flowtube flowmeter	mV
PT-1	Inlet (lower) pressure transducer	mV
PT-2	Outlet (upper) pressure transducer	mV
TCxx	Thermocouple XX (see Fig. 1)	
	XX = 1-15 (flowtube TCs)	K
	XX = 16, 19, 20 and 21 (in-flow TCs)	K
	XX = 22 and 23 (loop gas plenum TCs)	K
	XX = 24-29 (flowmeter magnet TCs)	K
	XX = 30-34 (loop wall TCs)	K
IB	ALIP current (phase B)	amp
SSG	Shutdown signal generator	—

Heat balance transients M5-HB1, M6-HB, and M7-HB2

Heat balance transients M5-HB2 and M7-HB1

---

a) Power corrected to be consistent with the energy; both power and energy adjusted by the rod shadowing factor.

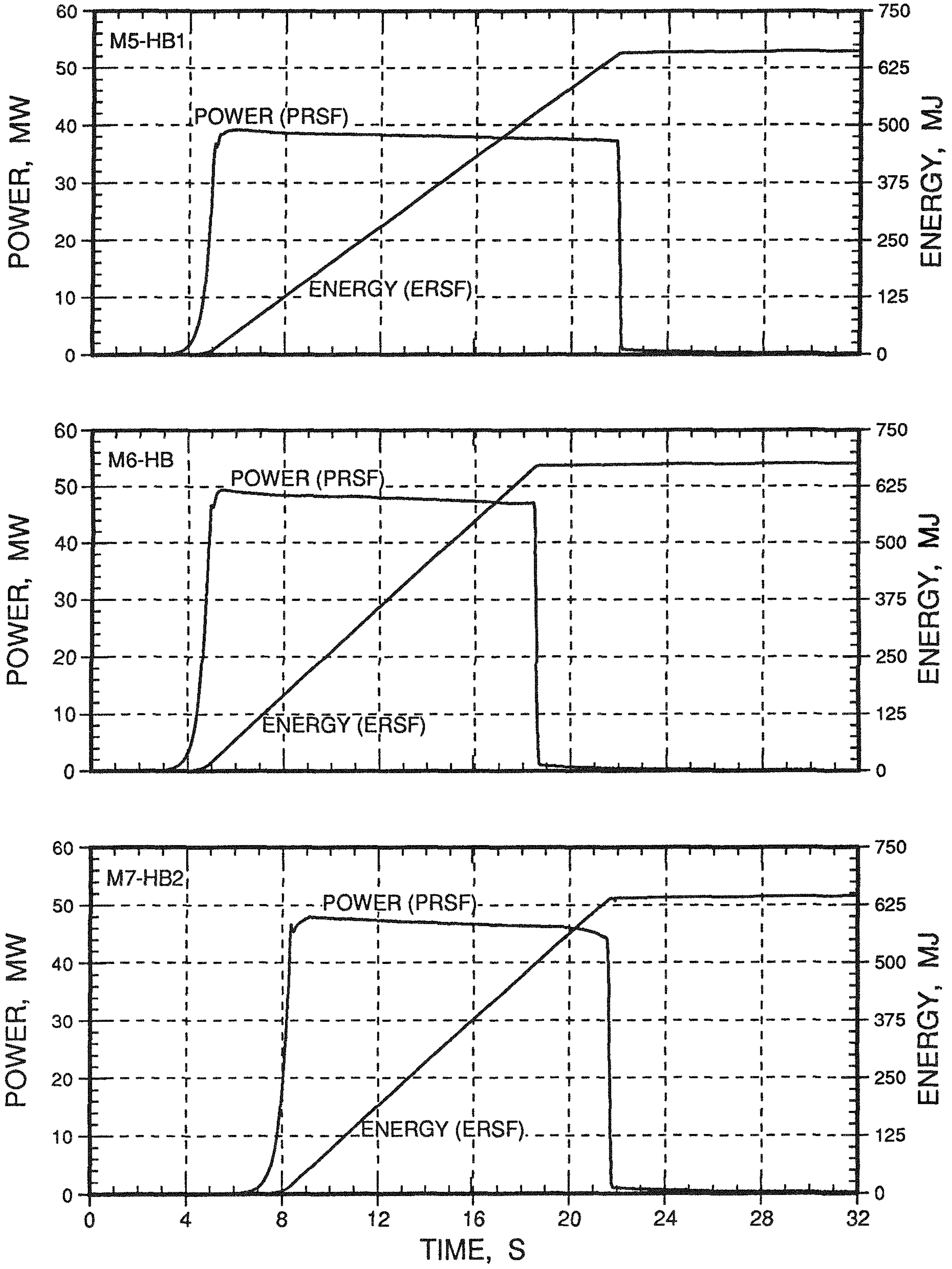

Fig. E.1. Corrected TREAT Power and Energy, Including RSF Variation

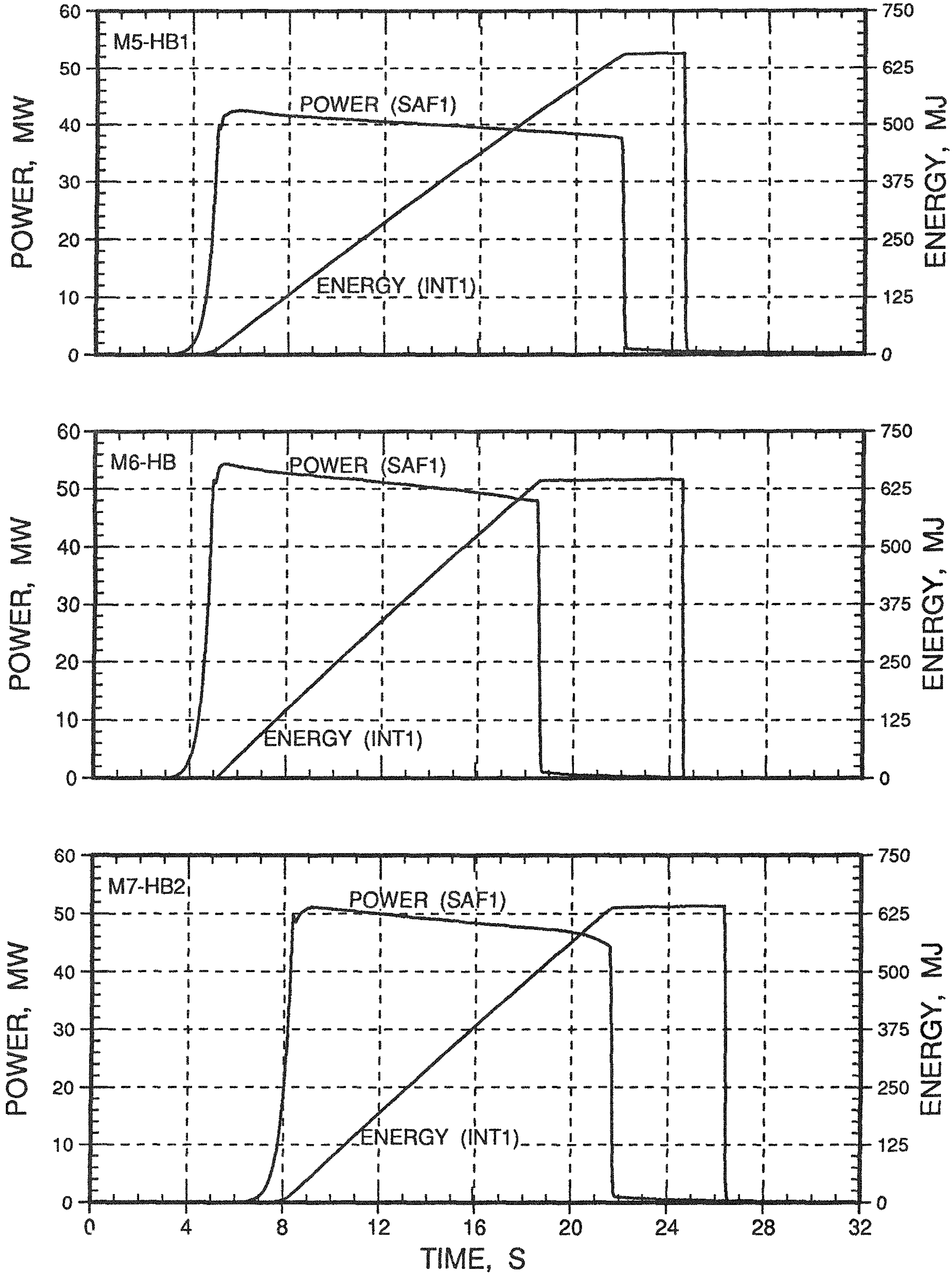

Fig. E.2. TREAT Power and Energy from Instruments S1 and I1

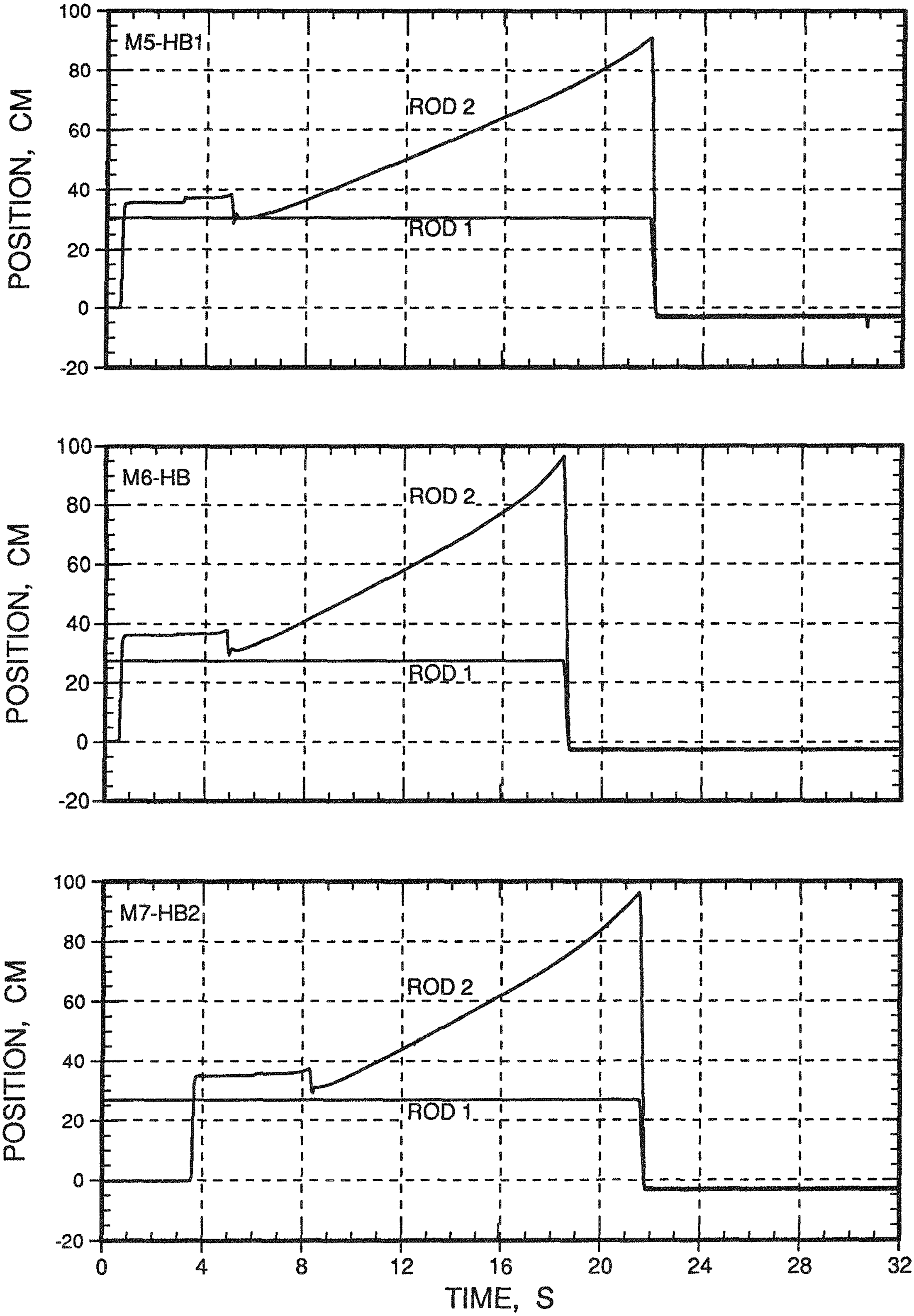

Fig. E.3. Transient-rod Motions

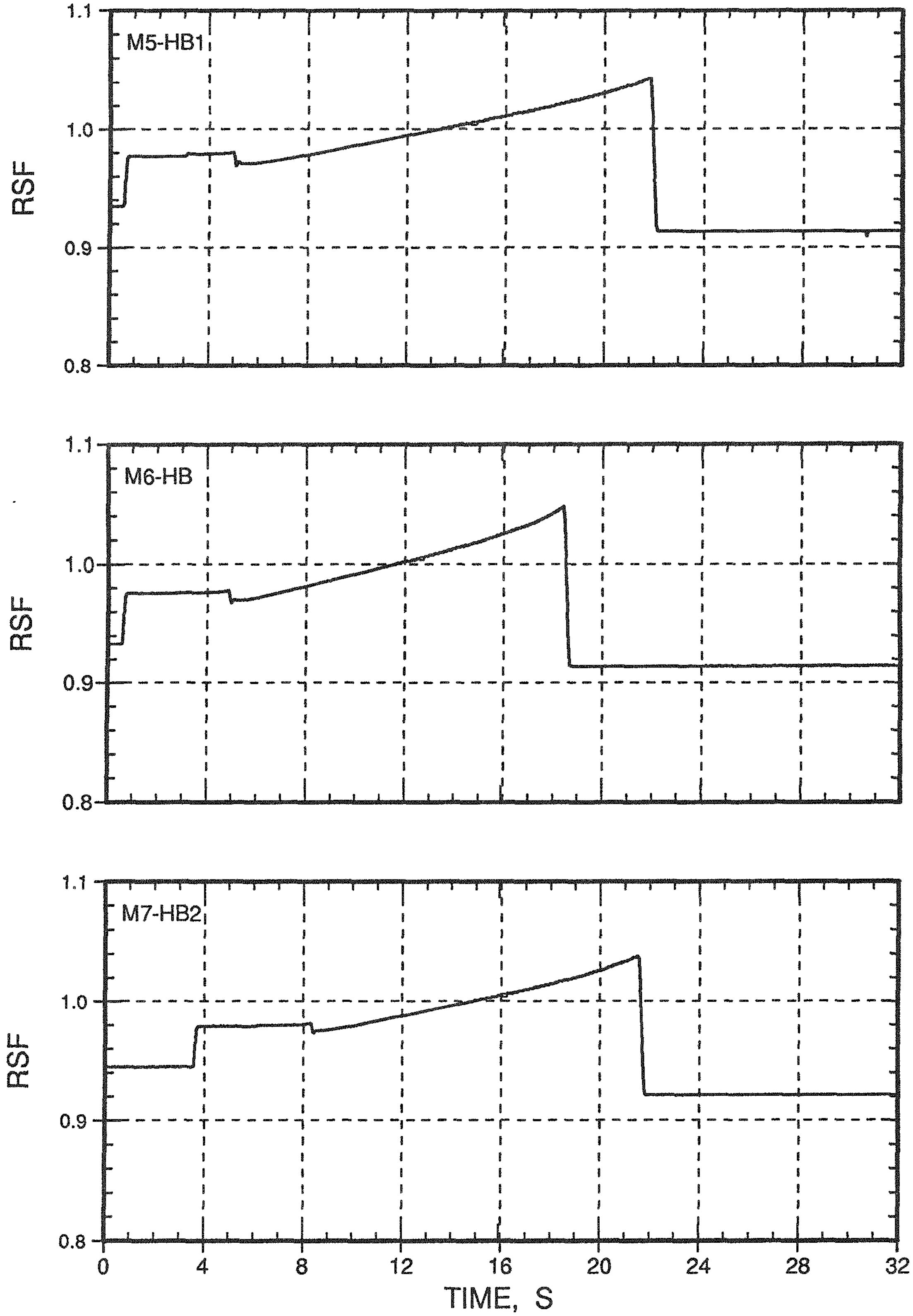

Fig. E.4. Calculated Normalized Rod Shadowing Factor (RSF)

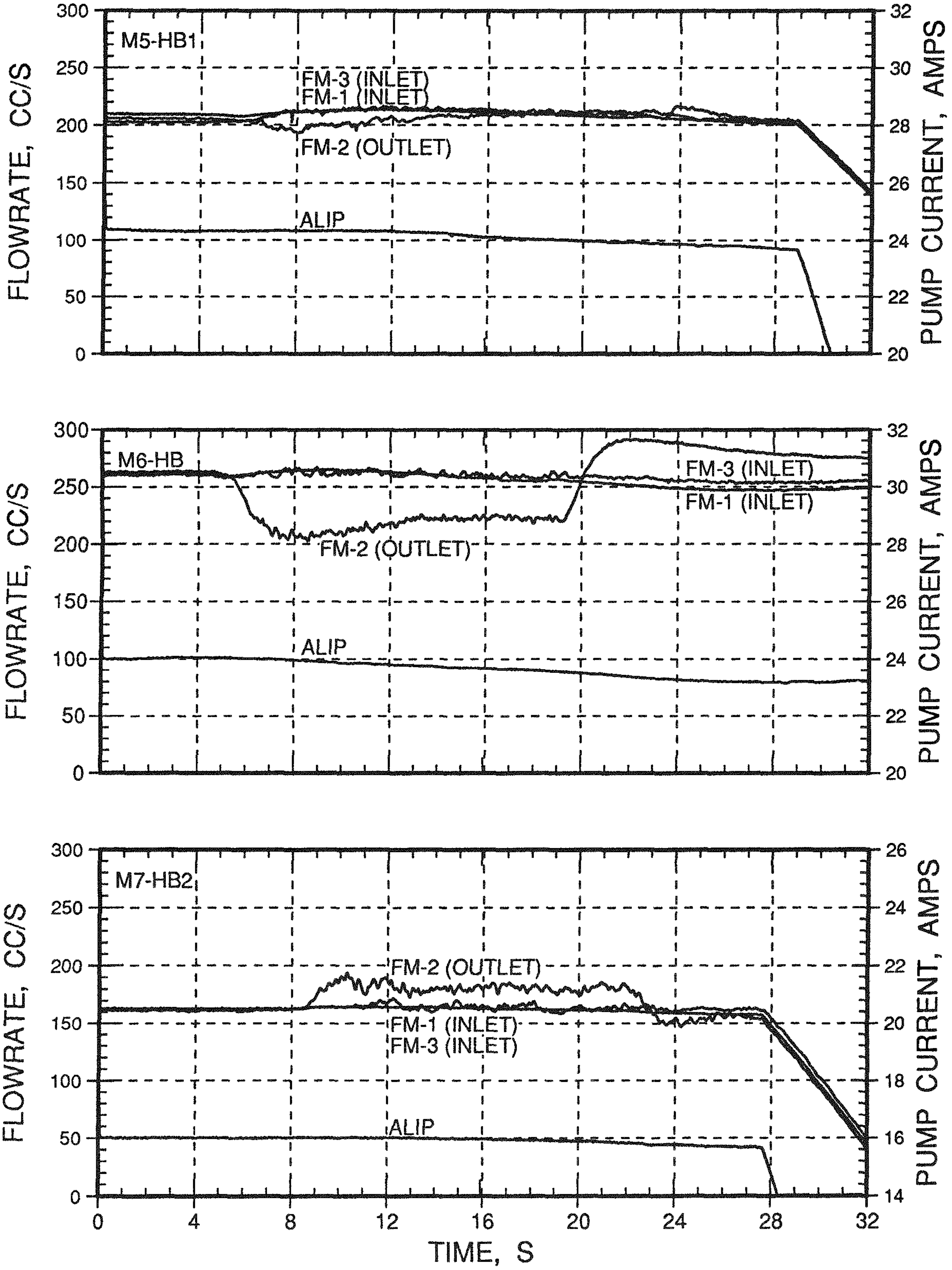

Fig. E.5. Sodium Total Loop Flowrates and Pump Current

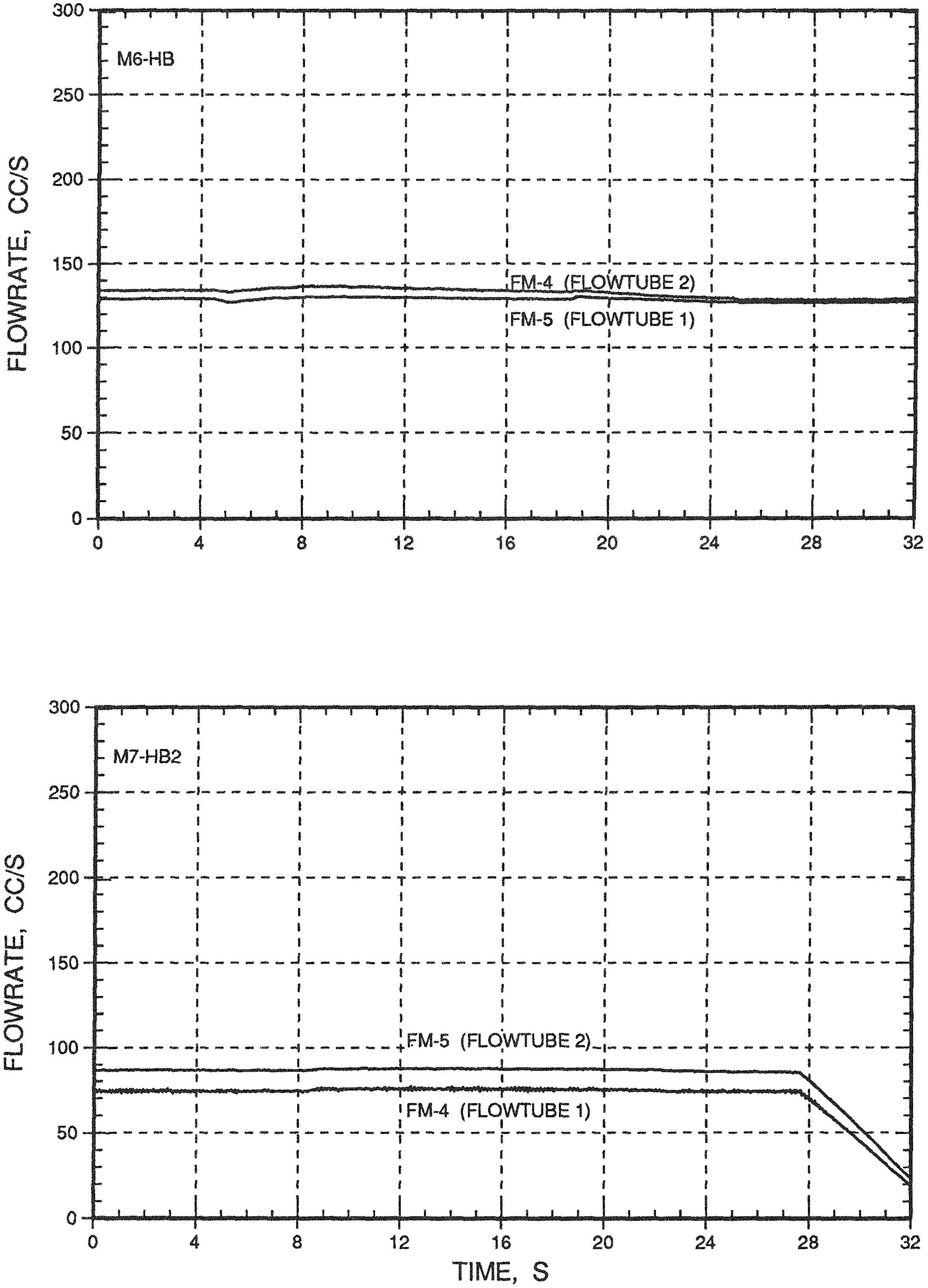

Fig. E.6. Sodium Individual Flowtube Flowrates

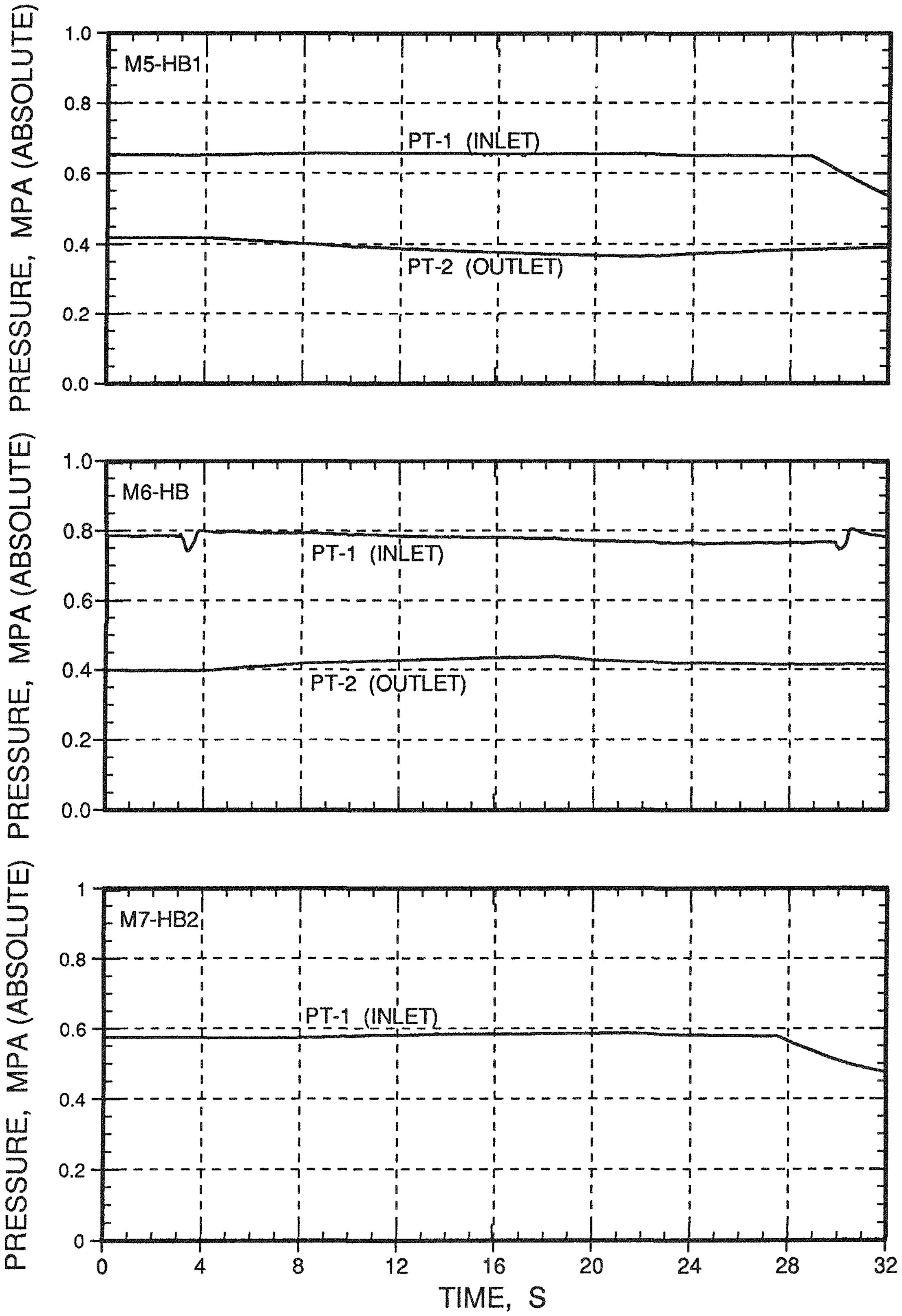

Fig. E.7. Sodium Inlet and Outlet Pressures

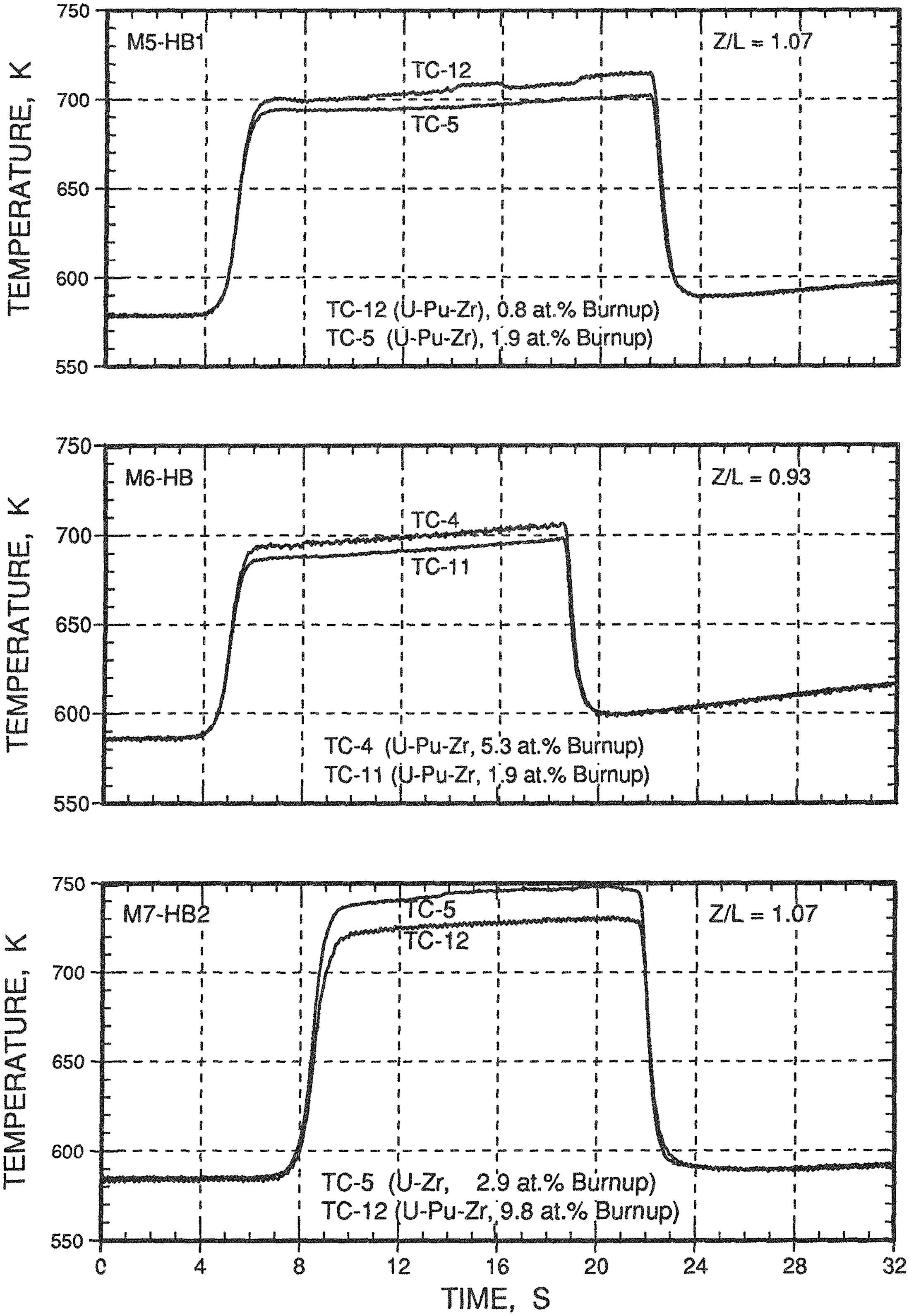

Fig. E.8. Flowtube Temperature Rises near the Top of the Active Fuel Column

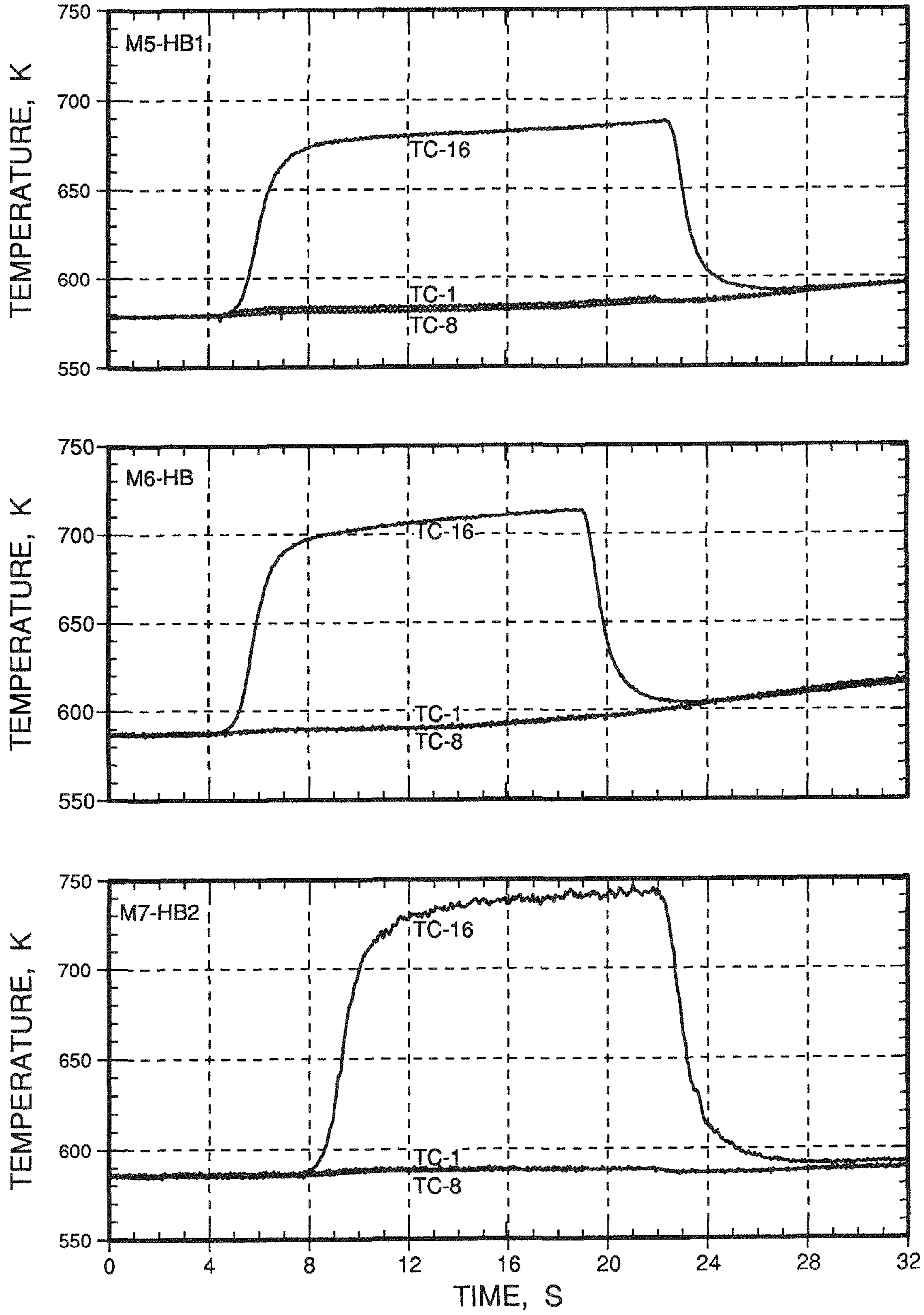

Fig. E.9. Flowtube at Base of Fuel Column and Outlet Sodium Temperatures

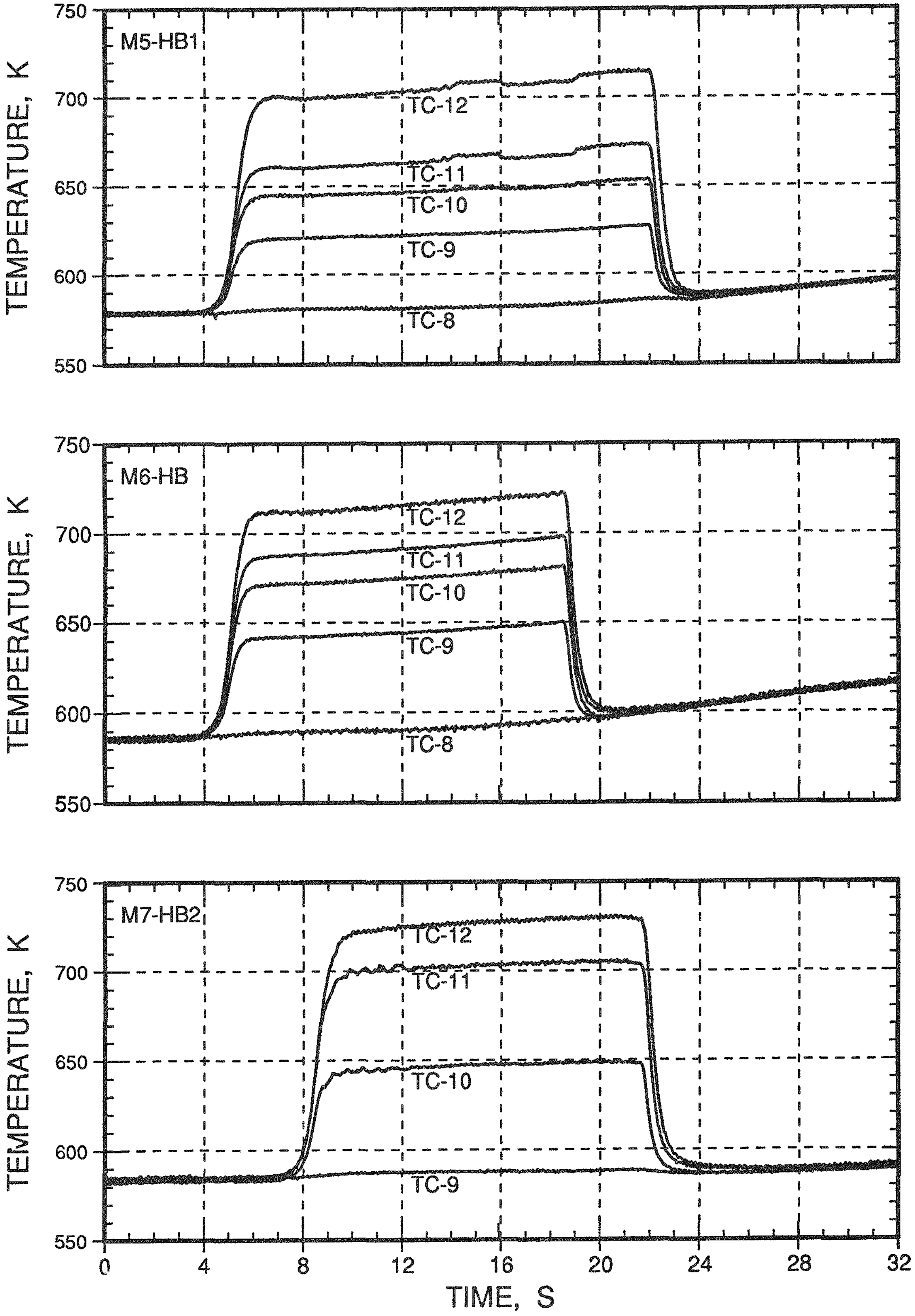

Fig. E.10. Flowtube 1 Temperatures (Z/L = -0.04 to 1.07)

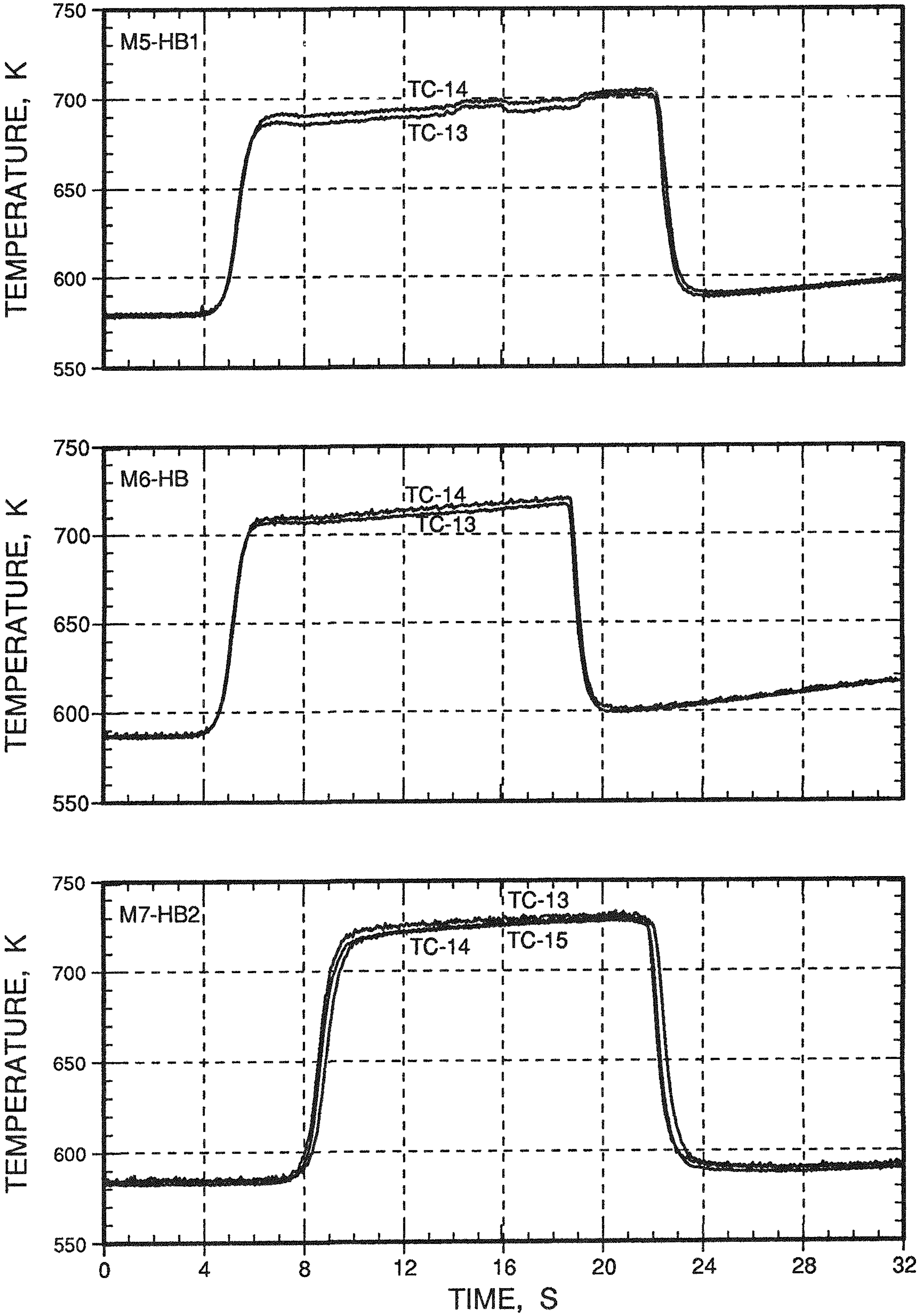

Fig. E.11. Flowtube 1 Temperatures (Z/L = 1.15 to 1.87)

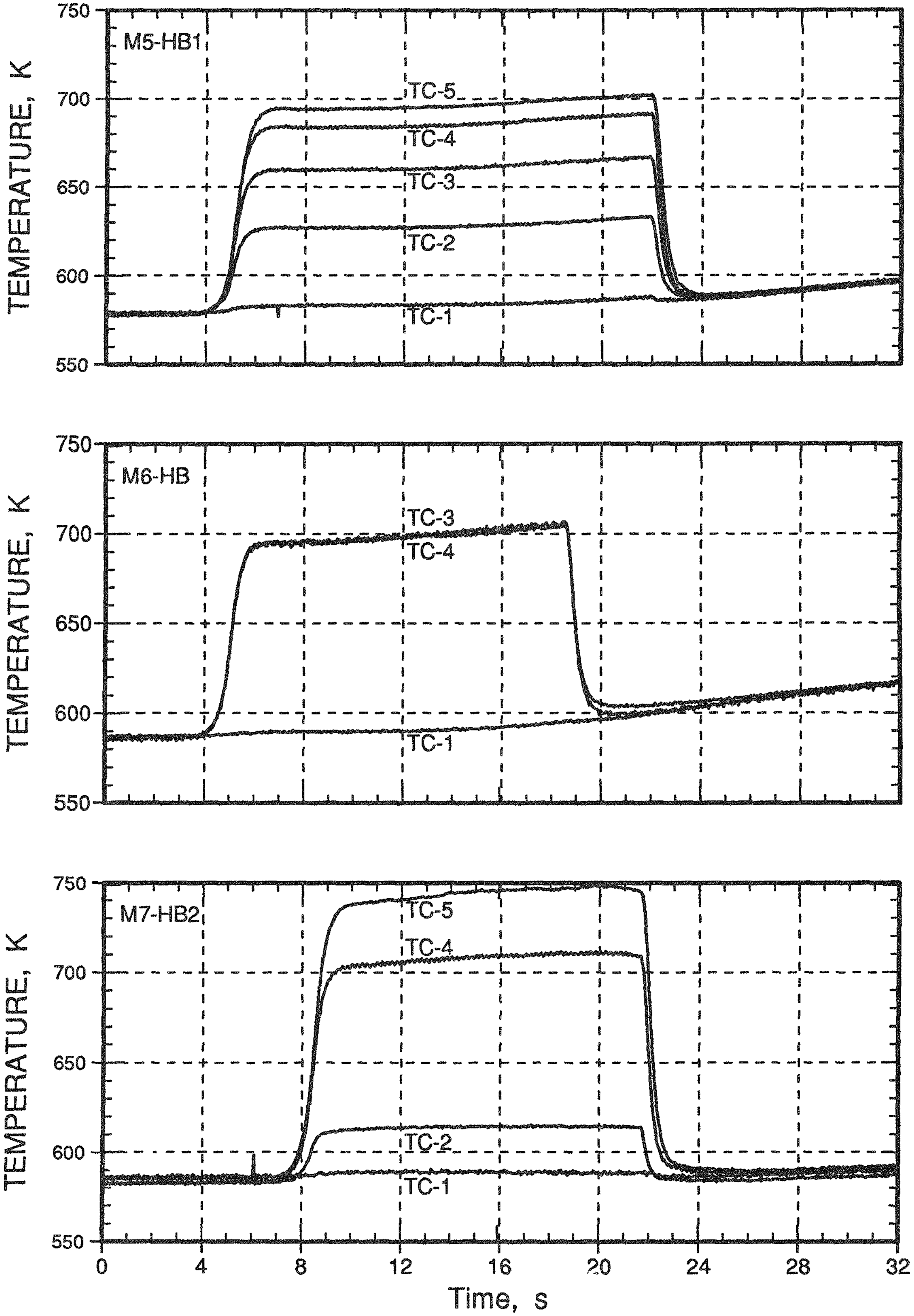

Fig. E.12. Flowtube 2 Temperatures (Z/L = -0.04 to 1.07)

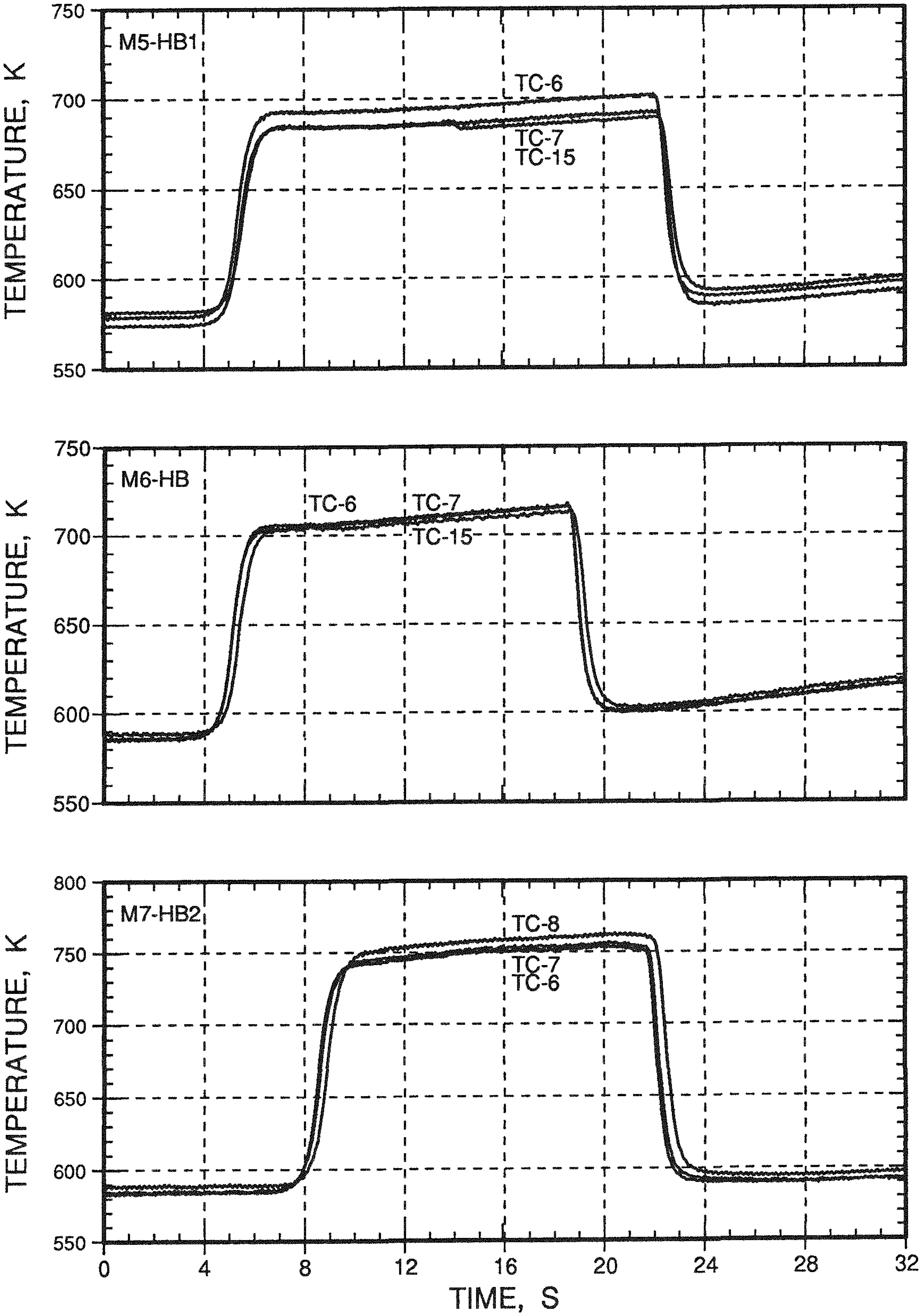

Fig. E.13. Flowtube 2 Temperatures (Z/L = 1.15 to 1.87)

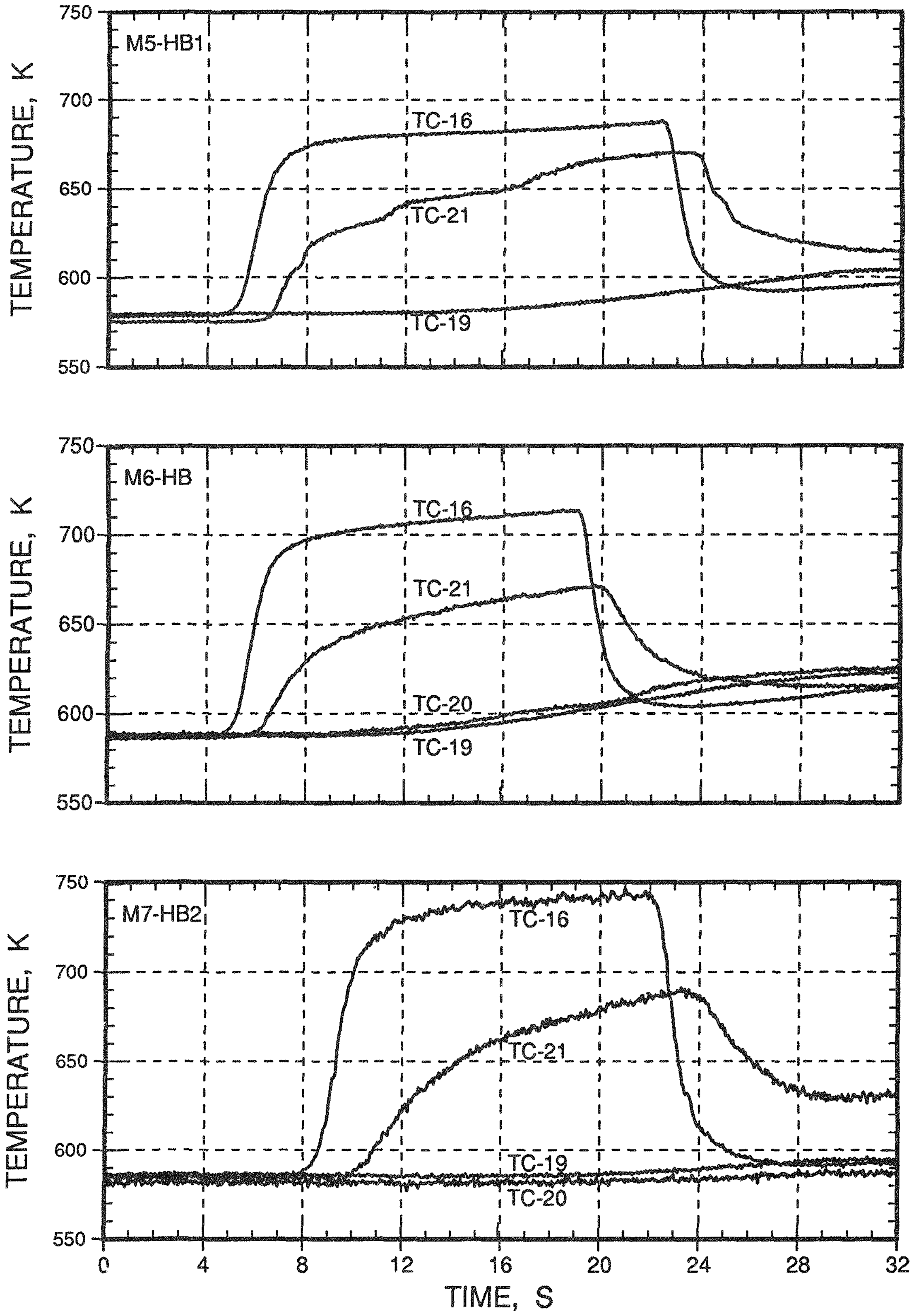

Fig. E.14. Temperatures in the Sodium Flow

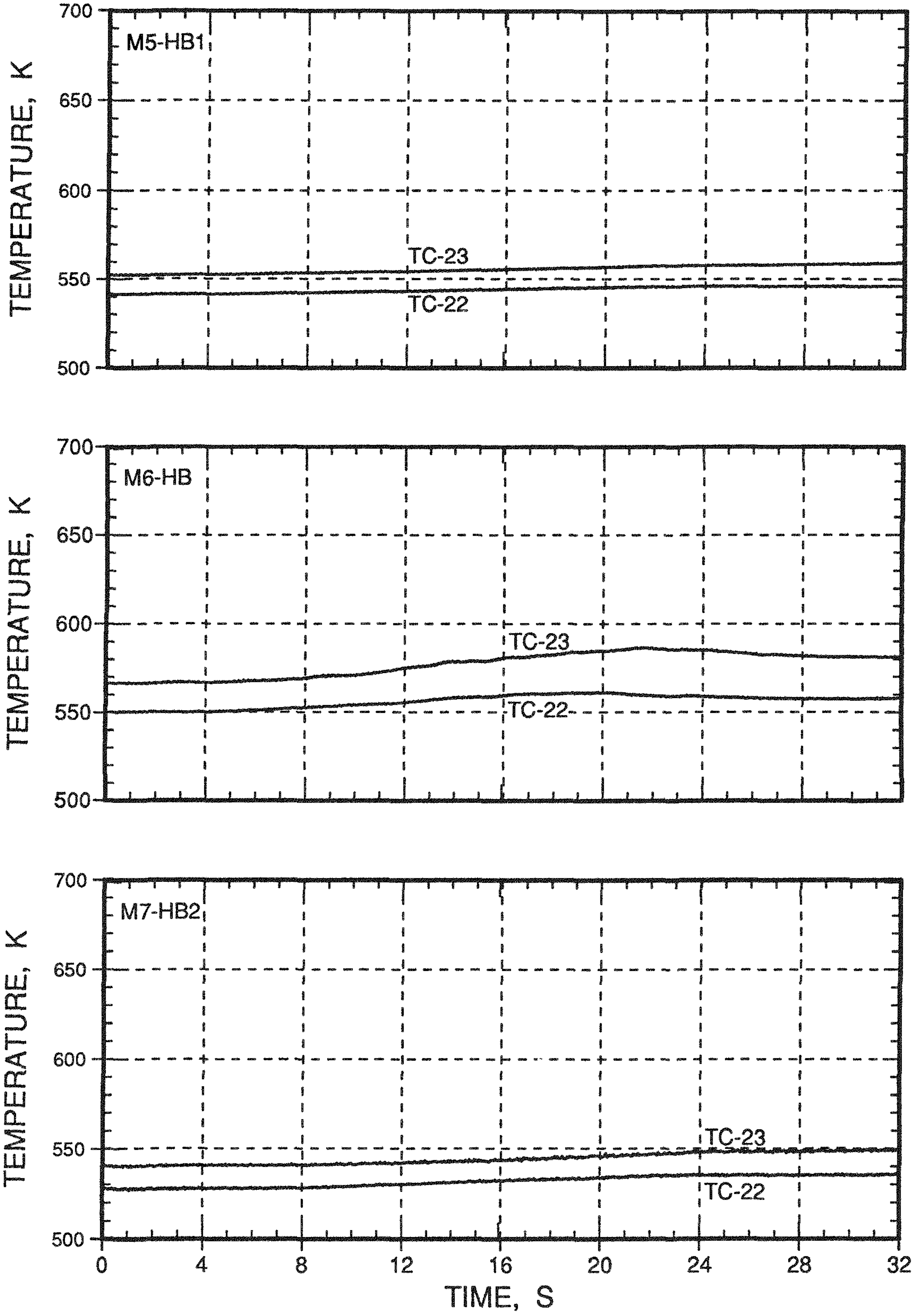

Fig. E.15. Temperatures in the Gas Plenum

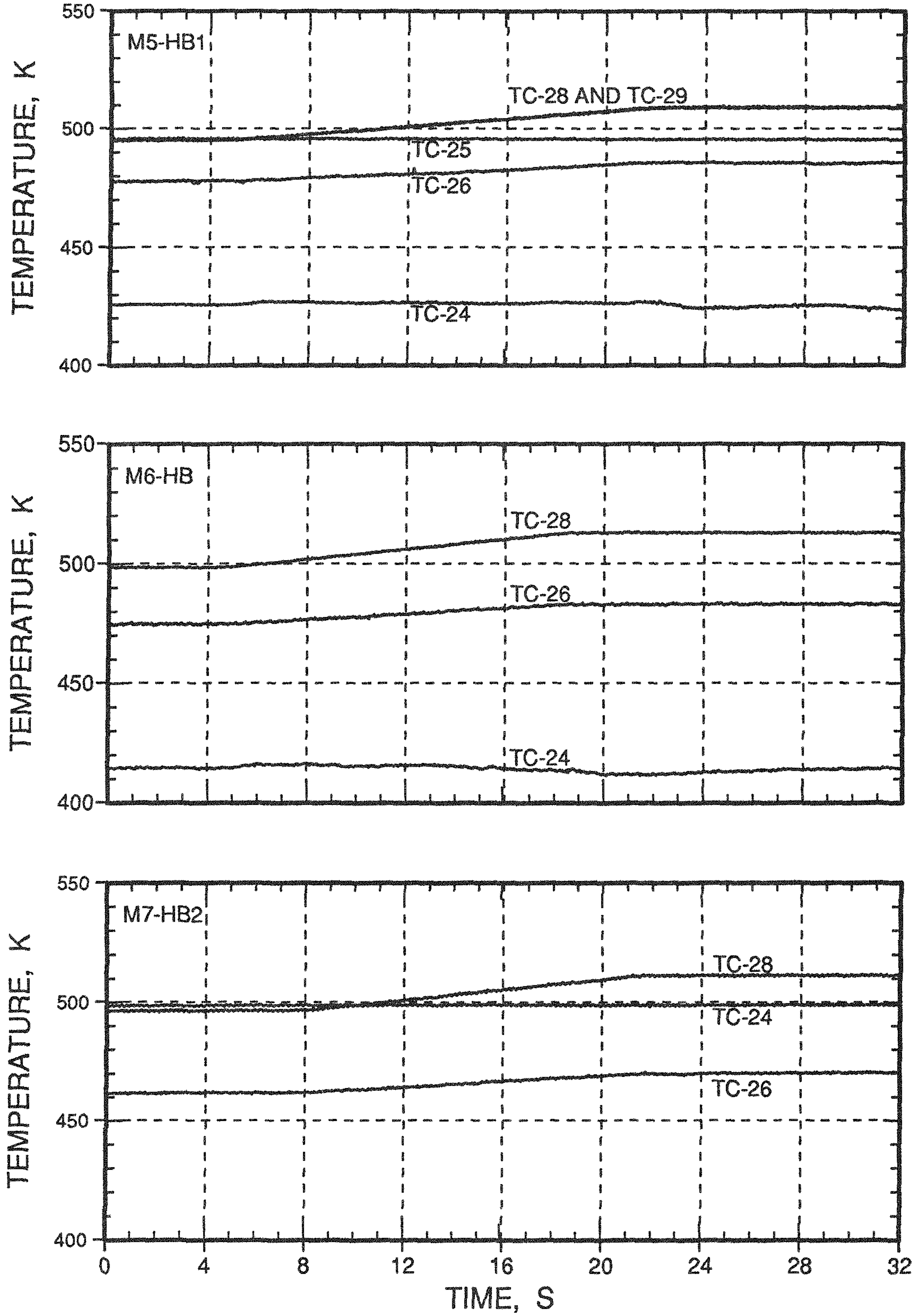

Fig. E.16. Flowmeter Magnet Temperatures

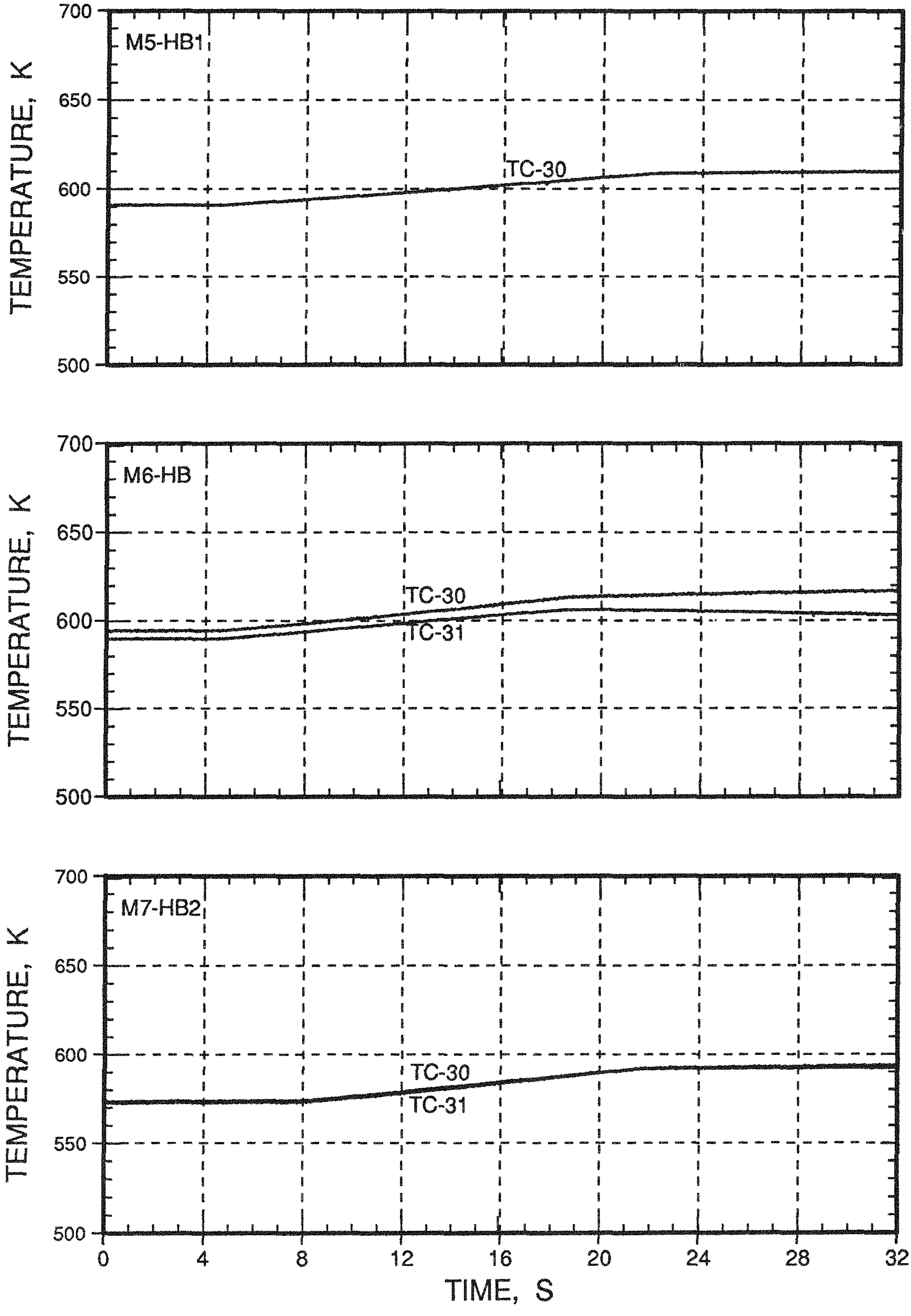

Fig. E.17. Temperatures of the Wall of the Loop Test Section

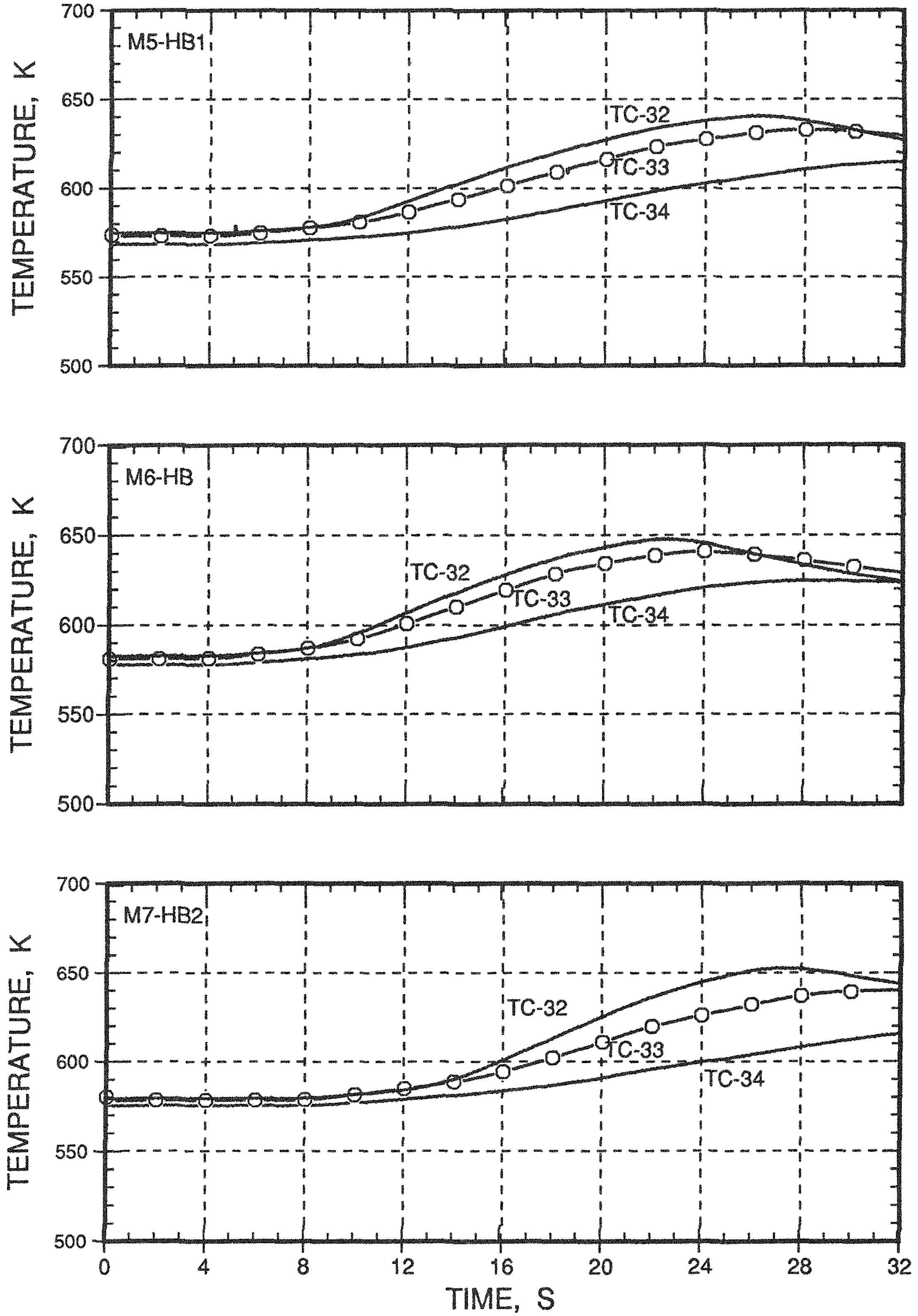

Fig. E.18. Temperatures of the Wall of the Loop Pump Leg

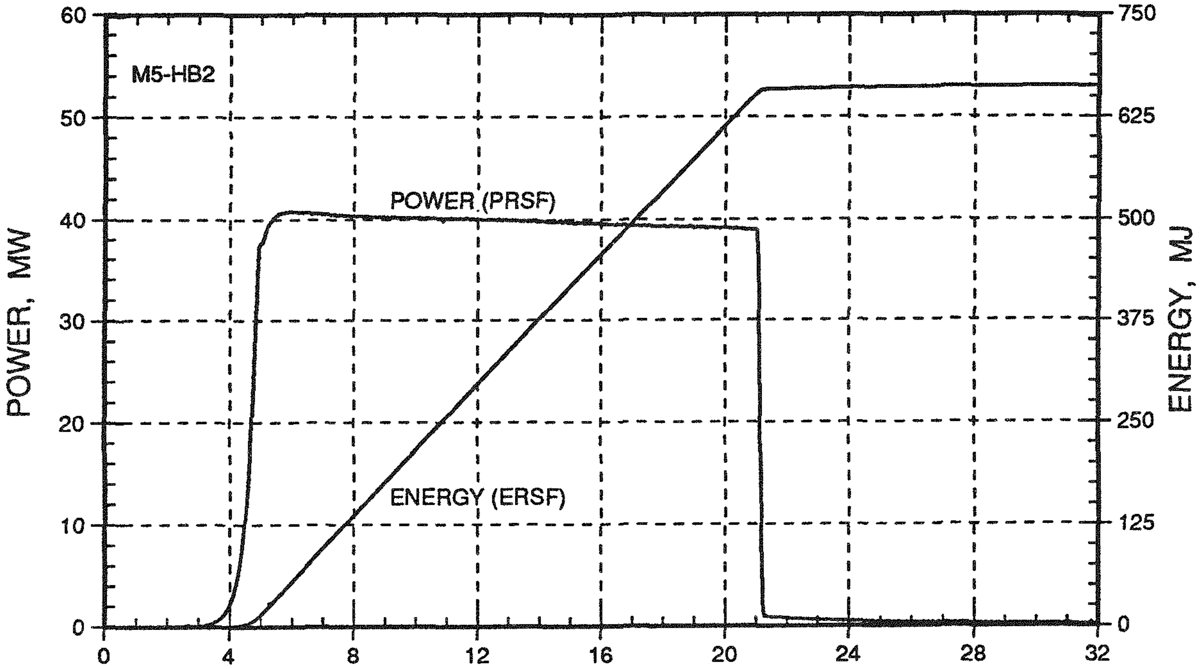

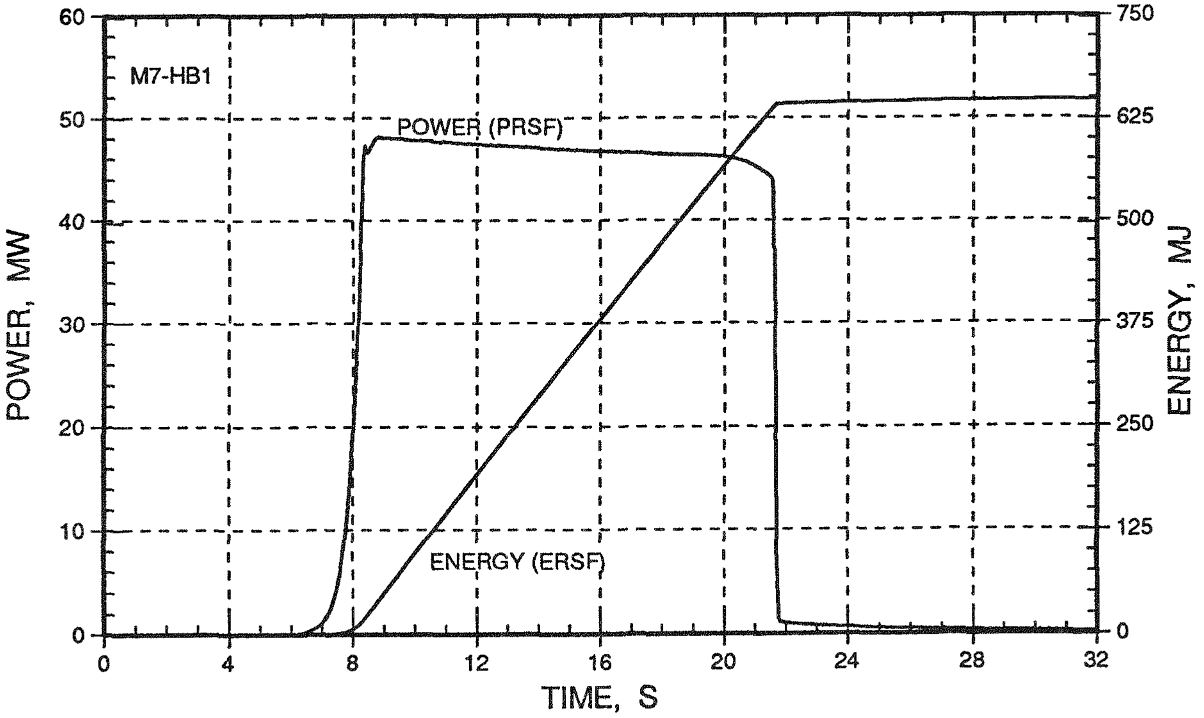

Fig. E.19. Corrected TREAT Power and Energy, Including RSF Variation

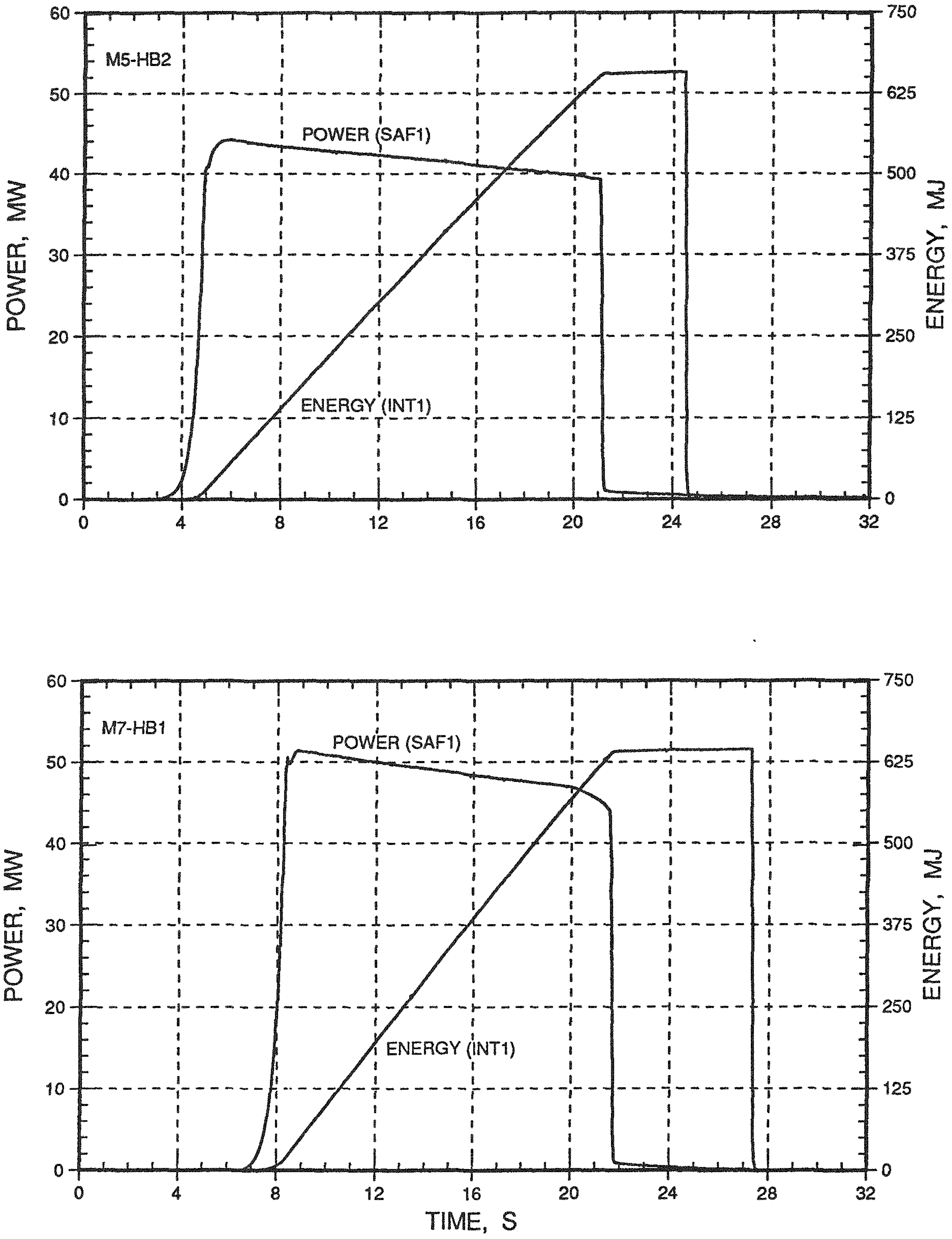

Fig. E.20. TREAT Power and Energy from Instruments S1 and I1

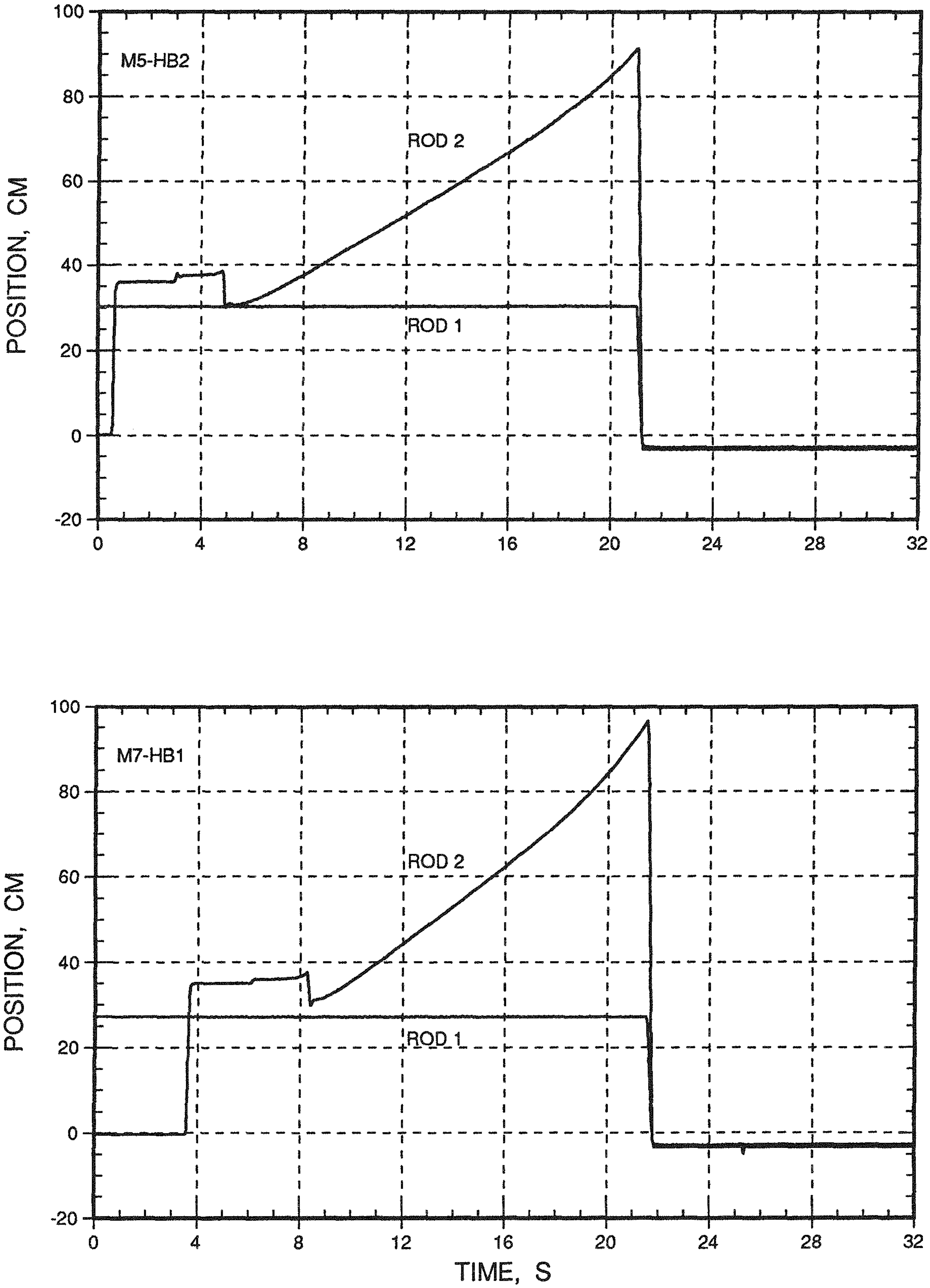

Fig. E.21. Transient-rod Motions

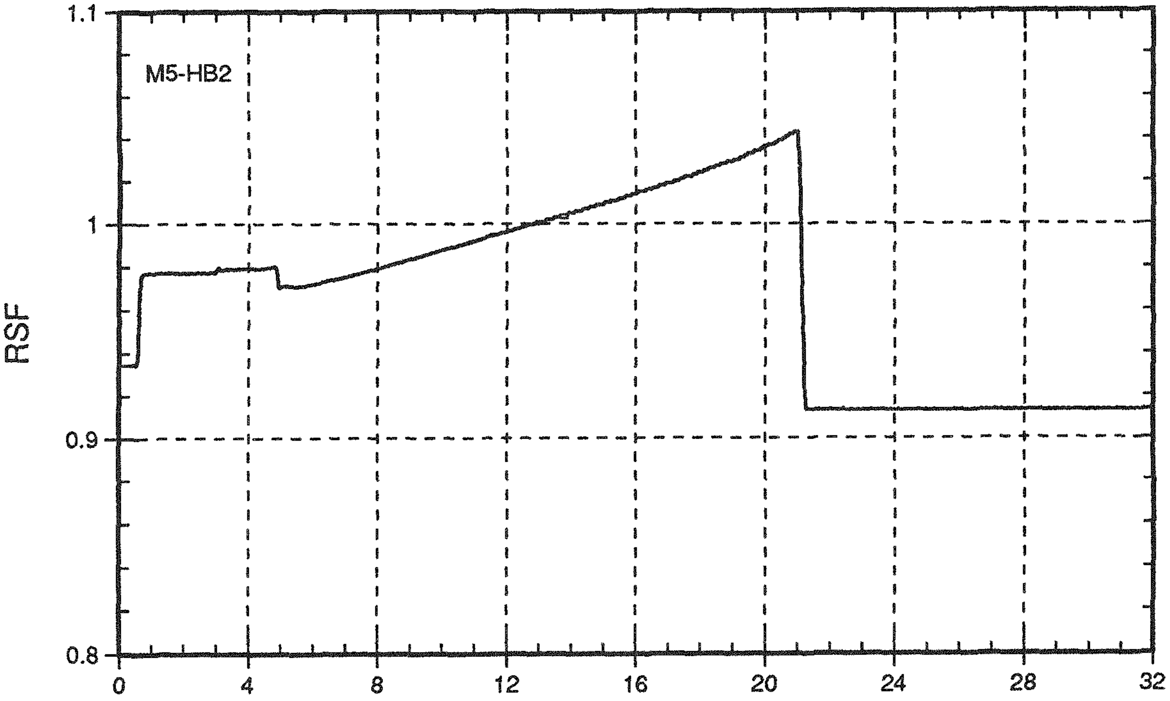

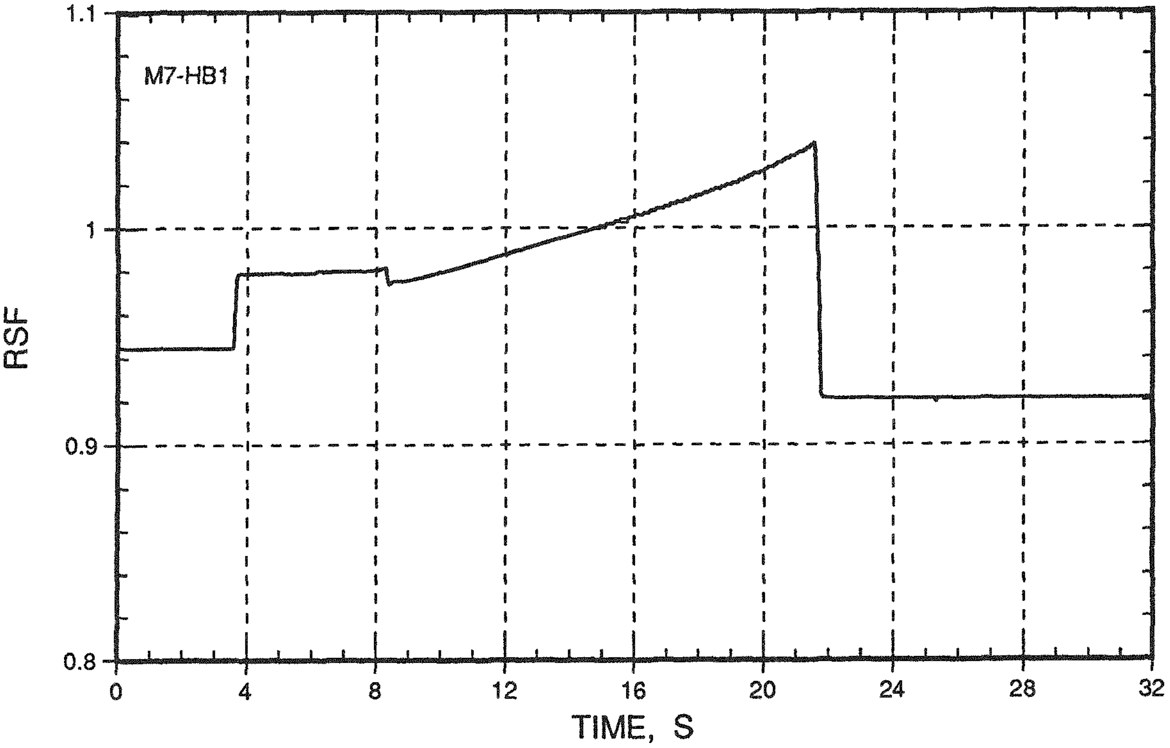

Fig. E.22. Calculated Normalized Rod Shadowing Factor (RSF)

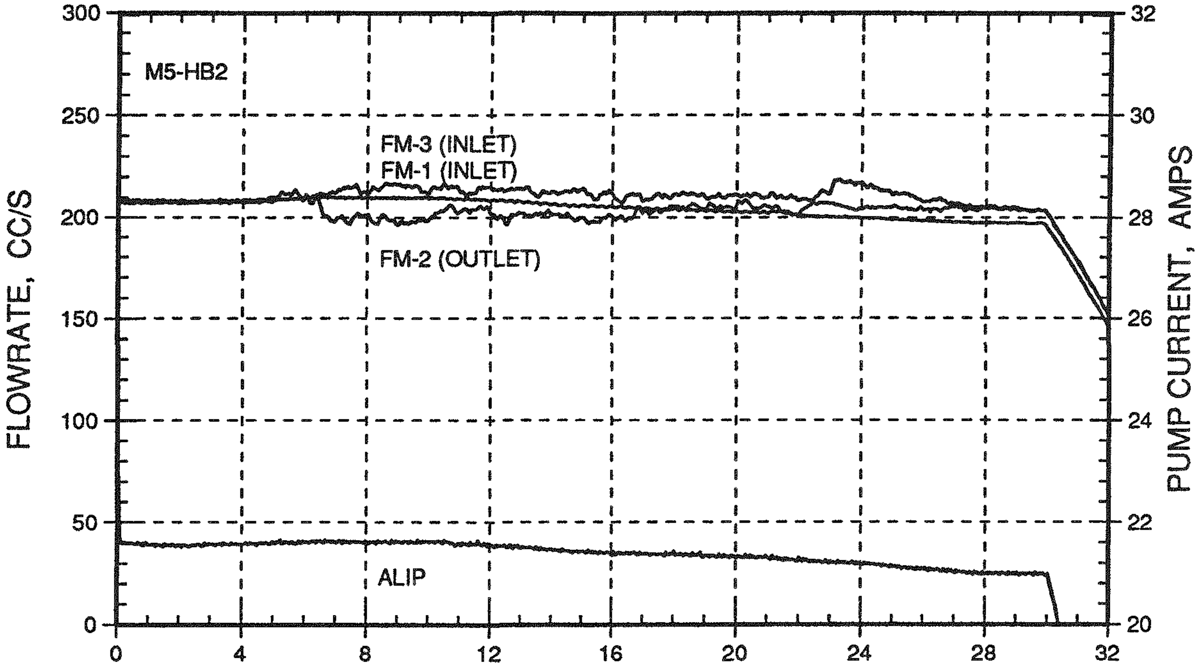

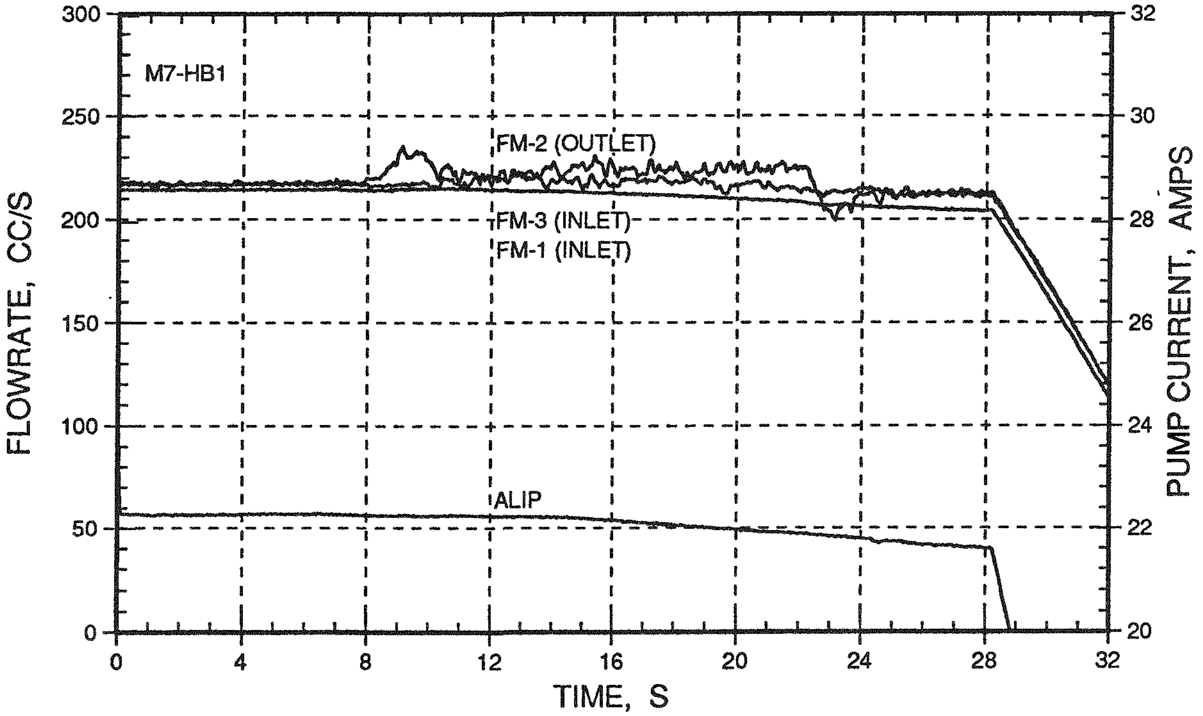

Fig. E.23. Sodium Total Loop Flowrates and Pump Current

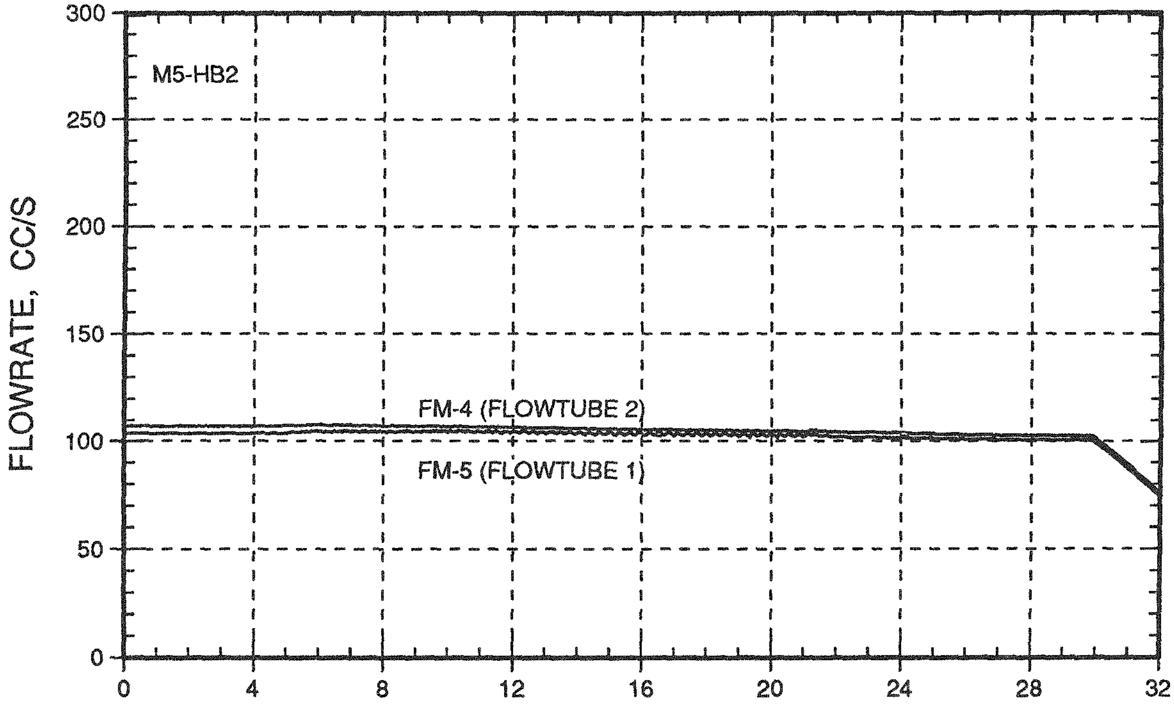

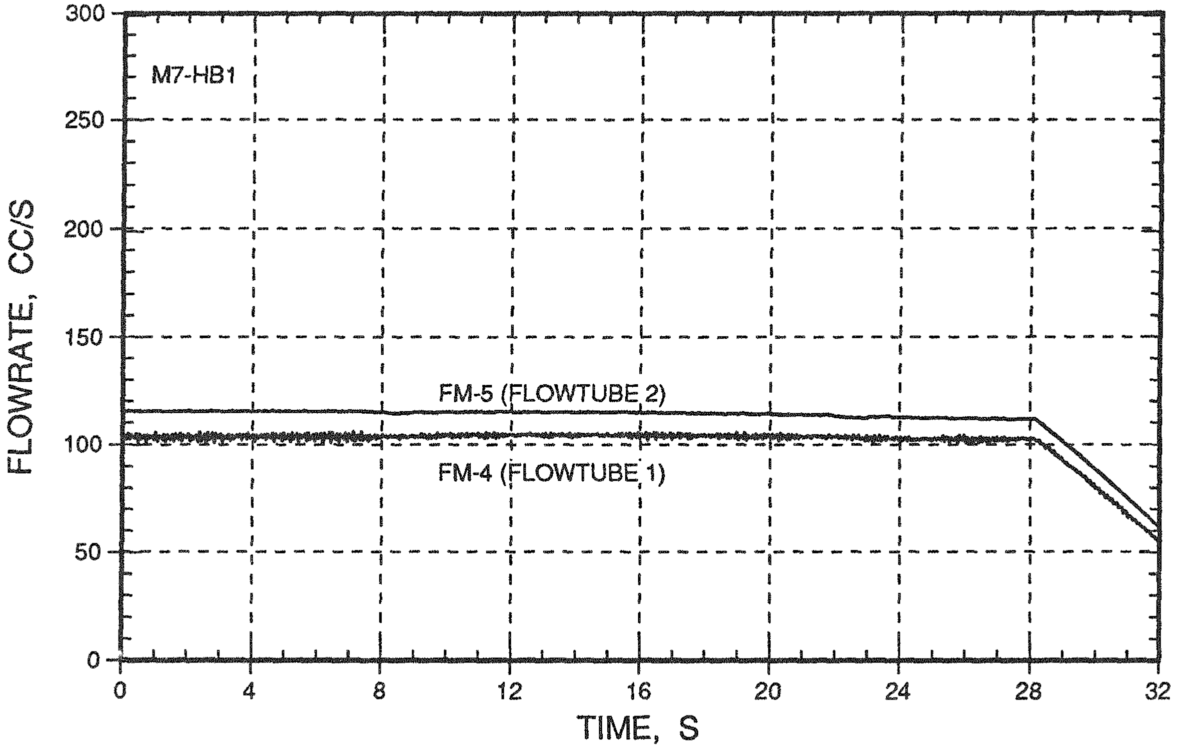

Fig. E.24. Sodium Individual Flowtube Flowrates

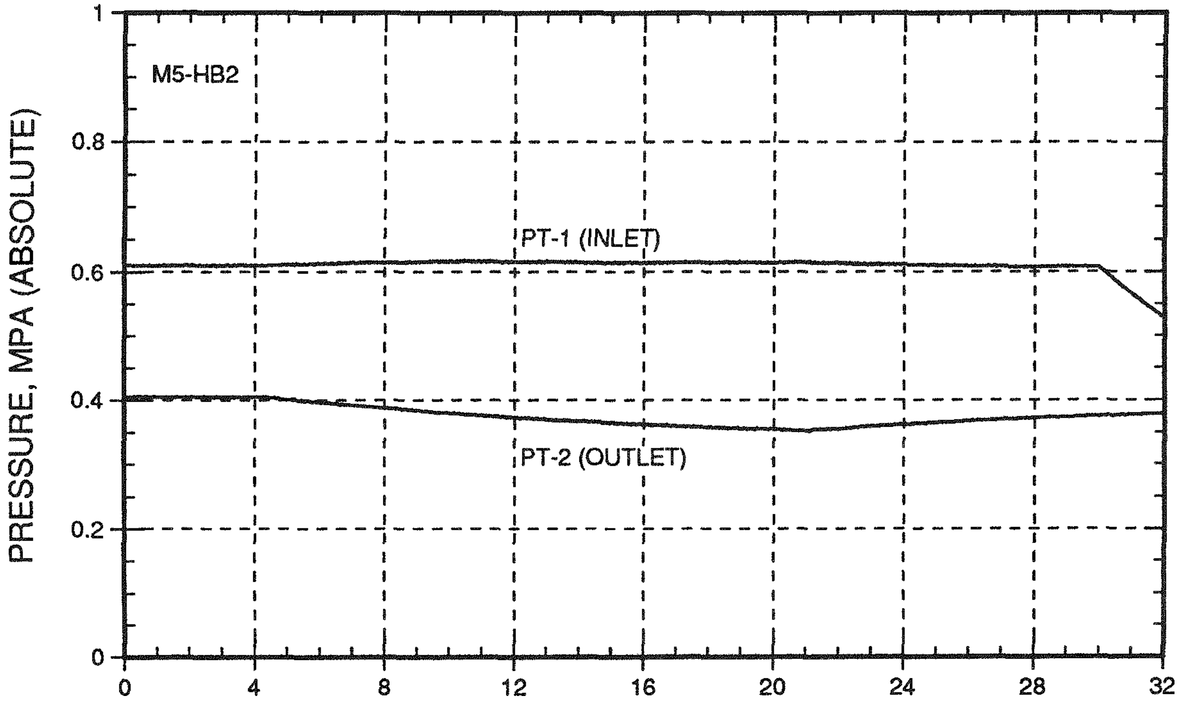

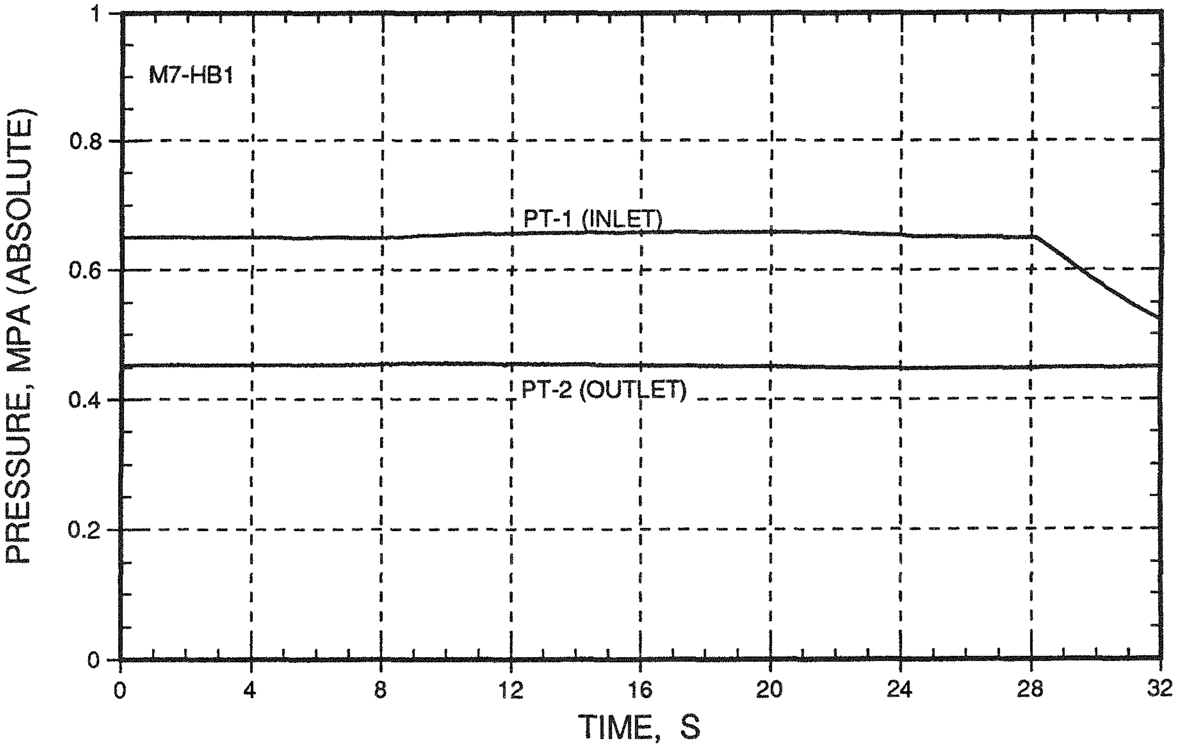

Fig. E.25. Sodium Inlet and Outlet Pressures

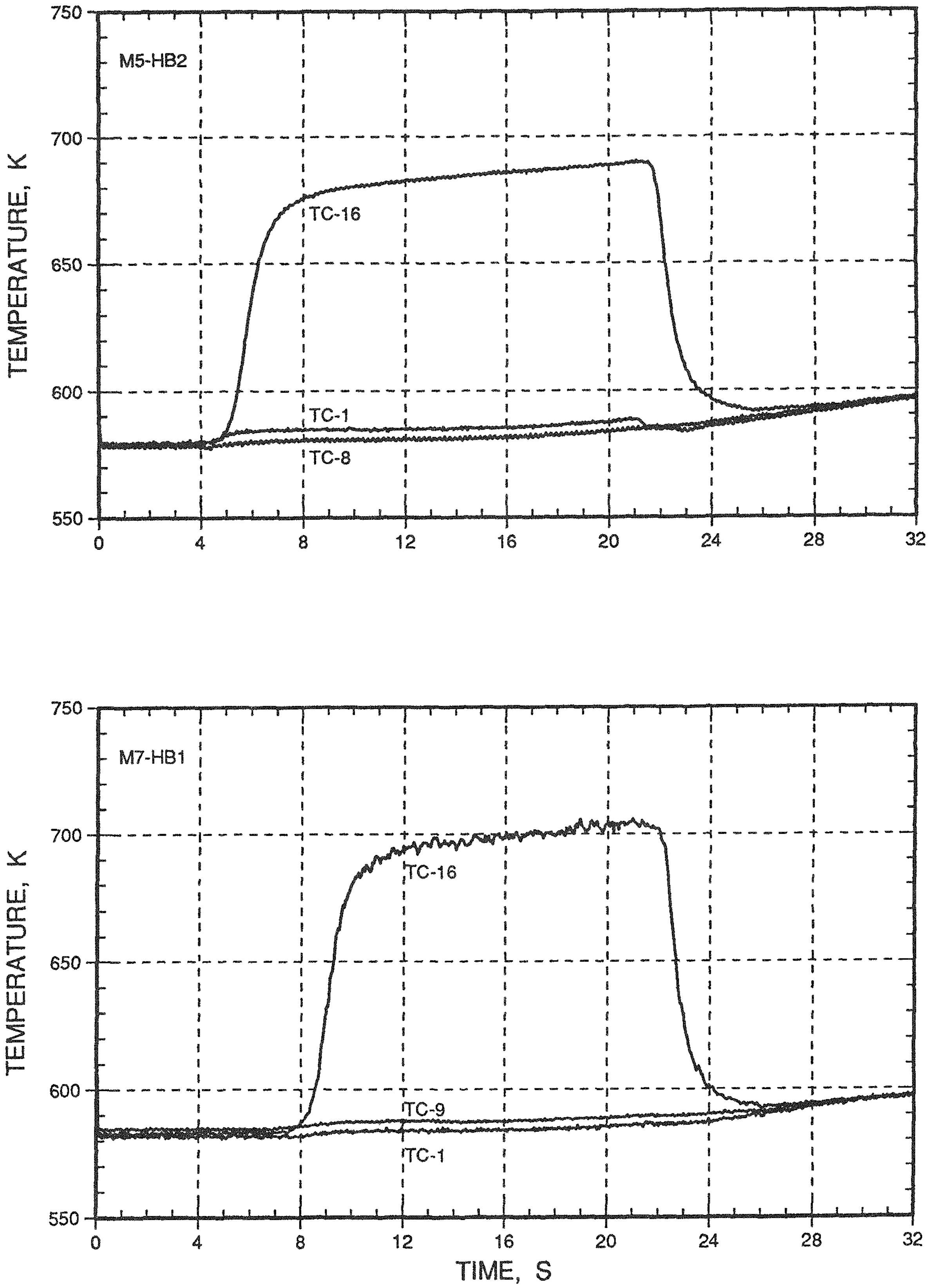

Fig. E.26. Flowtube (base of active fuel column) and Outlet Sodium Temperatures

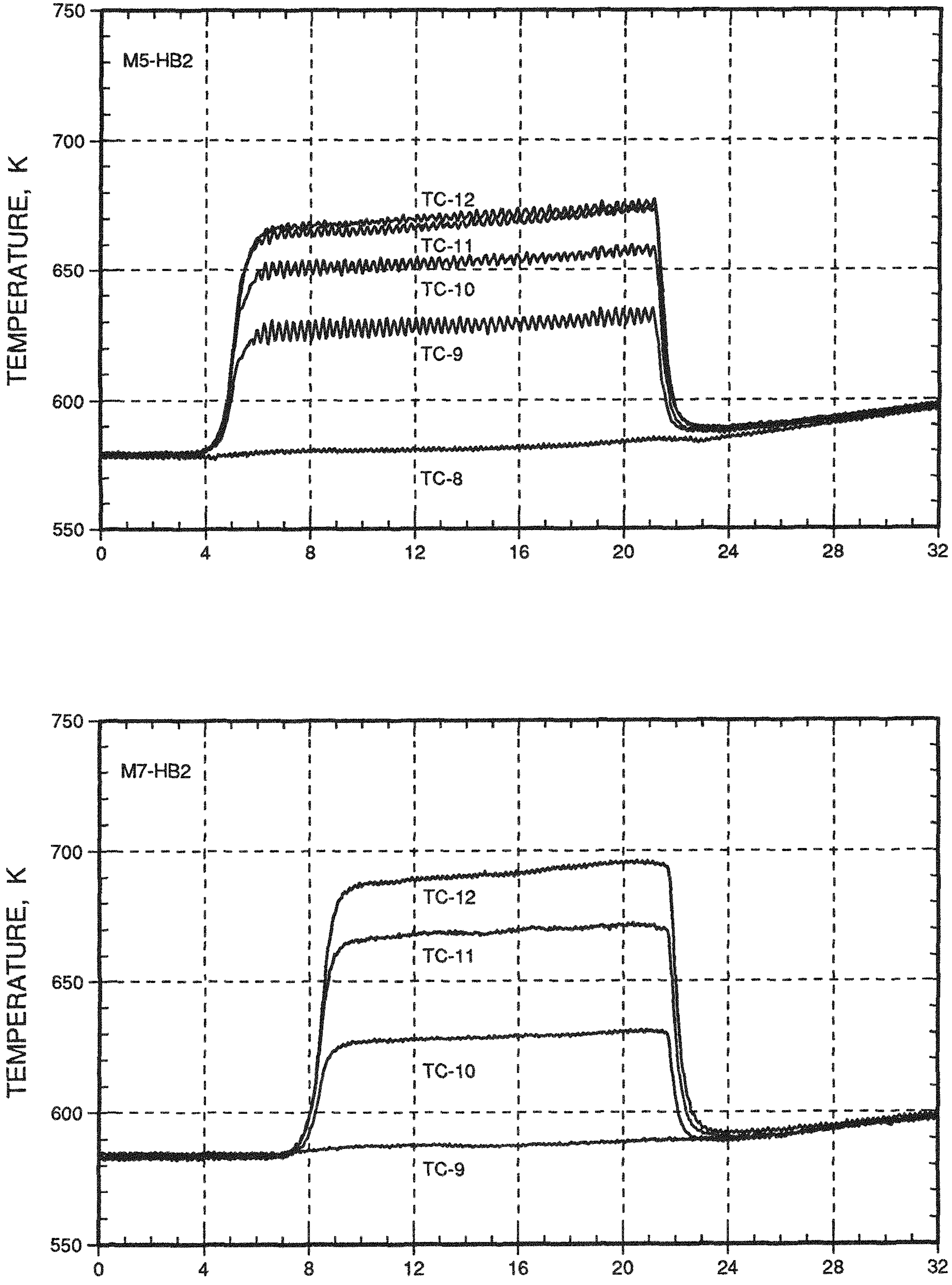

Fig. E.27. Flowtube 1 Temperatures (Z/L = -0.04 to 1.07)

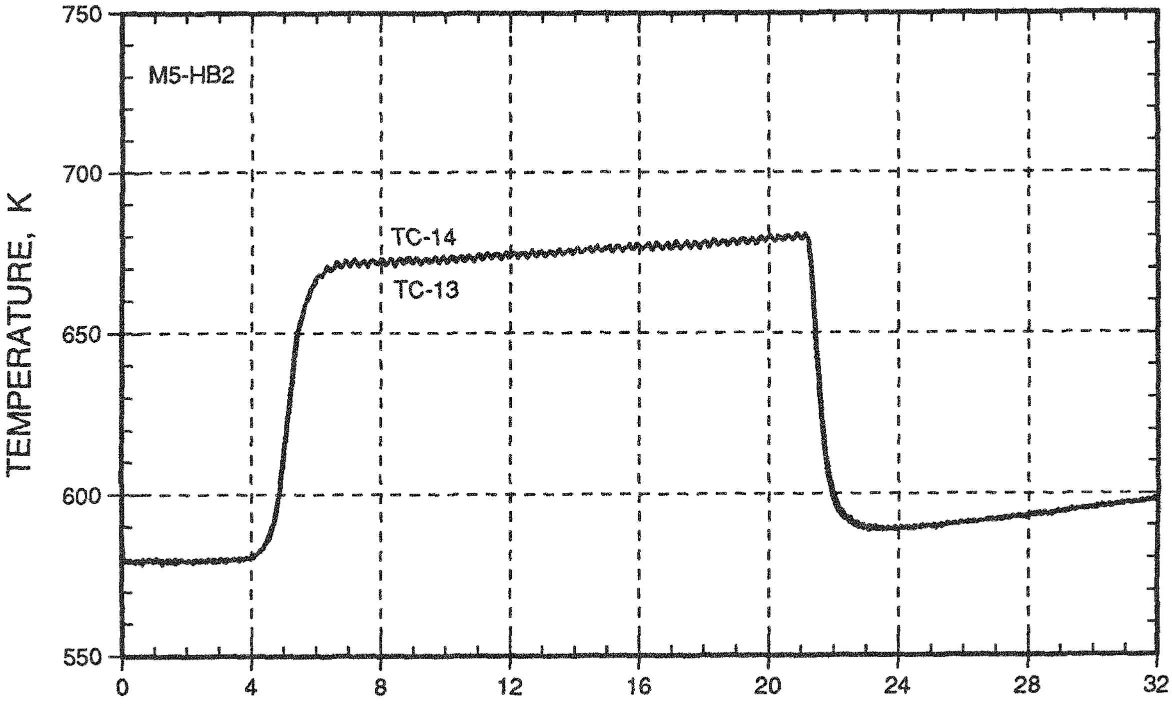

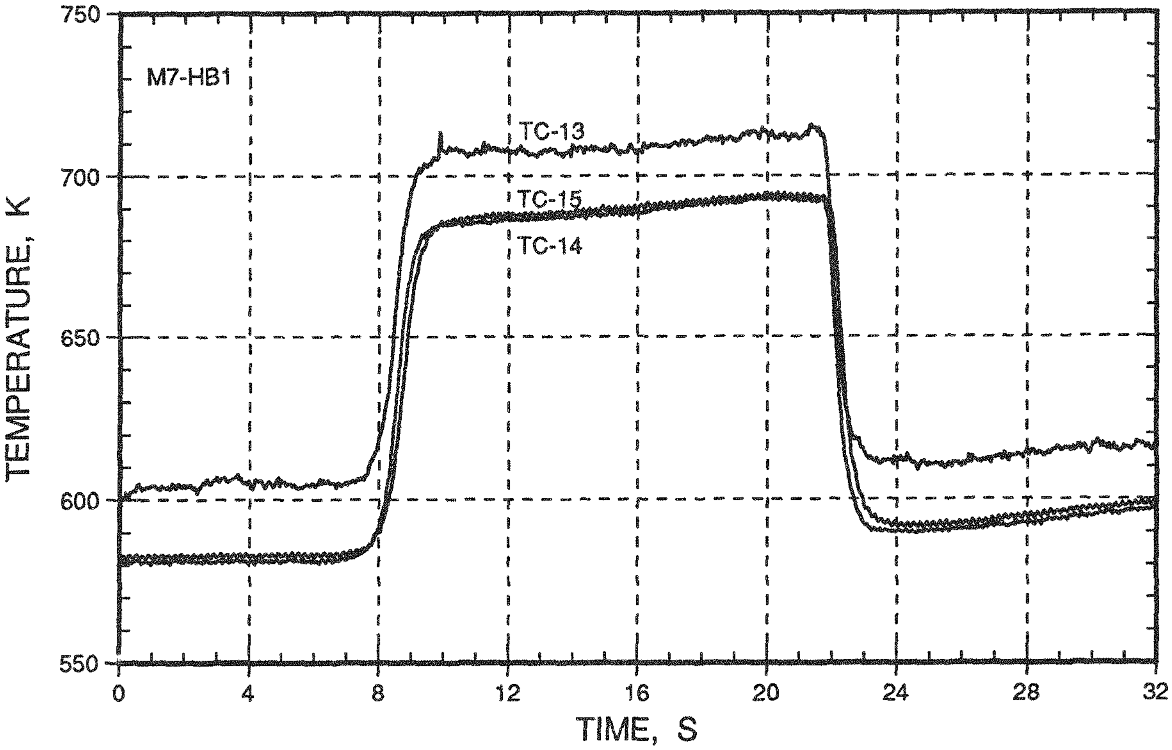

Fig. E.28. Flowtube 1 Temperatures (Z/L = 1.15 to 1.87)

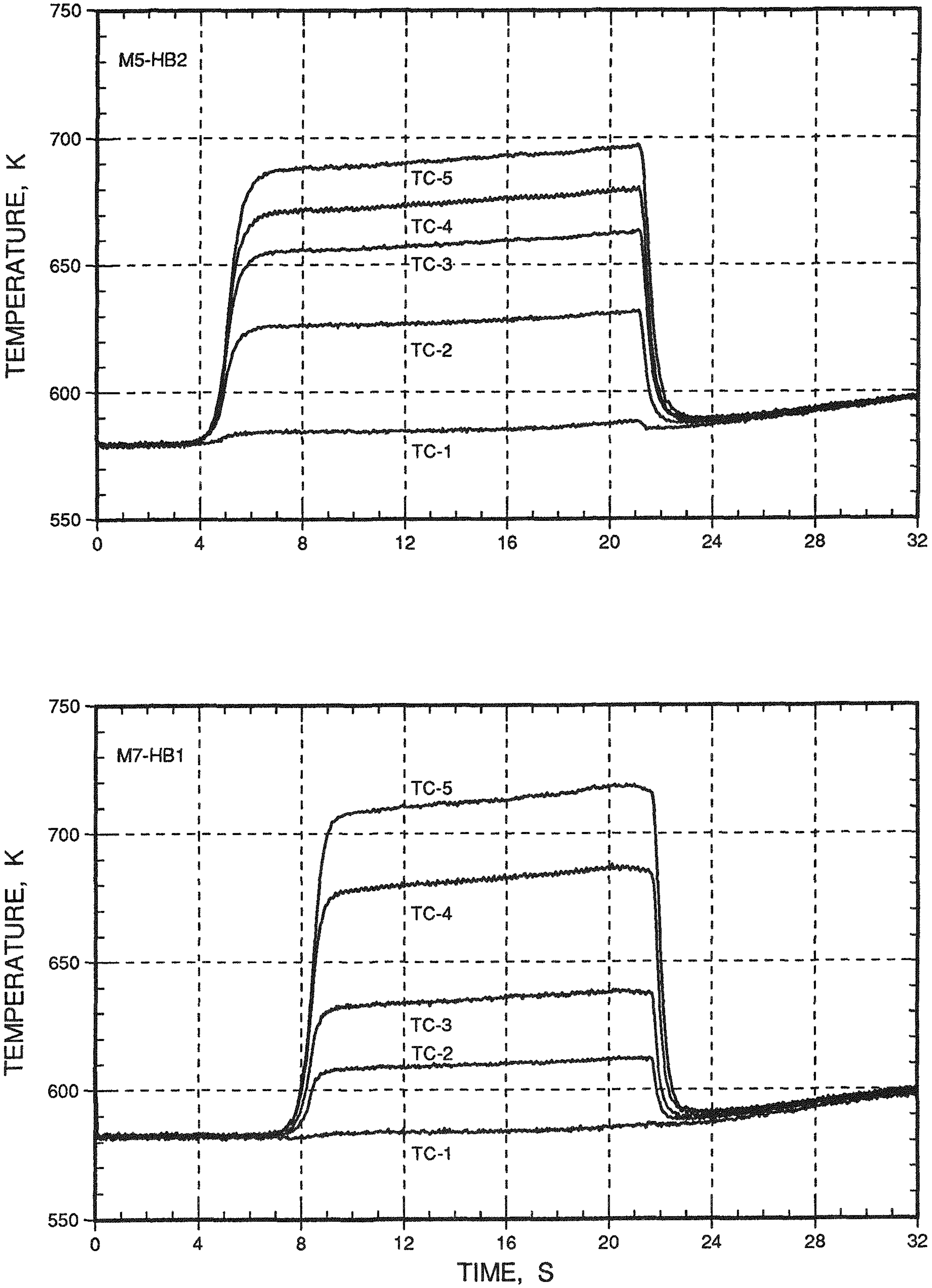

Fig. E.29. Flowtube 2 Temperatures (Z/L = -0.04 to 1.07)

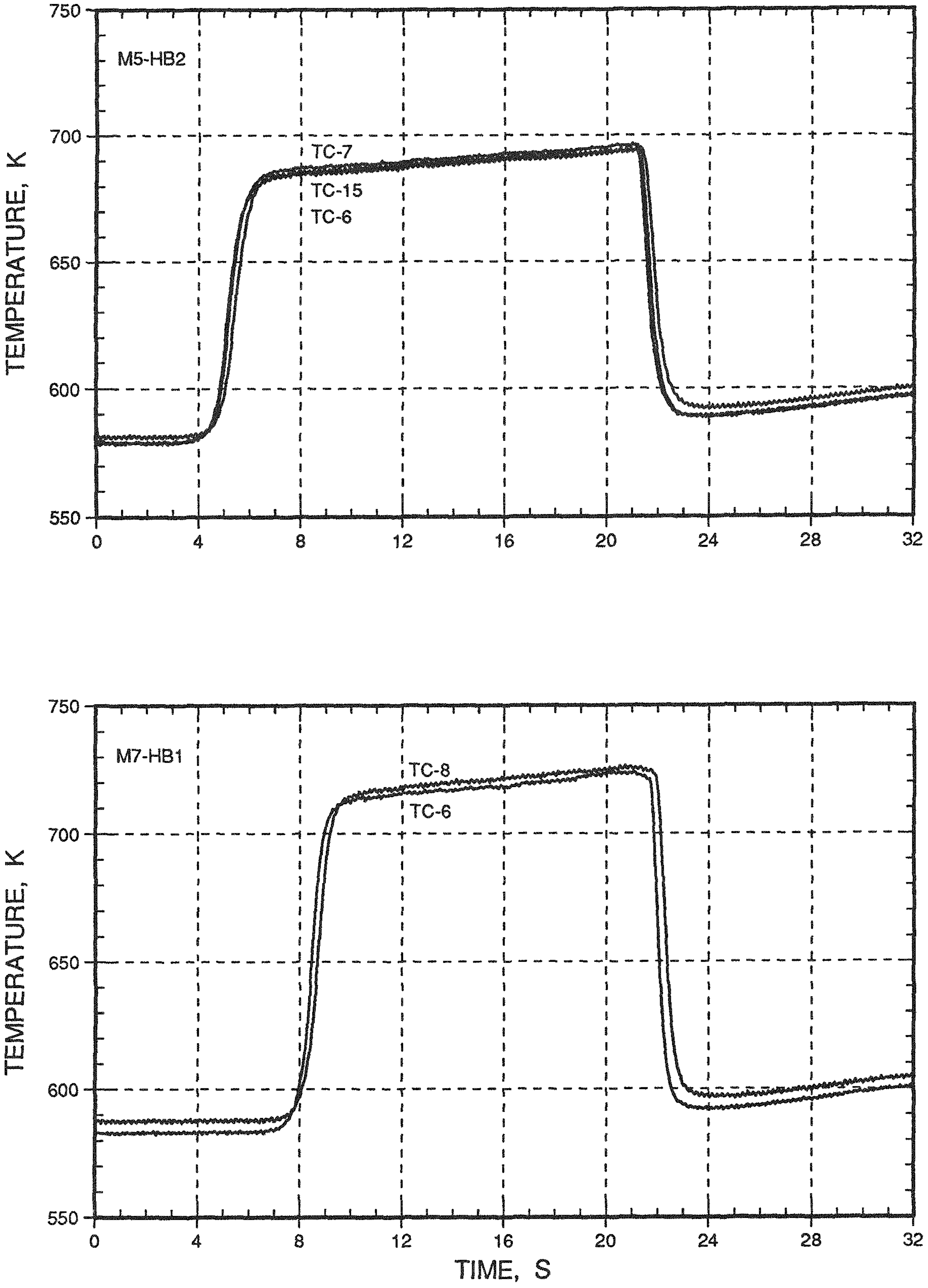

Fig. E.30. Flowtube 2 Temperatures (Z/L = 1.15 to 1.87)

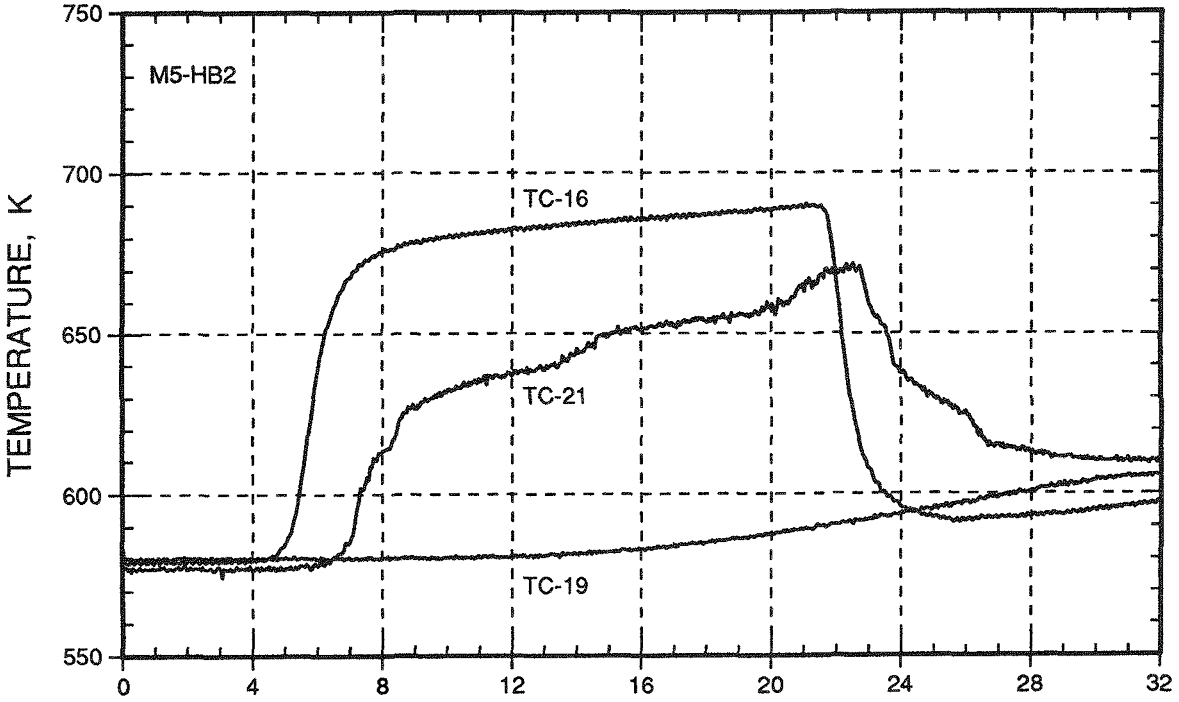

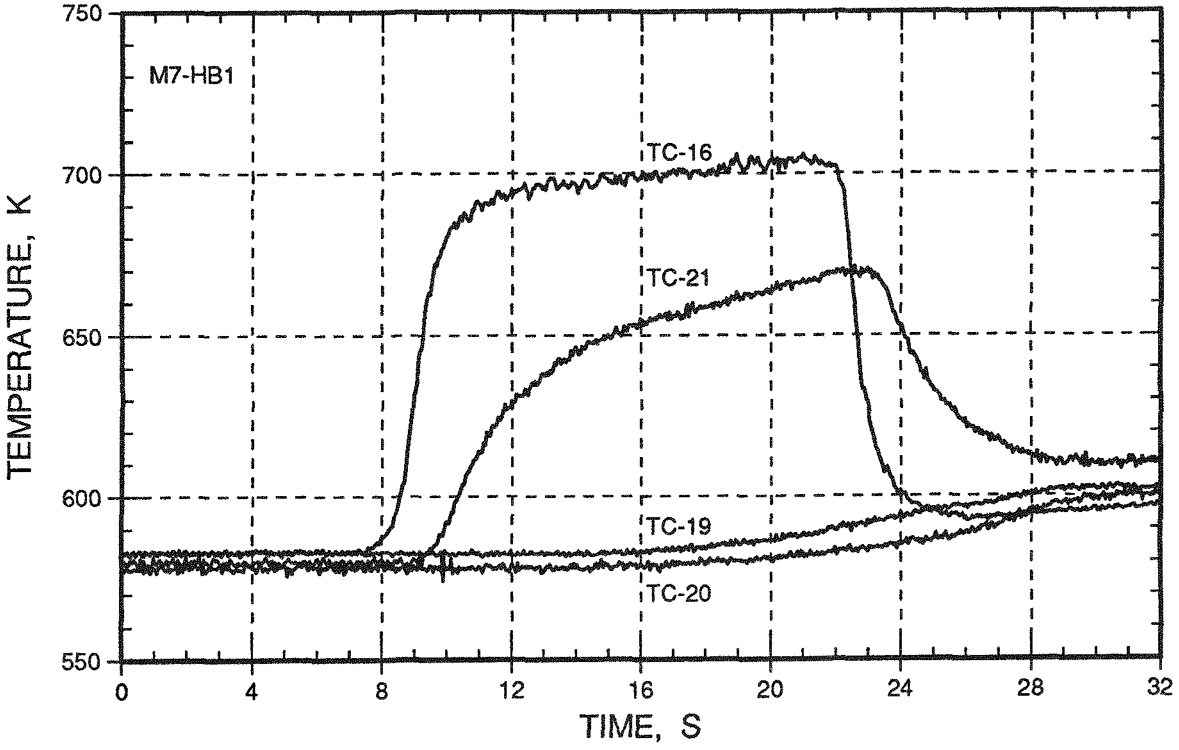

Fig. E.31. Temperatures in the Sodium Flow

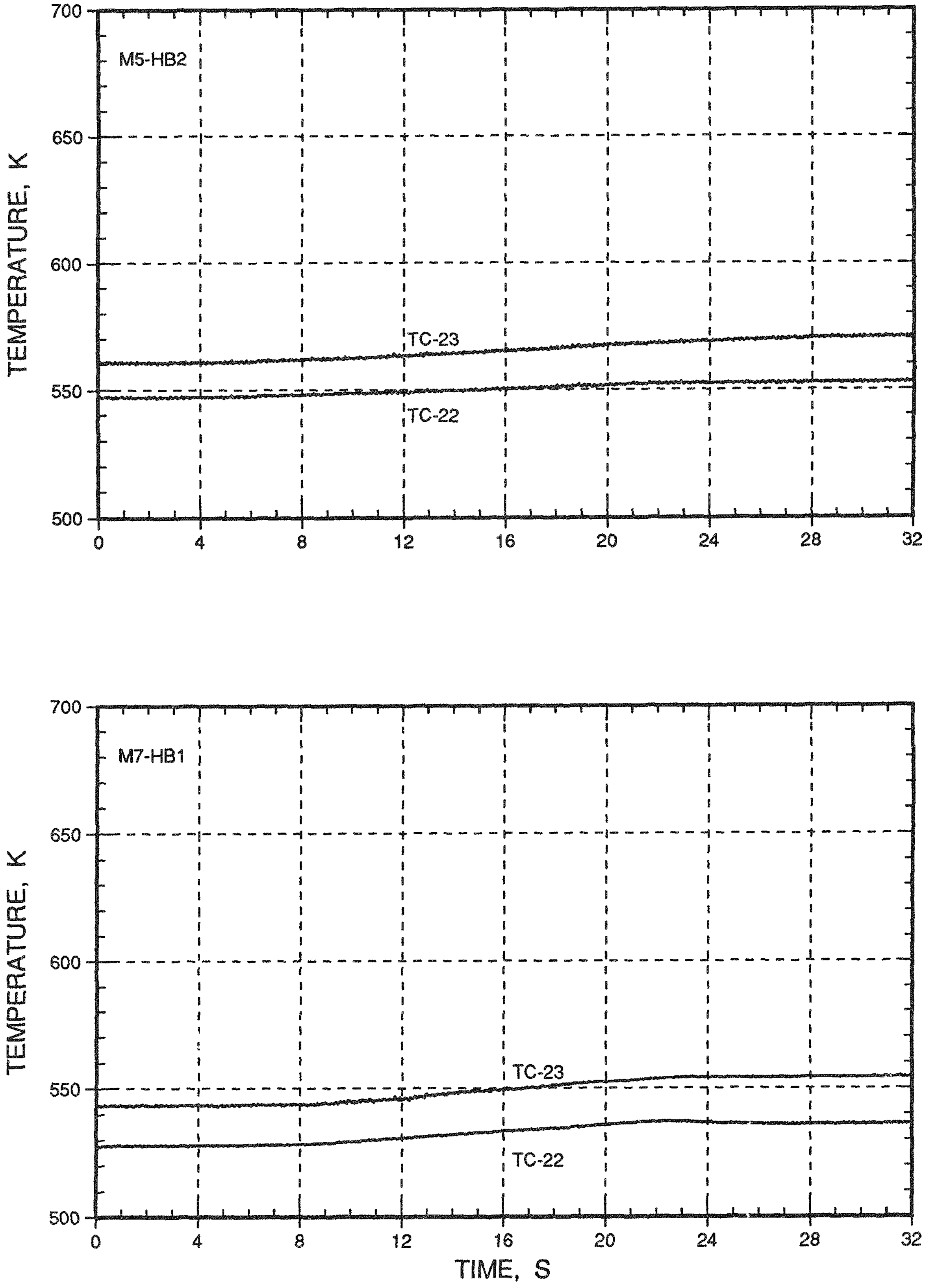

Fig. E.32. Temperatures in the Gas Plenum

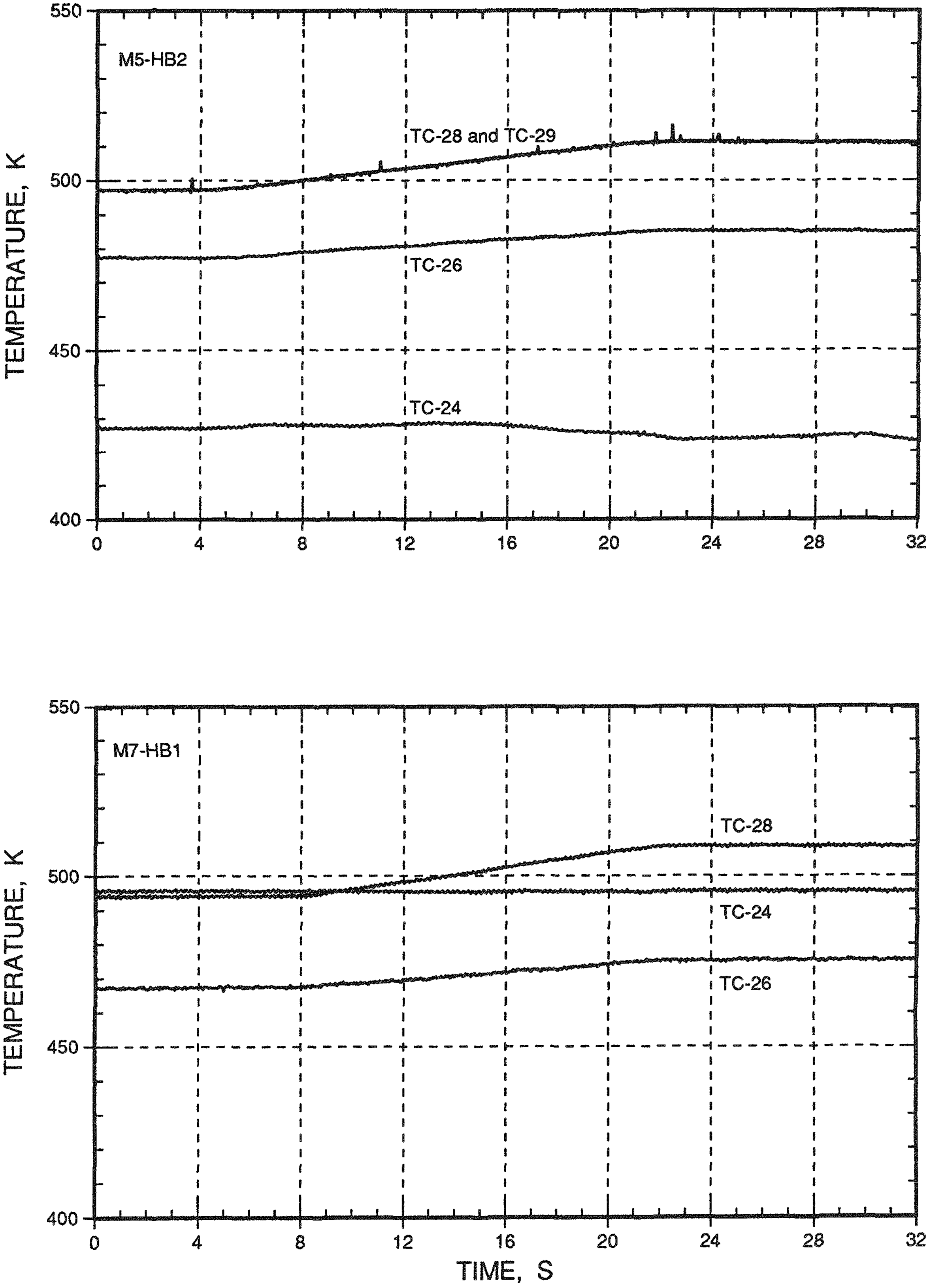

Fig. E.33. Flowmeter Magnet Temperatures

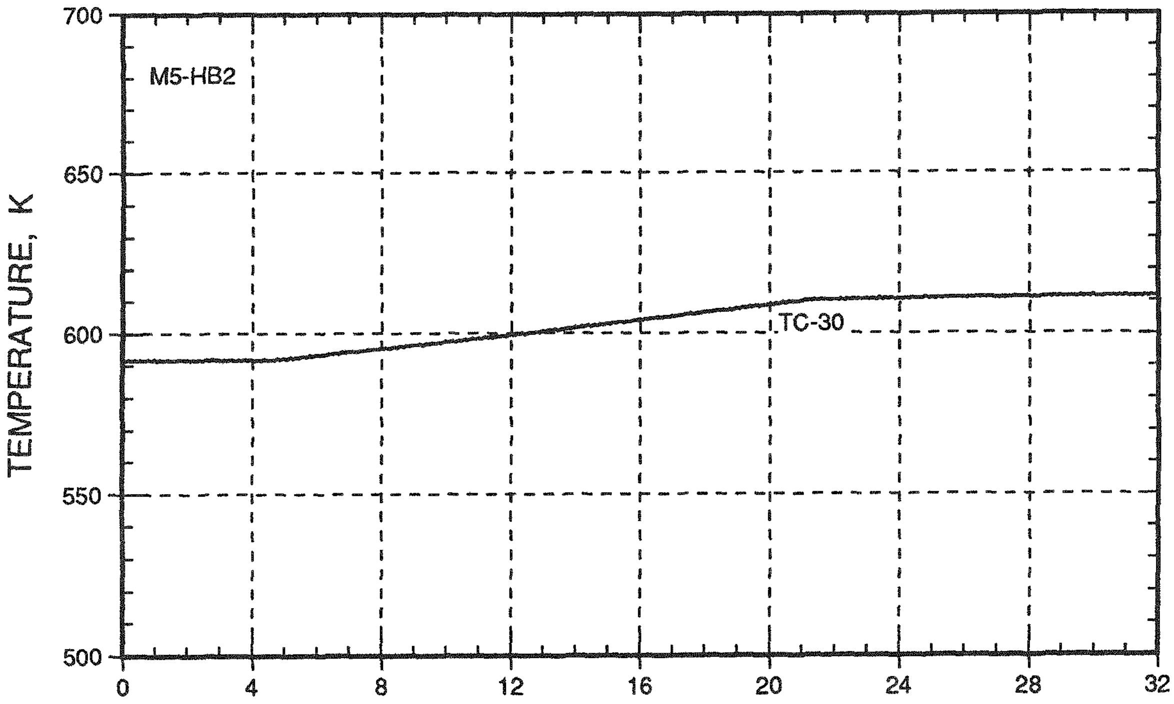

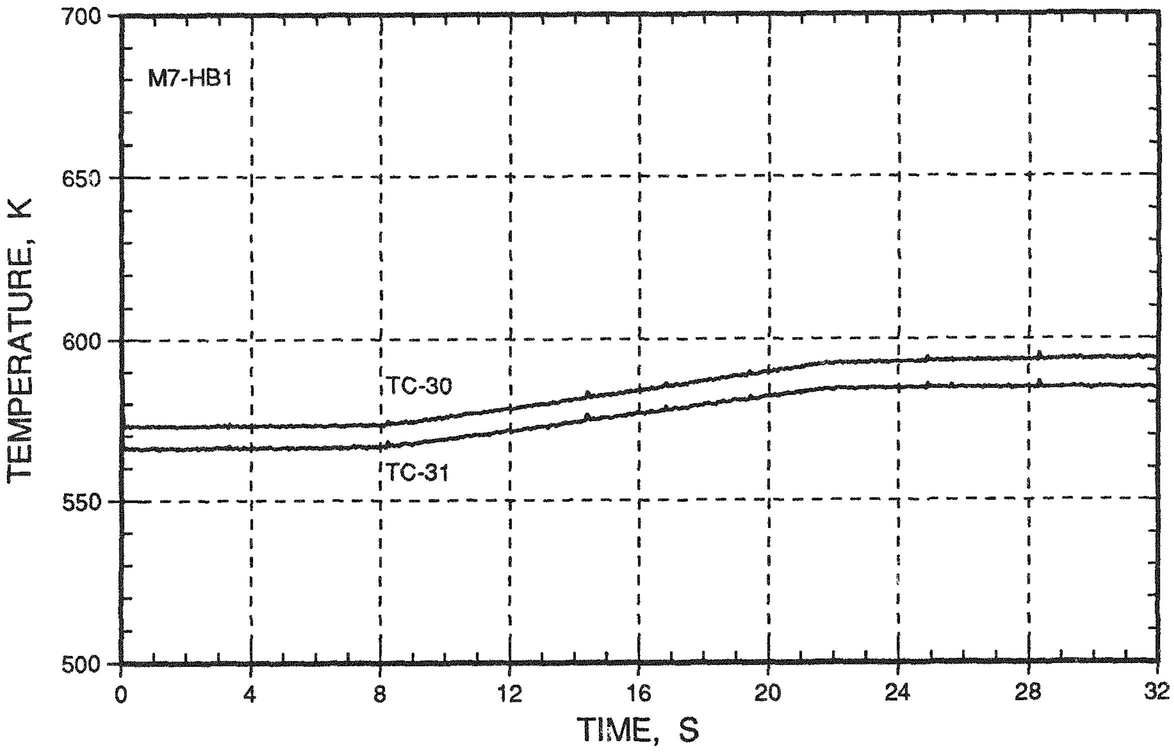

Fig. E.34. Temperatures of the Wall of the Loop Test Section

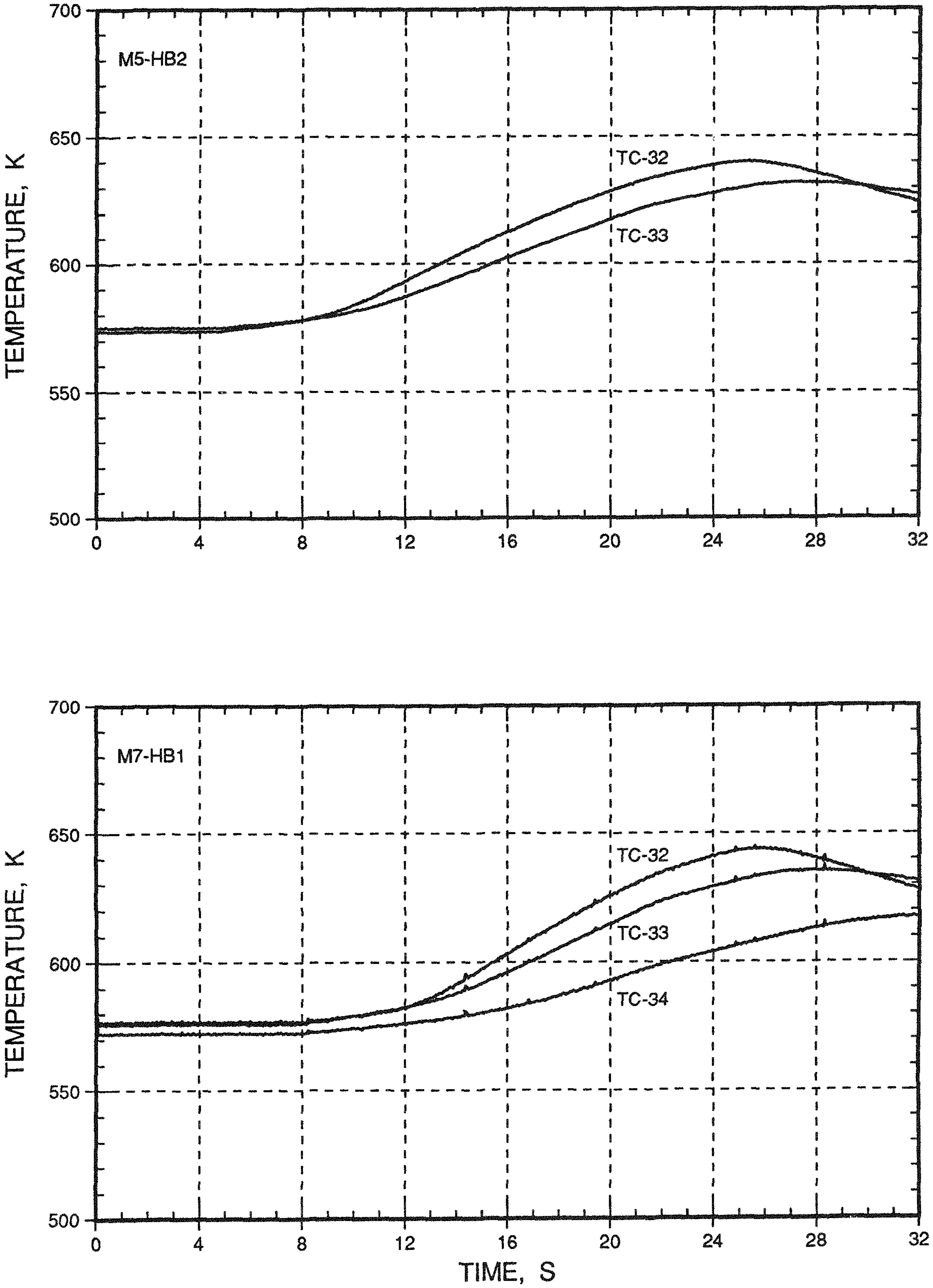

Fig. E.35. Temperatures of the Wall of the Loop Pump Leg

APPENDIX F

Details of the Final Overpower Transients

F.1 Overpower Transient Summaries

Table F.1 summarizes performance and test conditions assumed in analysis of the four overpower transients: M5-F1, M5-F2, M6-F, and M7-F.

In each M5 transient when the reactor power reached 43 MW the power rose exponentially on an 8 sec period. The power was then allowed to increase until a preset transient termination signal was received at 161 MW. Neither of the fuel pins failed during the M5 transients.

In the M6 transient when the reactor power reached 75 MW the power rose exponentially on an 8 sec period. The two fuel pins were heated under nominally-identical thermal-hydraulic conditions. The power rise was rapidly terminated upon detection of cladding breach which occurred at over four times normal power in both pins. The ternary 5.3 at.% burnup pin failed at 13.240 sec.

In the M7 transient the reactor power reached 75 MW whereupon the reactivity period was changed to an 8 sec period. The ternary 9.8 at.% burnup pin indicated first failure at a power-to-flow ratio of about 4.0. The time of failure was placed at 17.719 sec.

F.2 Graphical Data from the Final Overpower Transients

This section (Figs. F.1 and F.44) contains general graphical data from the four overpower transients: M5-F1, M5-F2, M6-F, and M7-F.

Unusual responses of the individual fuel pin flowmeters were noted in M5. The response of FM-5 (flowtube 1 with the 0.8 at.% pin) was nearly flat. The response of FM-4 (on flowtube 2 with the 1.9 at.% pin) showed a large bell-shaped curve (Fig. F.16) which peaked at a "flowrate" of about 180 cc/s at 18 sec in M5-F1 and about 350 cc/s at 17.6 s in M5-F2. The reason for this

Table F.1. Final Overpower Transient Test Conditions Summary and Analysis Assumptions

	M5-F1	M5-F2	M6-Final	M7-Final
TREAT transient number	2712	2714	2734	2775
Date of performance	8/8/86	8/15/86	2/6/87	10/15/87
Initial total flowrate, cc/s	195	153	193	195
g/s	167	133	167	168
Flowtube 1:				
Fuel pin identification	T-280	T-280	T-186	T-131
Burnup, at.%	0.8	0.8	1.9	9.8
Length of fuel assumed for analysis, mm	343	343	343	343
Preirradiated fuel length, mm	351	351	348	354
Fuel radius, mm	2.54	2.54	2.54	2.54
Axial linear fuel density, gm/cm	2.25	2.25	2.27	2.24
Fuel porosity, %	13.5	13.5	27.0	19.0
Sodium logging, % of porosity	0.0	0.0	30.0	42.0
Trapped fission gas, moles/cc (x10-E4)	0.14(a)	0.14(a)	0.50(a)	2.16
Pin plenum gas volume, ml	3.5	3.5	3.5	3.5
Pin plenum pressure, psia	39	39	94	705
at Temperature, K	293	293	293	298
Power coupling factor, W/g/MW	4.95	4.95	4.96	3.97
Peak TREAT power, MW (+)	160	159	206	220
Peak Axial Linear Power, (kW/m)				
Peak power-to-flow ratio				
(relative to 150 K coolant temperature rise)	3.4	4.4	>4	
Thermocouples	8-14	8-14	8-14	9-15
Flowmeter identification	FM-5	FM-5	FM-5	FM-4
Flowtube Orifice Size, cm	none	none	none	0.432
Hodoscope column(s)	4	4	4	4
Flowtube 2:				
Fuel pin identification	T-154	T-154	T-102	T-427
Burnup, at.%	1.9	1.9	5.3	2.9
Length of fuel, mm	343	343	343	343
Preirradiated fuel length, mm	348	348	348	373
Fuel radius, mm	2.54	2.54	2.54	2.54
Axial linear fuel density, gm/cm	2.28	2.28	2.23	2.30
Fuel porosity, %	27.0(a)	27.0(a)	23.0	31.0(a)
Sodium logging, % of porosity	30.0	30.0	35.0	42.0
Trapped fission gas, moles/cc (x10-E4)	0.51	0.51	1.38	1.03
Pin plenum gas volume, ml	3.5	3.5	3.5	3.5
Pin plenum pressure, psia	94	94	332	205
at Temperature, K	273	273	298	309
Power coupling factor, W/g/MW (+)	4.91	4.91	4.94	5.31
Peak TREAT power, MW	160	159	206	217
Axial Peak Linear Power, (kW/m)				
Peak power-to-flow ratio				
(relative to 150 K coolant temperature rise)	3.3	4.2	>4	
Thermocouples	1-7,15	1-7,15	1-7,15	1-8
Flowmeter identification	FM-4	FM-4	FM-4	FM-5
Flowtube Orifice Size, cm	none	none	none	none
Hodoscope column(s)	6,7	6,7	6,7	6,7
Flowsplit, %				
Flowtube 1	50	50	50	47
Flowtube 2	50	50	50	53

Table F.1. Final Overpower Transient Test Conditions Summary and Analysis Assumptions (Cont'd)

			6-Final	M7-Final
Initial temperature, K	573	578	583	586
Initial Total Loop Plenum Pressure, psia	60	60	60	66
Initial pressure drop, MPA	0.20	0.10	0.48	0.16
Initial ALIP current, A	22.6	14.8	20.2	19.4
Flattop power, MW (+)	43	43	70	70
Flattop duration, s	0	0	0	0
Overpower period, s	8	8	8	8
TREAT energy at peak power, MJ (+)	880	889	1033	1159
Transient rod sequence	T2,T1	T2,T1	T2,T1	T2,T1
Initial shutdown rods	T1&T2	T1&T2	T1 only	T1 only
Transient correction factor (from trial transients)	0.89	0.89	0.90	0.97
Duration of shutdown low-power shelf, s	15	15	15	15
Total TREAT energy	955	955	1180	1300
Peak-to-average axial pin power	1.09	1.09	1.09	1.09
Radial edge-to-center pin power ratio	3.8	3.8	3.8	3.8

(+) Including "rod shadowing" effects.
(a) Uniform fuel density assumed.

effect is unknown at this time. Peak power occurred at about 15.4 sec in M5-F1 and about 16.1 sec in M5-F2.

During M7 the pressure transducer (PT) signal to the analog tape recorder saturated; consequently the 0.1 ms data from the analog tape recorder is omitted. The PT data have been corrected to eliminate the zero offset that was measured at zero sodium flowrate shortly before the test was performed. The corrected mV data were then multiplied by the transducer manufacturer's calibration factor, and the product was added to the initial loop-setpoint pressure indicated in Table F.1.

F.3 Events at Transient Termination

Events taking place at transient termination and/or pin failure are highlighted in Figs. F.45 to F.49.

Temperature responses from the thermocouples along flowtube 1 showed oscillating temperatures in M5 and M6, whereas the thermocouples along flowtube 2 showed little if any oscillations (Figs. F.45 and F.46).

In all four transients, quenching the fuel at incipient failure or immediately after failure was important to preserve, for posttest examination, the state of the fuel at that instant. Such quenching was effective upon reactor scram due to the high thermal conductivity of the metal fuel. Preservation of the conditions at failure was also greatly aided by the fact that the breaches that occurred were very localized and relatively little additional cladding damage occurred while most of the fuel inventory was being expelled from the cladding.

The output signal from inlet flowmeter FM-1 was input to a shutdown signal generator (SSG) and the output from the SSG was fed into the reactor control rod program which was programmed to initiate reactor shutdown when the SSG tripped. Figure F.47 shows the event sequence at termination of the M6 overpower test. (A similar sequence occurred during M7, but the SSG signal was inadvertently recorded only on the oscillograph). The sequence in M6 proceeded as follows:

1) The decrease in the total loop flowrate was sensed by the inlet flowmeter (FM-1). The loop flowrate decreased from about 1 mv to 0.2 mv (200 cc/s to 40 cc/s) in about 4 ms (13.240 to about 13.244 sec).

2) When the flowrate decreased to 20% of its original value the SSG was activated and tripped after about a 6 ms time delay (the time delay is governed by the time constant of the fast amplifier in the SSG circuit). The reactor control rod program was programmed to initiate reactor shutdown when the SSG tripped.

3) At about 13.24 sec (Fig. F.48) thermocouples along the axial length of the flowtube indicated a sharp rise in temperature. Thermocouples near the top of the fuel column responded first followed by those at lower elevations (in M6, TC-2 and TC-5 have an unexplained systematic offset, but they seem to accurately mark the time of cladding breach). A similar progression of flowtube temperature rise in the flowtube of the failed fuel pin in M7 is shown in Fig. F.49.

4) At about 13.26 sec reactor transient rod pair T-1 (which had been being withdrawn from the reactor to provide the 8 sec reactivity period) indicates its peak withdrawal (about 65 cm) and the start of reentry into the reactor.

5) At about 13.28 sec the reactor power trace indicates peak power (about 205 MW) and the start of power decrease. Termination of the M6 and M7 transients were by means of driving hydraulic rod pair T-1 in at its highest rate of speed. The remaining hydraulic rod and the eight pneumatic rods were inserted 15 sec after the command to insert rod pair T-1.

6) The reactor power decreased a factor of two in about 0.12 sec.

F.4 Comparison of Measured and Calculated Temperature Rises

Figures F.50 to F.66 show comparisons of measured and calculated temperature rises during the four overpower transients. Comparison includes flowtube thermocouples both above and below the top of the active fuel. Measured Z/L refers to actual thermocouple location relative to the top of the fuel column (pretest). Calculated Z/L refers to the calculation from the closest of the 10 axial nodes (used in the COBRA-PI code) that was below the measurement.

Figure F.67 shows alternate calculations of peak melting compared to measurements (see Sect. 5.2). The assumptions indicated on the figures lead to plausible but low values of thermal conductivity and consequently, large amounts of melting. The model used for thermal conductivity is described in Appendix G. The comparison with measurements tend to support the "best estimate" computations presented in Fig. 5.6.

F.5 Tabulated and Graphical Data

Data, and values of calculated functions derived from the data, are shown in tabulated form on microfiche in the pocket on the back cover of this report. The listings consist of 1 ms data averaged over 50 ms intervals from 0 to 25 sec for all but a few sensors. The following 1 ms data itself is also included: for M6-F; flowrate, pressure transducer, and the shutdown signal generator data over the time range 13 to 13.5 sec and for M7-F; the flowrate and pressure transducer data over the time range 17.5 to 18 sec. For M6-F, 0.1 ms digitized data is provided for the pressure transducer during the time range 13 to 13.5 sec. Table E.2 gives the order of the test sensor listings on the microfiche, the sensor designation and its units.

Section A.5 explains why certain test sensors have been omitted. Factors for converting the flowmeter and pressure transducer mv data to units of cc/s and MPa (absolute) may be found in Table A.3 and Section A.4.3, respectively. Data for these instruments have not been corrected for any zero offset in the instrument. A separate microfiche is provided for M5, M6, and M7.

The following graphs show 1-ms data averaged over 50-ms intervals, unless noted otherwise.

---

a) Power corrected to be consistent with the energy; both power and energy adjusted by the rod shadowing factors.

Fig. F.49 Progression of Flowtube Temperature Rise at Time of Fuel Pin Failure (M7 Test)

The following graphs compare measured and calculated temperature rises in each test transient starting from the base of the active fuel column and proceeding upward.

Fig. F.50 Measured and Calculated Flowtube Temperatures Below Top of Active Fuel Column (M5-F1, Z/L = 0.45 to 0.76)

Fig. F.51 Measured and Calculated Flowtube Temperatures Below Top of Active Fuel Column (M5-F1, Z/L = 0.85 to 0.90)

Fig. F.52 Measured and Calculated Flowtube Temperatures Above Top of Active Fuel Column (M5-F1, Z/L = 1.05 to 1.12)

Fig. F.53 Measured and Calculated Flowtube Temperatures Above Top of Active Fuel Column (M5-F1, Z/L = 1.25 to 1.83)

Fig. F.54 Measured and Calculated Flowtube Temperatures Below Top of Active Fuel Column (M5-F2, Z/L = 0.45 to 0.76)

Fig. F.55 Measured and Calculated Flowtube Temperatures Below Top of Active Fuel Column (M5-F2, Z/L = 0.85 to 0.90)

Fig. F.56 Measured and Calculated Flowtube Temperatures Above Top of Active Fuel Column (M5-F2, Z/L = 1.05 to 1.12)

Fig. F.57 Measured and Calculated Flowtube Temperatures Above Top of Active Fuel Column (M5-F2, Z/L = 1.25 to 1.83)

Fig. F.58 Measured and Calculated Flowtube Temperatures Below Top of Active Fuel Column (M6, Z/L = 0.45 to 0.76)

Fig. F.59 Measured and Calculated Flowtube Temperatures Below Top of Active Fuel Column (M6, Z/L = 0.85 to 0.90)

Fig. F.60 Measured and Calculated Flowtube Temperatures Above Top of Active Fuel Column (M6, Z/L = 1.05 to 1.12)

Fig. F.61 Measured and Calculated Flowtube Temperatures Above Top of Active Fuel Column (M6, Z/L = 1.25 to 1.83)

Fig. F.62 Measured and Calculated Flowtube Temperatures Below Top of Active Fuel Column (M7, Z/L = 0.24 to 0.46)

Fig. F.63 Measured and Calculated Flowtube Temperatures Below Top of Active Fuel Column (M7, Z/L = 0.75 to 0.99)

Fig. F.64 Measured and Calculated Flowtube Temperatures Above Top of Active Fuel Column (M7, Z/L = 1.03 to 1.10)

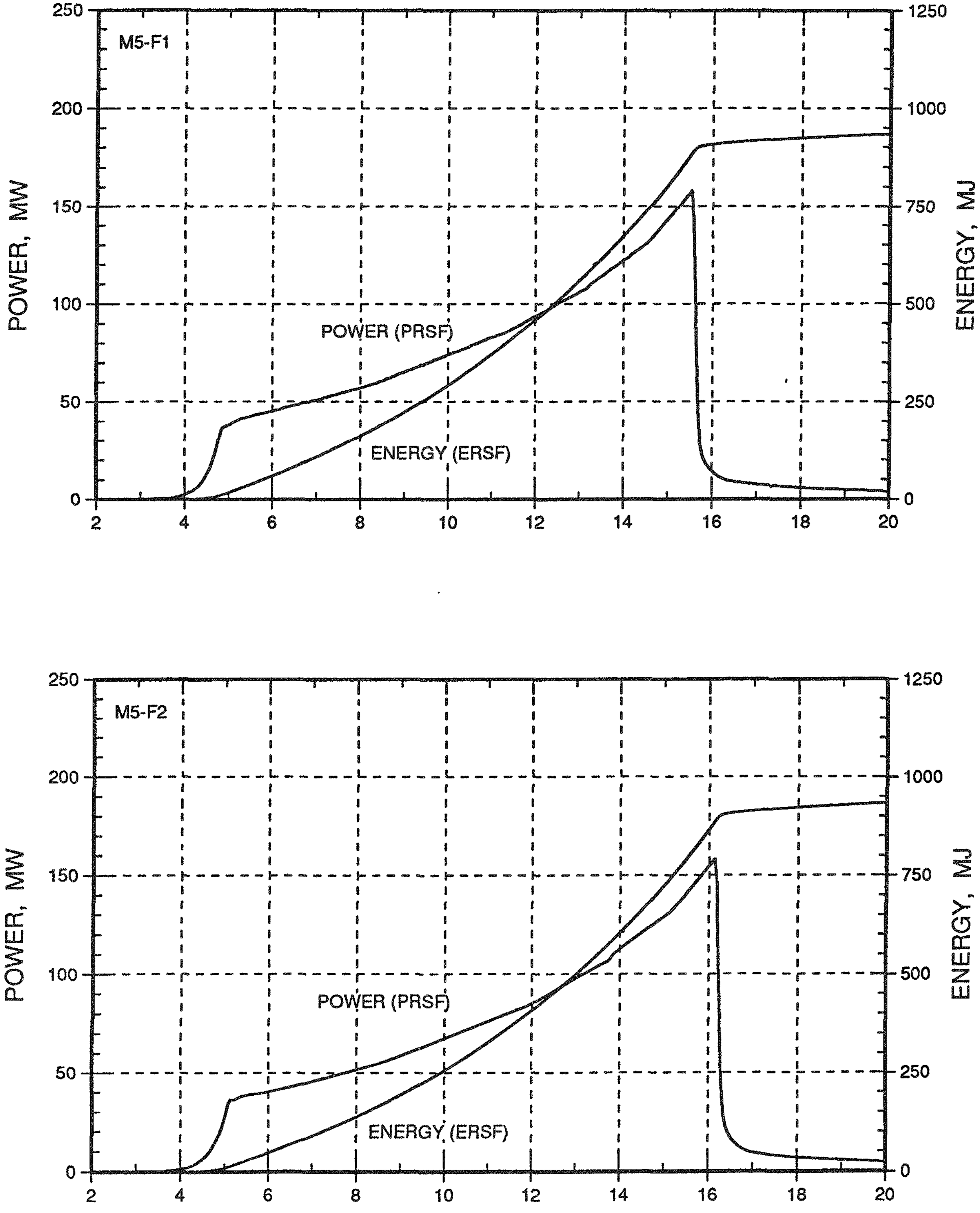

Fig. F.1. Corrected TREAT Power and Energy, Including RSF Variation

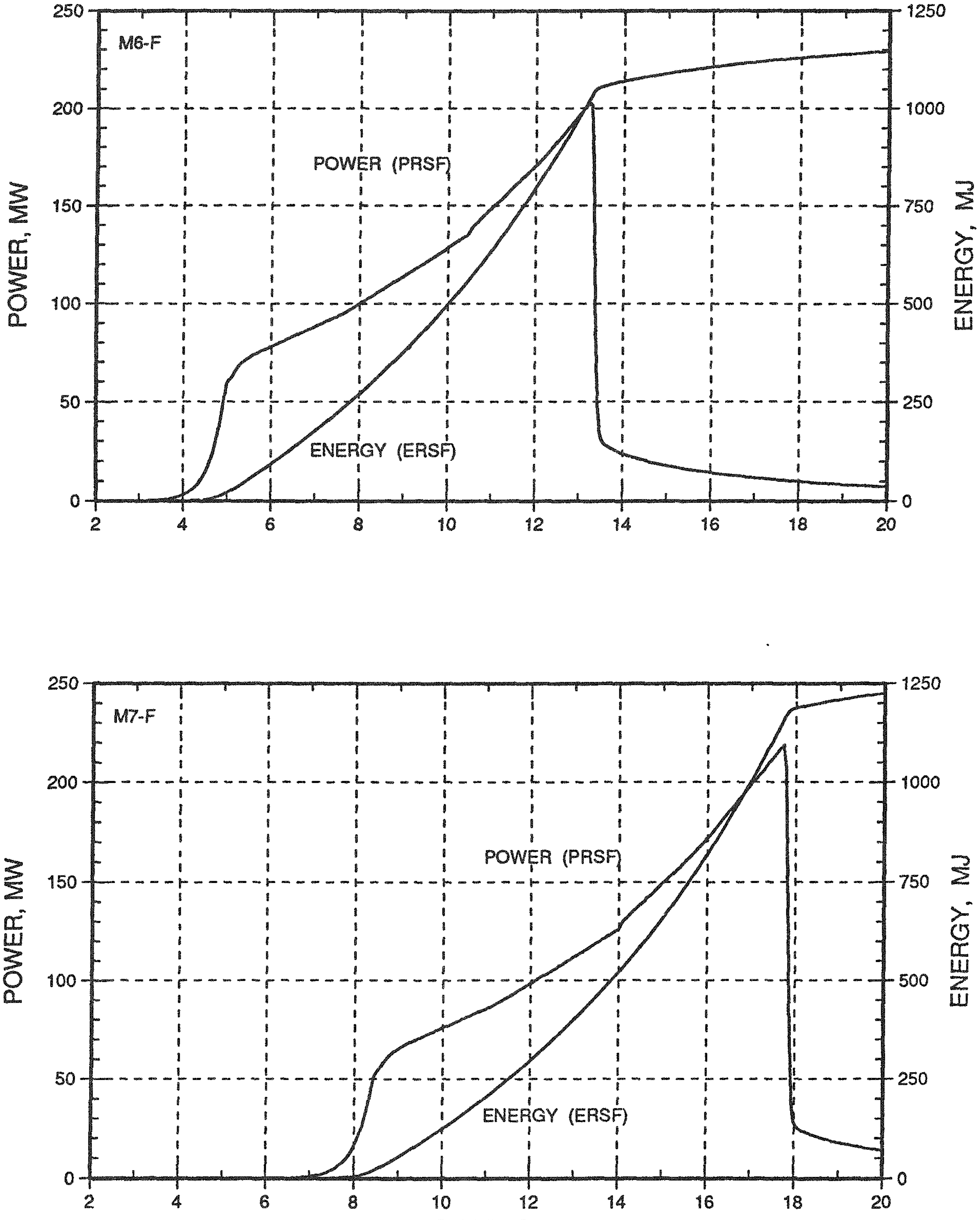

Fig. F.2. Corrected TREAT Power and Energy, Including RSF Variation

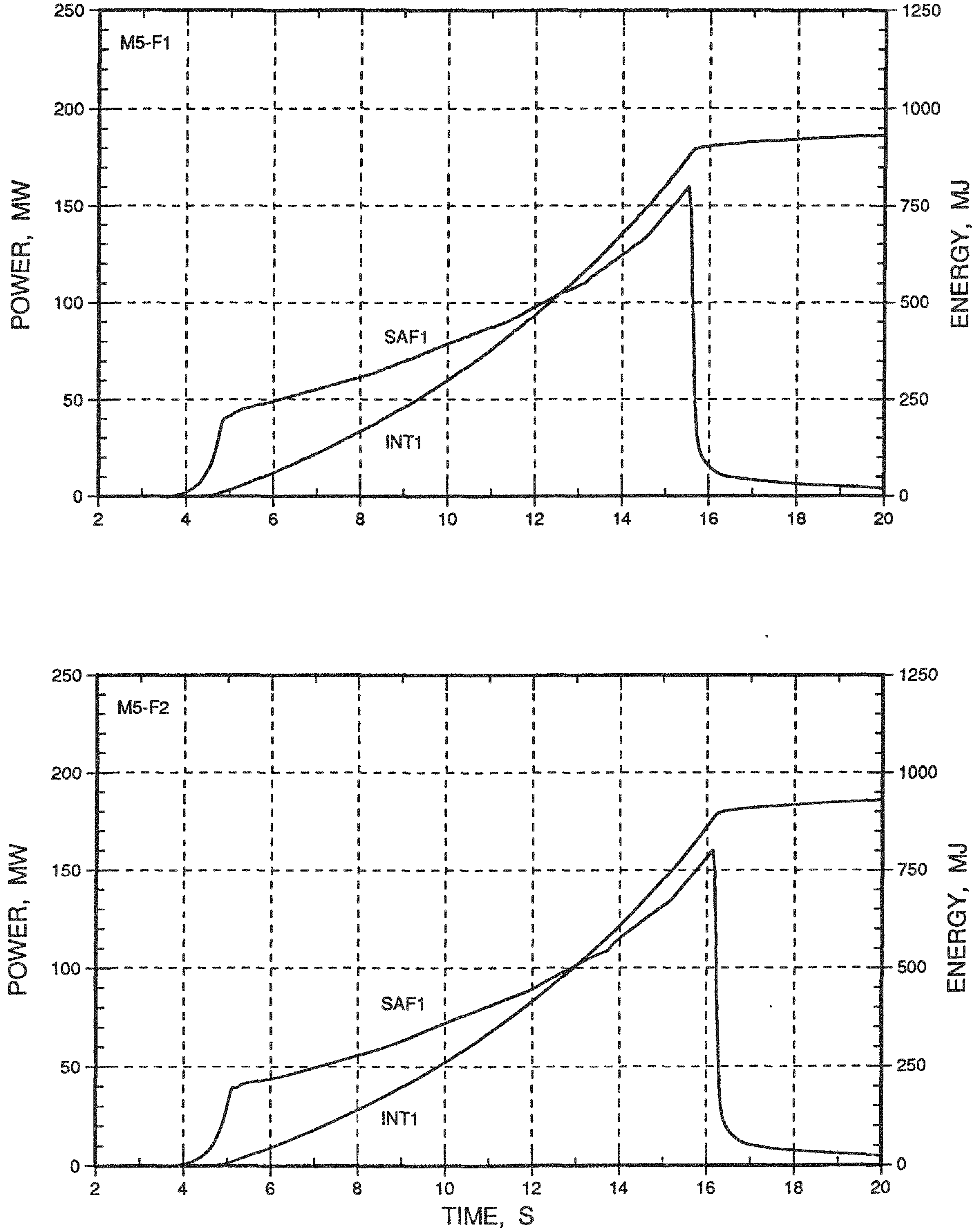

Fig. F.3. TREAT Power and Energy from Instruments S1 and I1

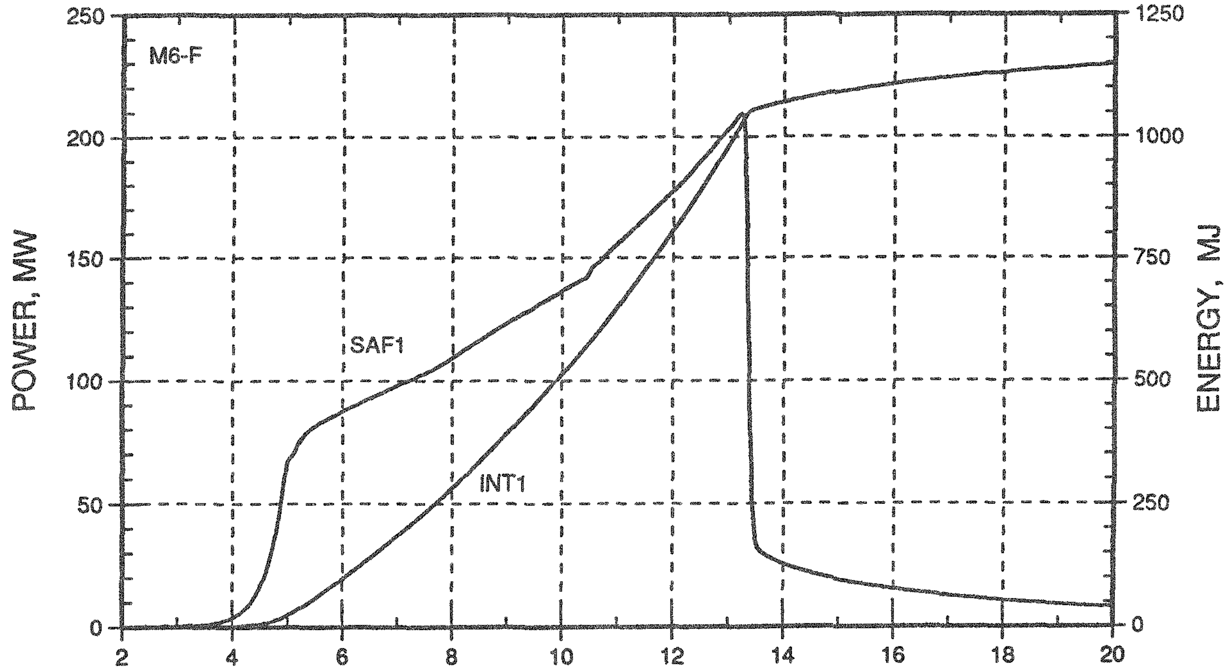

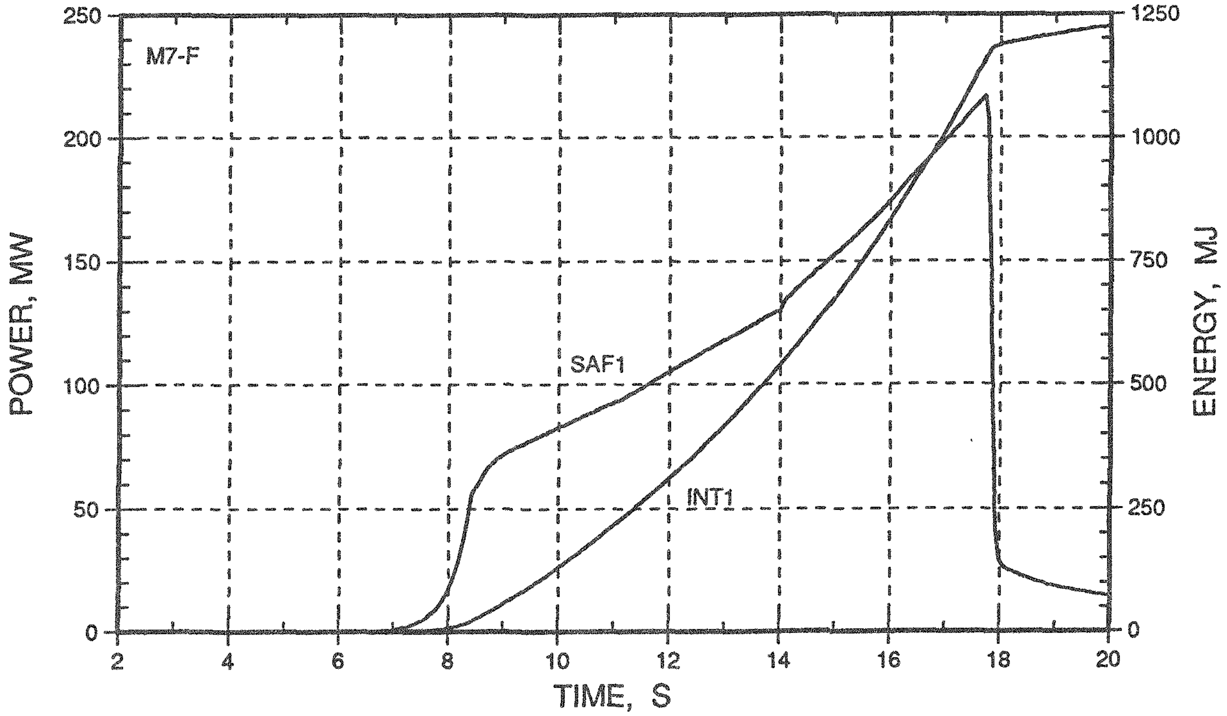

Fig. F.4. TREAT Power and Energy from Instruments S1 and I1

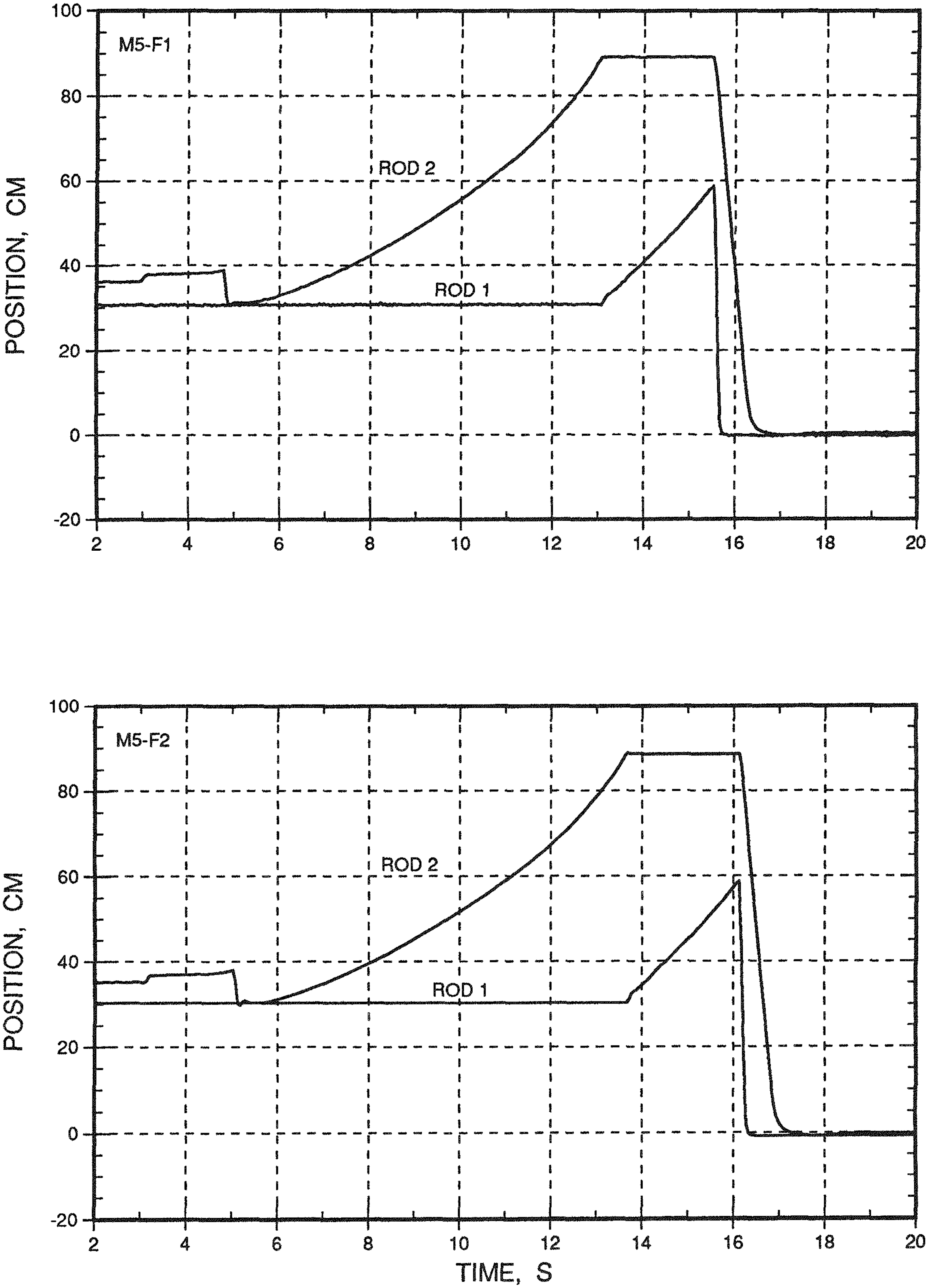

Fig. F.5 Transient-rod Motion

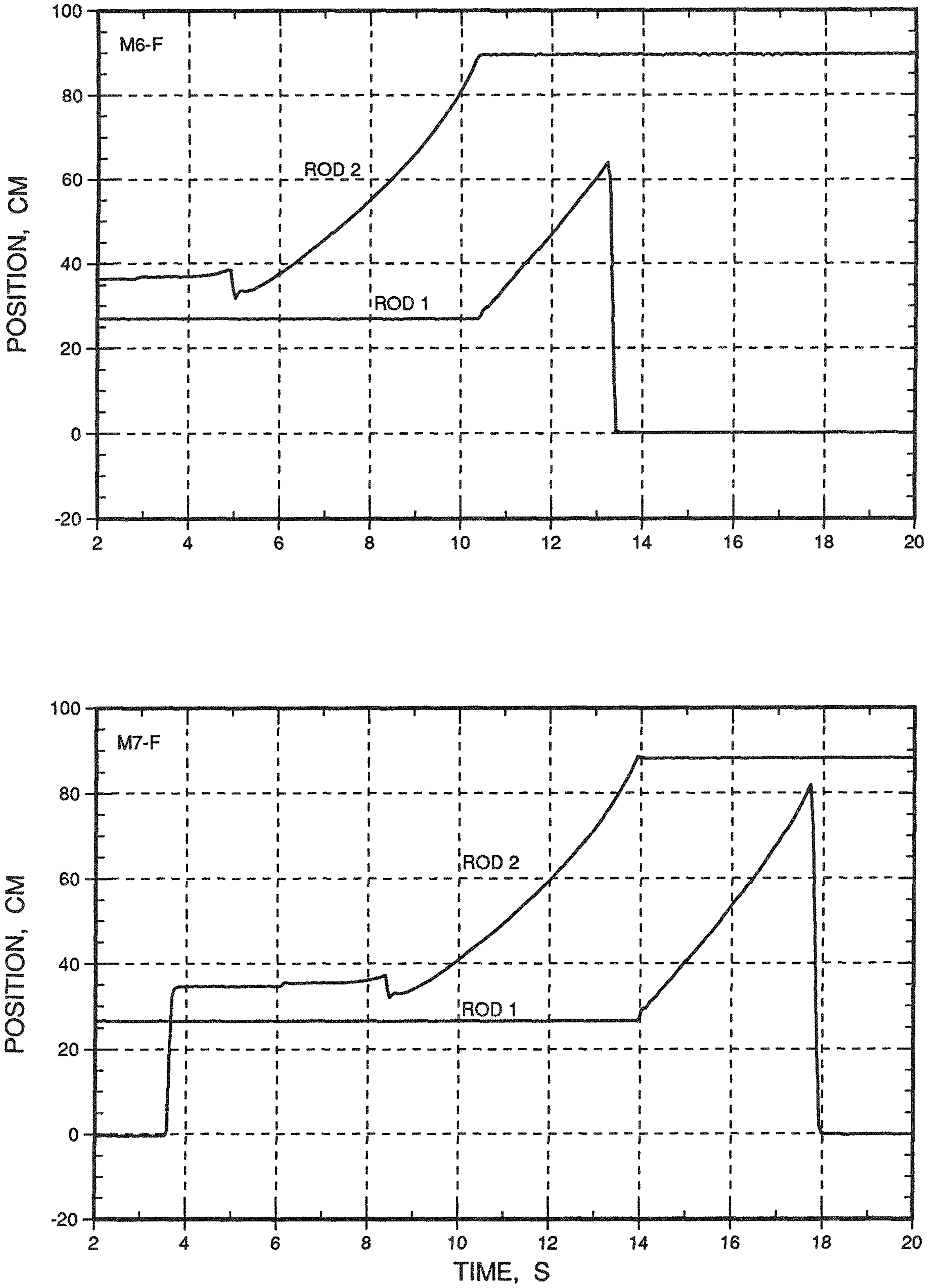

Fig. F.6. Transient-rod Motion

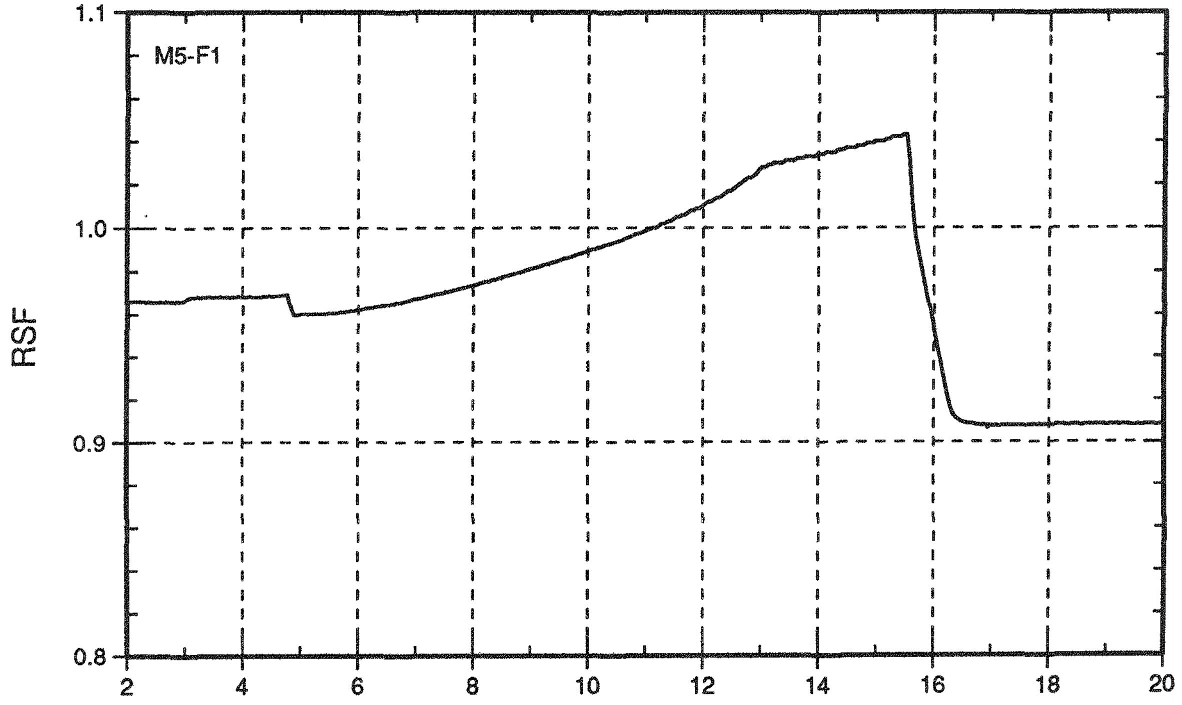

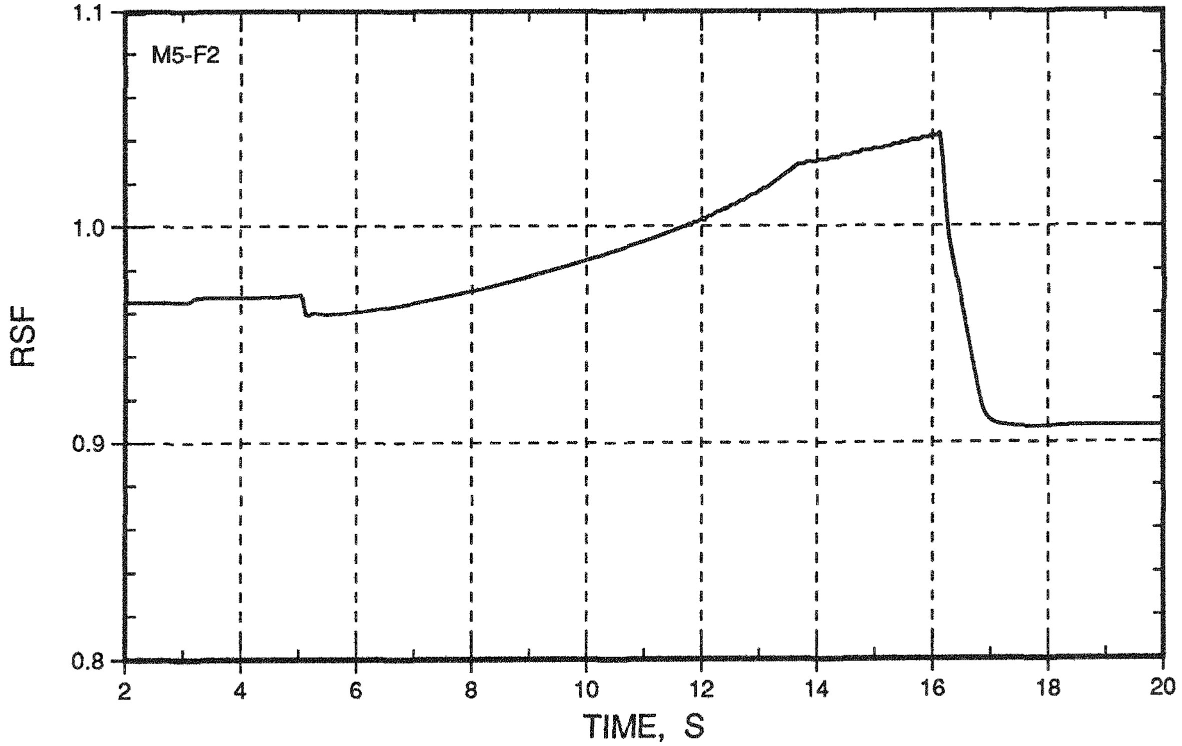

Fig. F.7 Calculated Normalized Rod Shadowing Factor (RSF)

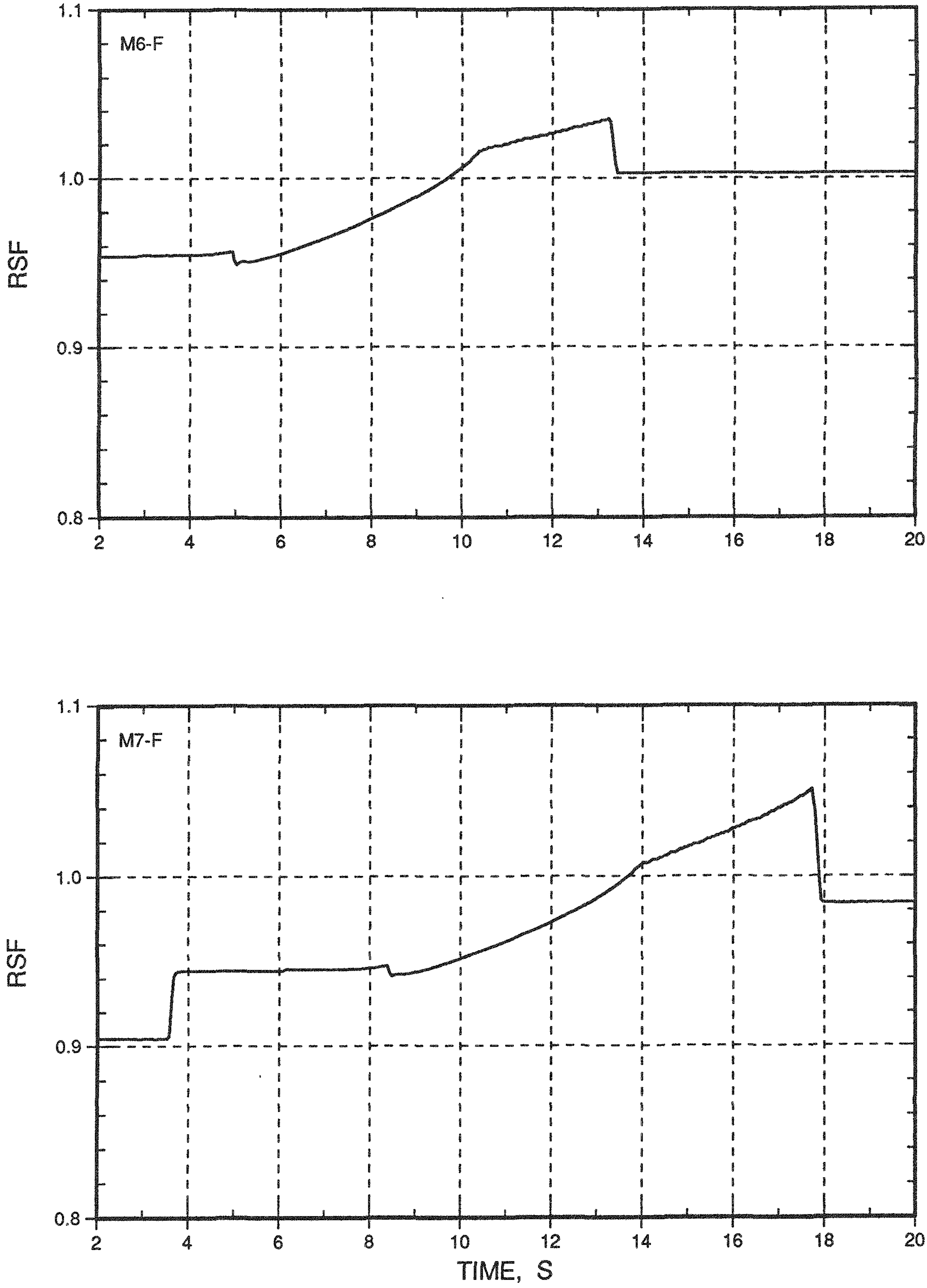

Fig. F.8. Calculated Normalized Rod Shadowing Factor (RSF)

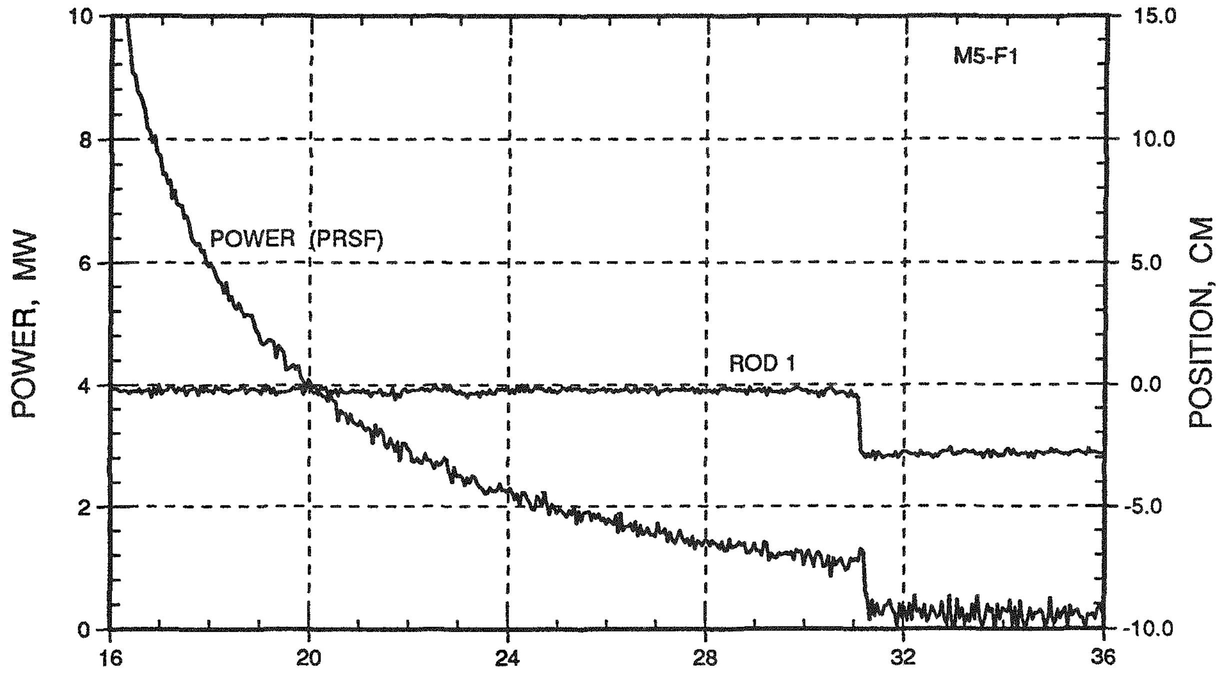

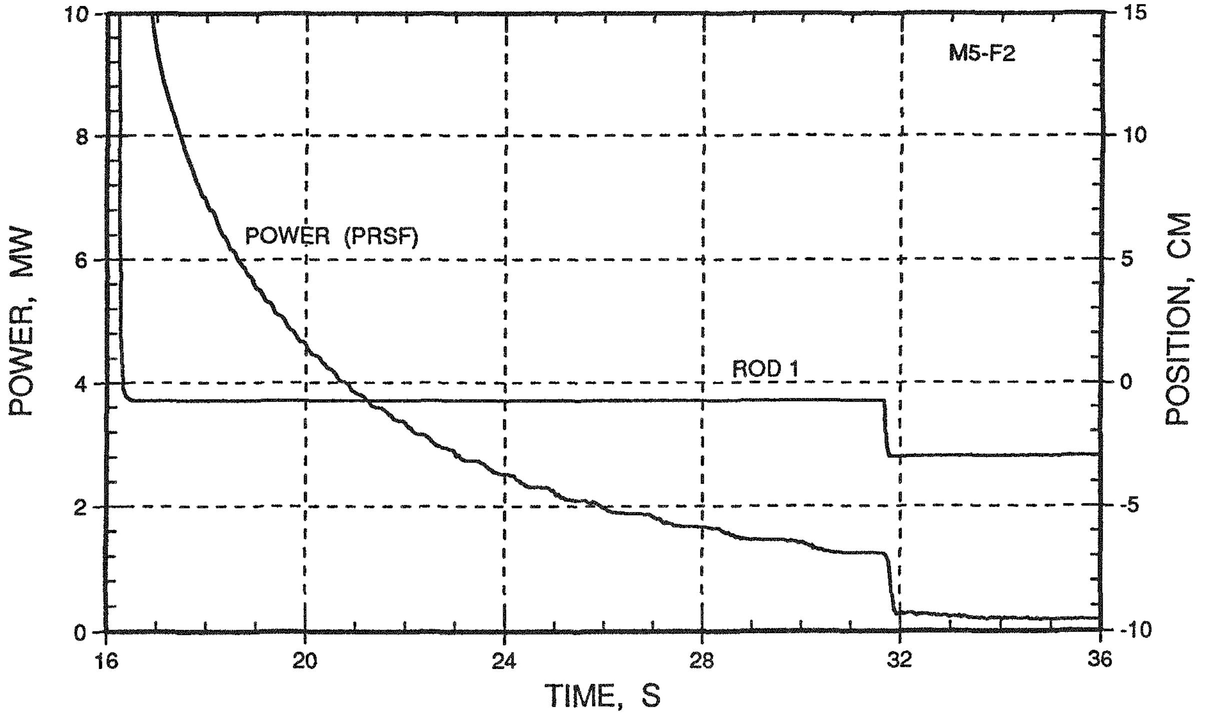

Fig. F.9 Low-power "Shelf" and Transient-rod-1 Motion

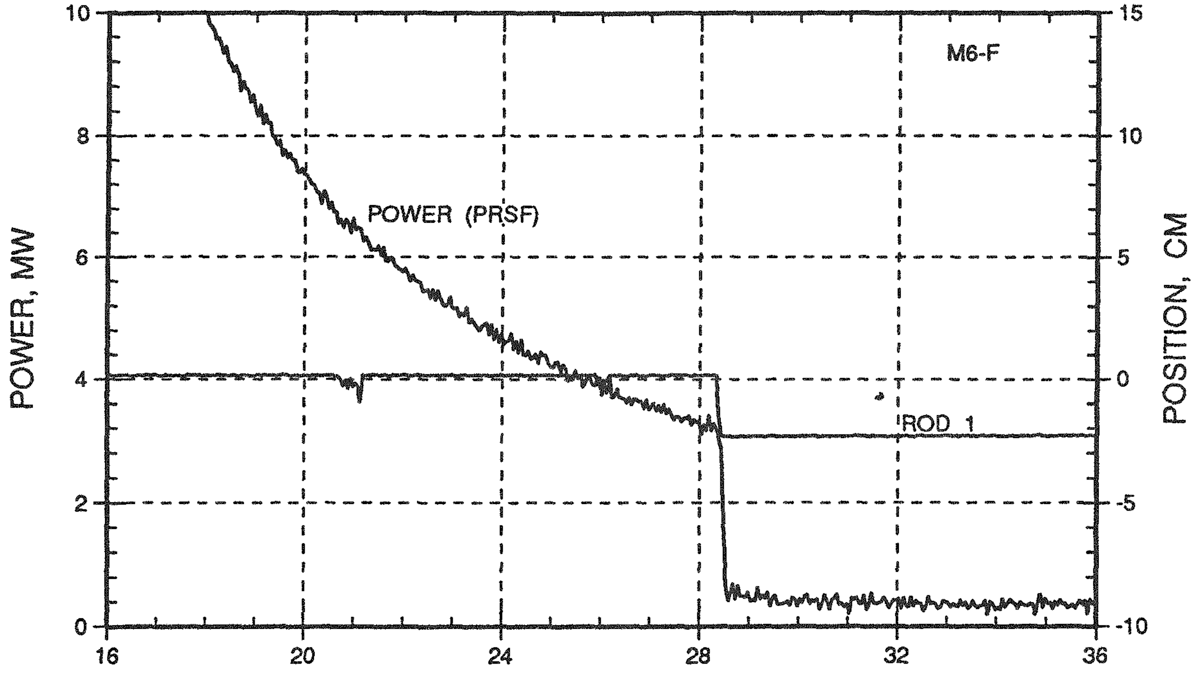

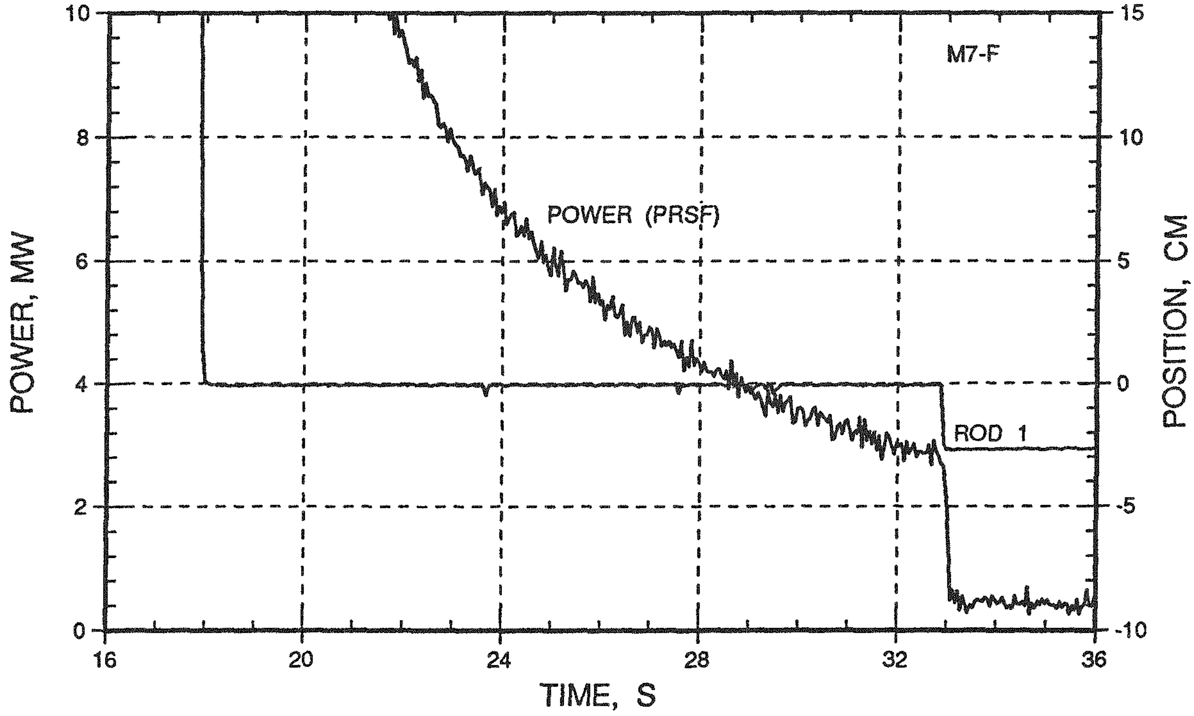

Fig. F.10. Low-power "Shelf" and Transient-rod-1 Motion

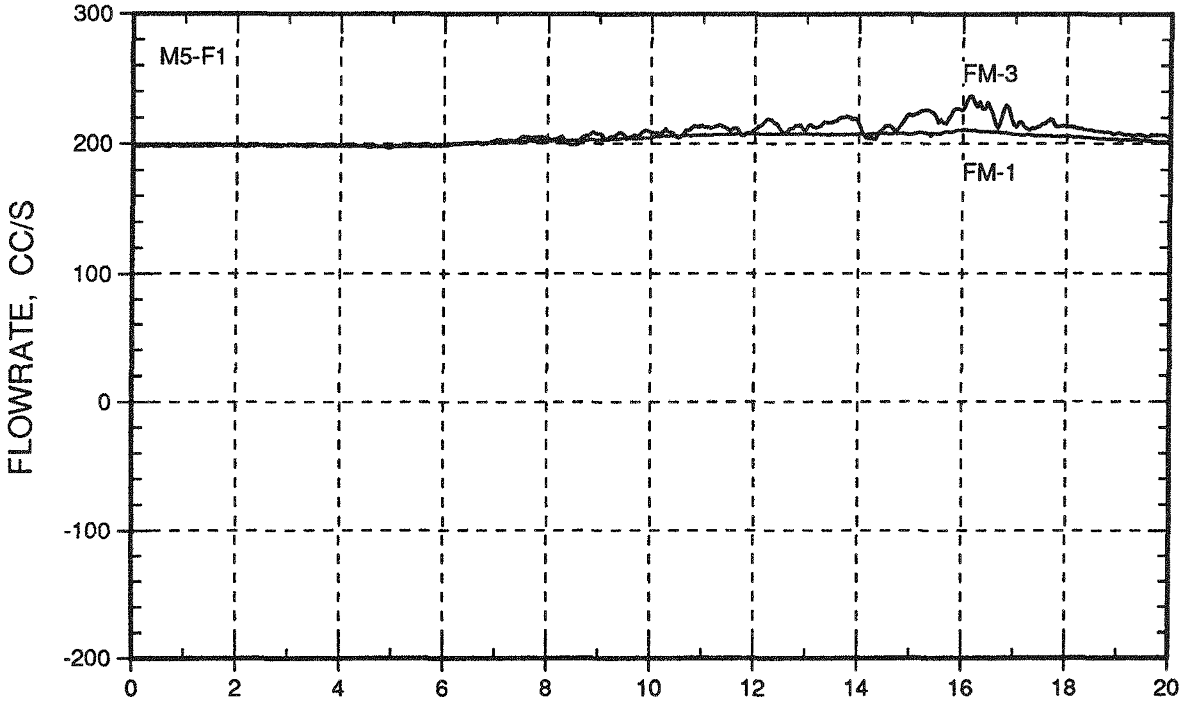

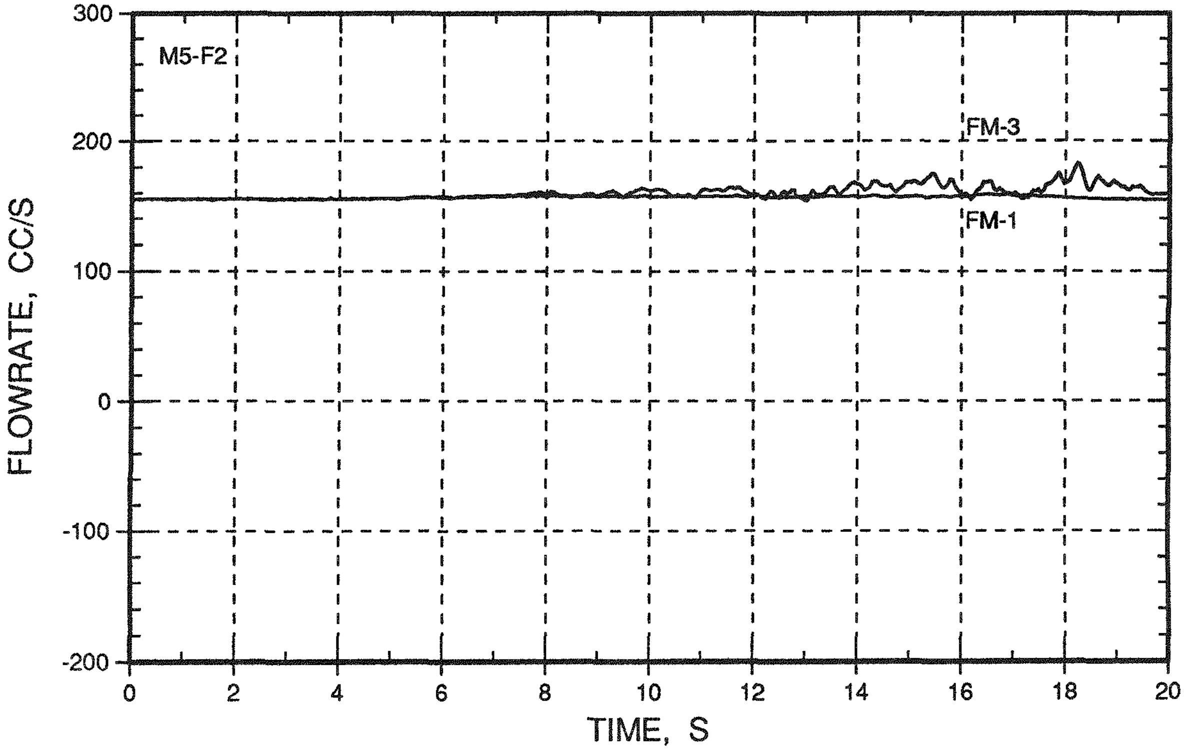

Fig. F.11. Sodium Total Loop Inlet Flowrates

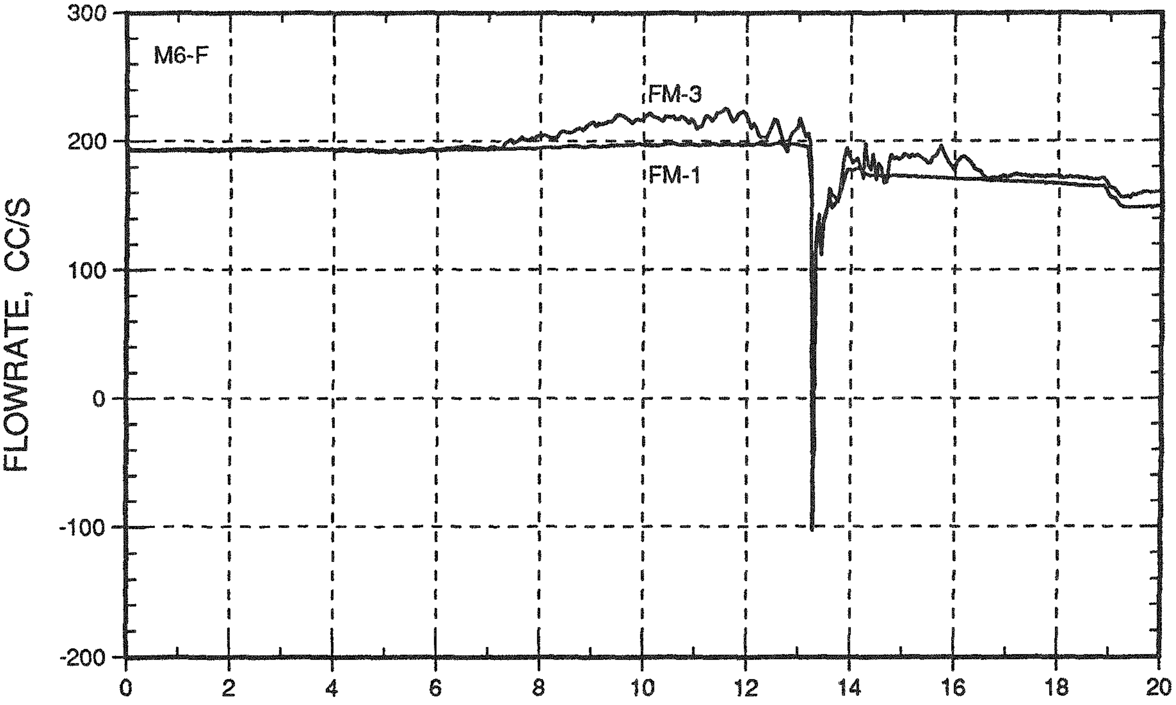

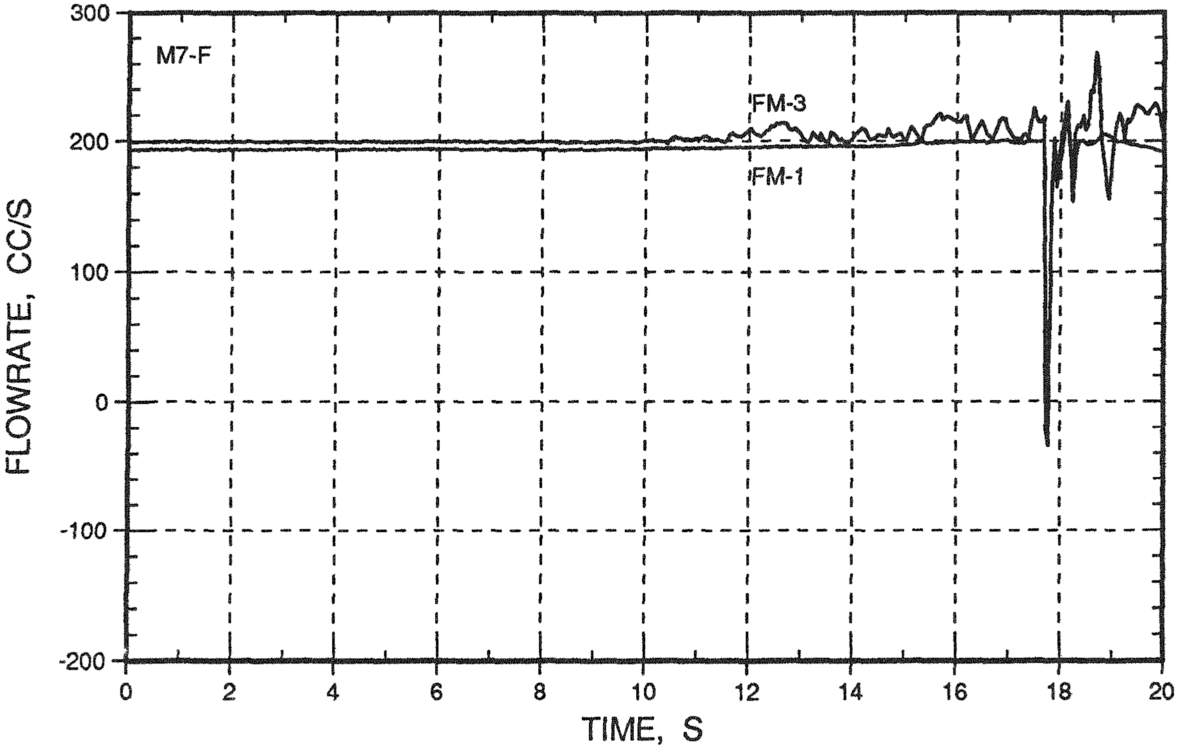

Fig. F.12. Sodium Total Loop Inlet Flowrates

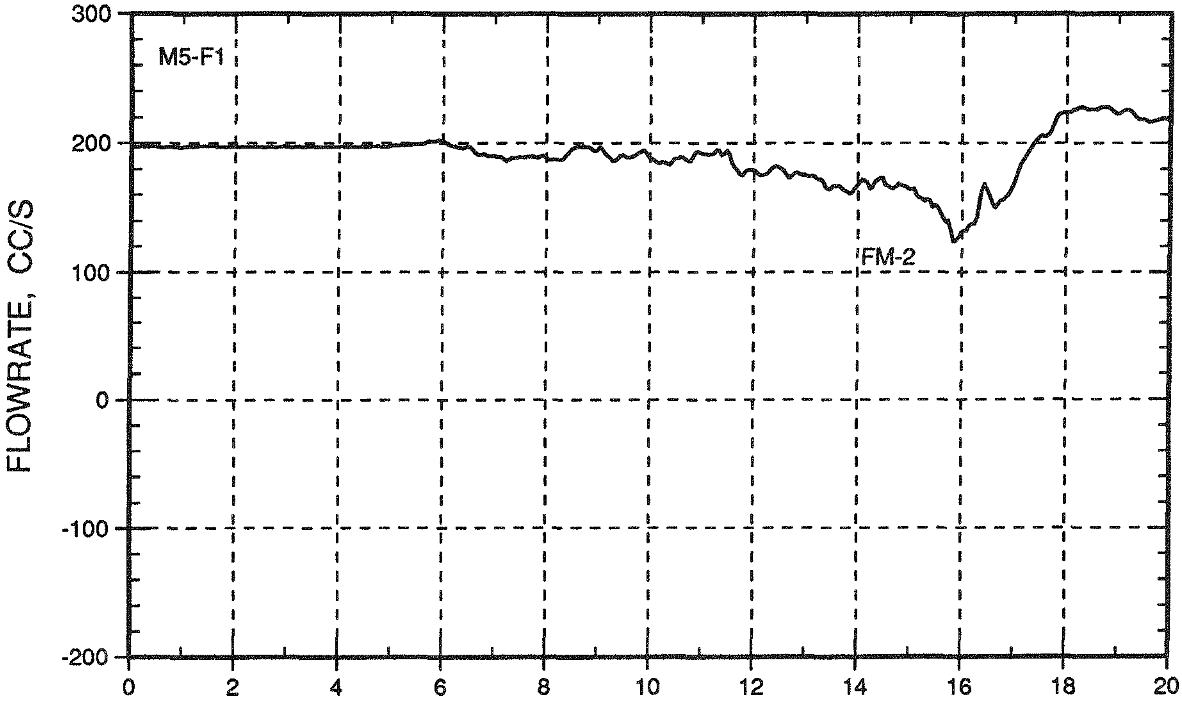

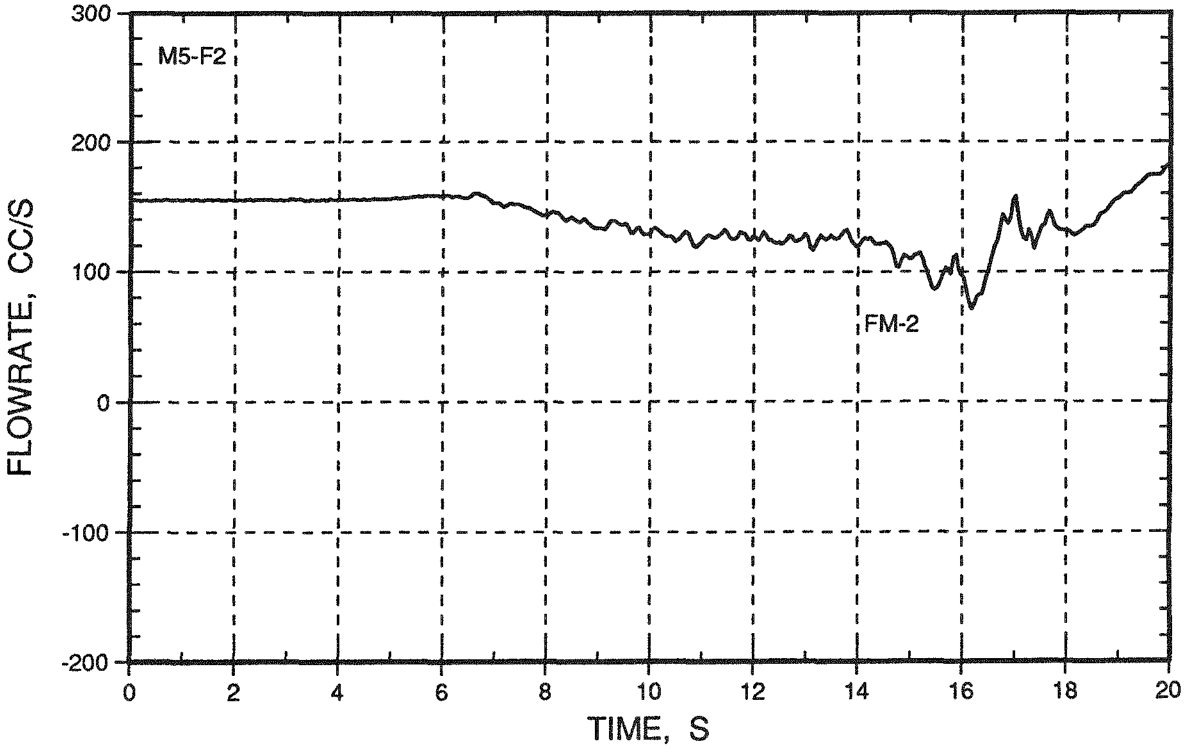

Fig. F.13. Sodium Total Loop Outlet Flowrate

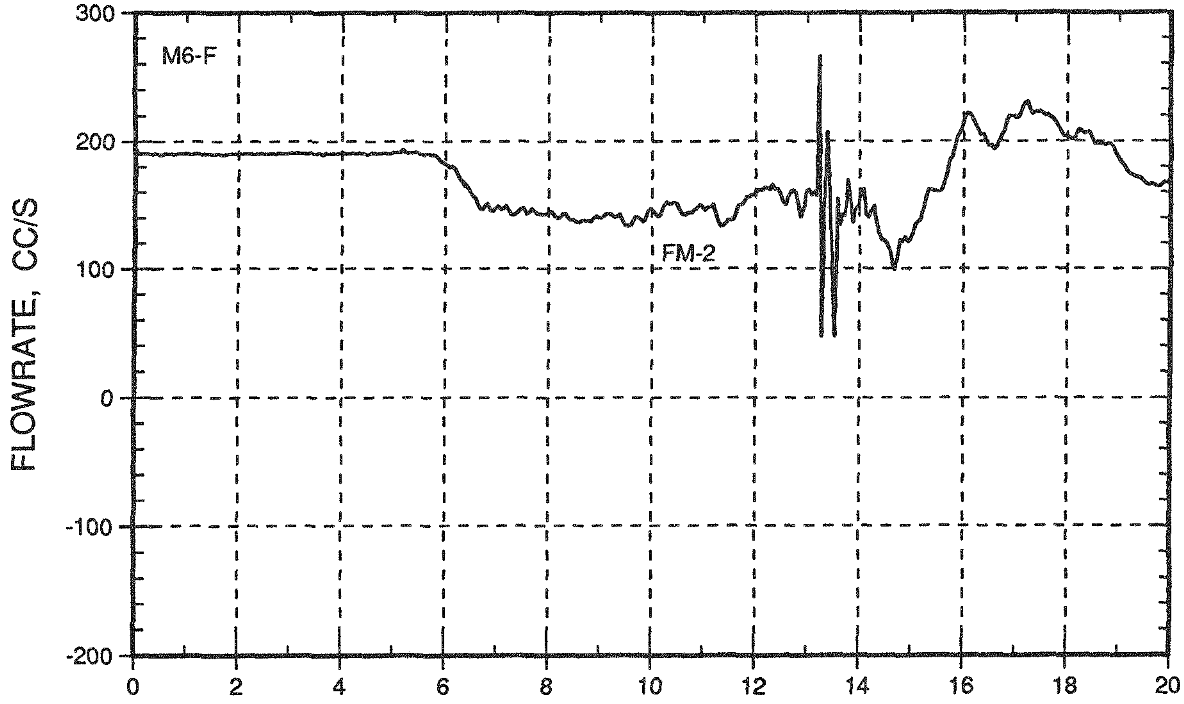

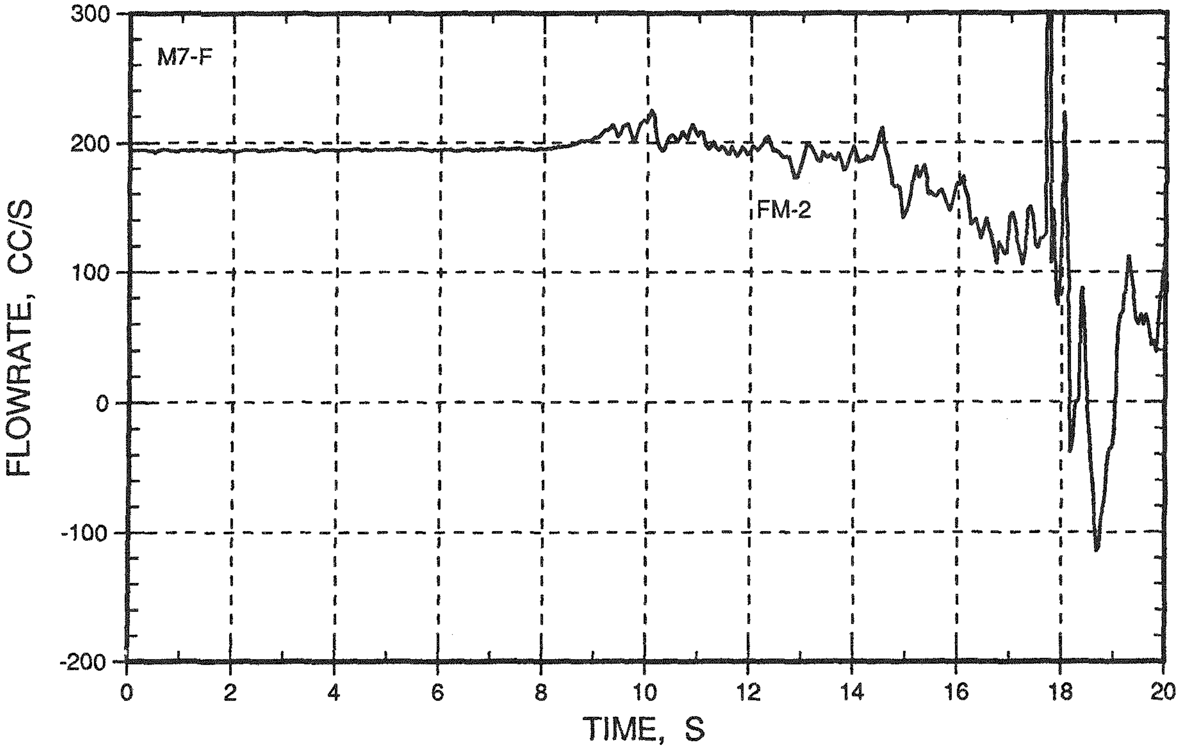

Fig. F.14. Sodium Total Loop Outlet Flowrate

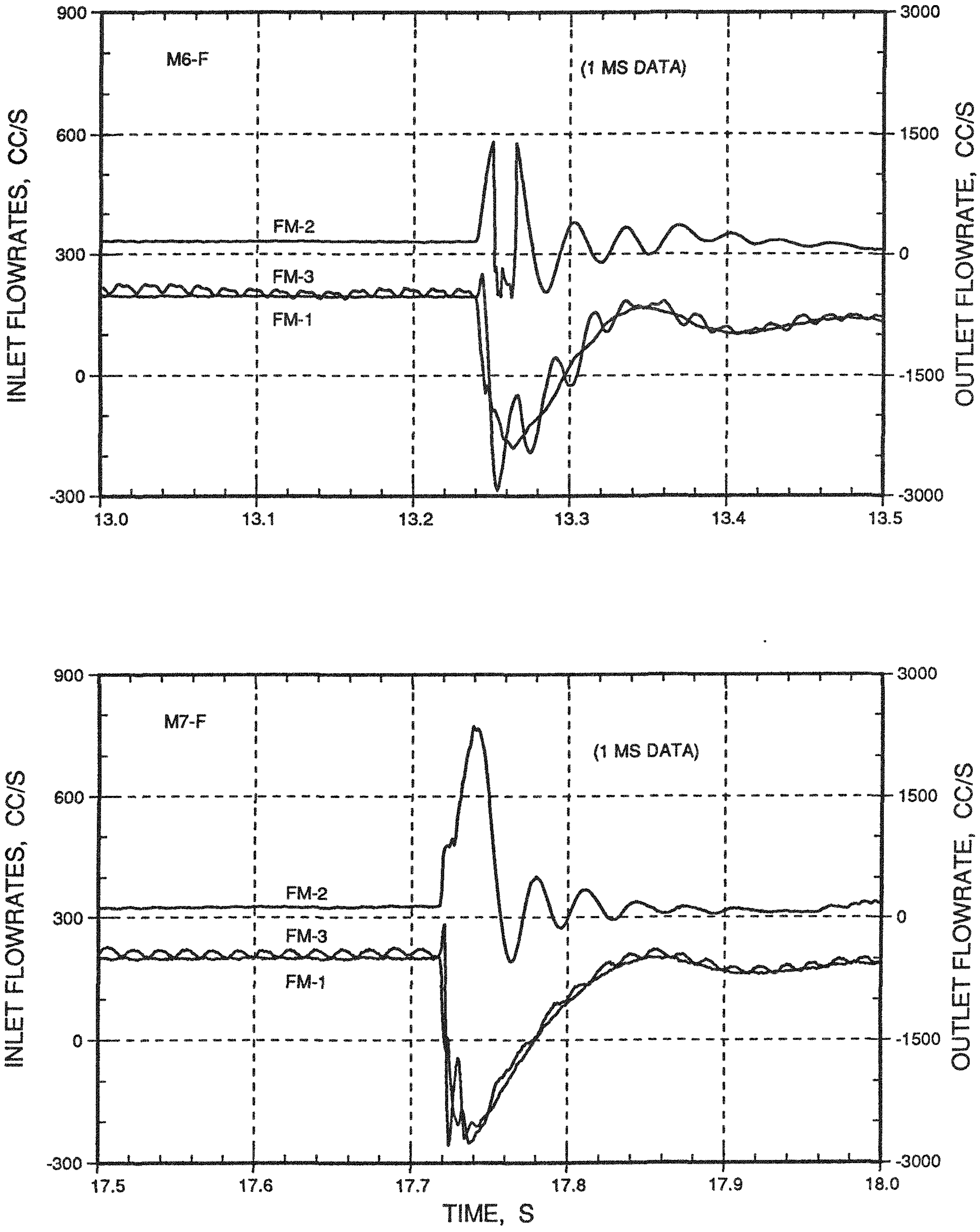

Fig. F.15. Sodium Total Loop Flowrate Details

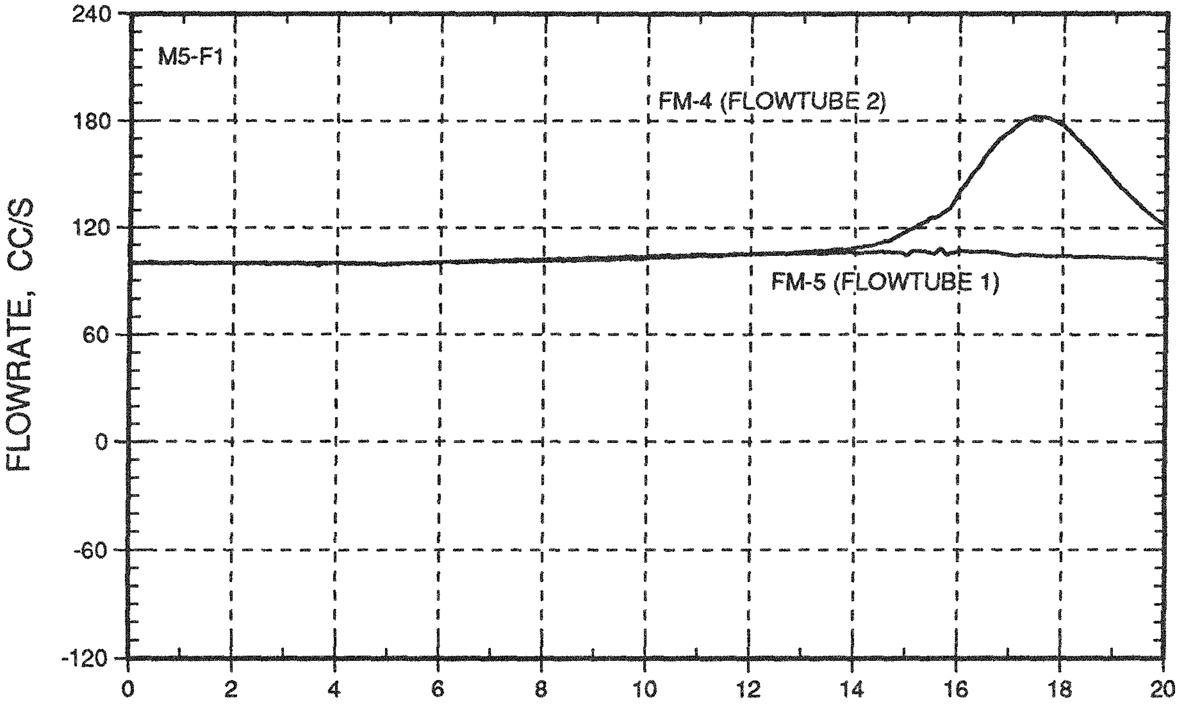

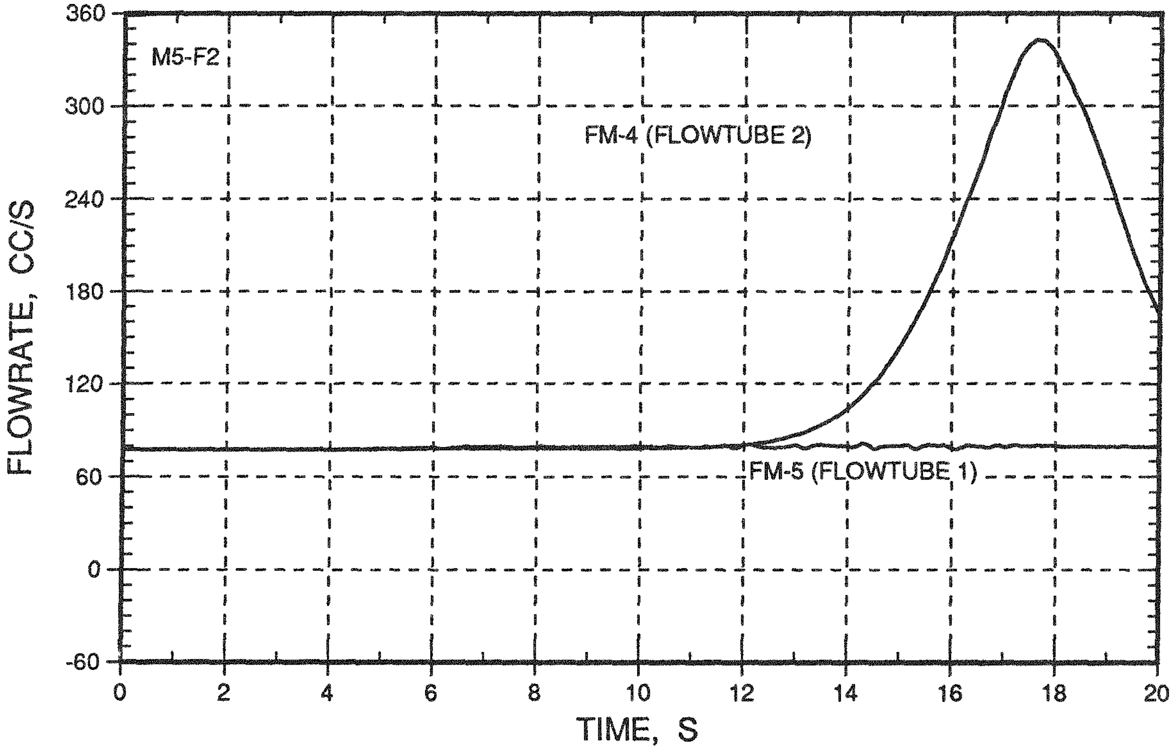

Fig. F.16. Sodium Individual Flowtube Flowrates

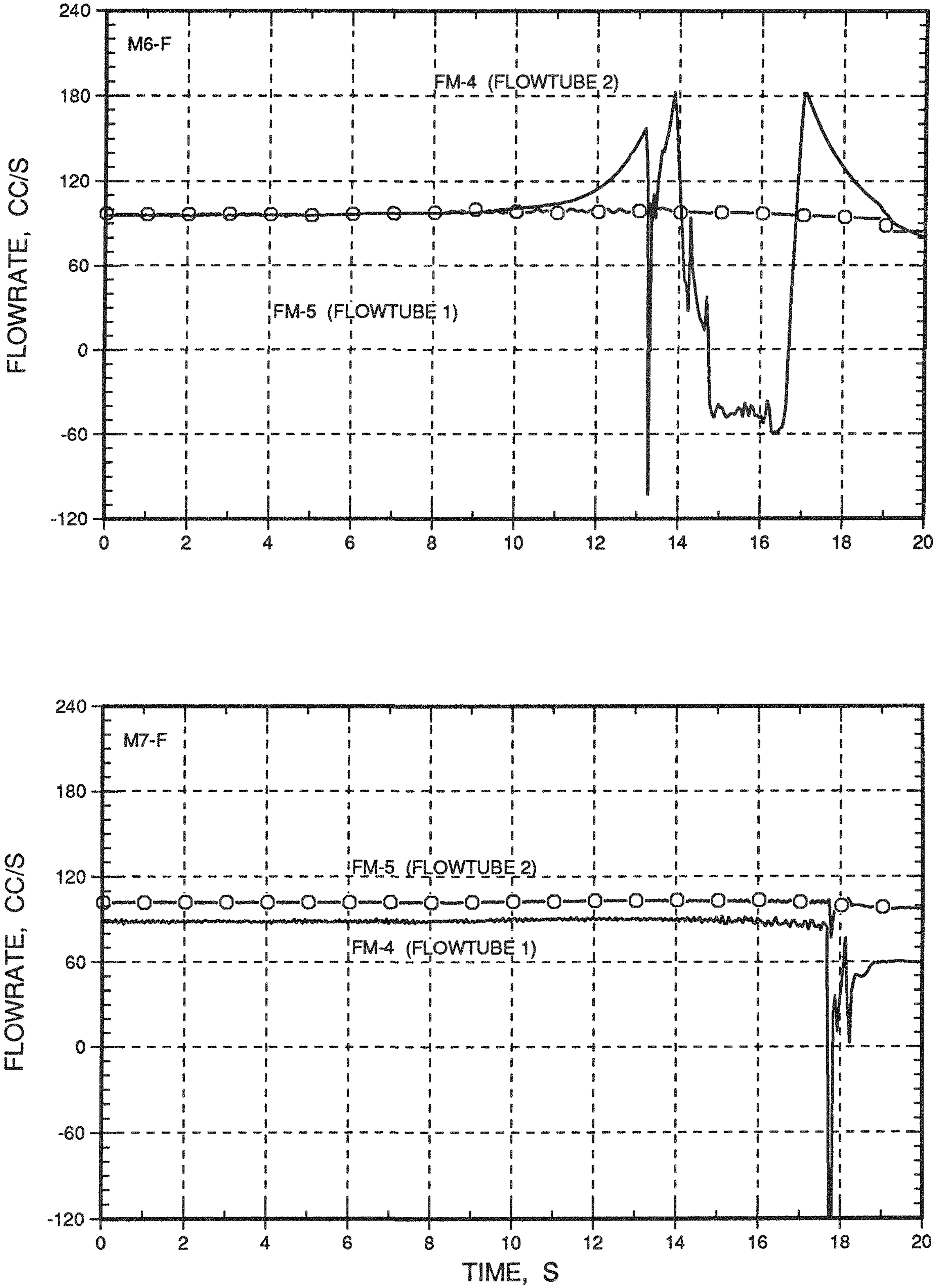

Fig. F.17. Sodium Individual Flowtube Flowrates

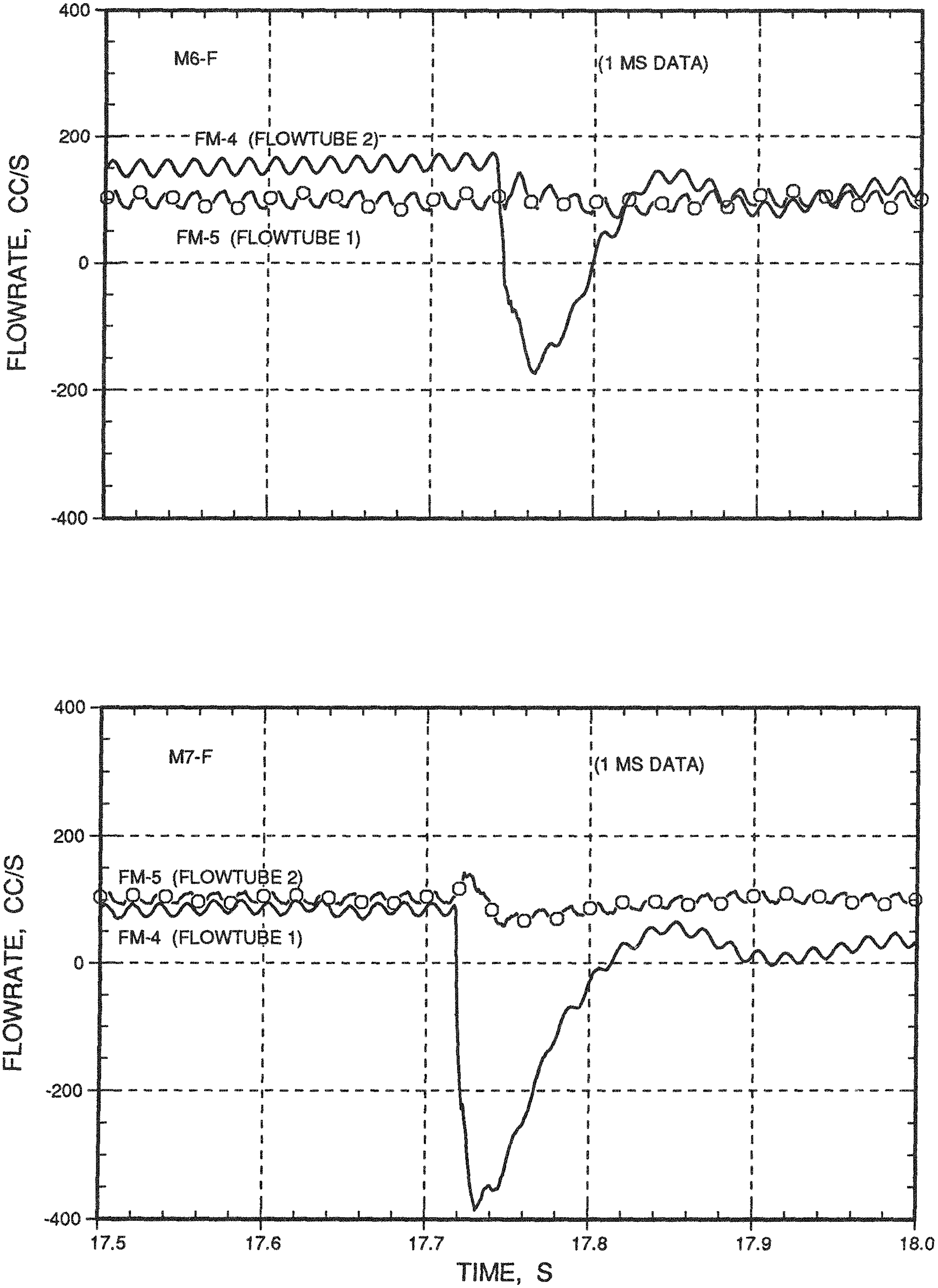

Fig. F.18. Sodium Individual Flowtube Flowrate Details

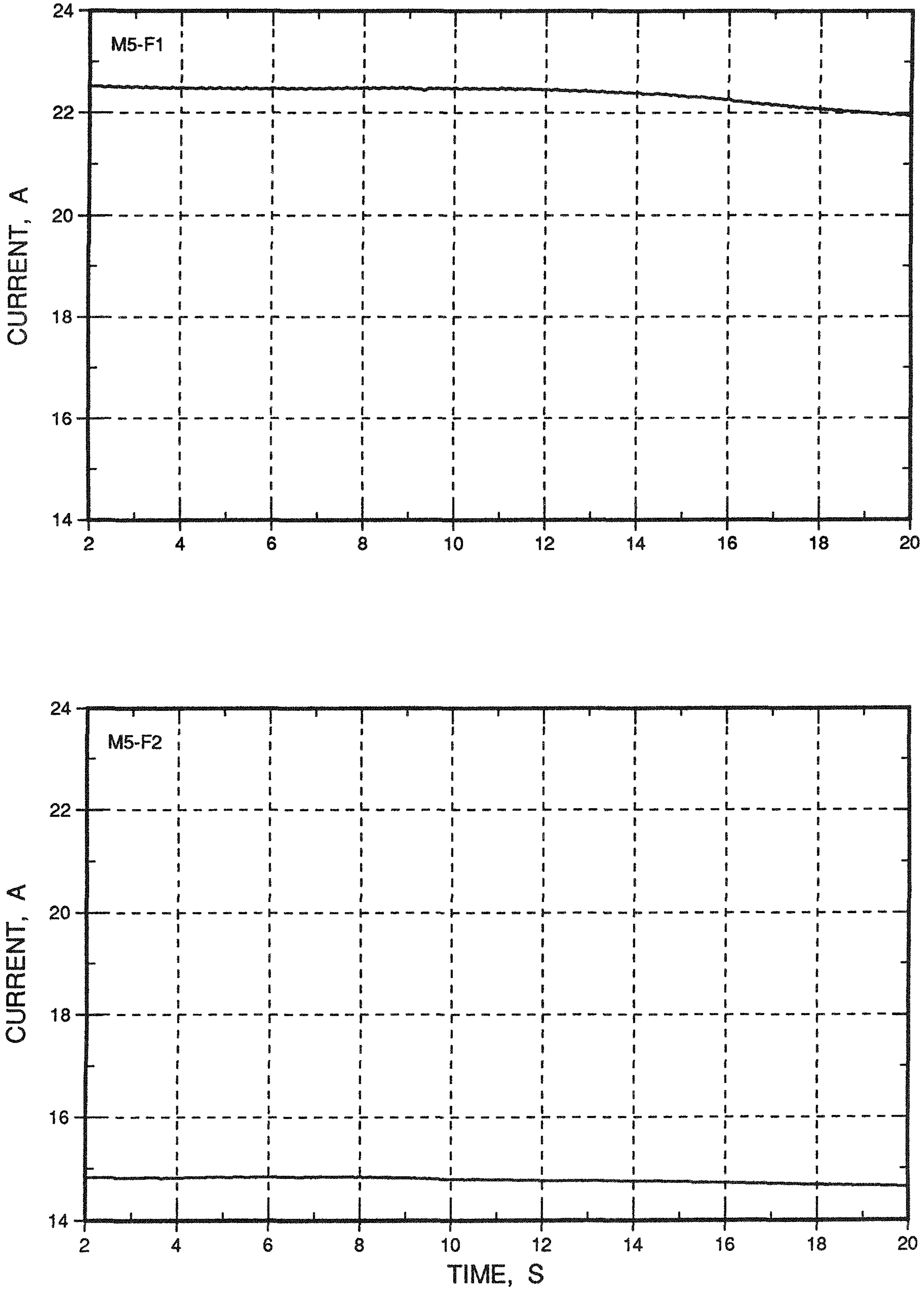

Fig. F.19. Sodium Pump (ALIP) Current

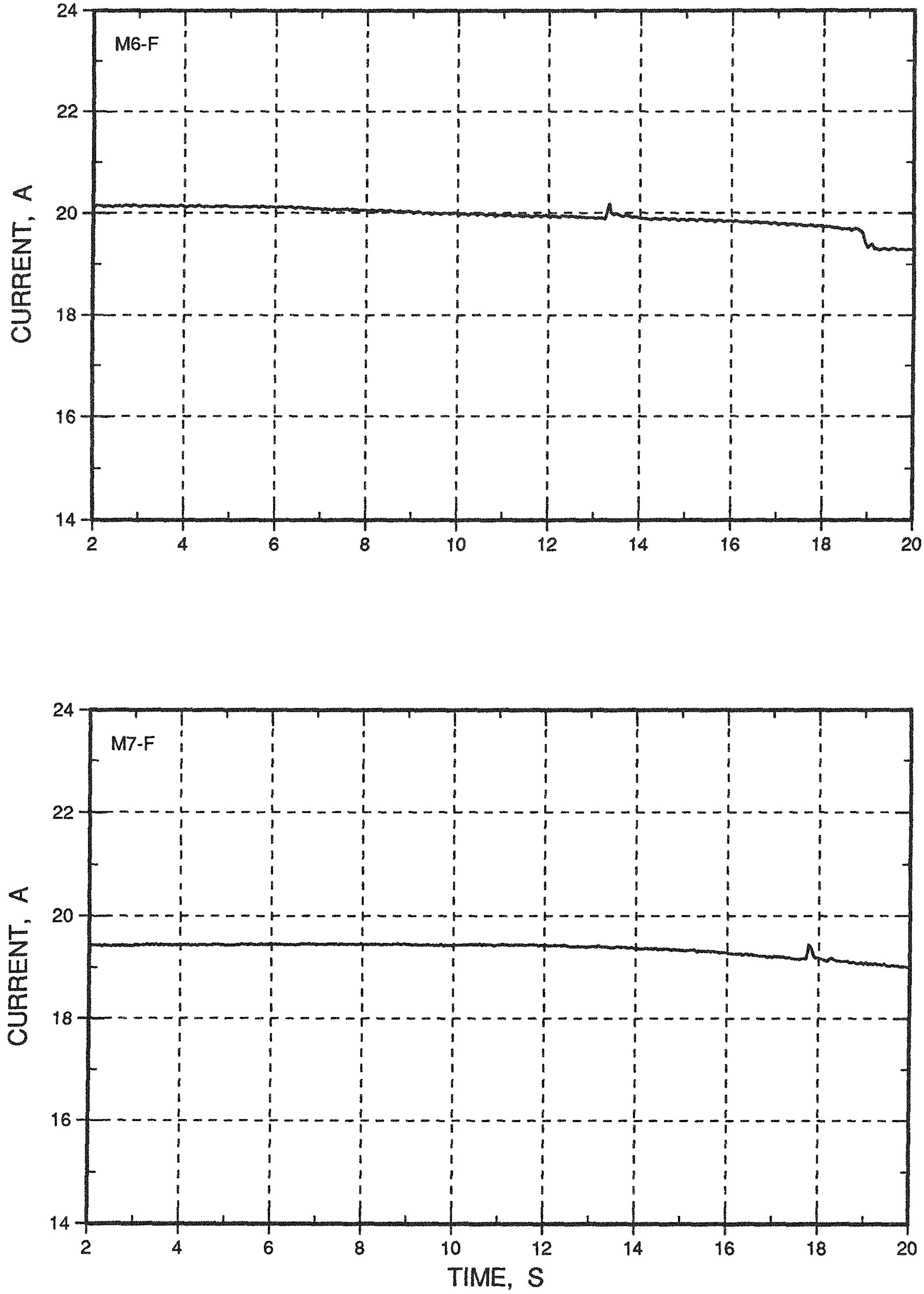

Fig. F.20. Sodium Pump (ALIP) Current

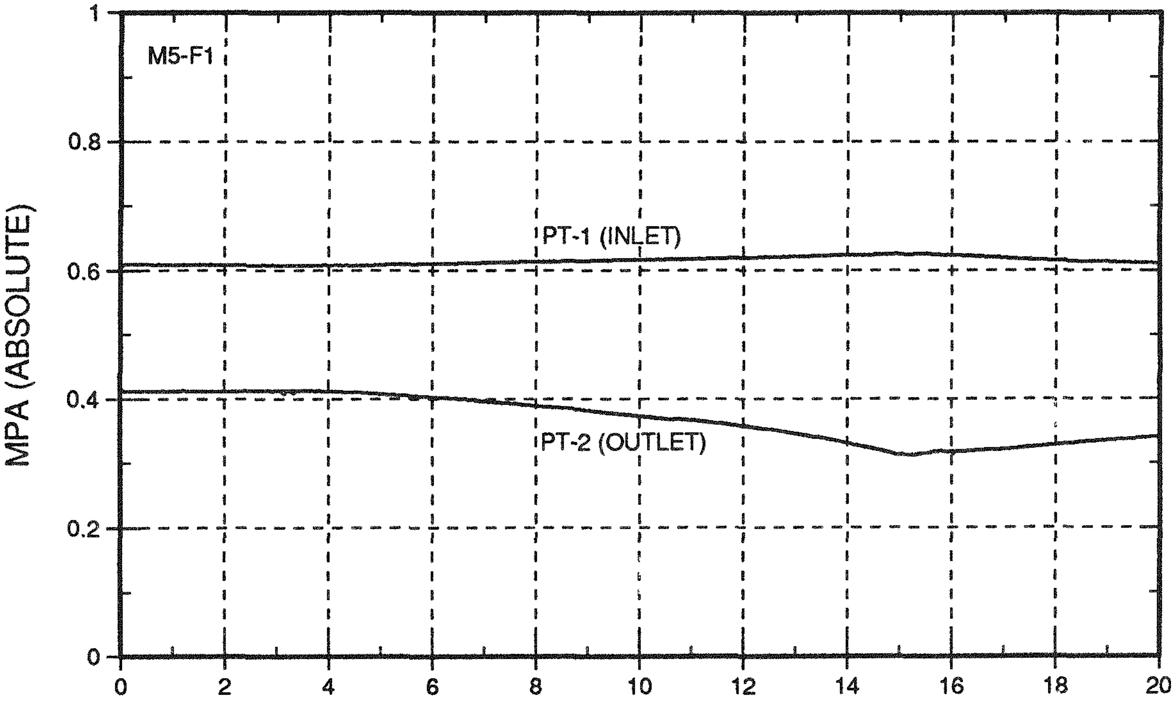

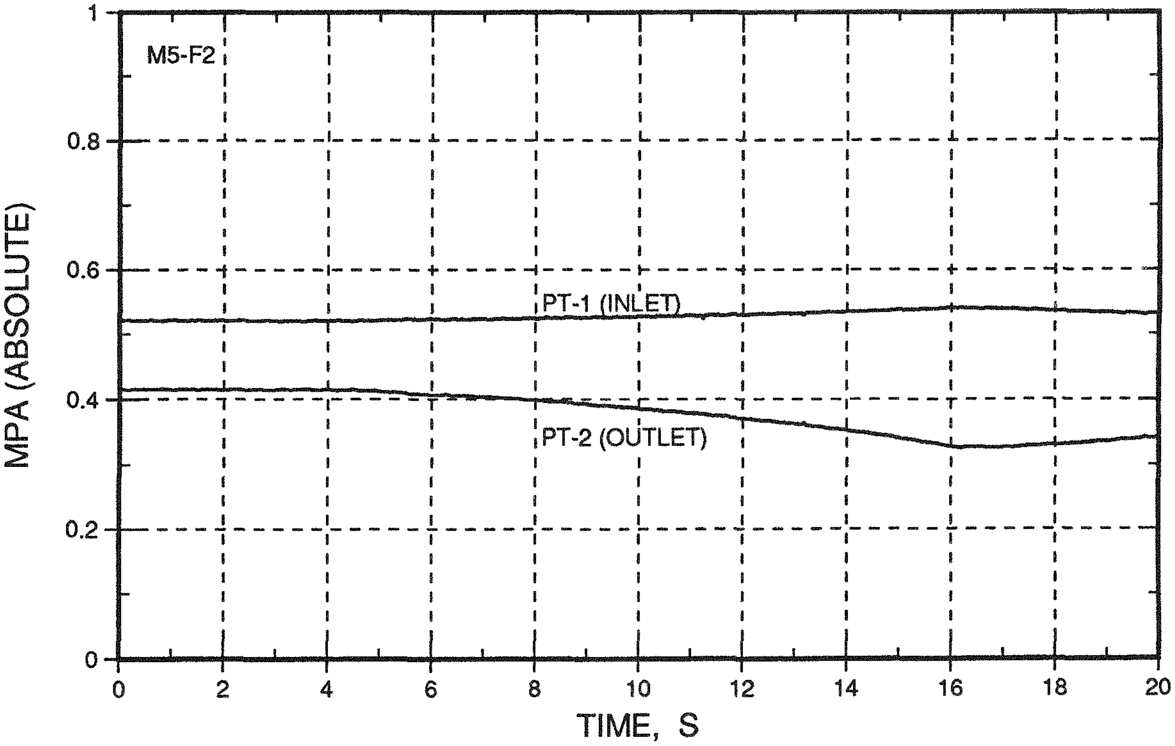

Fig. F.21. Sodium Inlet and Outlet Pressures

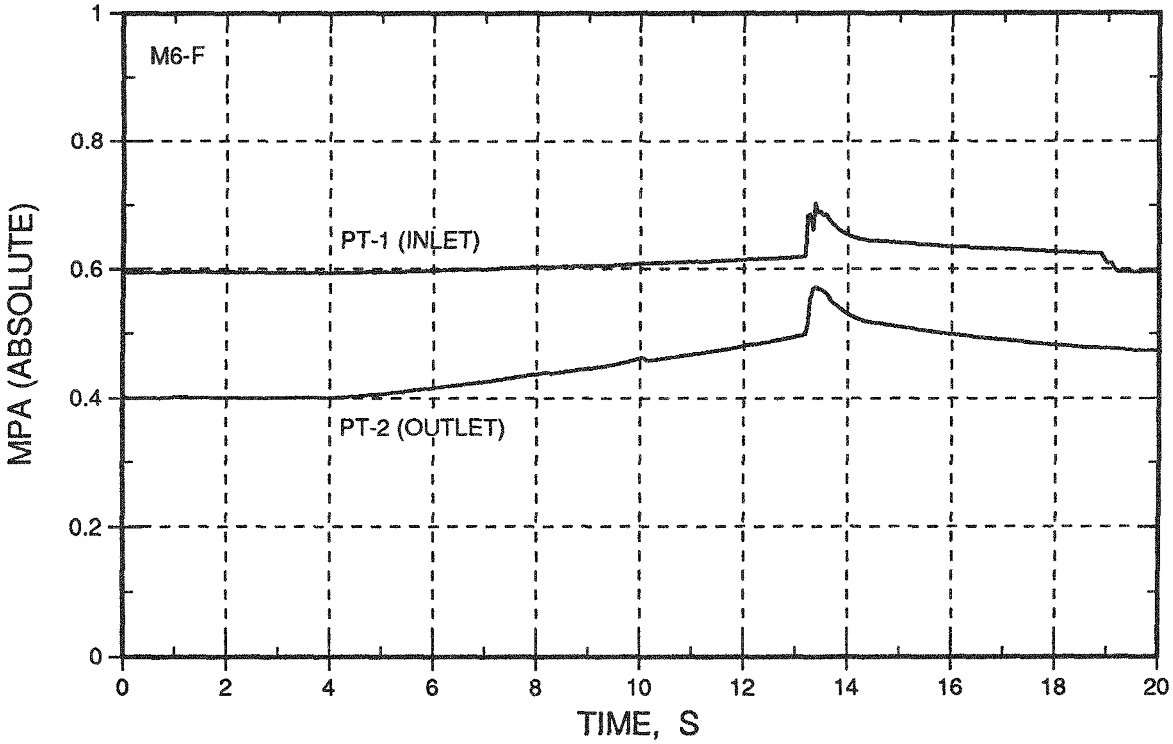

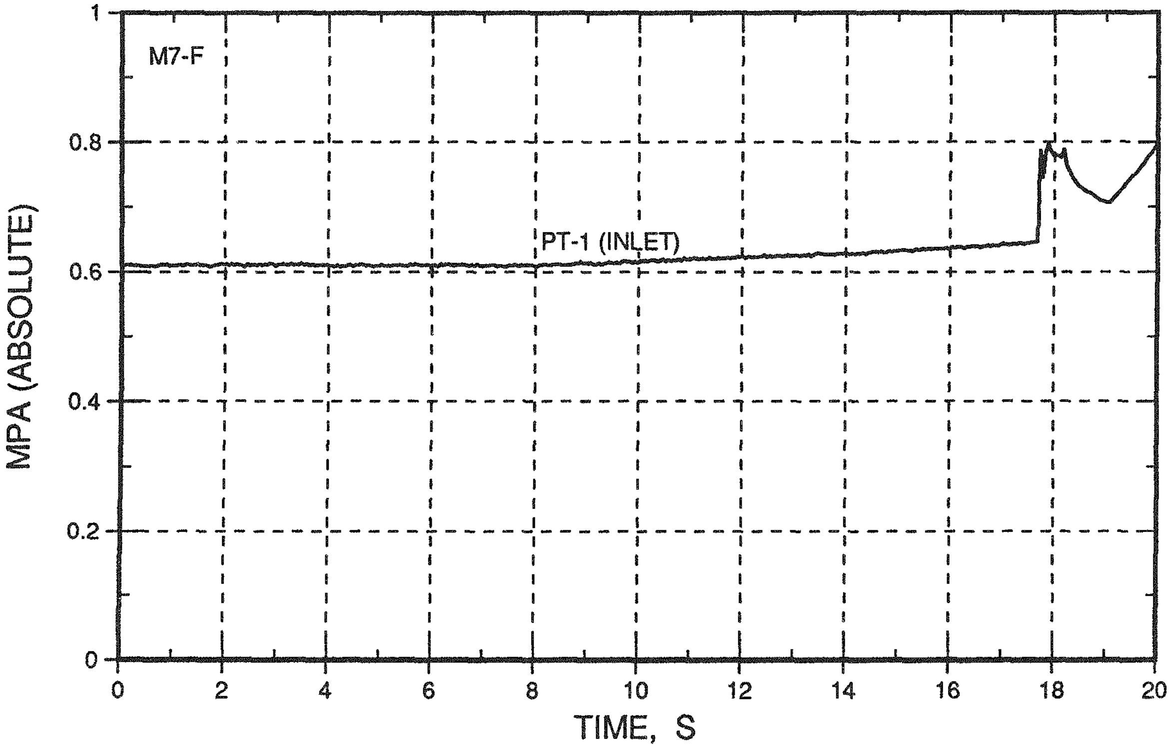

Fig. F.22. Sodium Inlet and Outlet Pressures

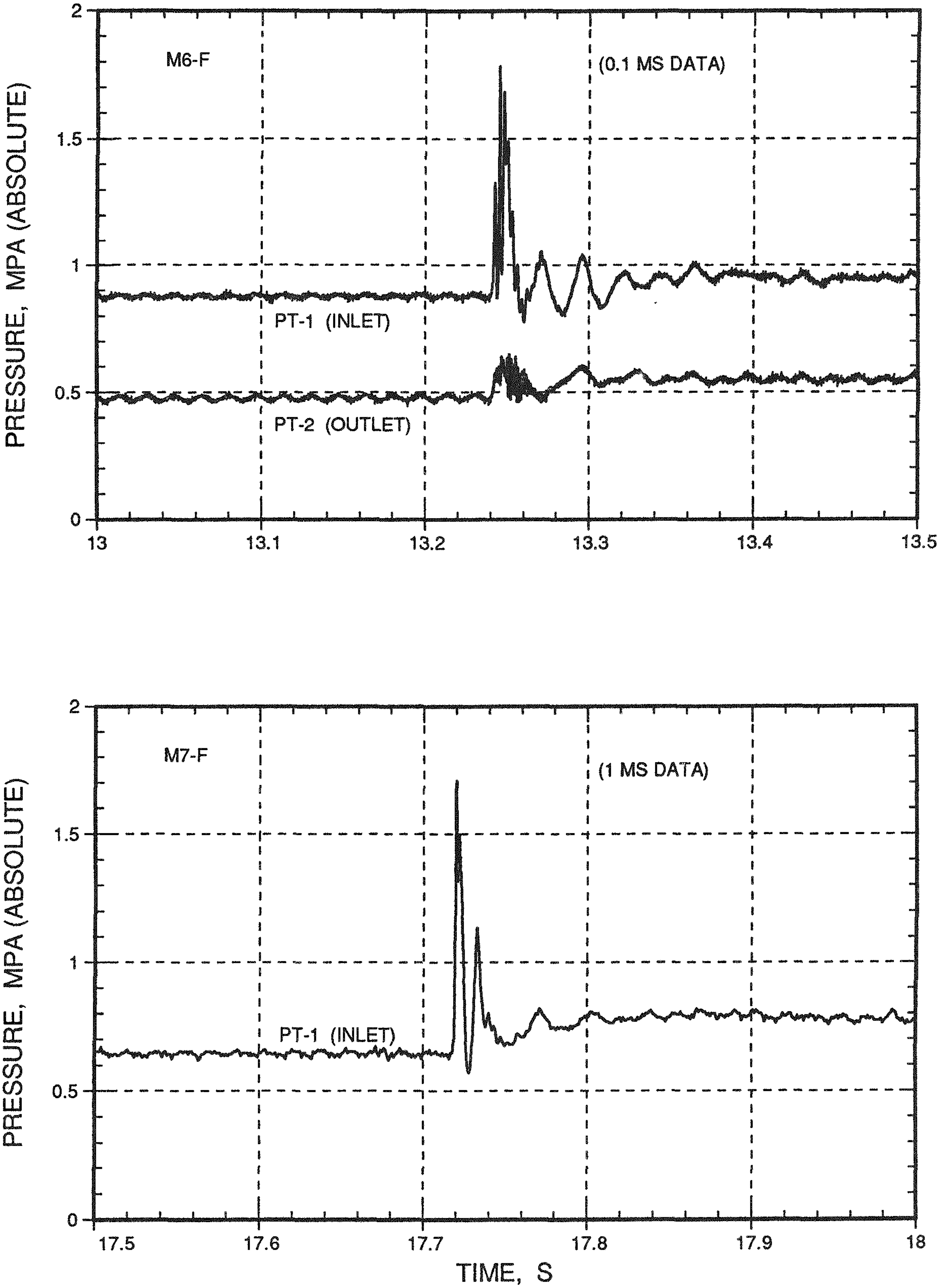

Fig. F.23. Inlet and Outlet Pressure Details (M6 and M7)

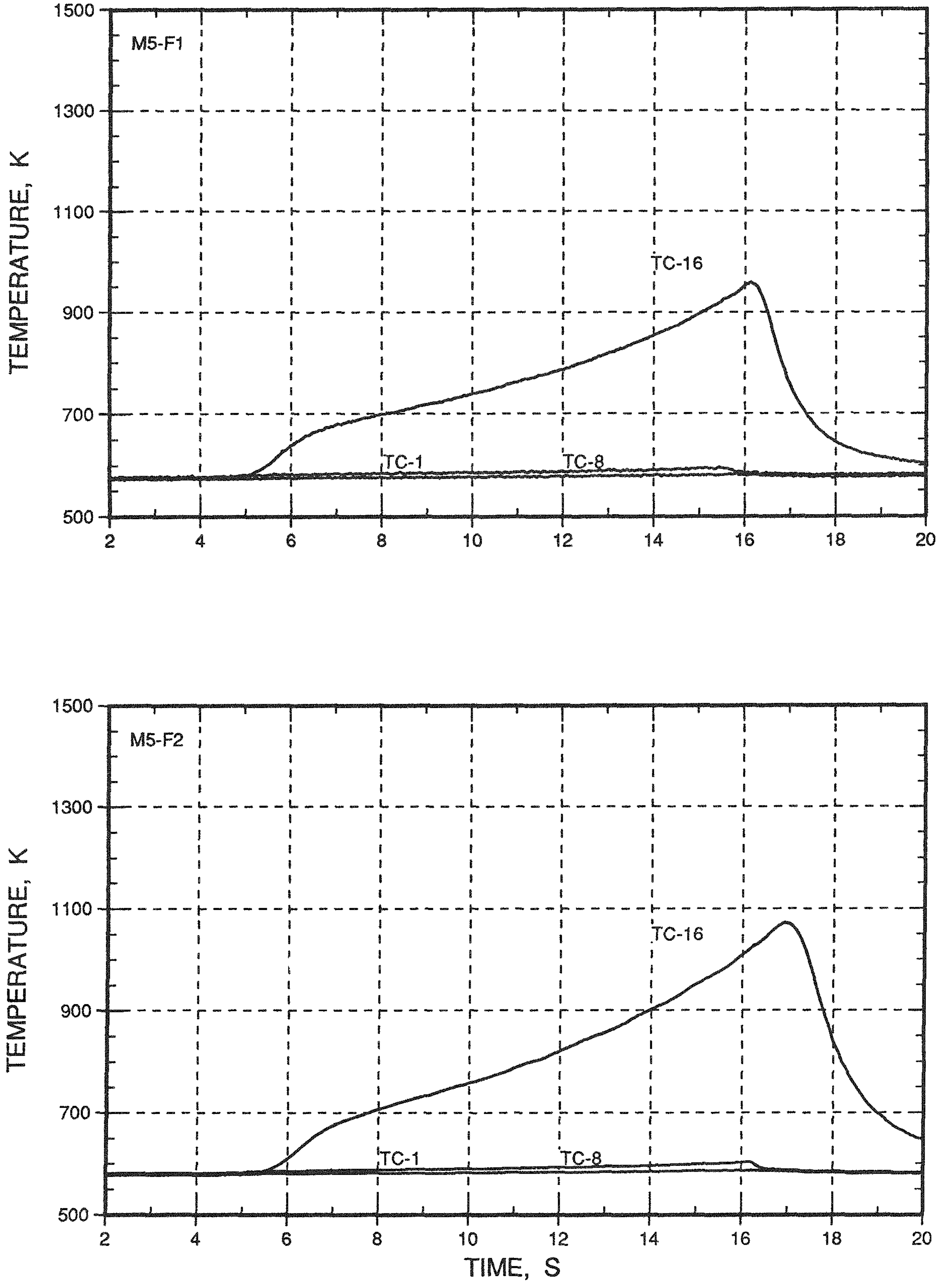

Fig. F.24. Flowtube at Base of Fuel Column and Outlet Sodium Temperatures

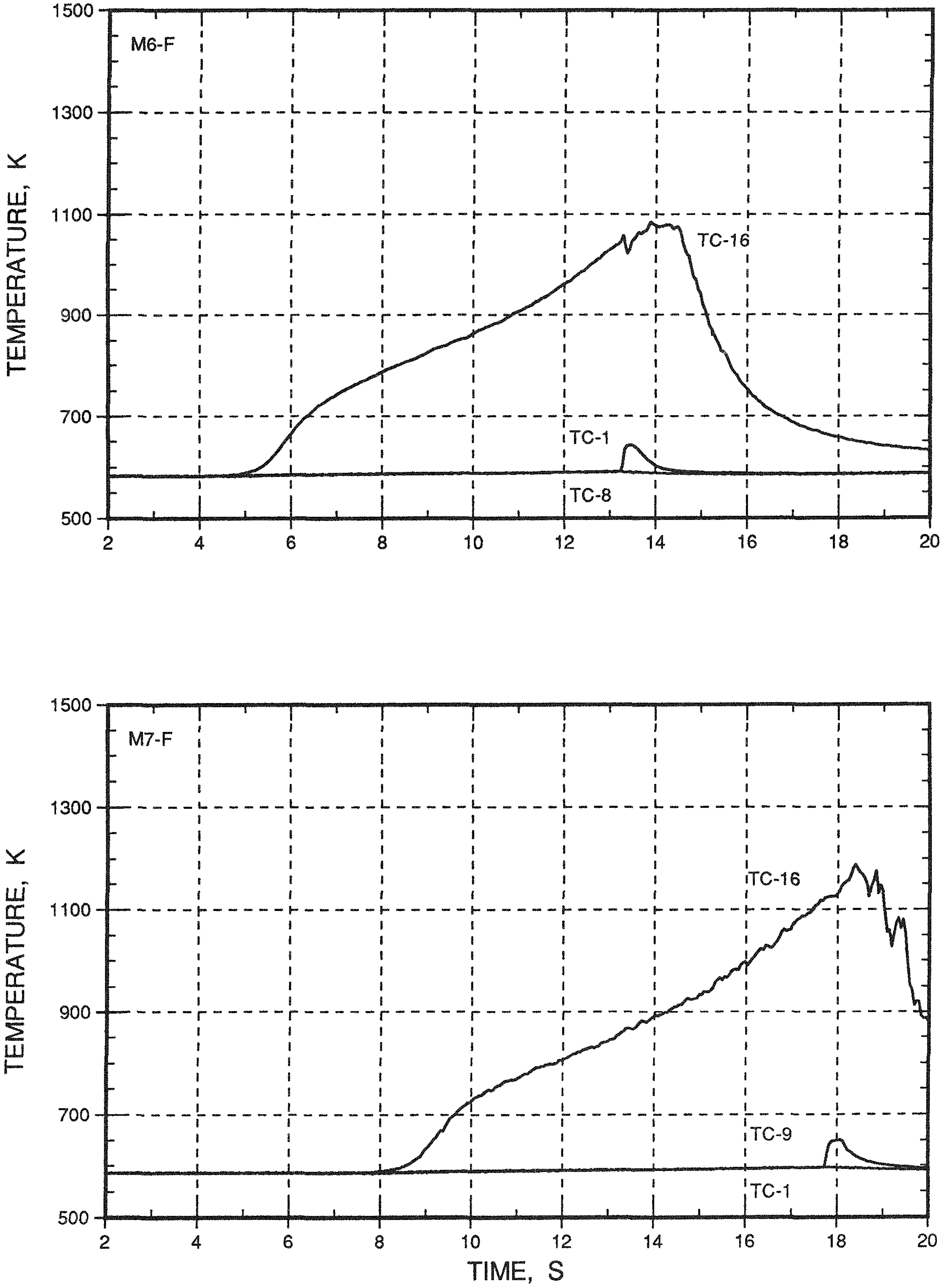

Fig. F.25. Flowtube at Base of Fuel Column and Outlet Sodium Temperatures

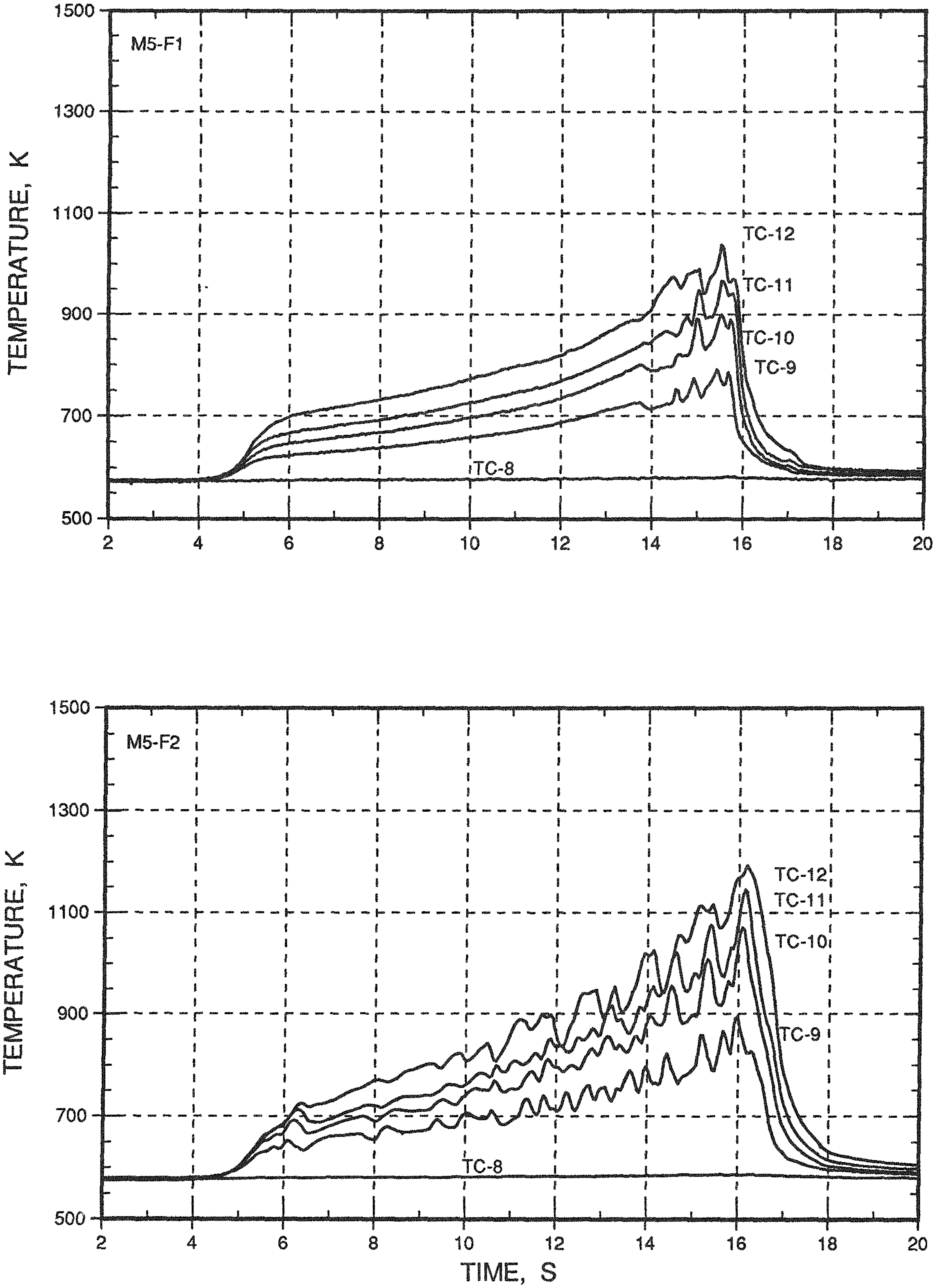

Fig. F.26. Flowtube 1 Temperatures (Z/L = -0.04 to 1.07)

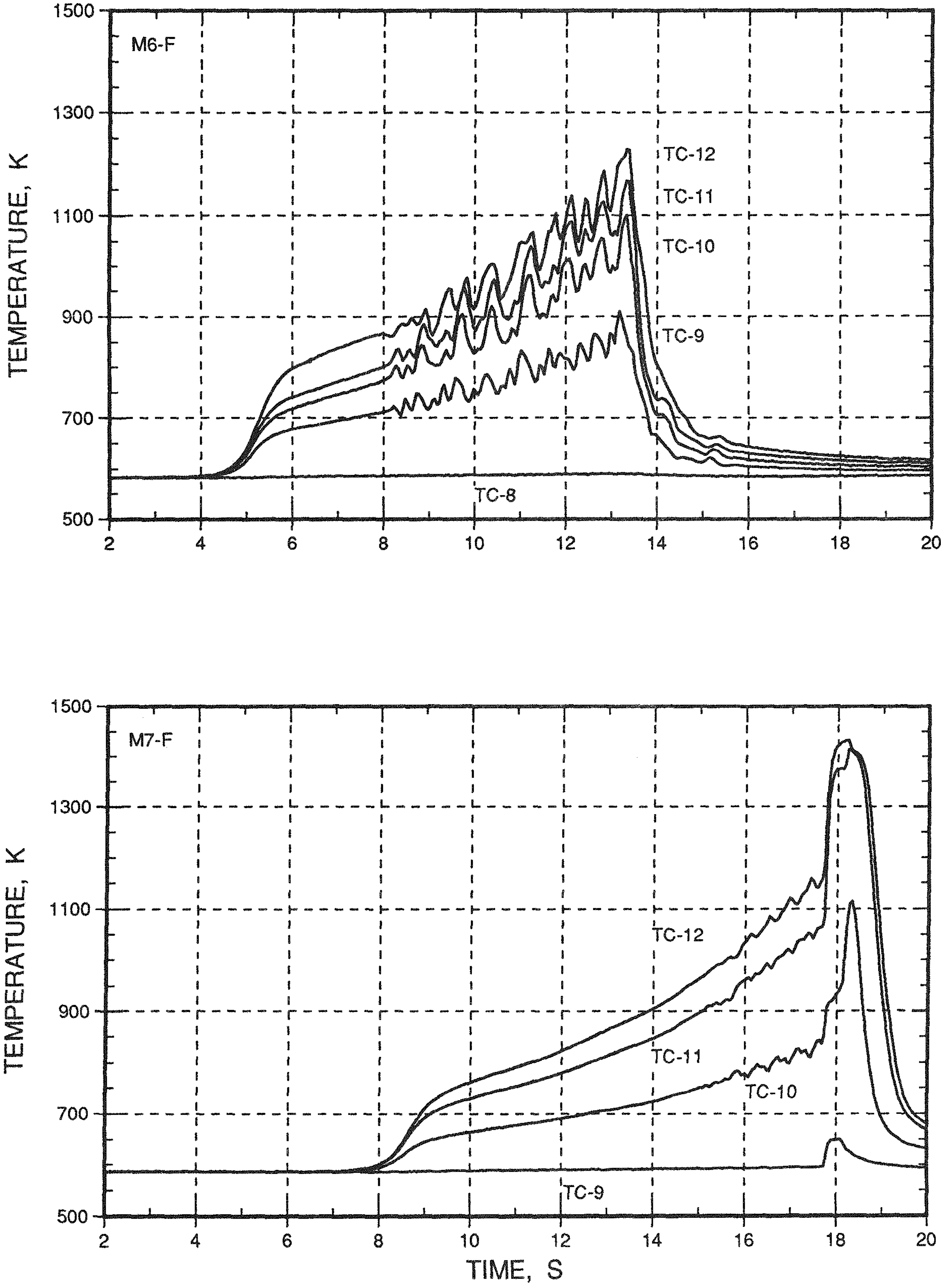

Fig. F.27. Flowtube 1 Temperatures (Z/L=-0.04 to 1.07)

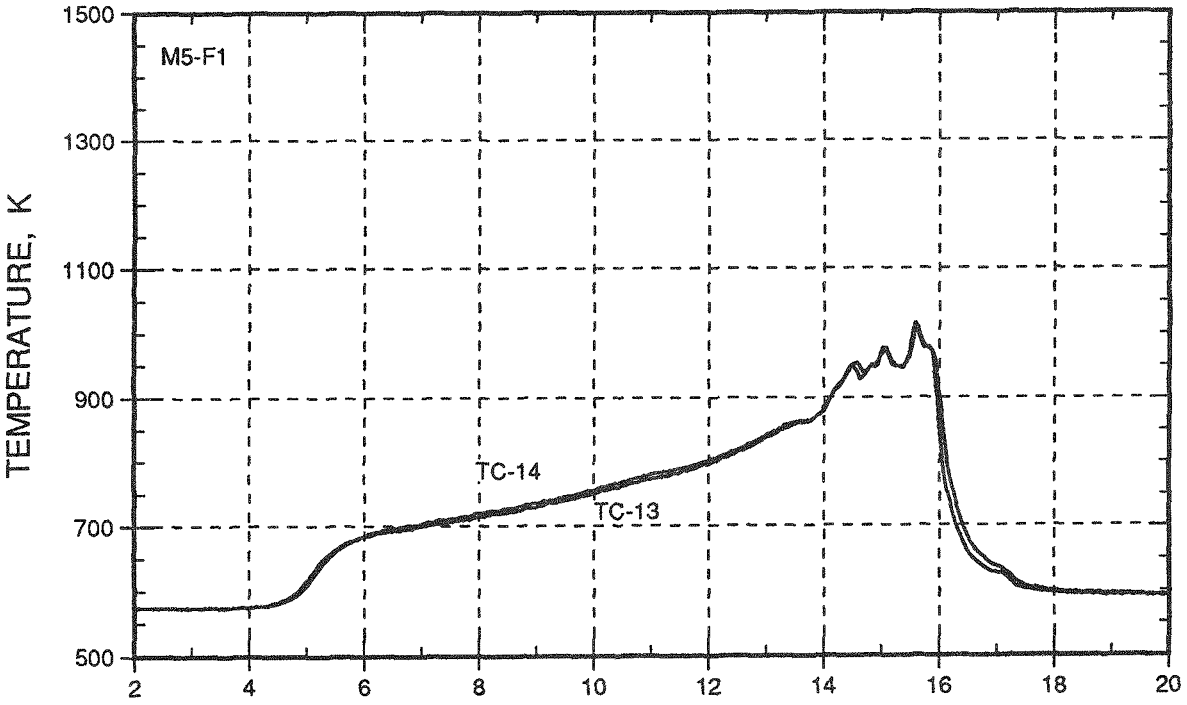

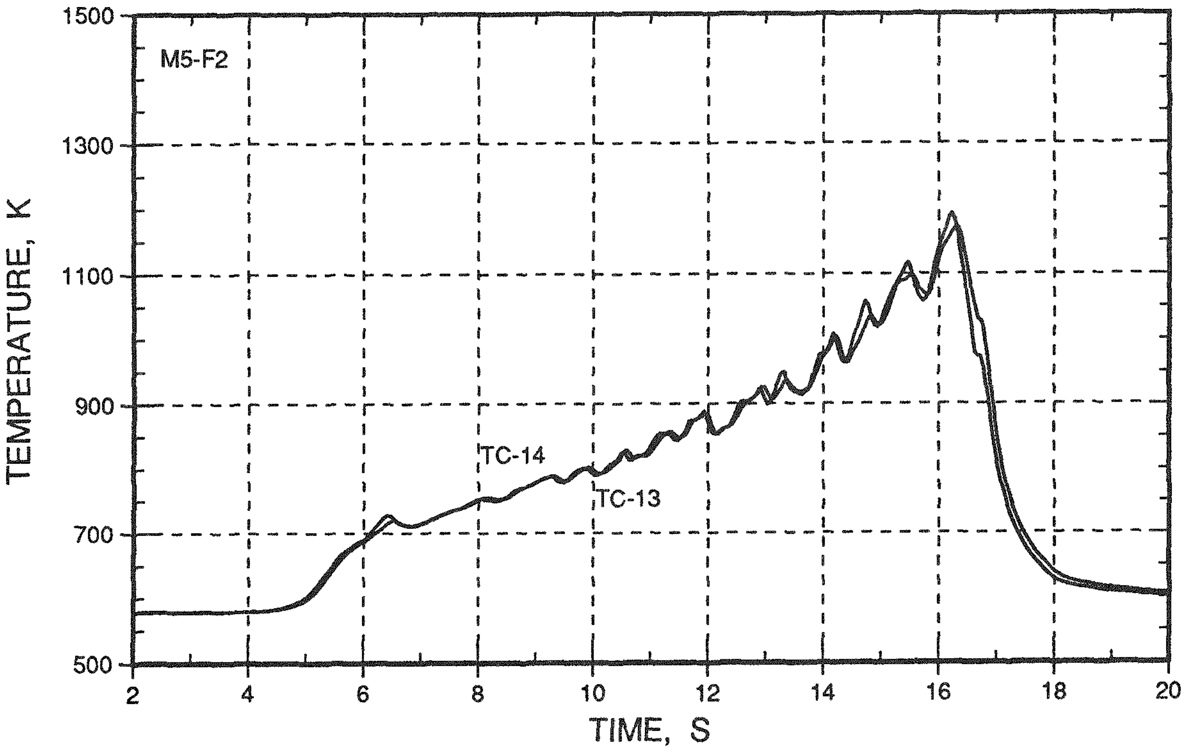

Fig. F.28. Flowtube 1 Temperatures (Z/L = 1.15 to 1.30)

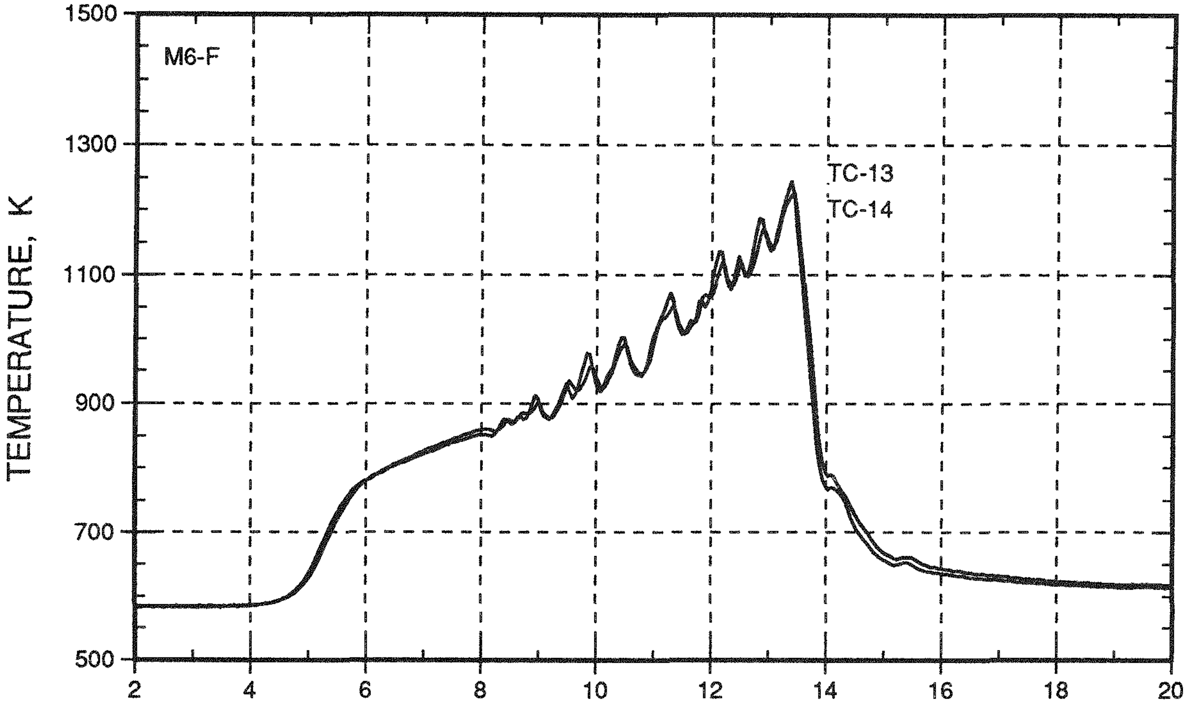

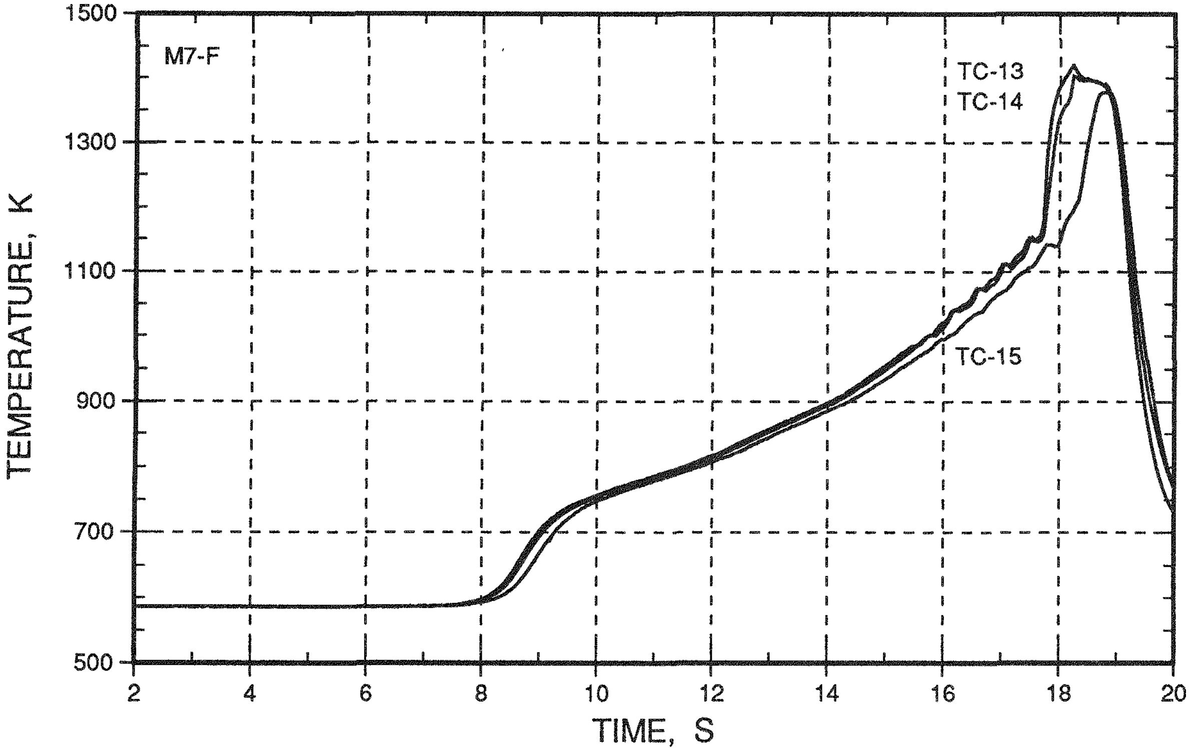

Fig. F.29. Flowtube 1 Temperatures (Z/L=1.15 to 1.87)

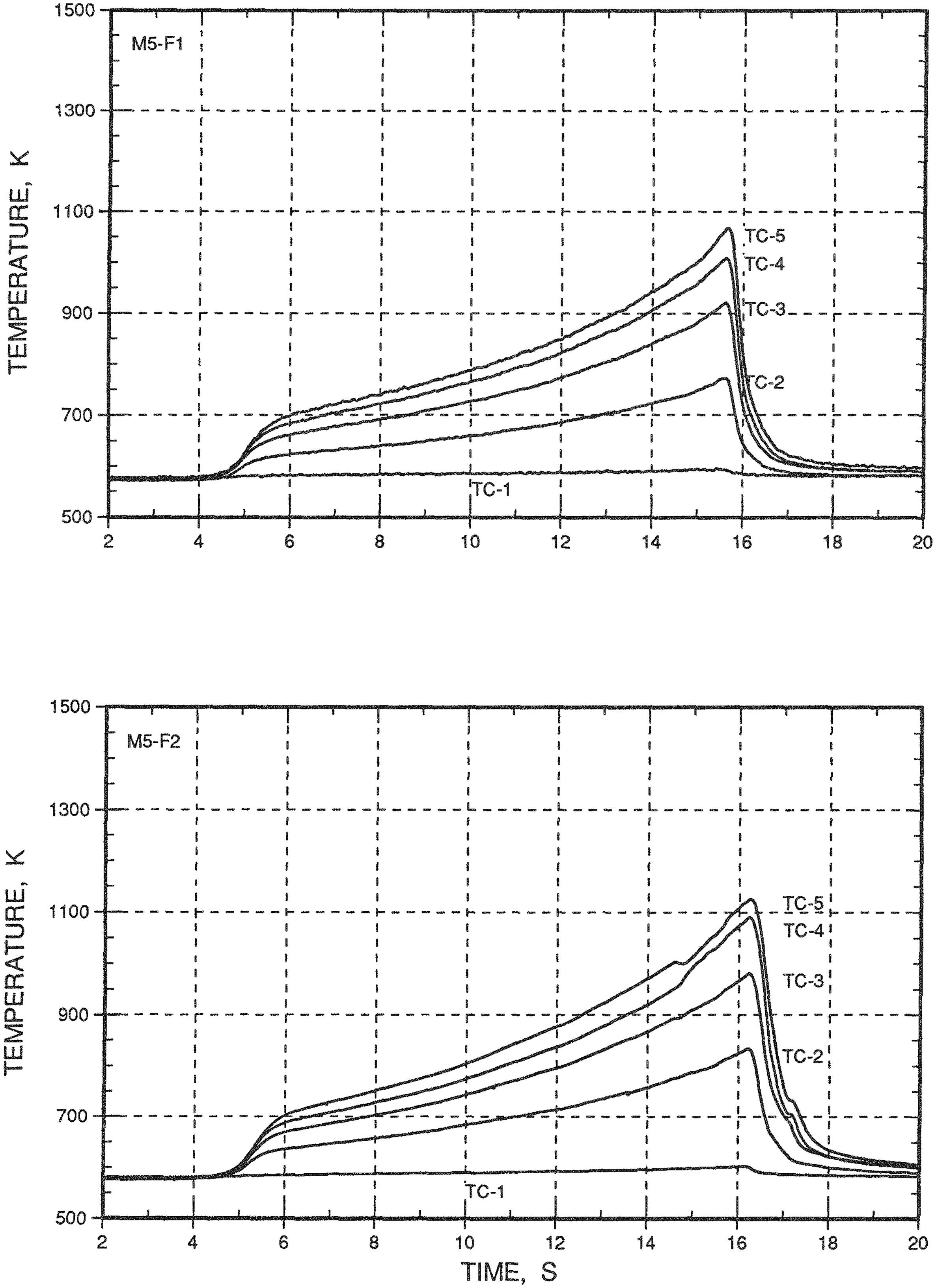

Fig. F.30. Flowtube 2 Temperatures (Z/L = -0.04 to 1.07)

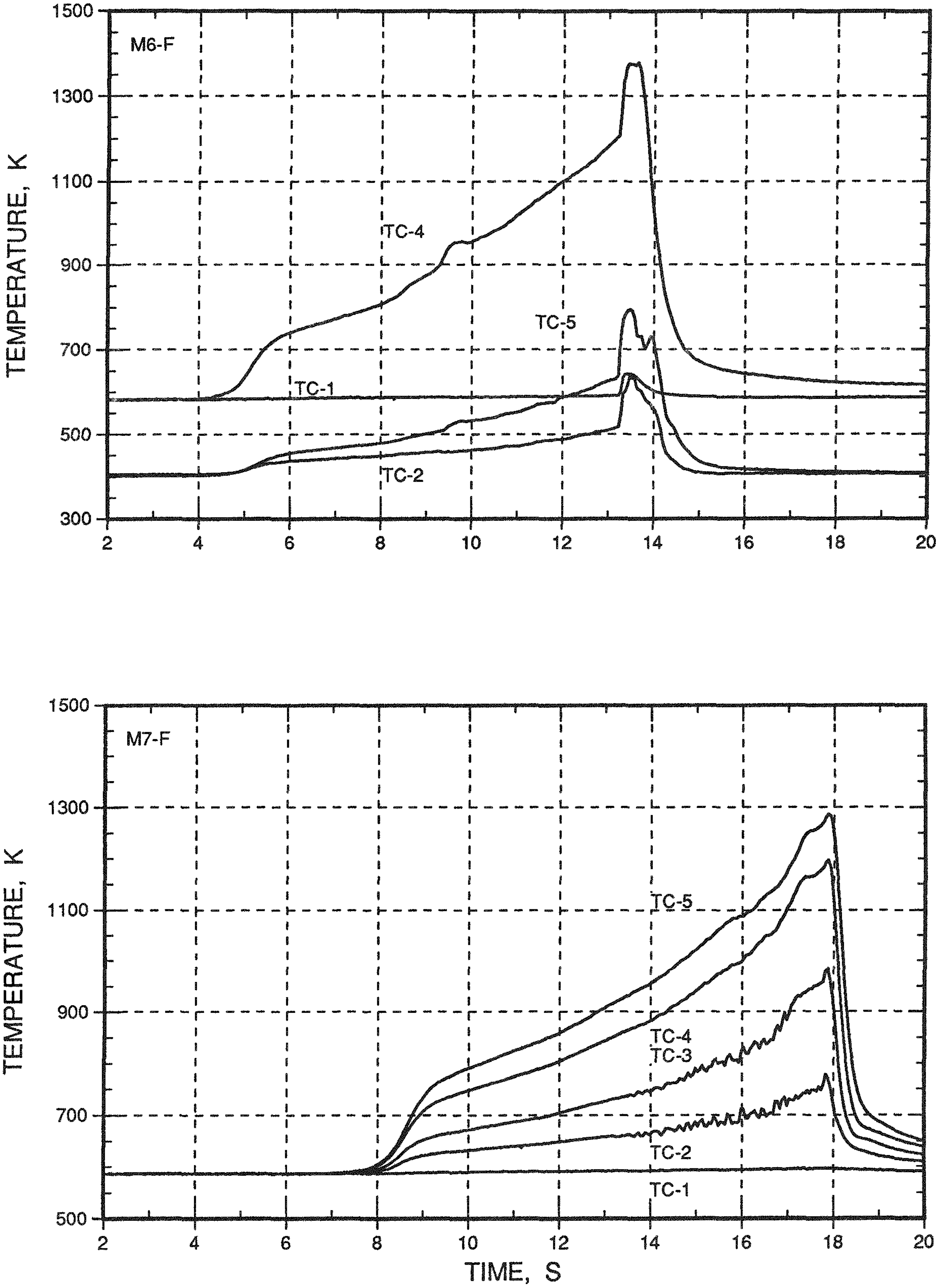

Fig. F.31. Flowtube 2 Temperatures (Z/L= -0.04 to 1.07)

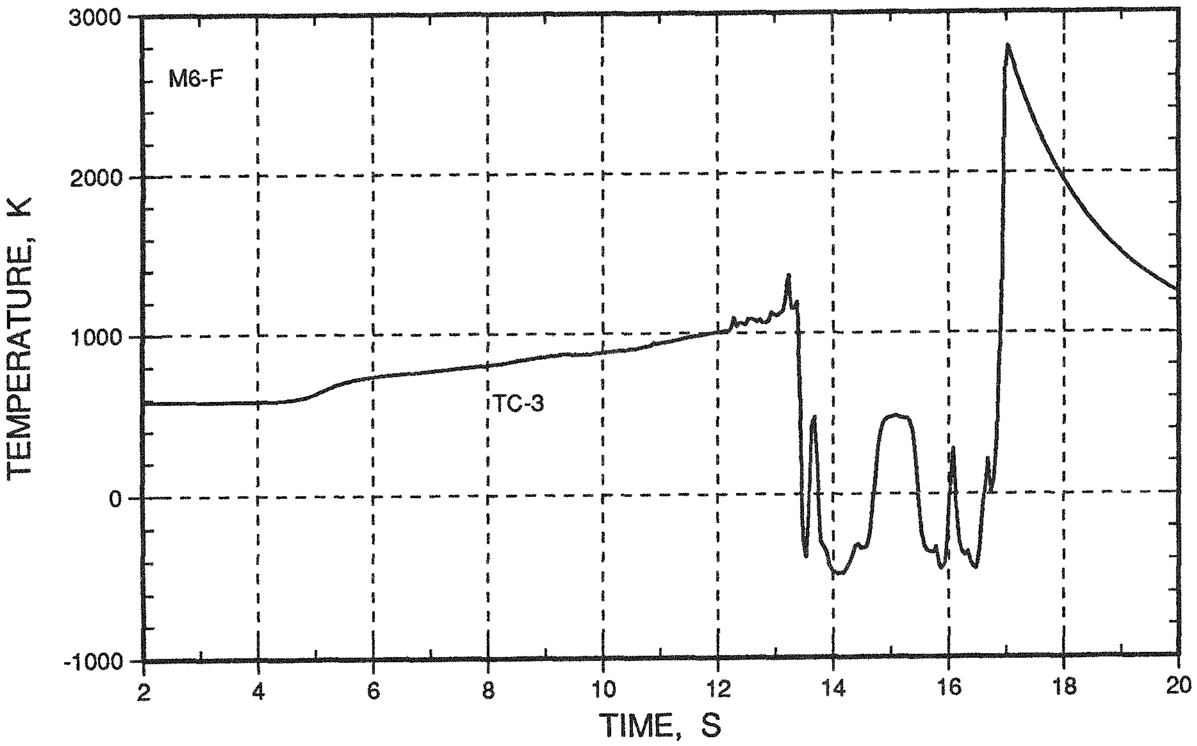

Fig. F.32. Flowtube 2 Temperature (Z/L = 0.78)

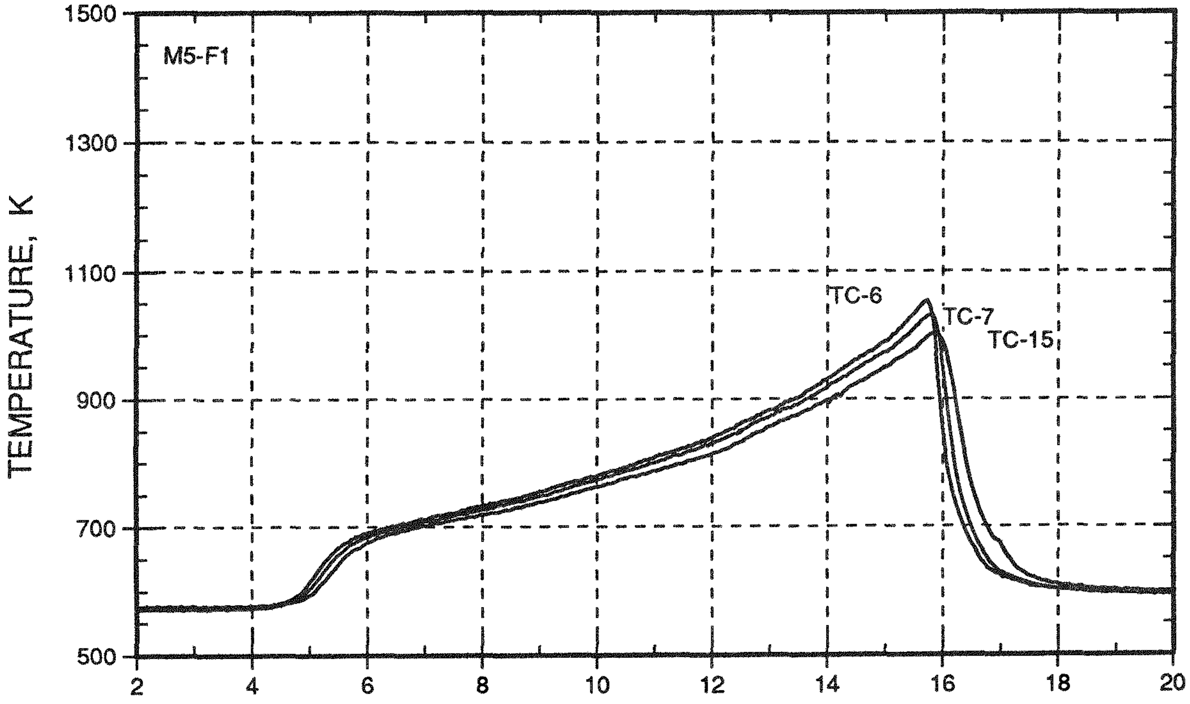

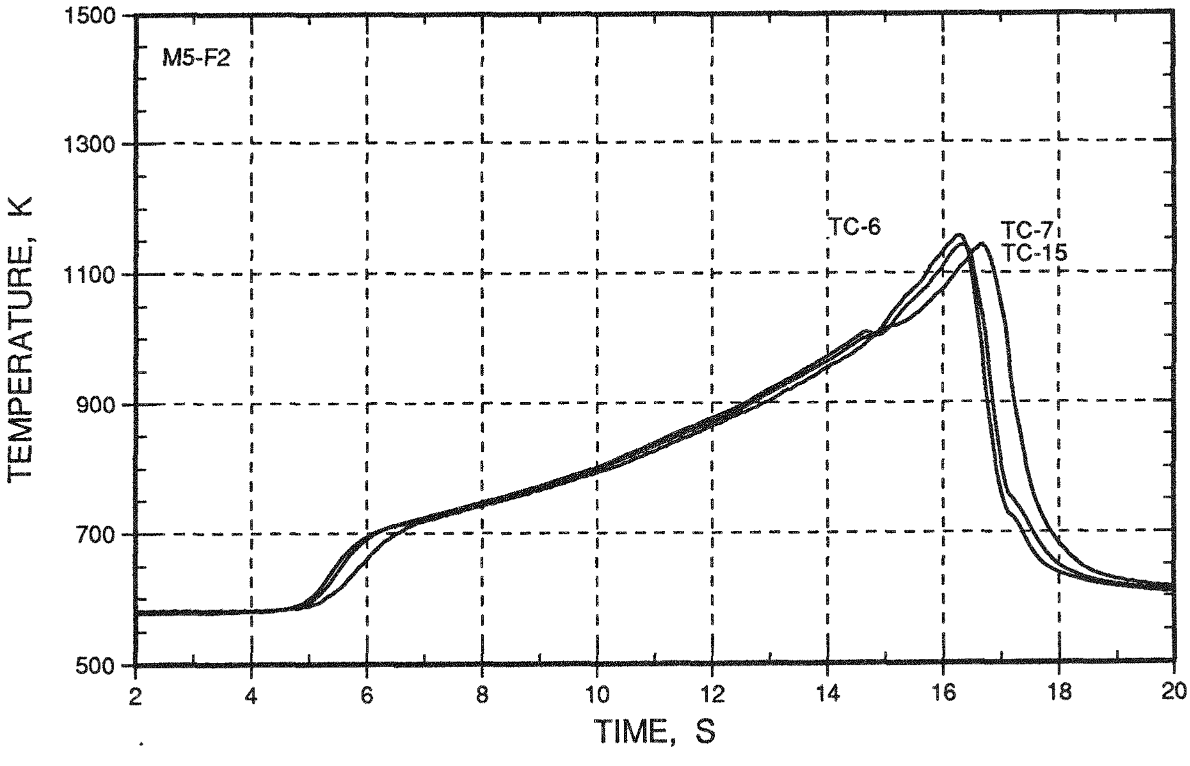

Fig. F.33. Flowtube 2 Temperatures (Z/L = 1.15 to 1.87)

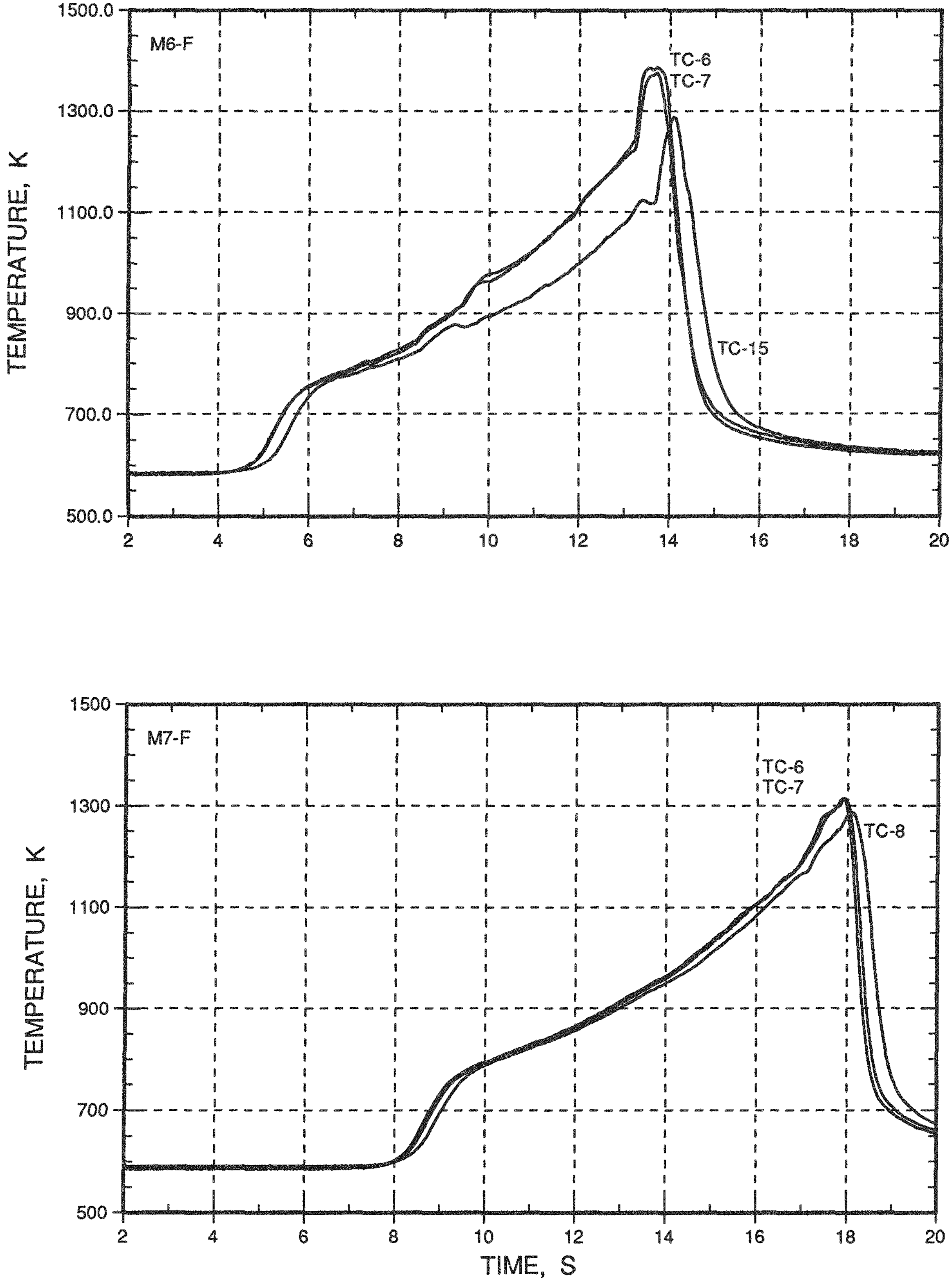

Fig. F.34. Flowtube 2 Temperatures (Z/L=1.15 to 1.87)

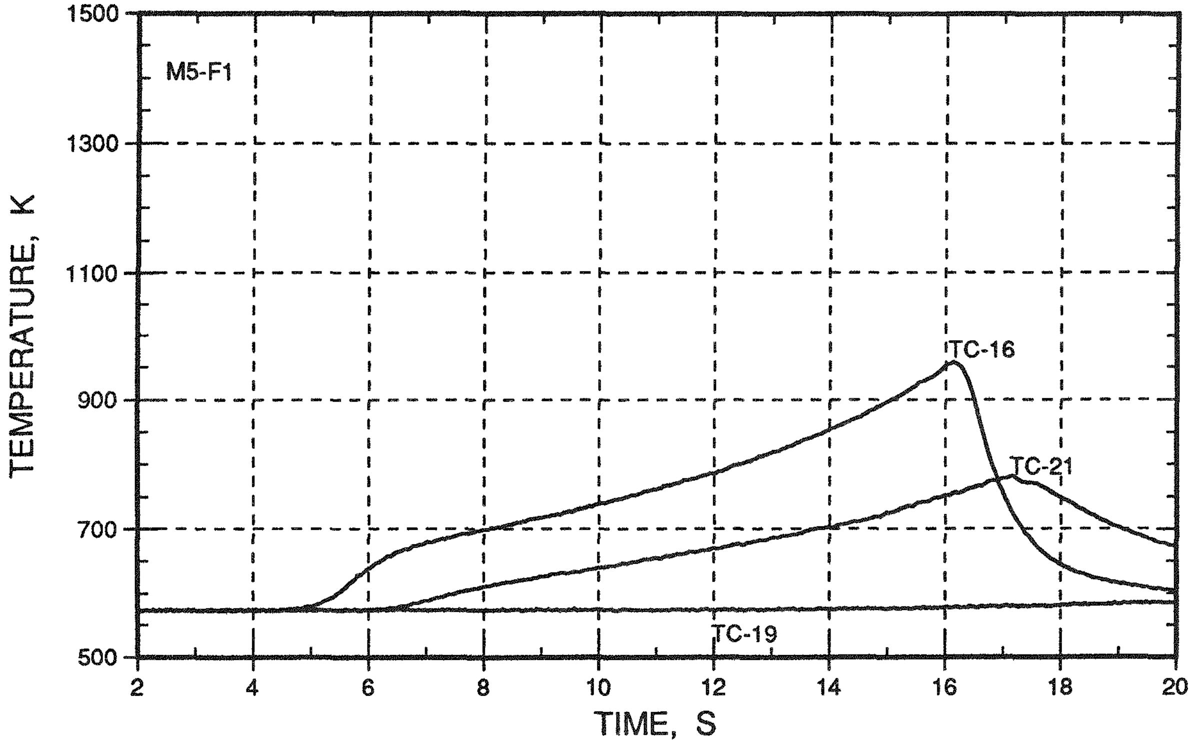

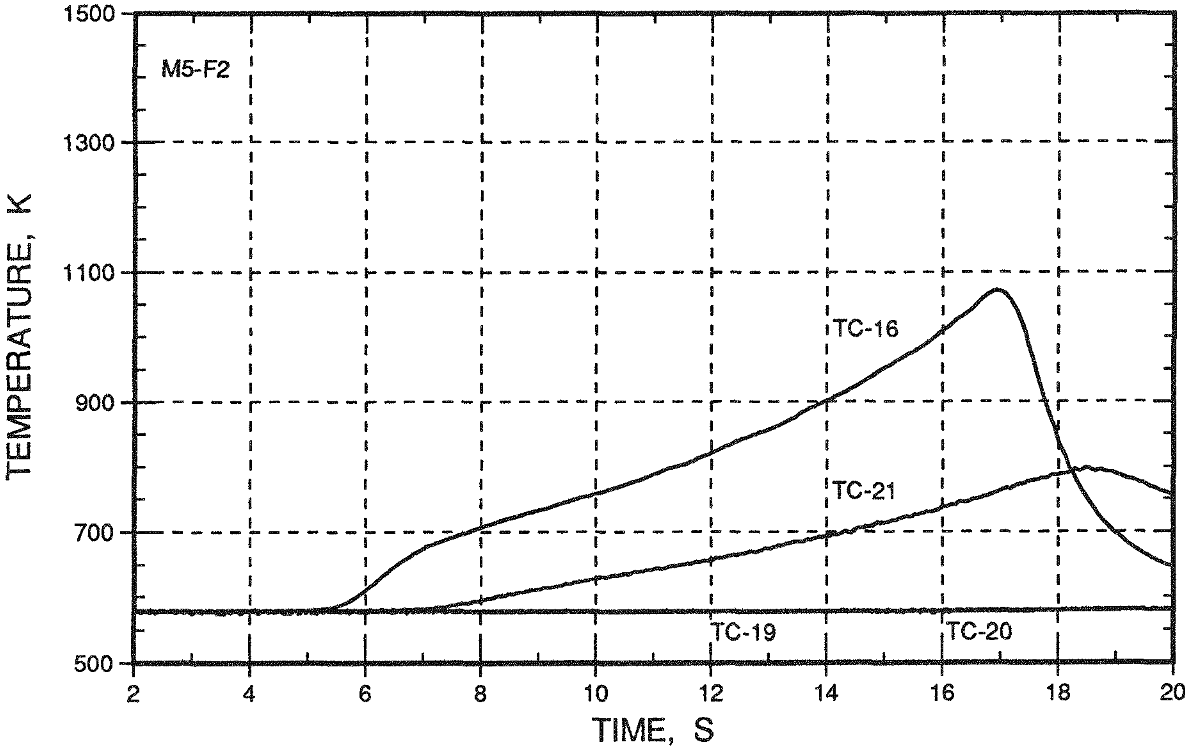

Fig. F.35. Temperatures in the Sodium Flow

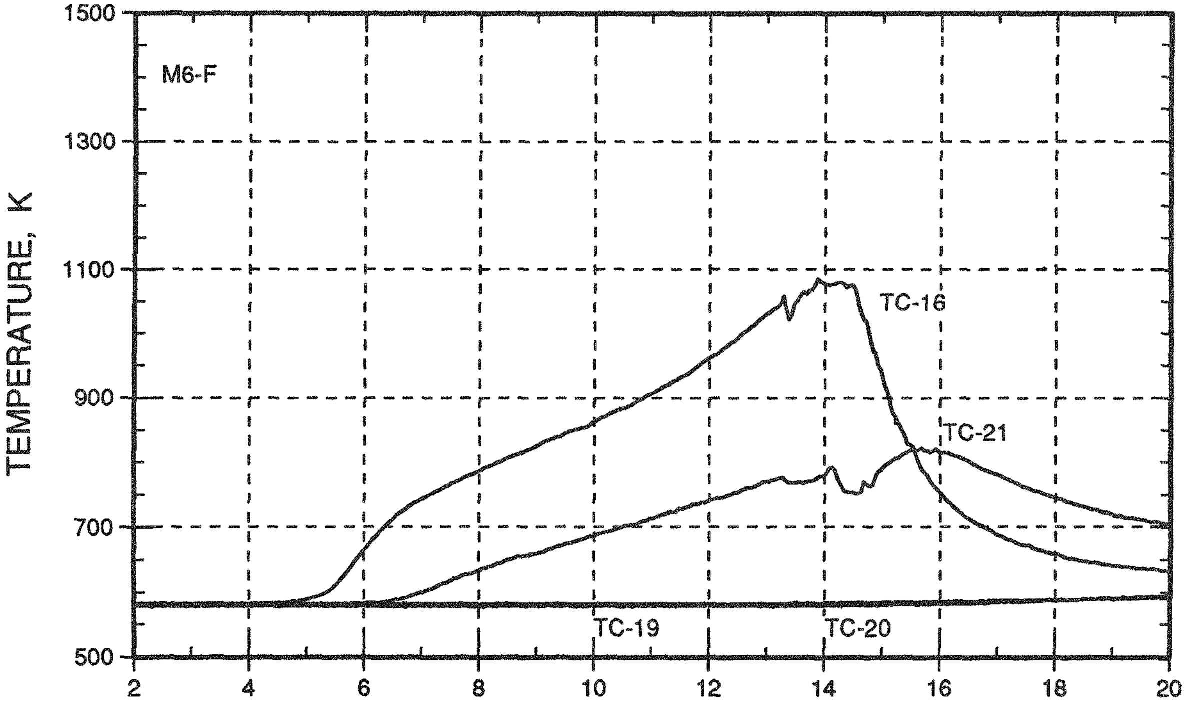

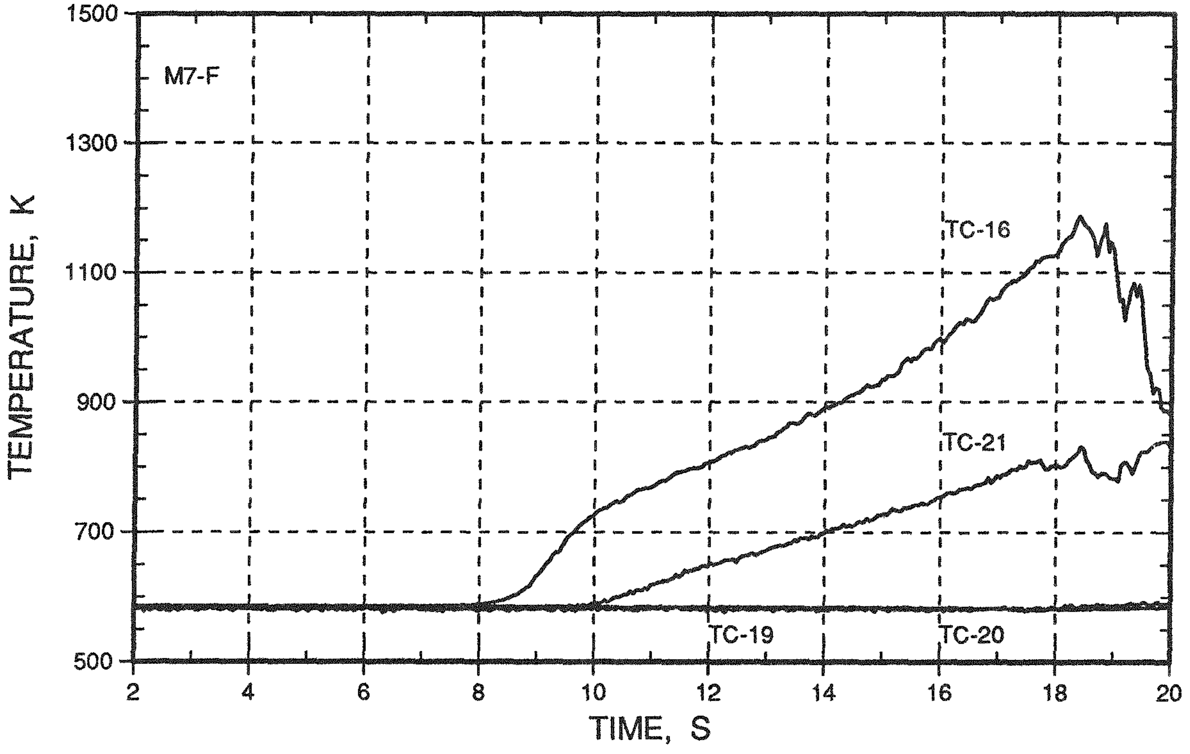

Fig. F.36. Temperatures in the Sodium Flow

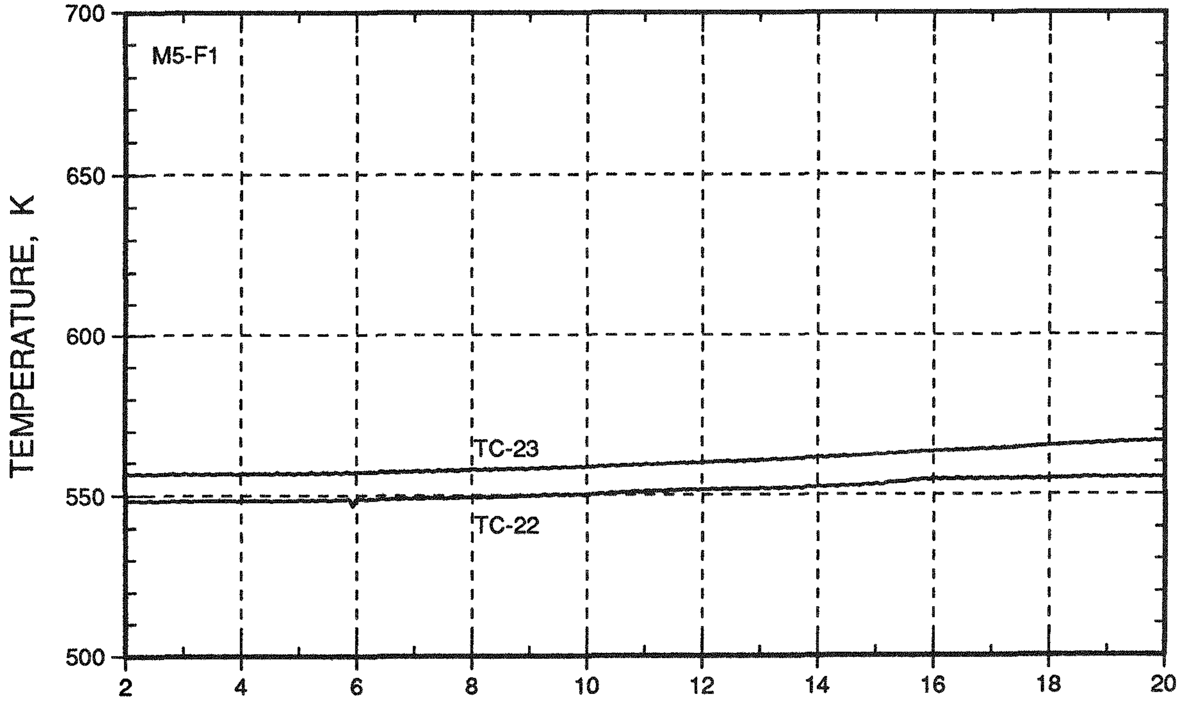

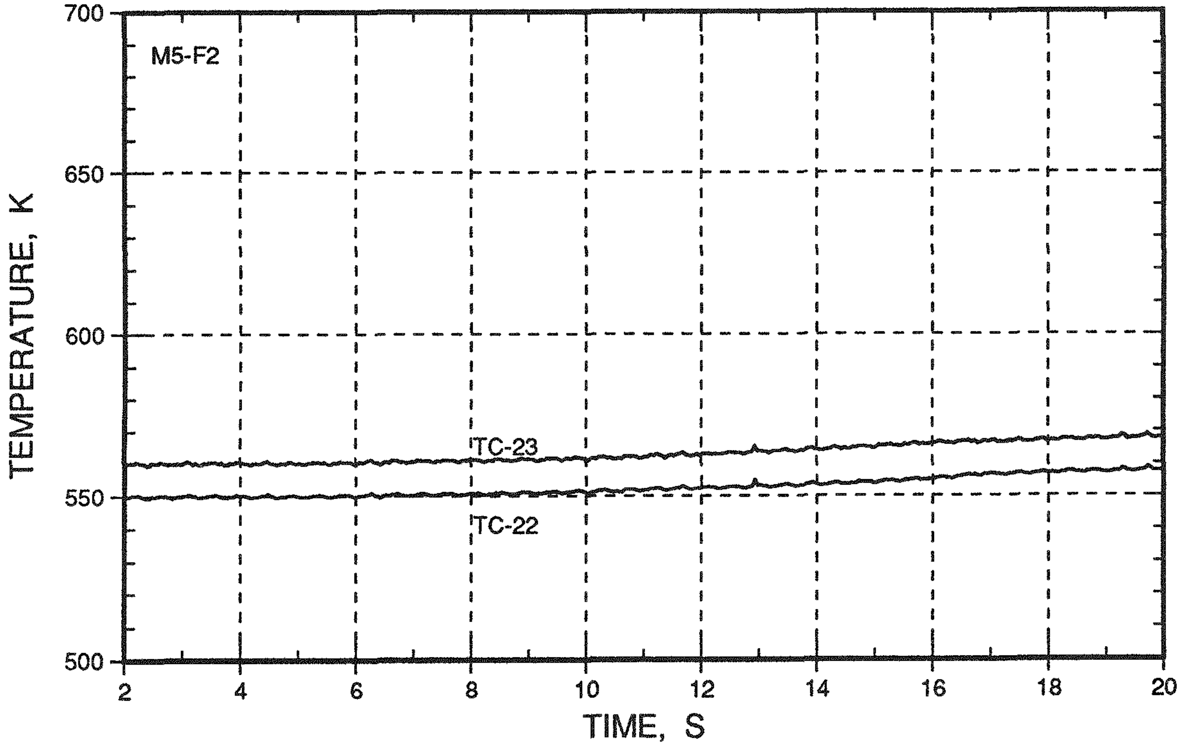

Fig. F.37. Temperatures in the Gas Plenum

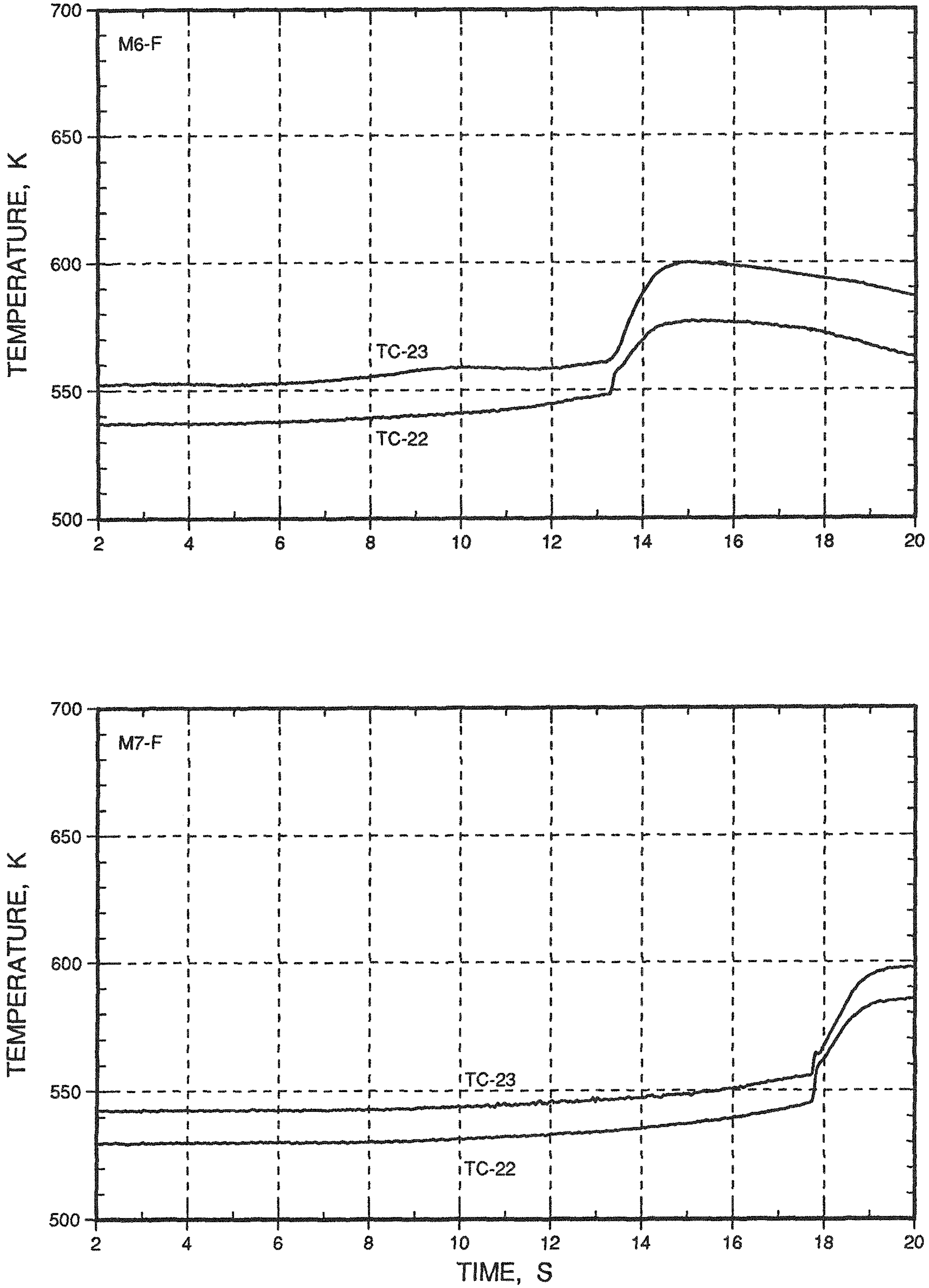

Fig. F.38. Temperatures in the Gas Plenum

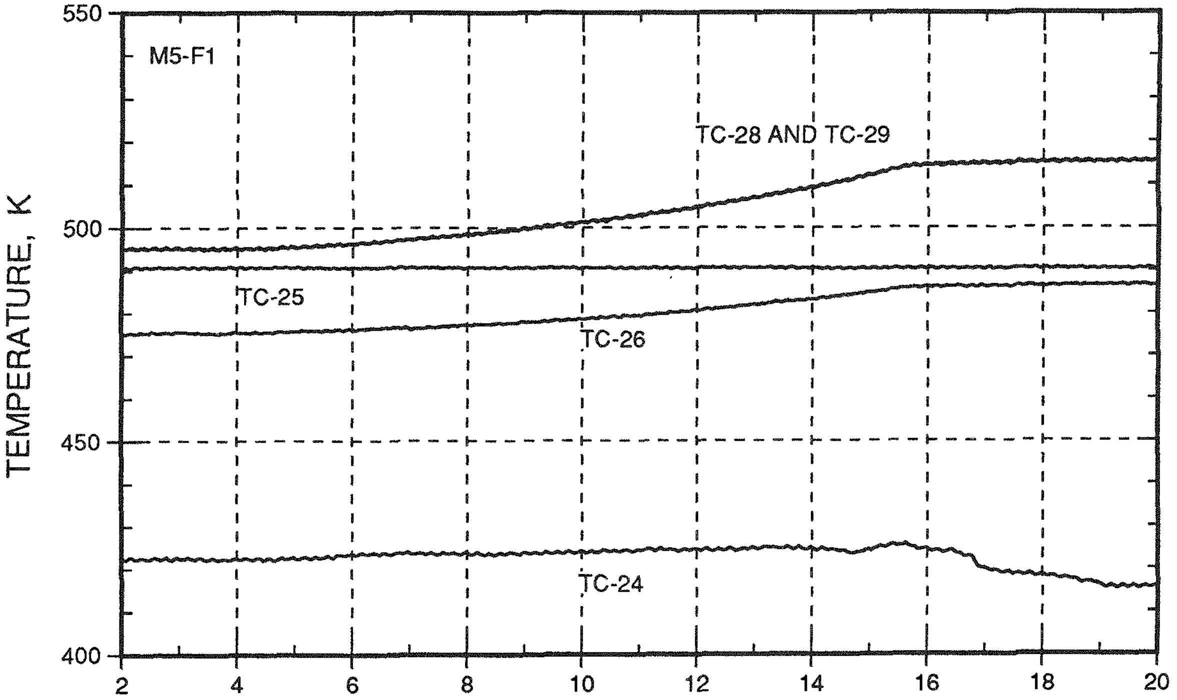

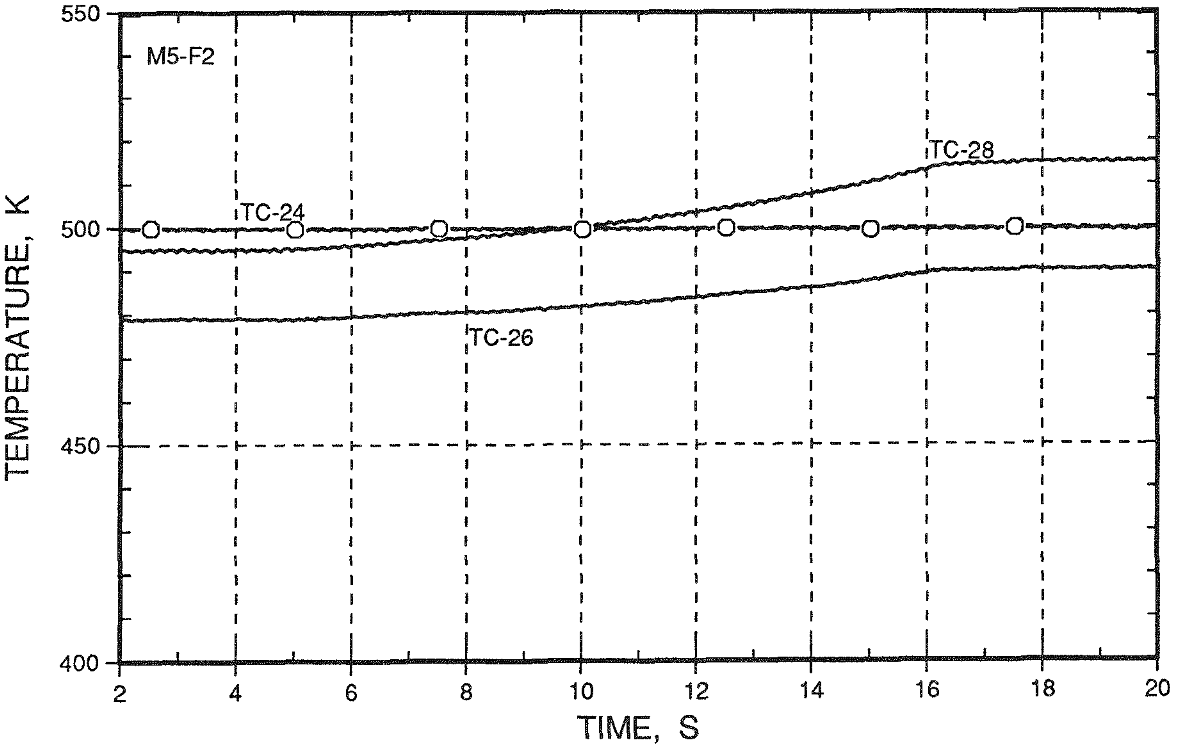

Fig. F.39. Flowmeter Magnet Temperatures

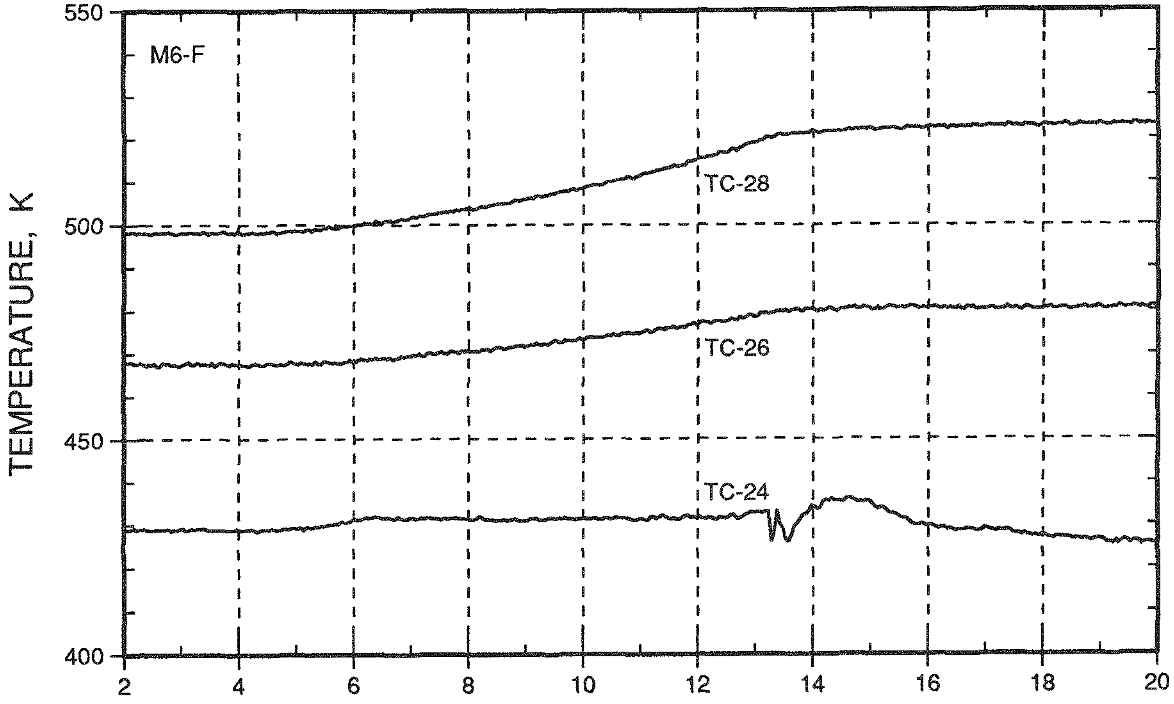

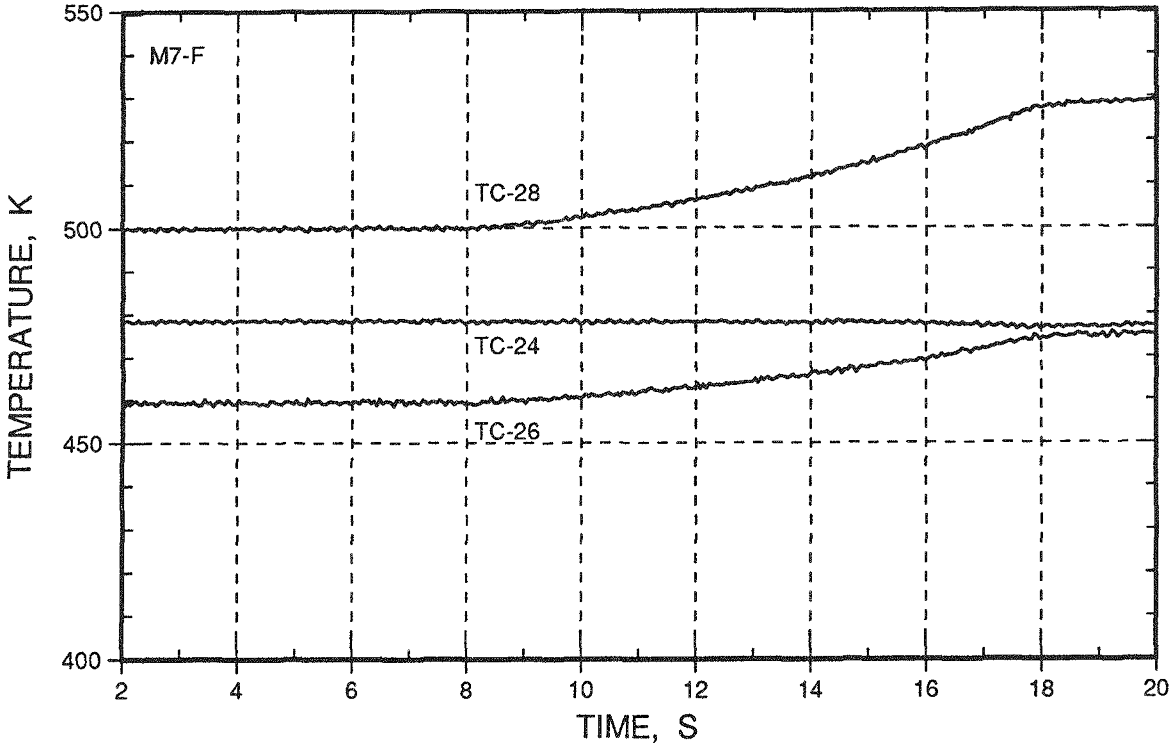

Fig. F.40. Flowmeter Magnet Temperatures

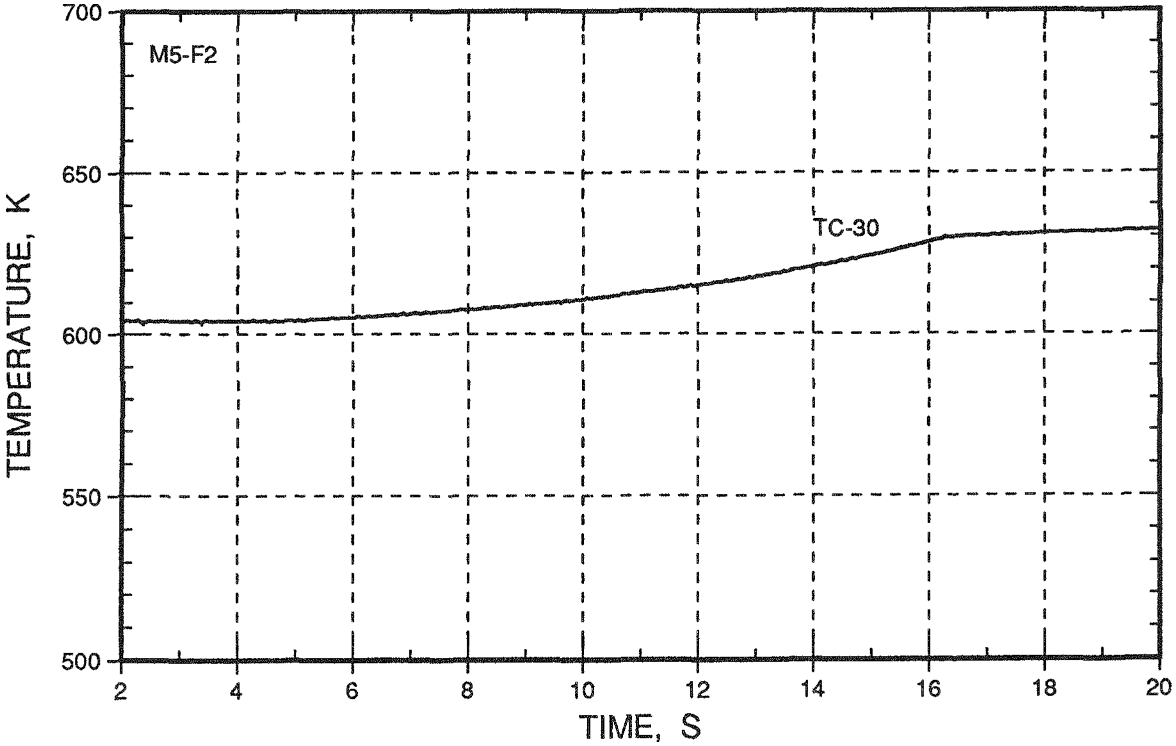

Fig. F.41. Temperatures of the Wall of the Loop Test Section

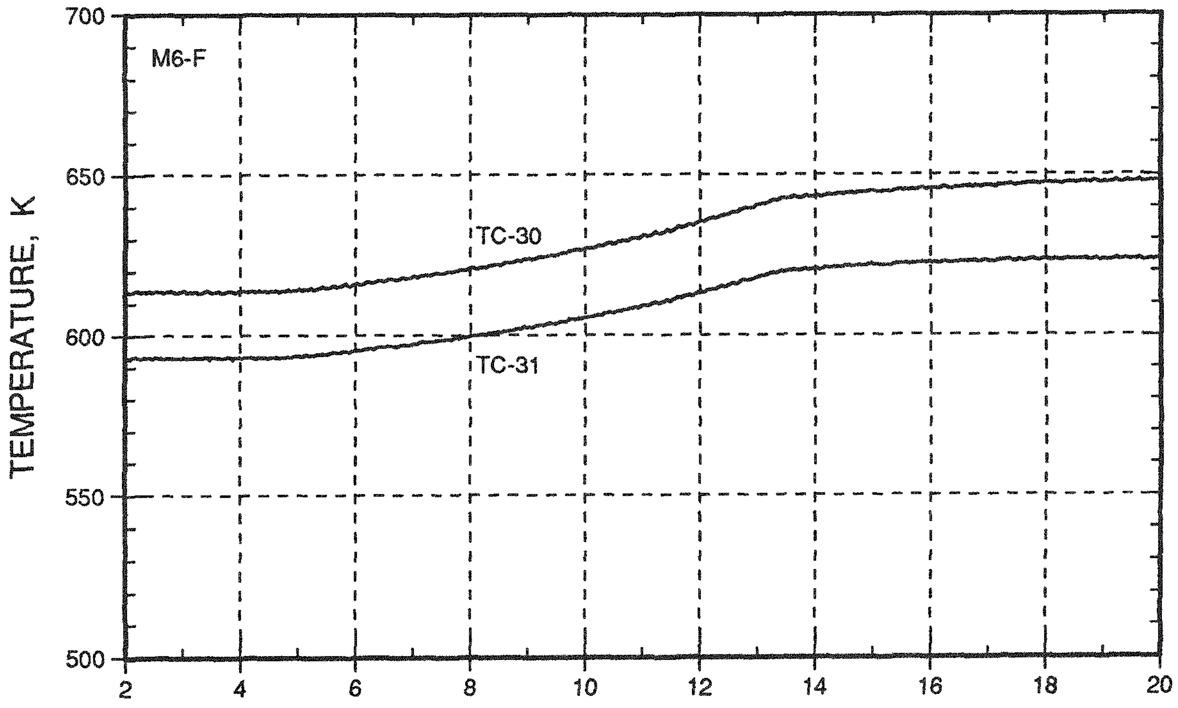

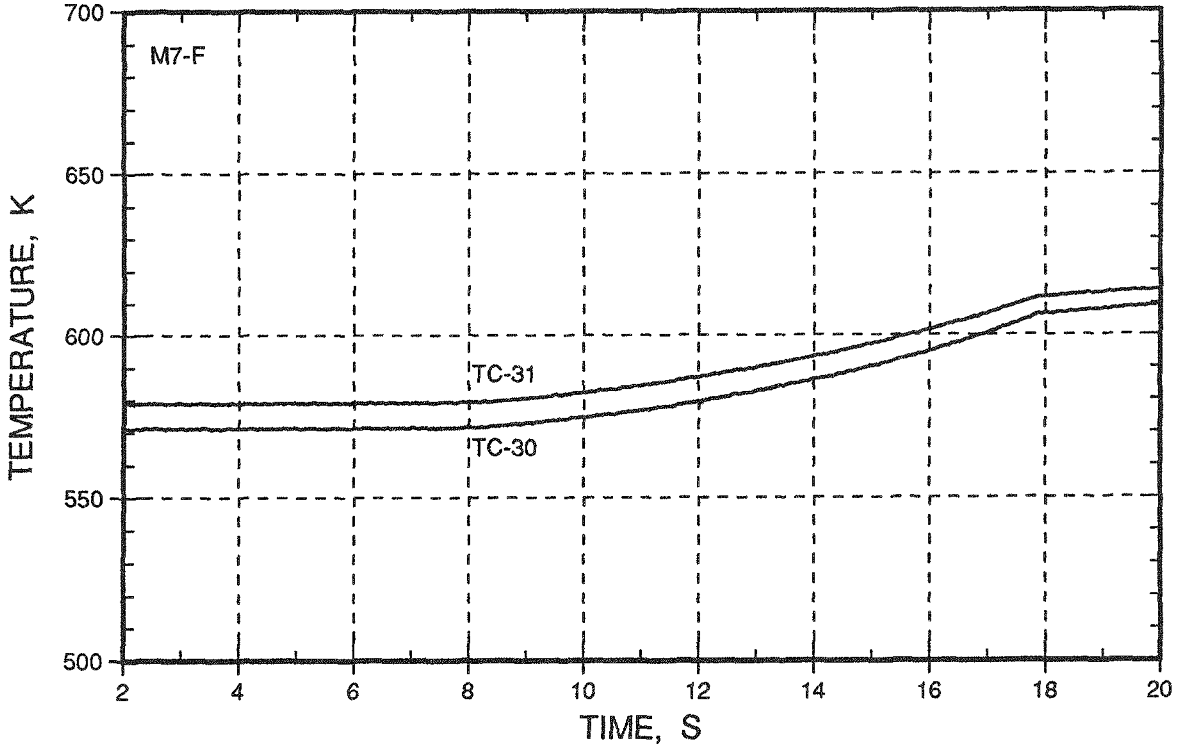

Fig. F.42. Temperatures of the Wall of the Loop Test Section

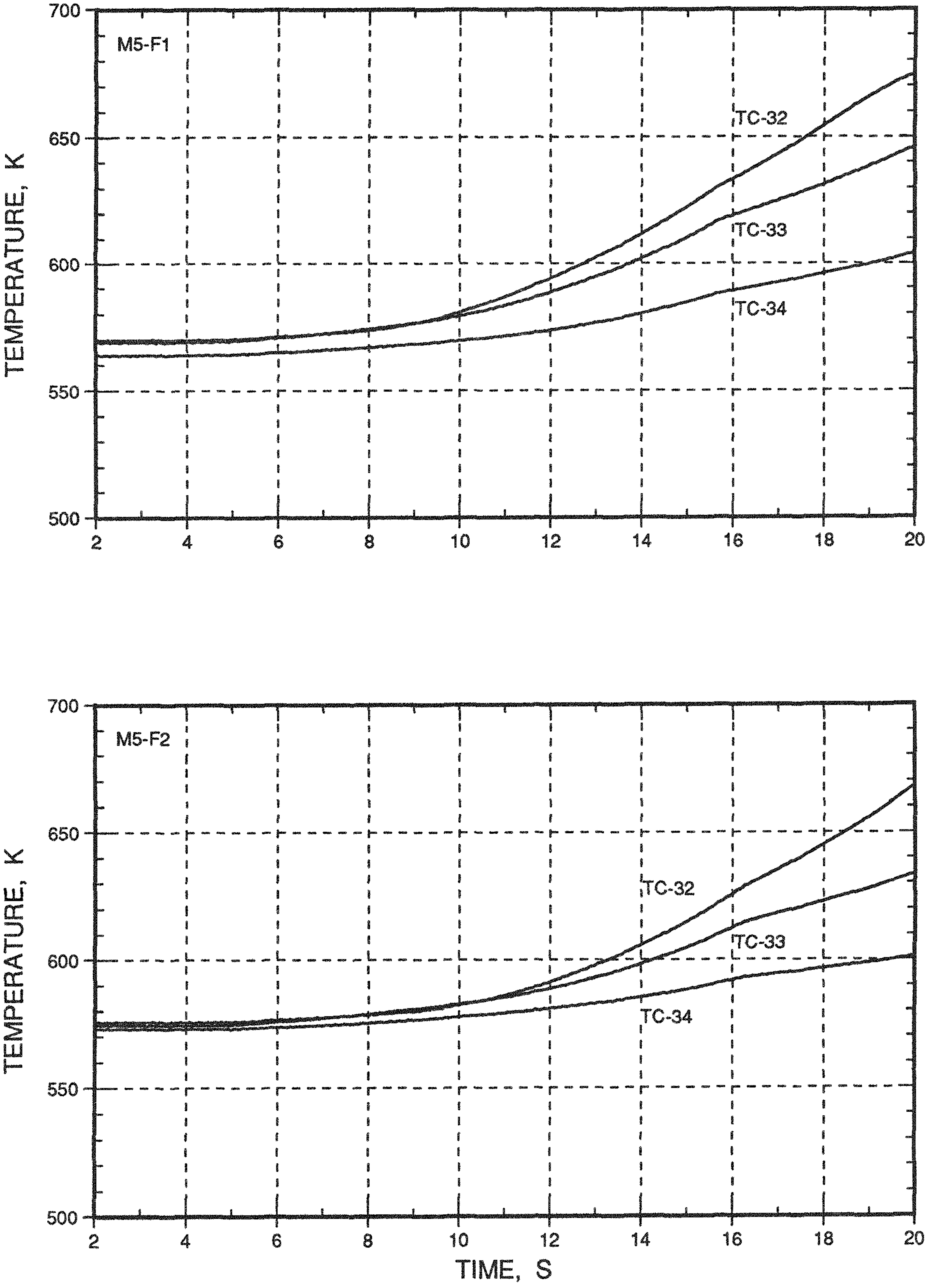

Fig. F.43. Temperatures of the Wall of the Loop Pump Leg

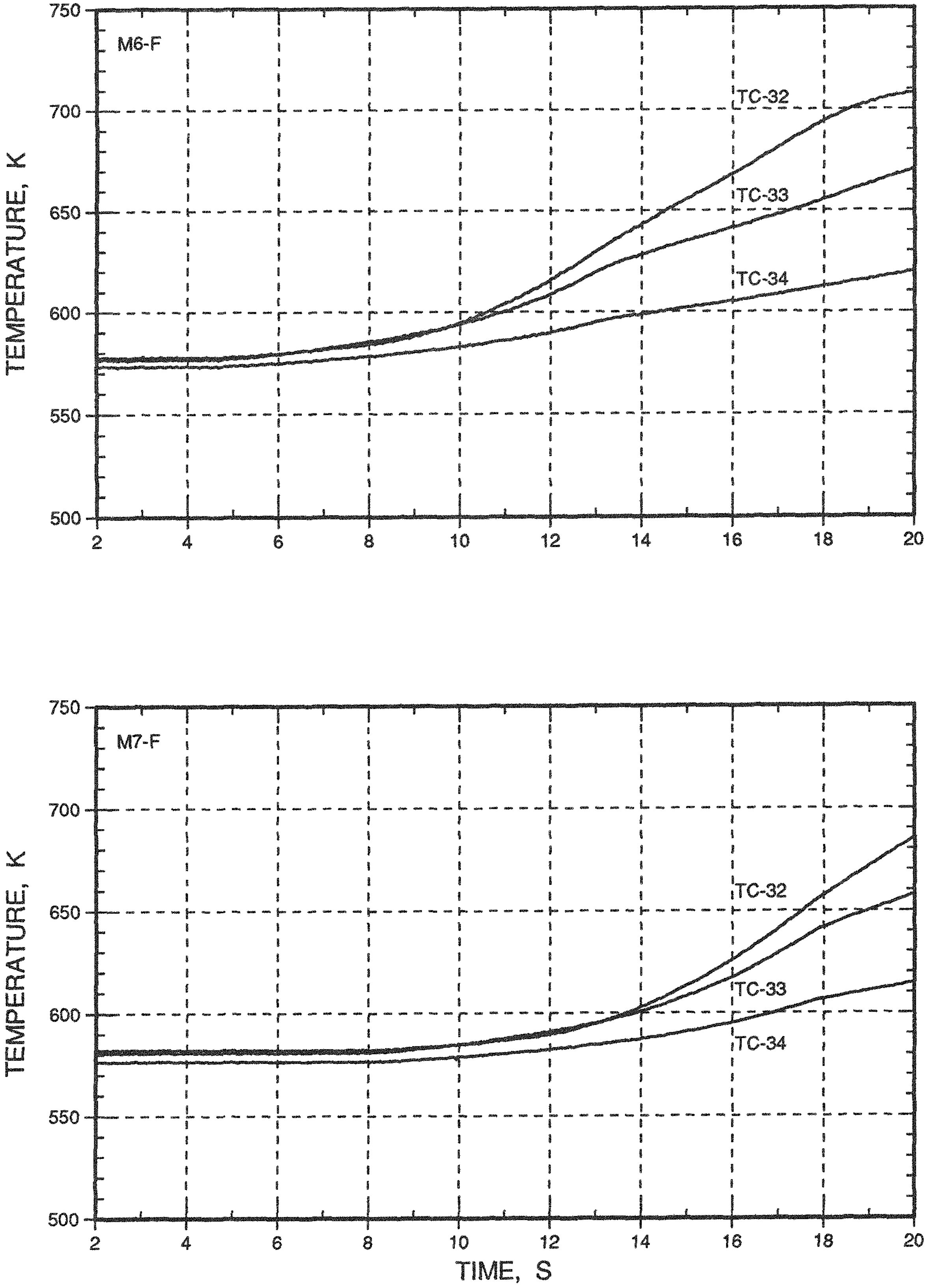

Fig. F.44. Temperatures of the Wall of the Loop Pump Leg

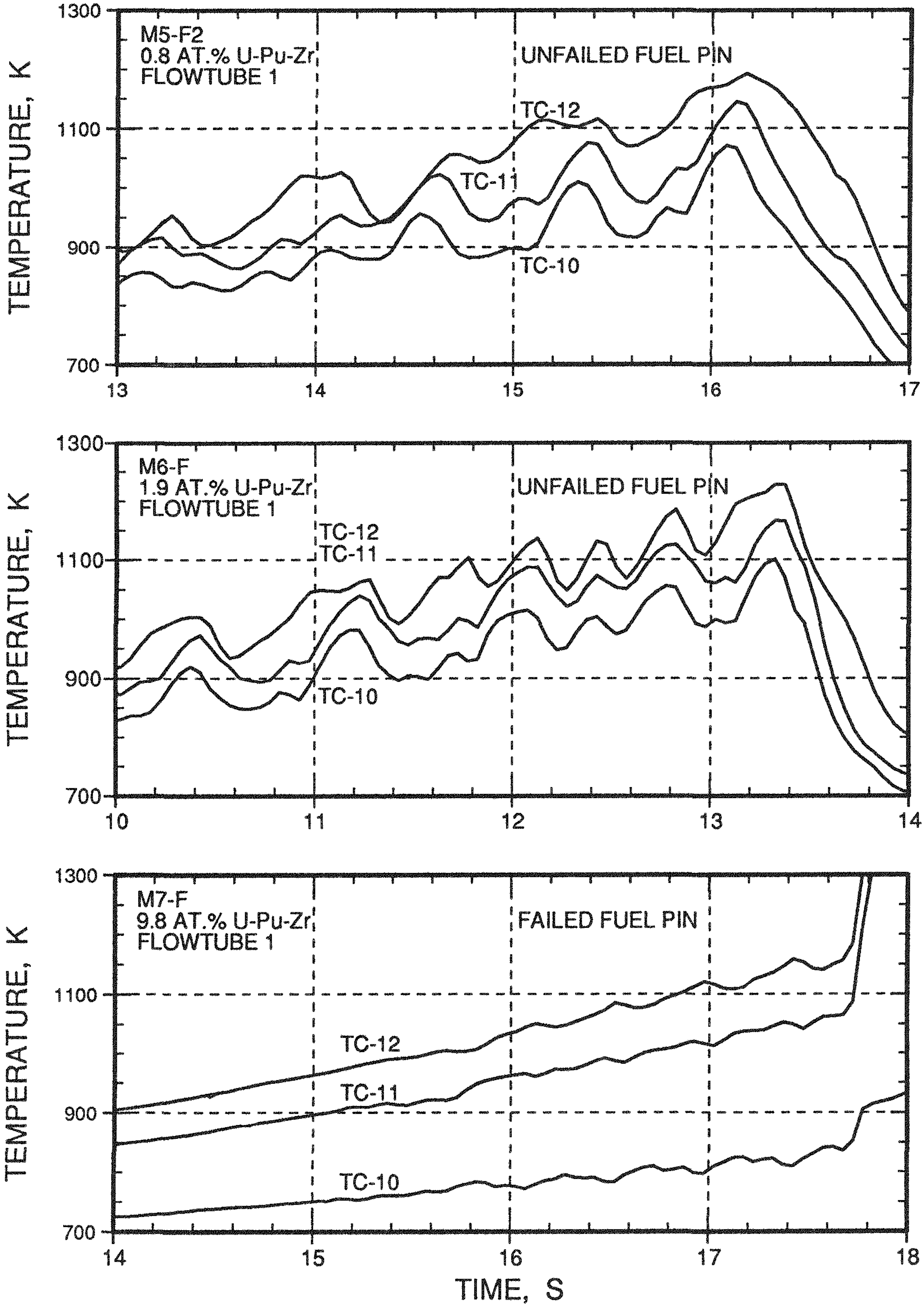

Fig. F.45. Temperature Oscillations along Flowtube 1

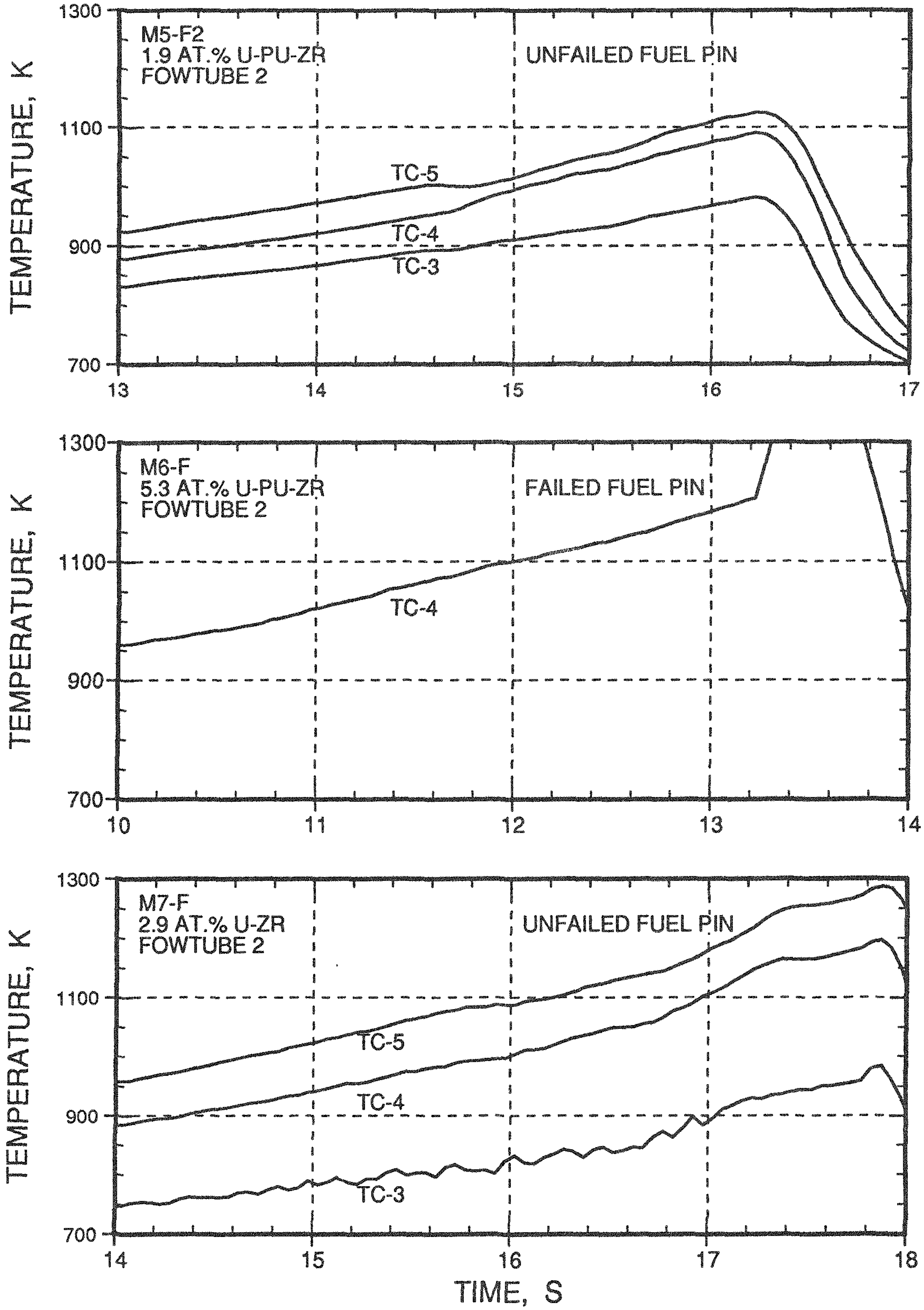

Fig. F.46. Temperatures along Flowtube 2

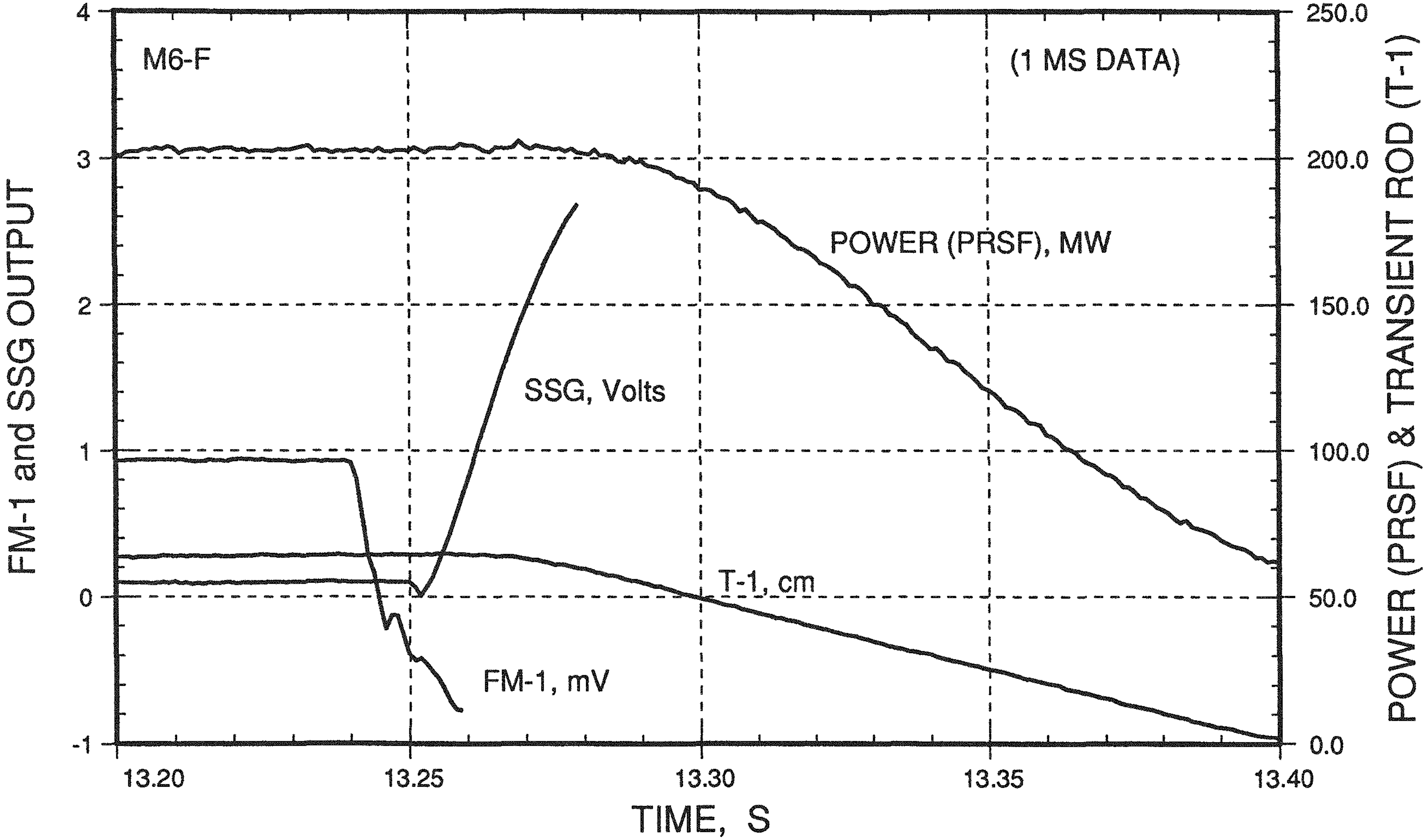

Fig. F.47. Event Sequence at Transient Termination

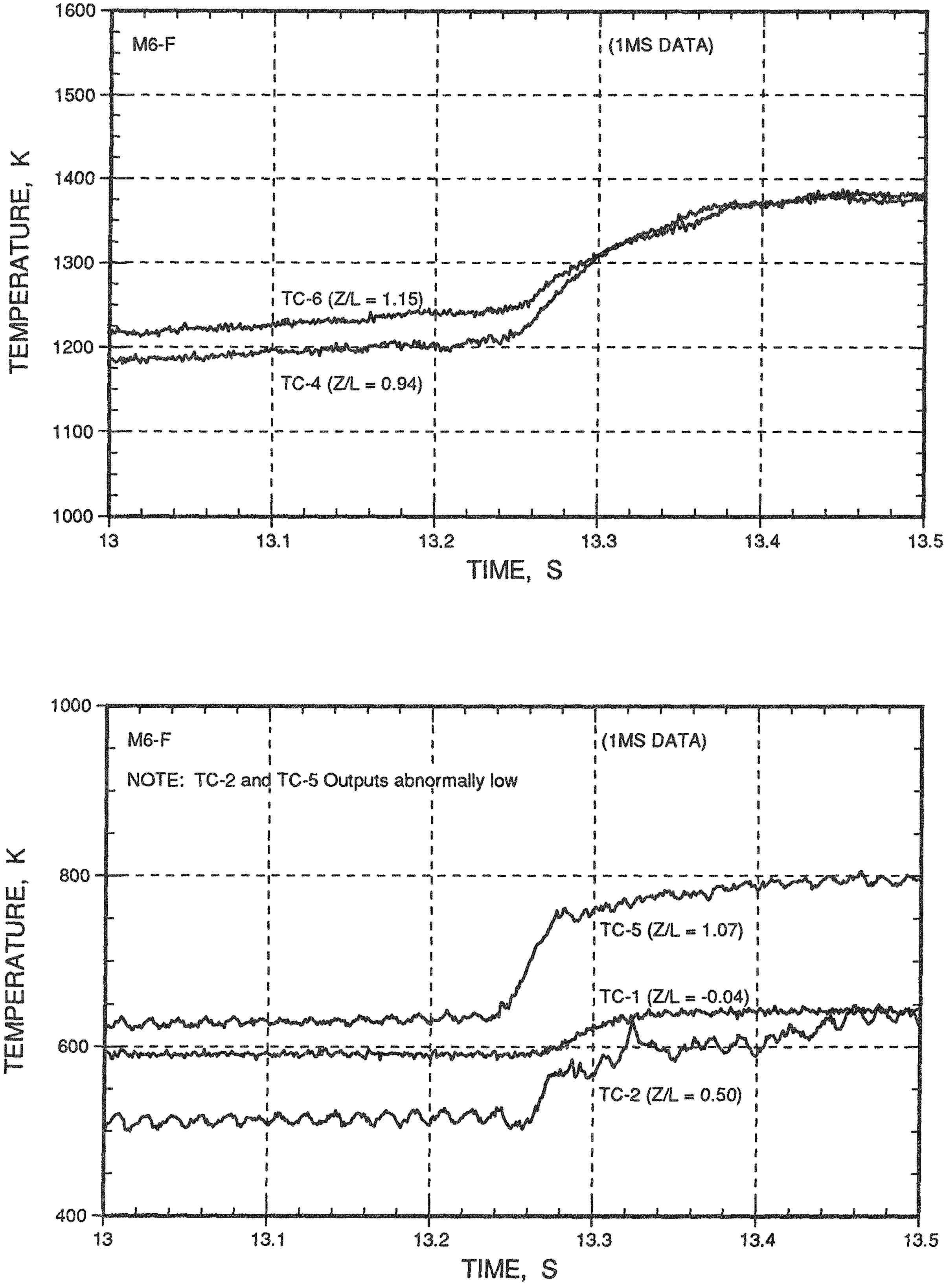

Fig. F48. Progression of Flowtube Temperature Rise at Fuel Pin Failure

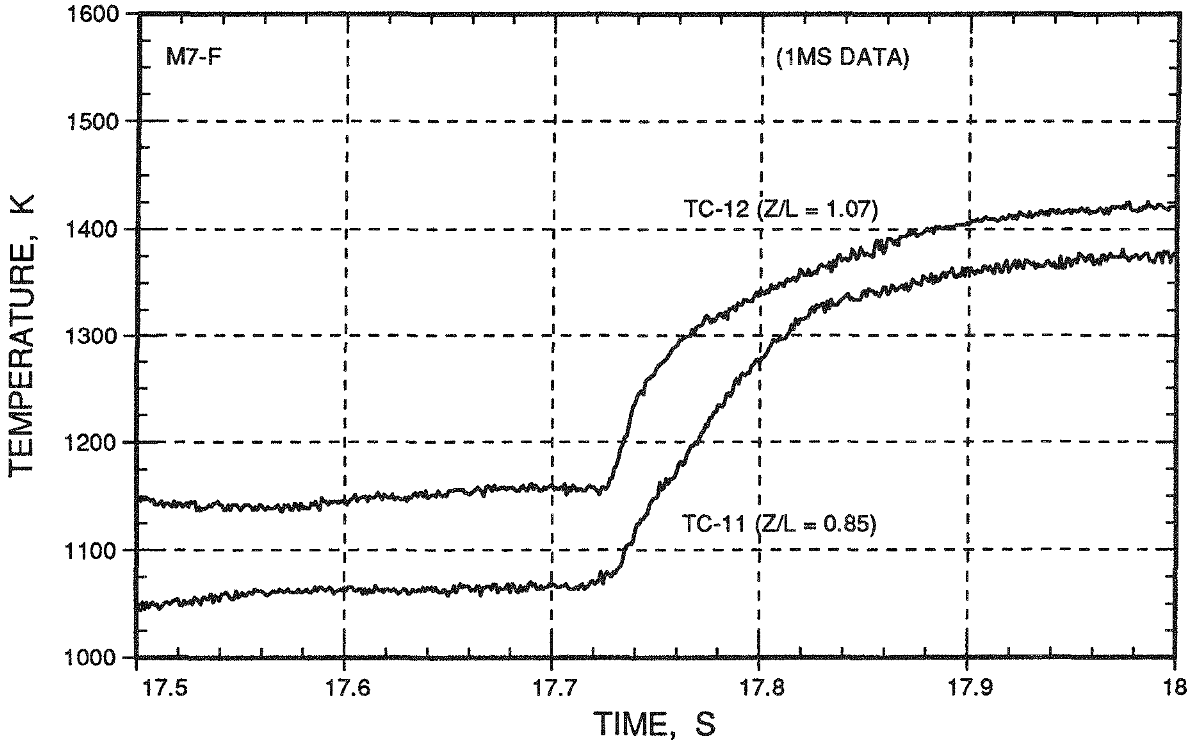

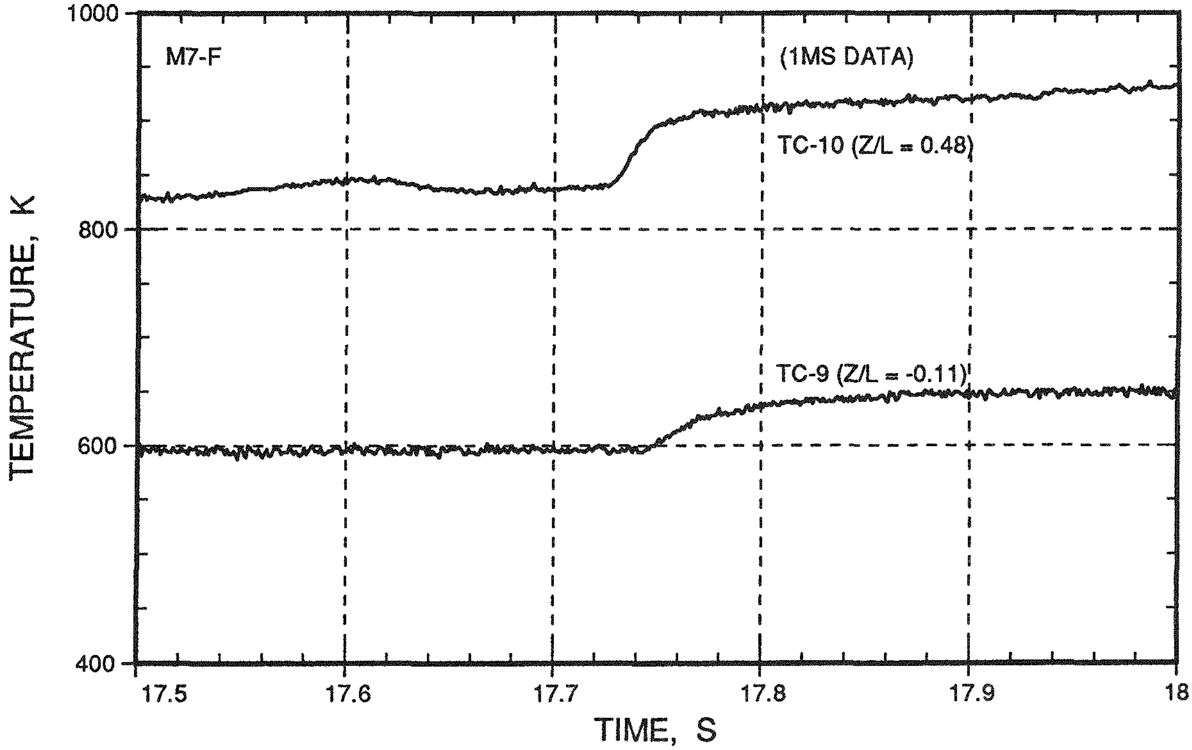

Fig. F.49. Progression of Flowtube Temperature Rise at Fuel Pin Failure

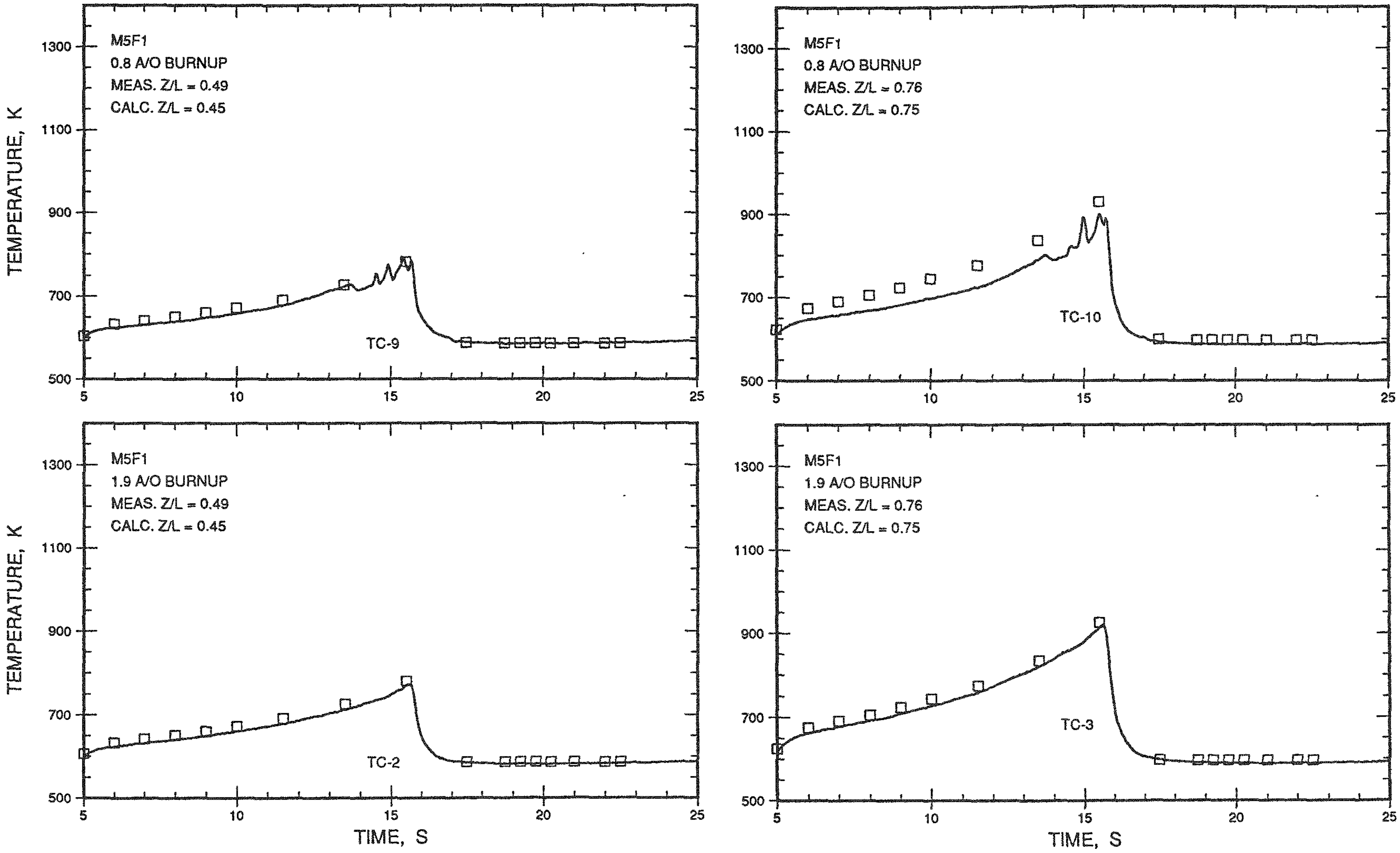

Fig. F.50. Measured and Calculated Flowtube Temperatures Below Top of Active Fuel Column (M5-F1, Z/L = 0.45 to 0.76)

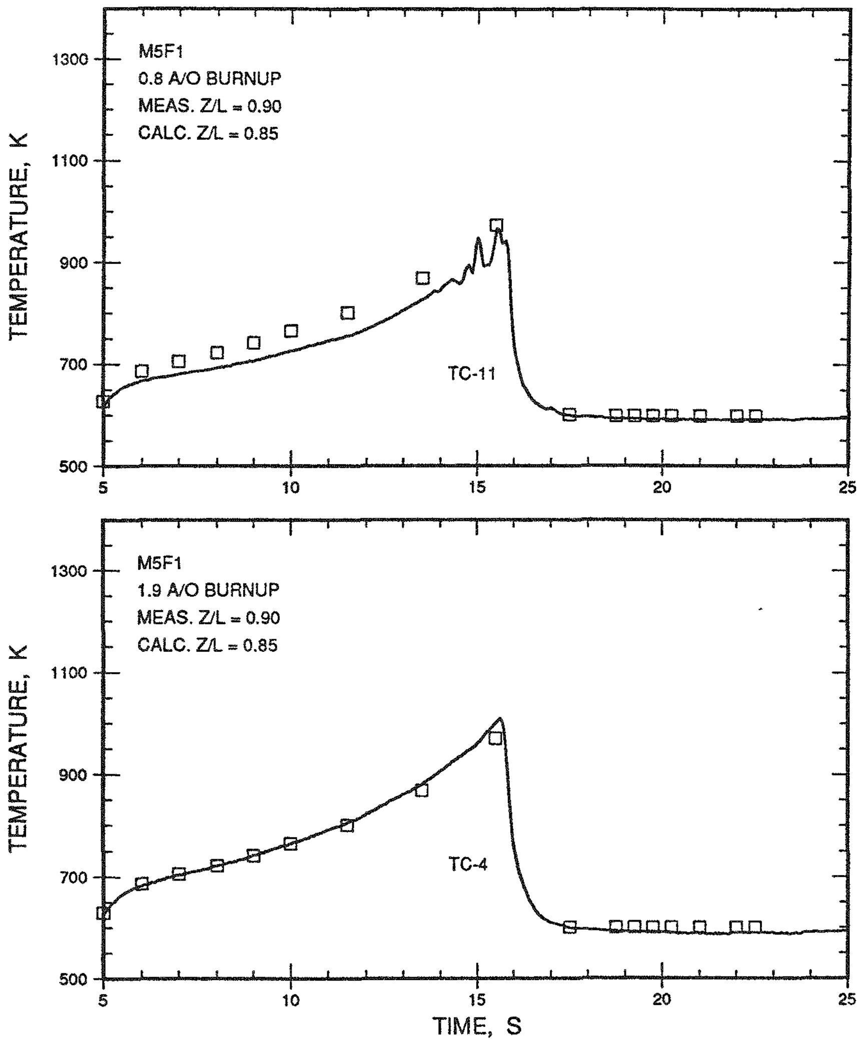

Fig. F.51. Measured and Calculated Flowtube Temperatures Below Top of Active Fuel Column (M5-F1, Z/L = 0.85 to 0.90)

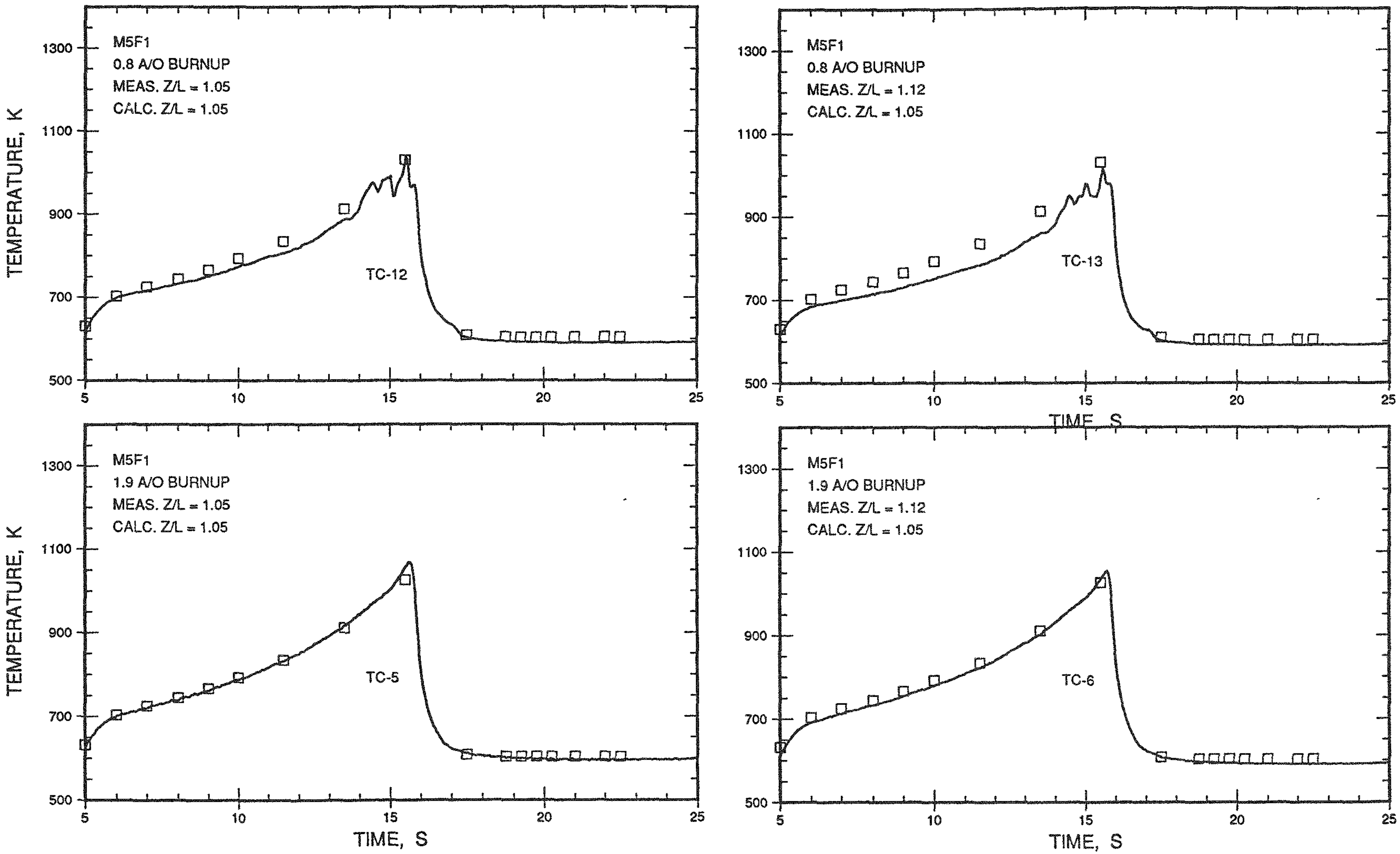

Fig. F.52. Measured and Calculated Flowtube Temperatures Above Top of Active Fuel Column (M5-F1, Z/L = 1.05 to 1.12)

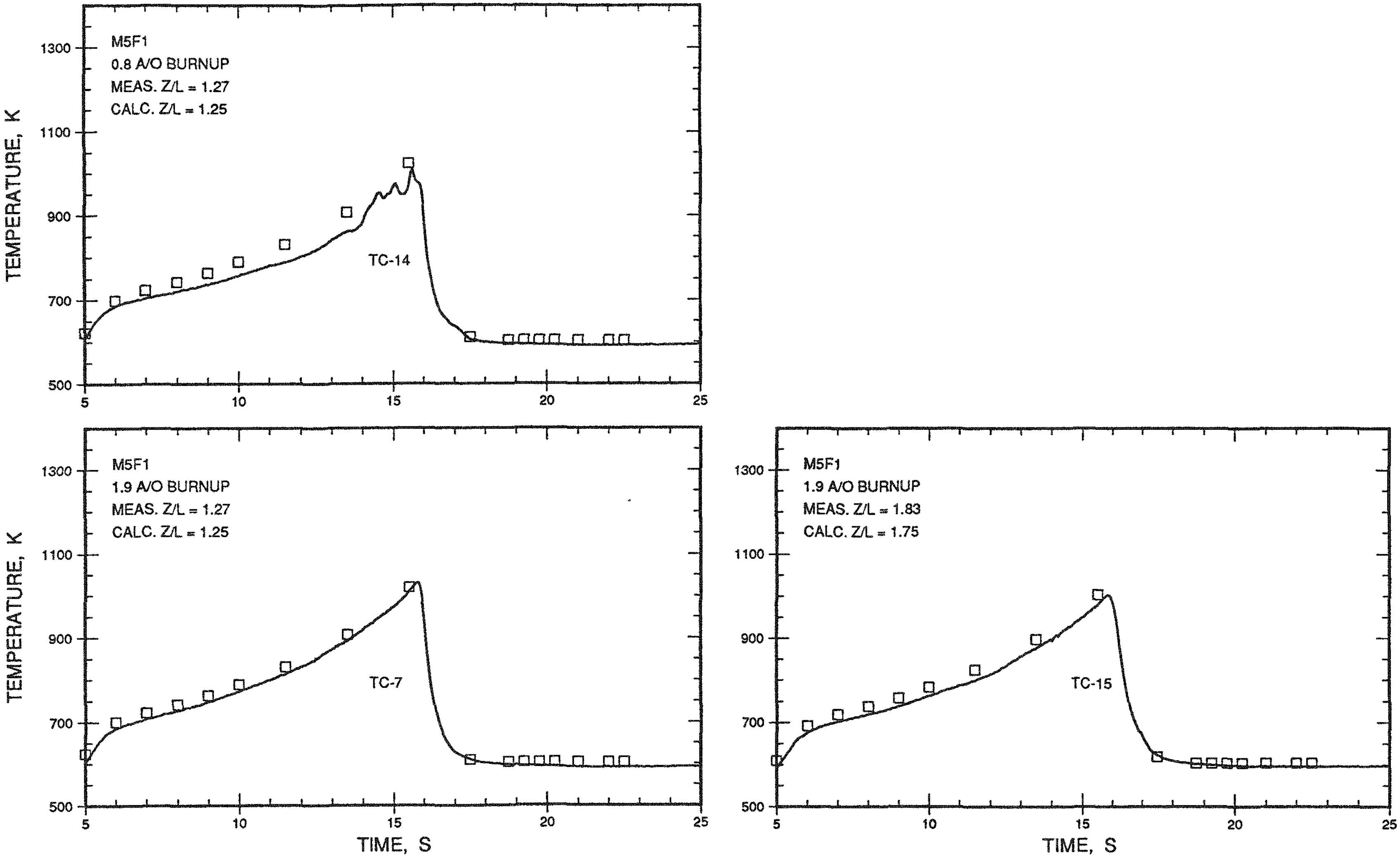

Fig. F.53. Measured and Calculated Flowtube Temperatures Above Top of Active Fuel Column (M5-F1, Z/L = 1.25 to 1.83)

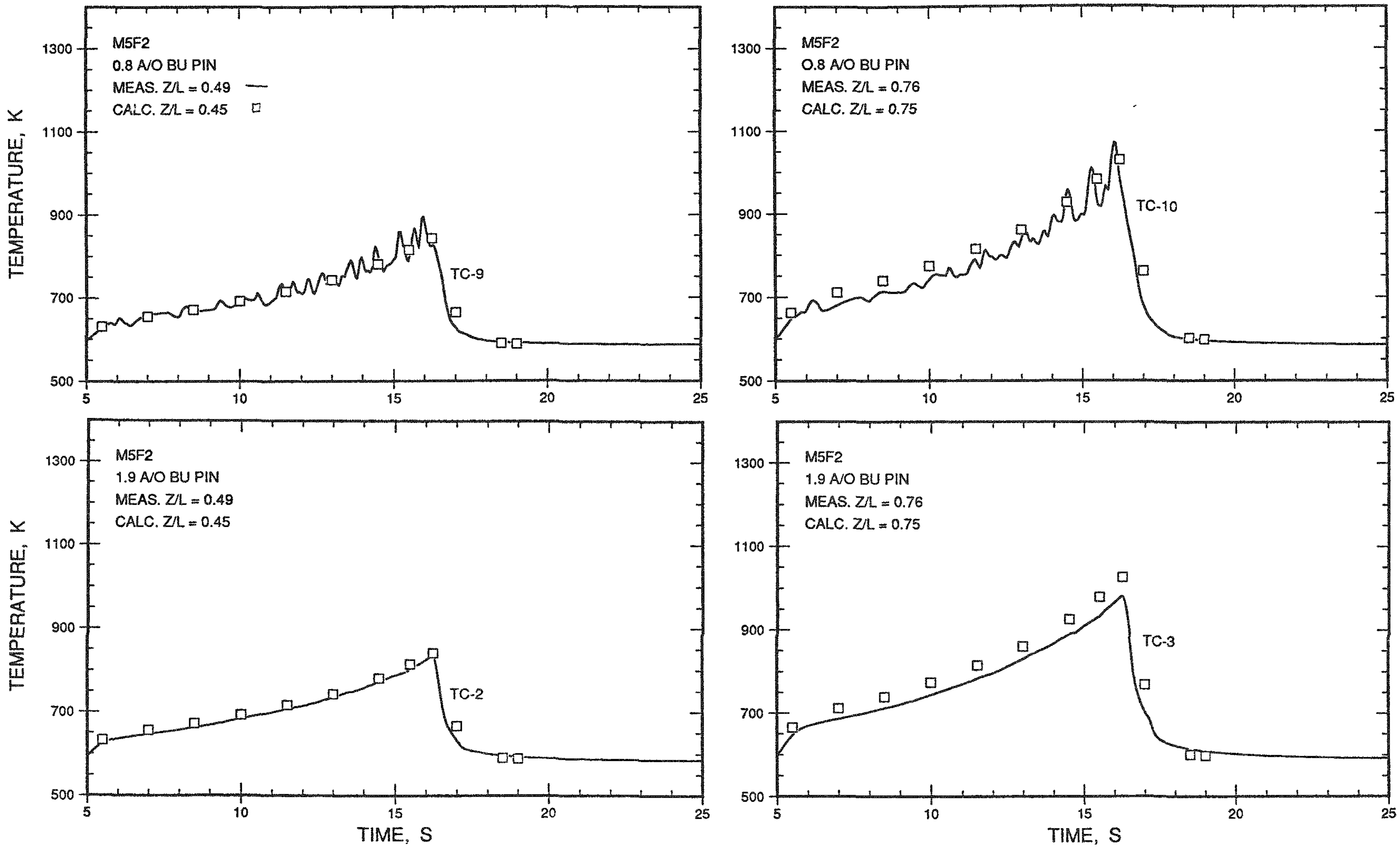

Fig. F.54. Measured and Calculated Flowtube Temperatures Below Top of Active Fuel Column (M5-F2, Z/L = 0.45 to 0.76)

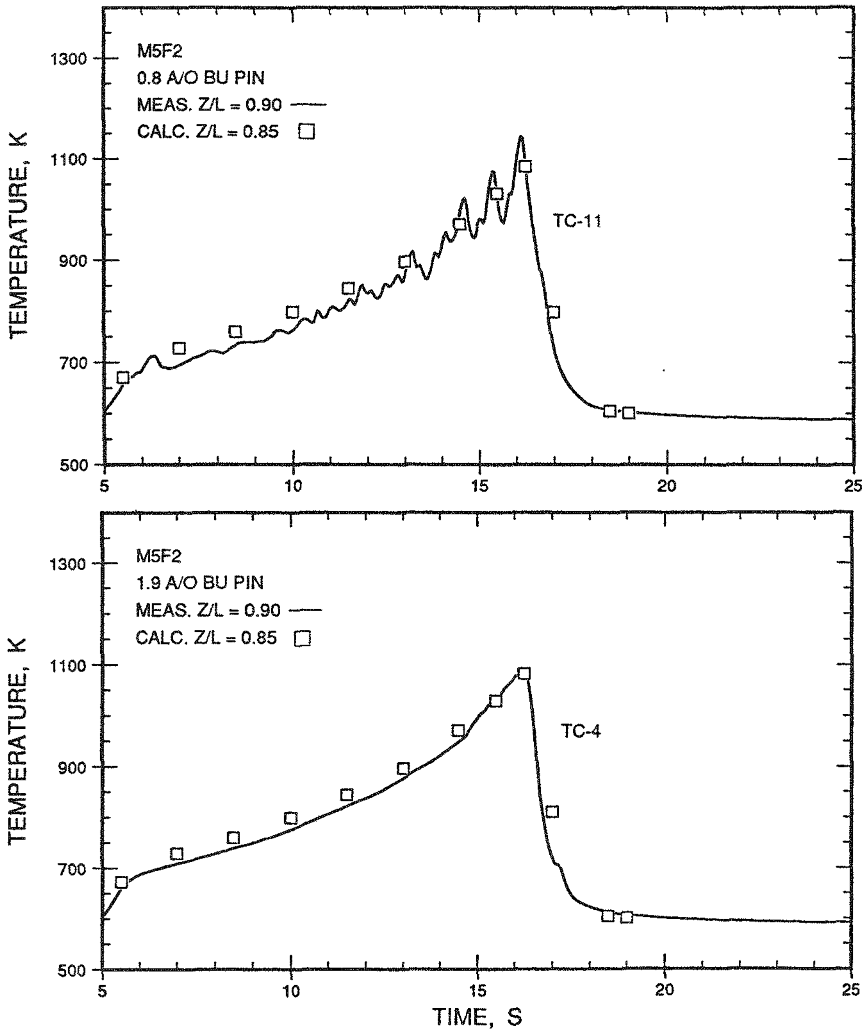

Fig. F.55. Measured and Calculated Flowtube Temperatures Below Top of Active Fuel Column (M5-F2, Z/L = 0.85 to 0.90)

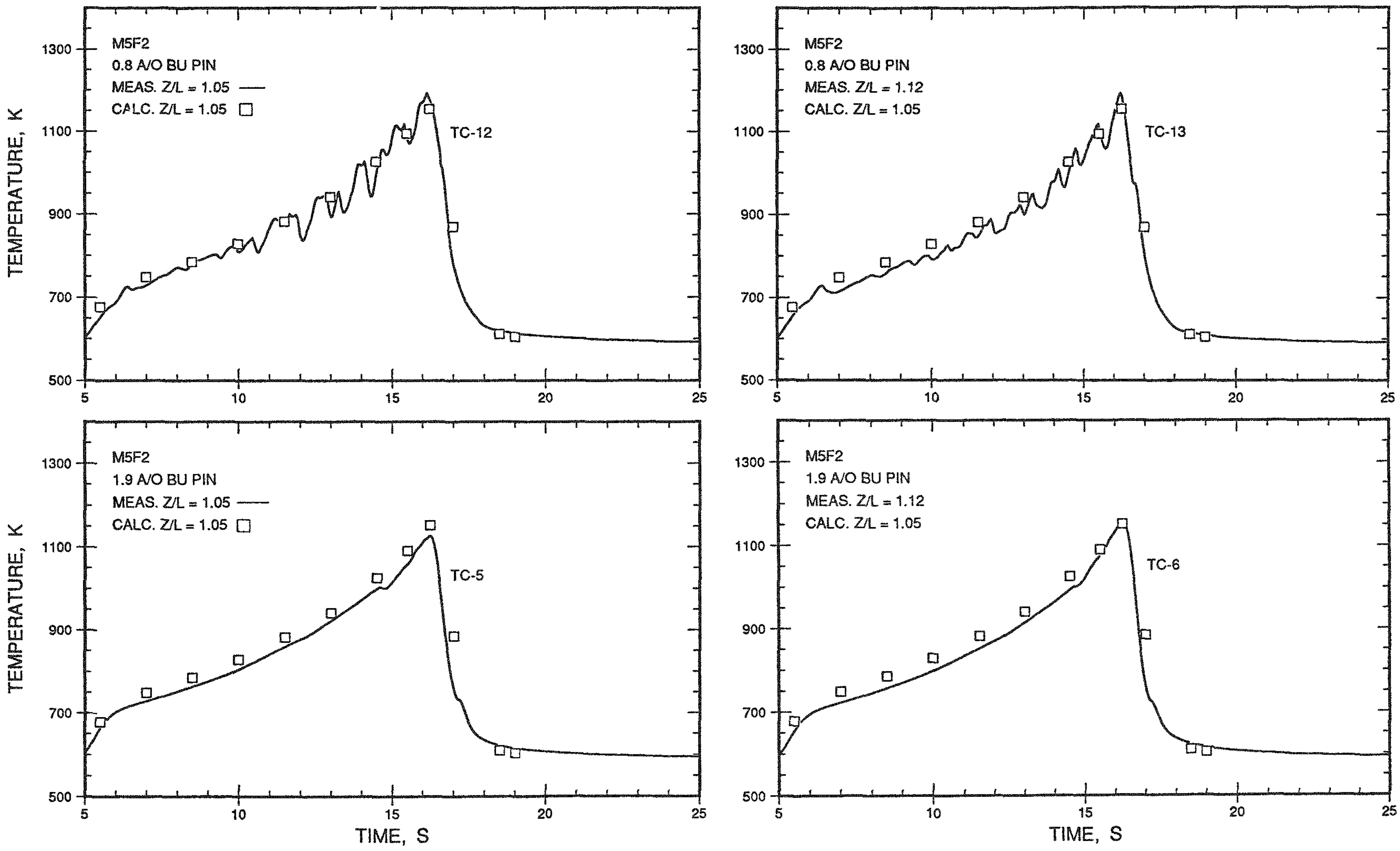

Fig. F.56. Measured and Calculated Flowtube Temperatures Above Top of Active Fuel Column (M5-F2, Z/L = 1.05 to 1.12)

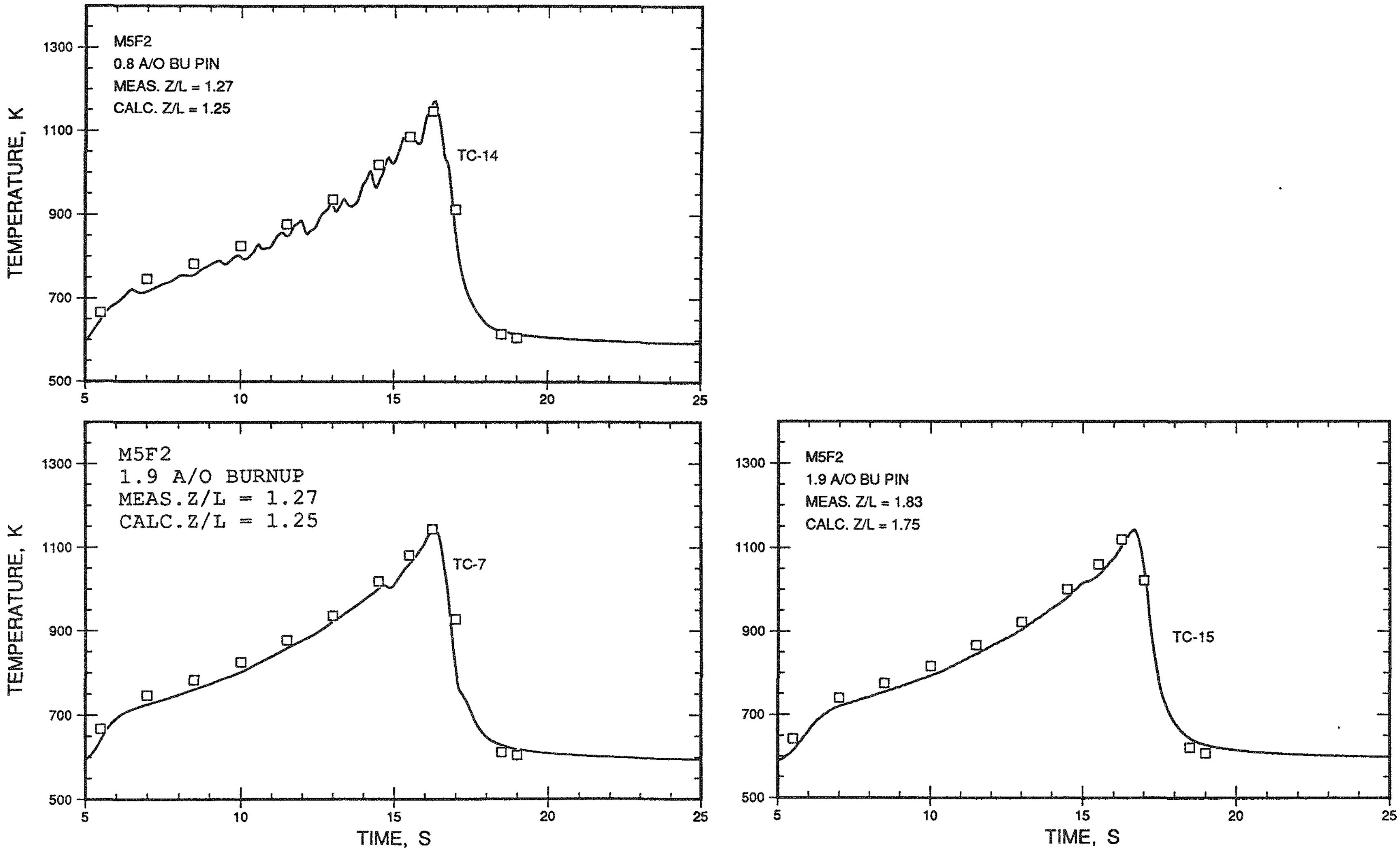

Fig. F.57. Measured and Calculated Flowtube Temperatures Above Top of Active Fuel Column (M5-F2, Z/L = 1.25 to 1.83)

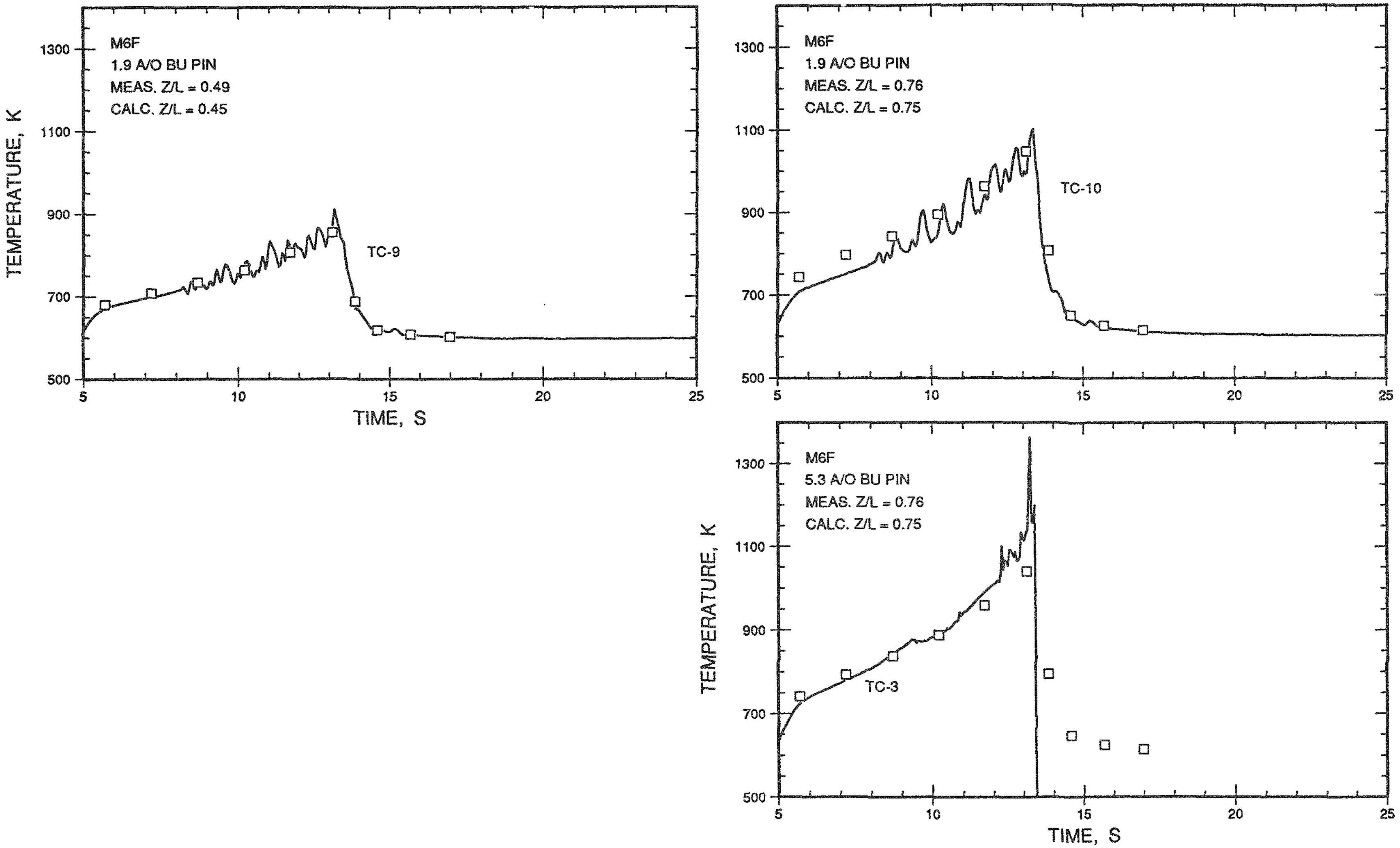

Fig. F.58. Measured and Calculated Flowtube Temperatures Below Top of Active Fuel Column (M6, Z/L = 0.45 to 0.76)

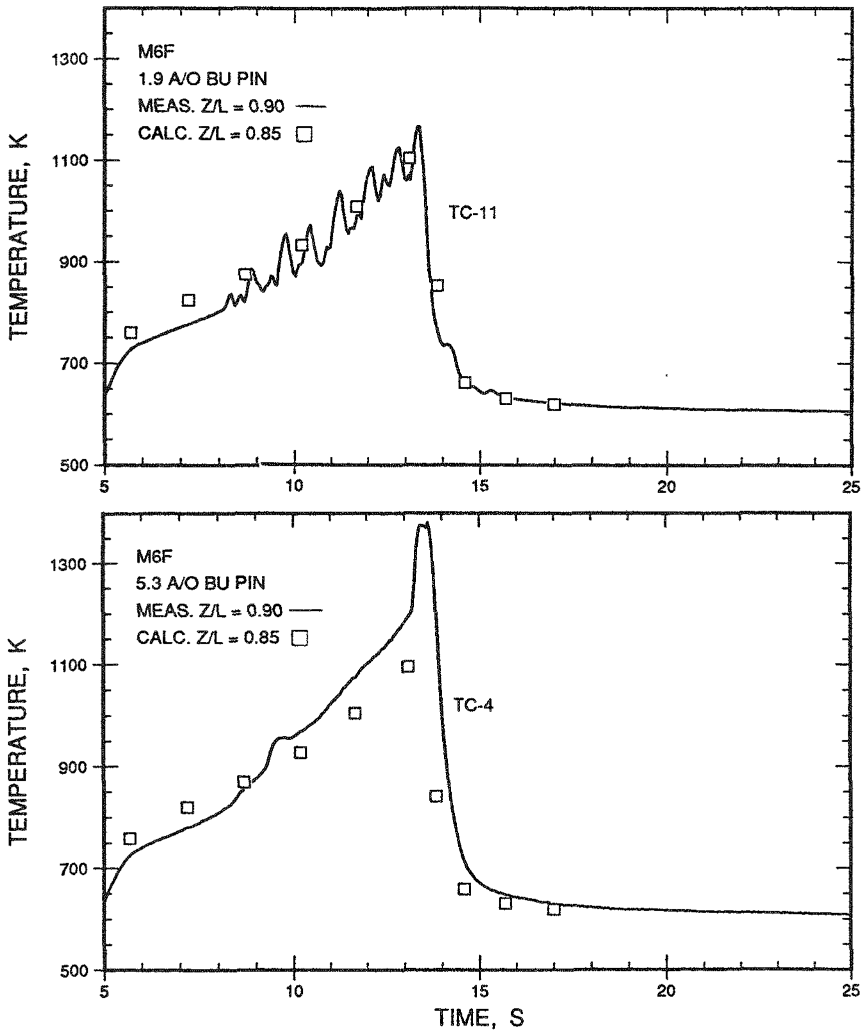

Fig. F.59. Measured and Calculated Flowtube Temperatures Below Top of Active Fuel Column (M6, Z/L = 0.85 to 0.90)

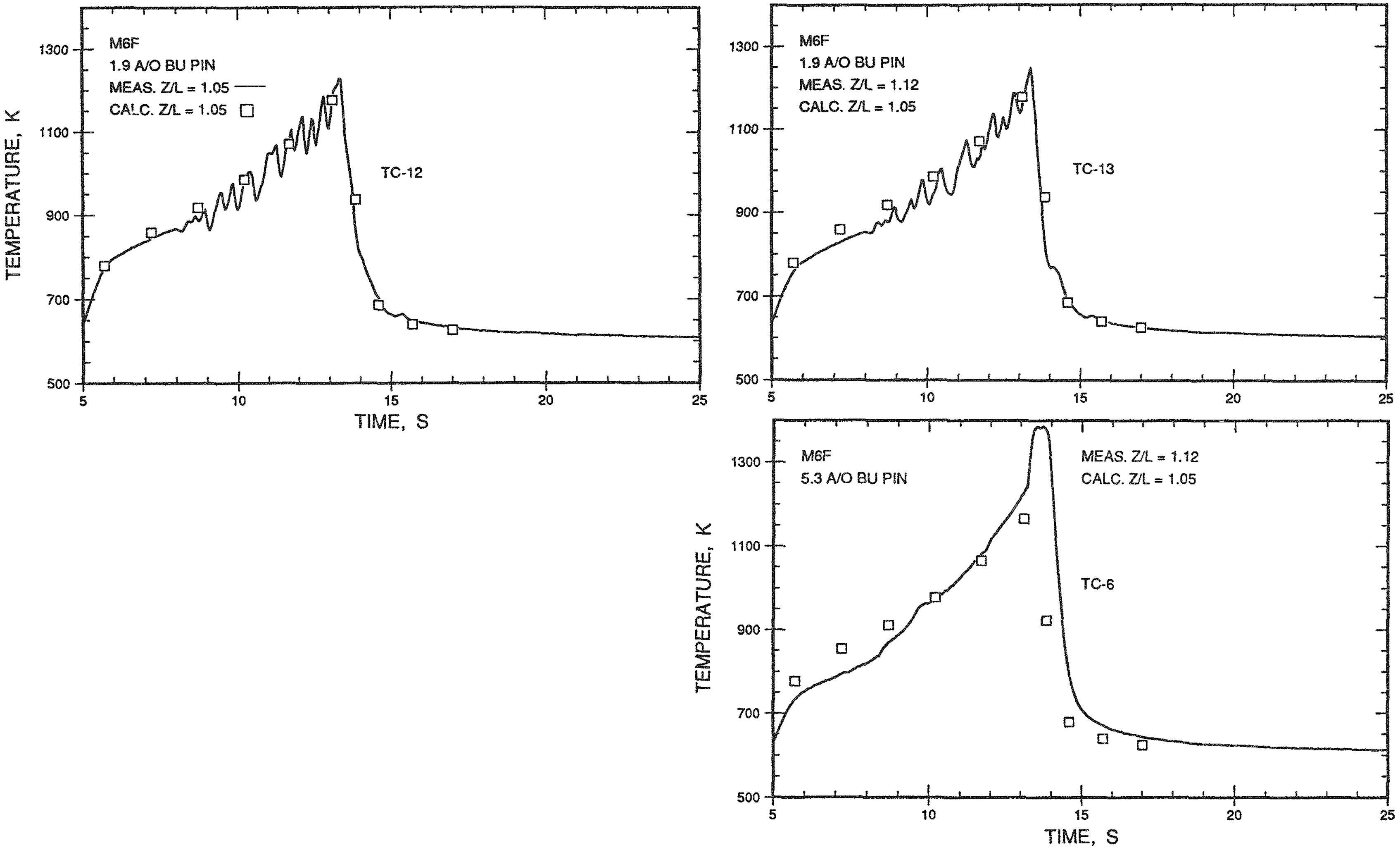

Fig. F.60. Measured and Calculated Flowtube Temperatures Above Top of Active Fuel Column (M6, Z/L = 1.05 to 1.12)

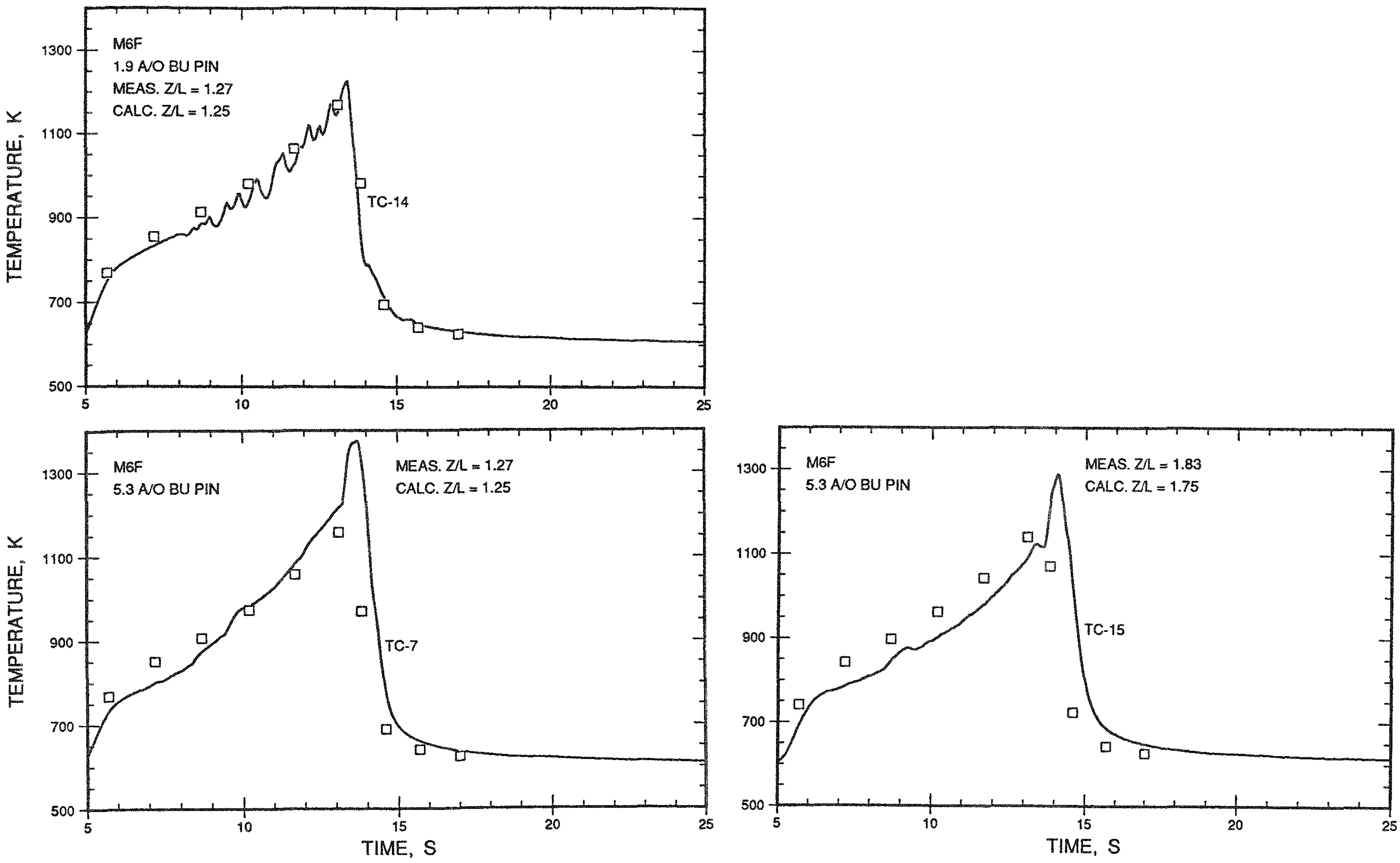

Fig. F.61. Measured and Calculated Flowtube Temperatures Above Top of Active Fuel Column (M6, Z/L = 1.25 to 1.83)

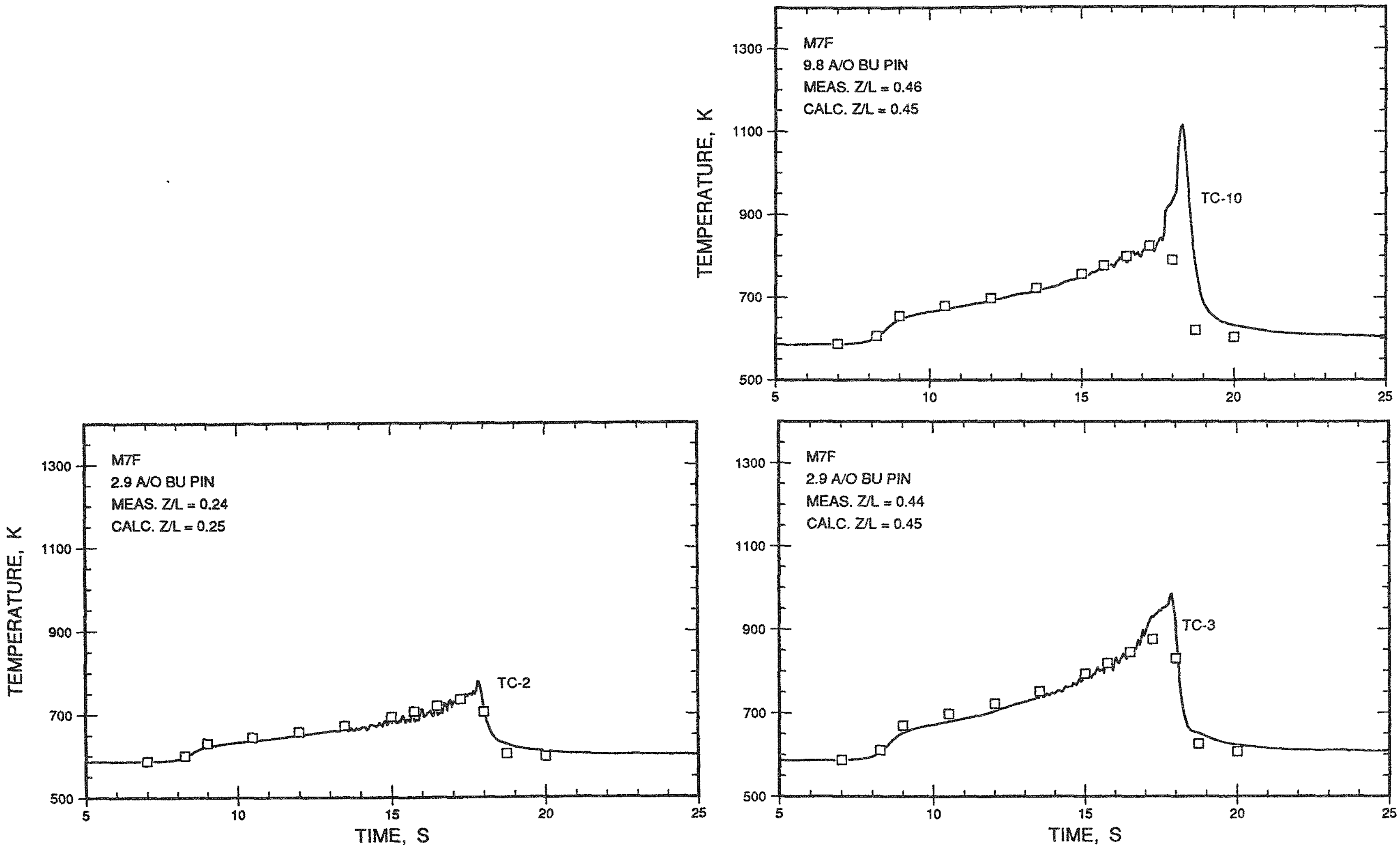

Fig. F.62. Measured and Calculated Flowtube Temperatures Below Top of Active Fuel Column (M7, Z/L = 0.24 to 0.46)

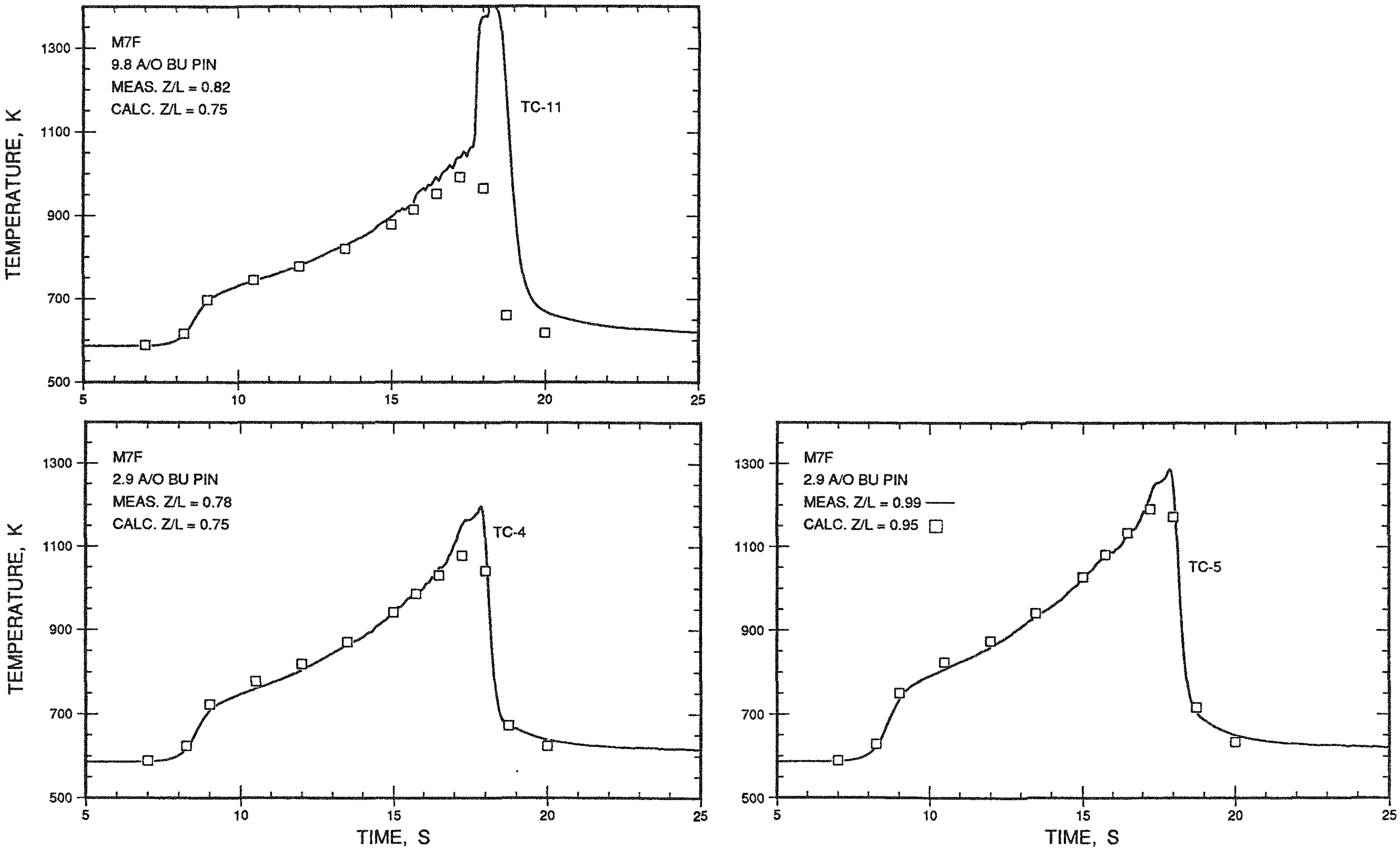

Fig. F.63. Measured and Calculated Flowtube Temperatures Below Top of Active Fuel Column (M7, Z/L = 0.75 to 0.99)

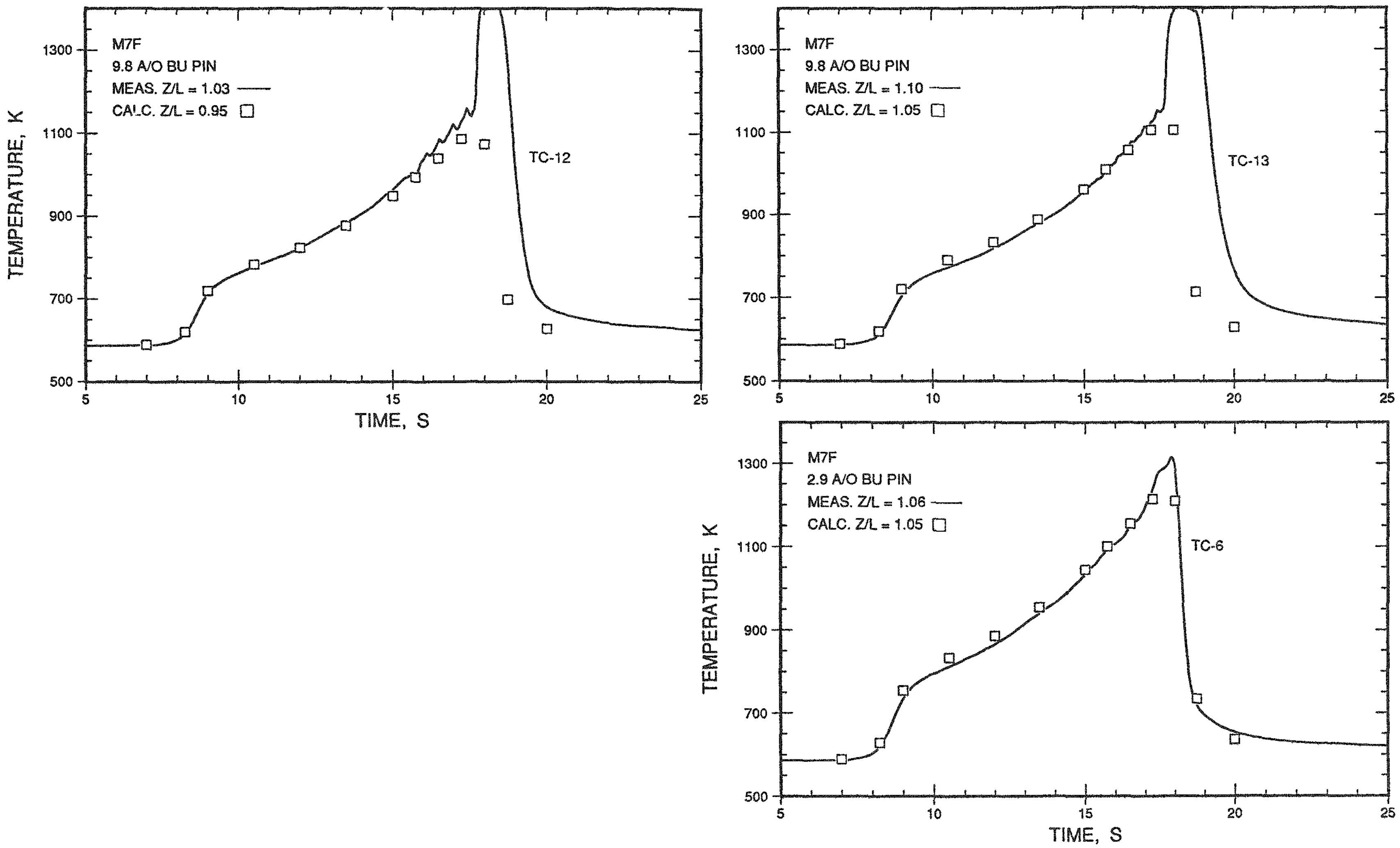

Fig. F.64. Measured and Calculated Flowtube Temperatures Above Top of Active Fuel Column (M7, Z/L = 1.03 to 1.10)

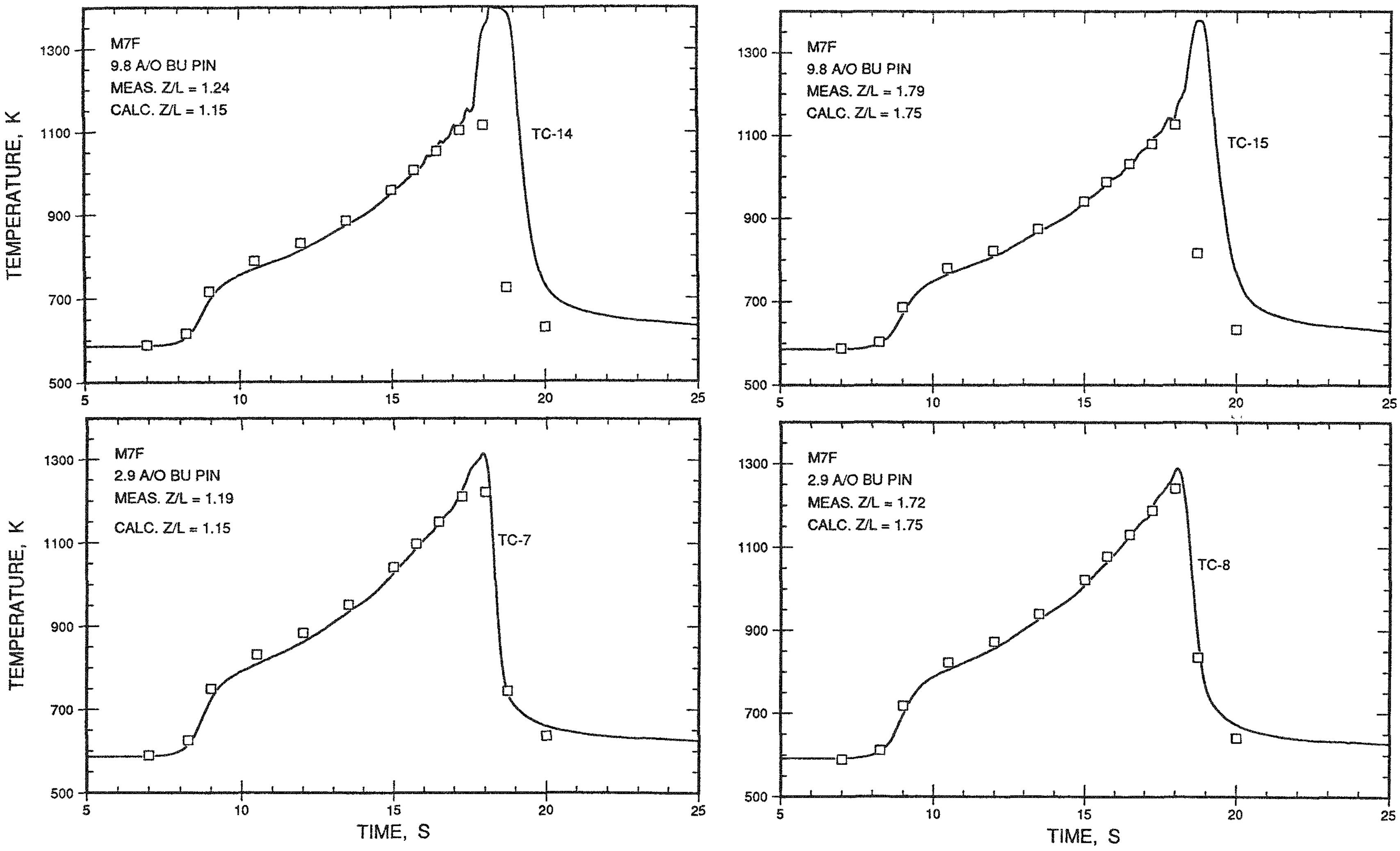

Fig. F.65. Measured and Calculated Flowtube Temperatures Above Top of Active Fuel Column (M7, Z/L = 1.15 to 1.79)

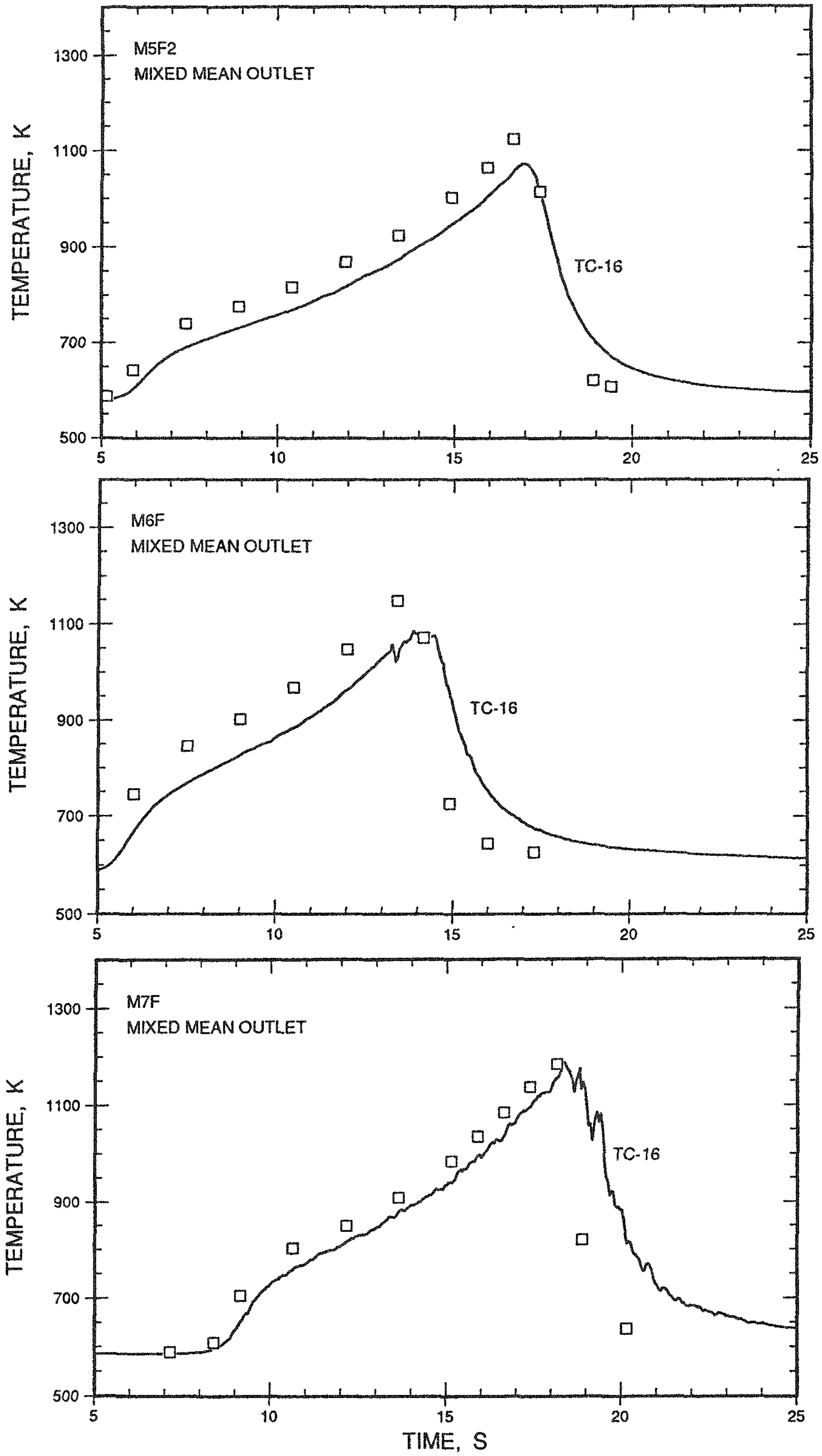

Fig. F.66. In-sodium Measured Temperatures (TC-16) and Mixed Mean Calculated Fuel Temperatures above the Top of the Fuel Column (with a simple time delay applied to the calculations for the coolant to reach the downstream location of TC-16)

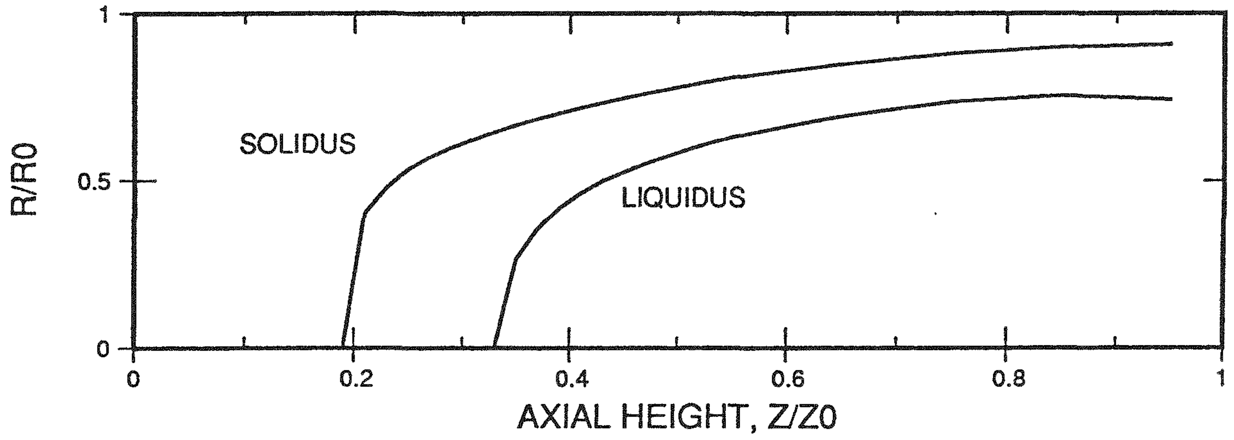

M7 TERNARY PIN WITH 19% POROSITY AND 20% SODIUM LOGGING

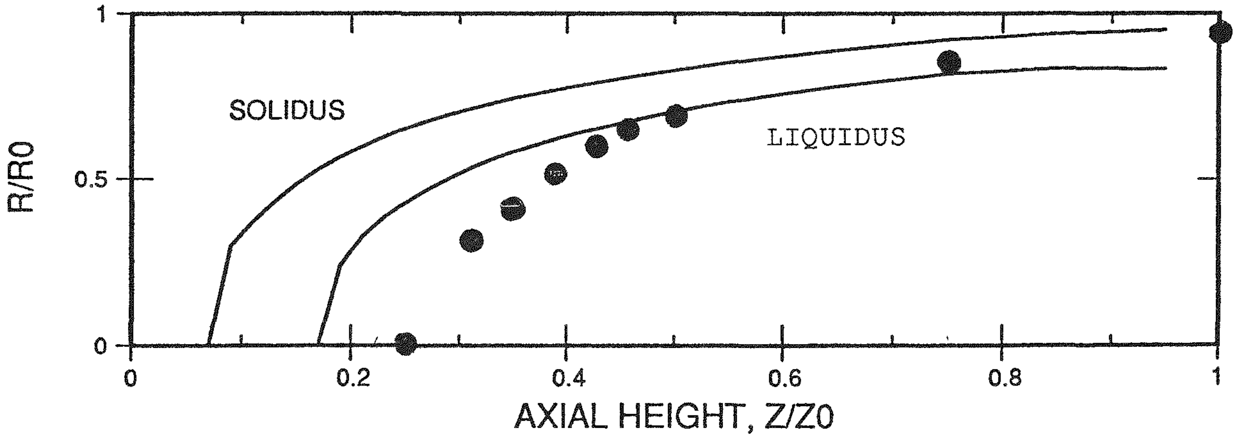

M7 BINARY PIN WITH 31% POROSITY AND 20% SODIUM LOGGING

Note: Measurements denoted by (●)

Fig. F. 67. Computed Melting (using alternate low thermal conductivity values) in the M7 Overpower Transient Compared to Measurement in the Intact Pin

APPENDIX G

Additional Information Useful for Test Analysis

G.1 Miscellaneous Information Useful for Test Analysis

This appendix provides a variety of information, both measured and assumed, useful to the reported analyses of the tests. Section A.2 describes flow channel geometry of a single pin within a flowtube. Flowtubes were thermally isolated from the rest of the loop structure (heat transfer coefficient of 0.02 W/cm^2-K assumed). Table G.1 provides tabular summaries of TREAT power histories (including rod shadowing effects). Axial peak power couplings (including TCF's), inlet flowrates (assumed constant prior to pin failure), and inlet coolant temperature are found in Table F.1. Radial and axial power distributions used in the calculations were given in Figs. C.2 and C.3 in Appendix C.

G.2 Dependence of Thermal Conductivity on Burnup

Thermal conductivity of fresh fuel from the "IFR Metallic Fuels Handbook" [2.4] was used as a baseline in test analyses. However, a strong dependence of thermal conductivity on swelling, sodium logging and solid/liquid fission product accumulation (all of which depend strongly with burnup) is expected, and suggests strong variability in the thermal conductivity among M-series test pins with burnup. Rather than apply "bounding" correction factors, such as recommended in Ref. 2.4, knowledge of irradiated fuel characteristics such as listed in Table 2.2 have been used along with a previously reported empirical model [G.1] to produce physically reasonable estimates of thermal conductivity corrections applicable to M-series test fuel.

The Ref. G.1 empirical model correlates known information on gas-filled and sodium-logged porosity to changes in fuel thermal conductivity. In that model a random distribution of pores alters the conductivity of uniform fuel by a correction factor:

$$C_f = 1 - A * P \tag{G.1a}$$

Table G.1. Suggested Power Histories for M5-M7 Overpower Transients

M5-F1

TIME (S)	POWER (MW)
3.50000	0.600000
4.00000	2.70000
4.50000	14.1000
5.00000	38.3000
5.50000	42.6000
6.50000	48.4000
7.50000	54.3000
8.50000	61.1000
9.50000	69.9000
10.5000	78.9000
11.5000	87.8000
12.5000	100.500
13.5000	114.400
14.5000	130.900
15.5000	158.200
17.0000	185.000
18.0000	212.000
19.0000	240.000
20.0000	275.000
21.0000	315.000
21.1000	90.0000
21.2000	29.0000
21.8000	10.0000

M5-F2

TIME (S)	POWER (MW)
4.00000	1.22000
4.50000	6.16000
5.00000	27.9000
5.40000	38.7000
6.00000	40.7000
7.00000	46.3000
8.00000	52.5000
9.00000	59.5000
10.0000	68.2000
11.0000	77.1000
12.0000	85.4000
13.0000	97.8000
14.0000	112.100
15.0000	128.400
15.6000	143.000
16.1250	157.800
16.2260	92.0000
16.9500	10.0000
18.0000	7.15000
20.0000	4.60000

M6-F

TIME (S)	POWER (MW)
3.60000	0.920000
4.20000	6.17000
4.75000	32.0200
5.00000	61.4500
5.50000	74.0400
6.00000	79.0700
7.00000	89.4300
7.50000	94.4200
8.00000	100.970
9.00000	114.550
10.0000	128.210
10.5000	136.530
11.0000	147.970
11.5000	158.590
12.0000	170.020
12.5000	182.470
13.0000	196.380
13.2500	203.050
13.3500	119.530
13.4500	37.5500
14.0000	23.5200
16.0000	14.1700
20.0000	7.15000

M7-F

TIME (S)	POWER (MW)
7.00000	1.03000
7.50000	4.24000
7.80000	9.40000
8.00000	16.8000
8.20000	28.6000
8.40000	48.2000
8.60000	57.0000
9.00000	65.5000
9.50000	71.0000
10.0000	76.2000
10.5000	81.0000
11.0000	85.9000
11.5000	91.7000
12.0000	98.5000
12.5000	105.400
13.0000	112.300
13.5000	119.200
14.0000	126.600
14.5000	139.200
15.0000	149.900
15.5000	160.500
16.0000	172.300
16.5000	185.700
17.0000	199.300
17.5000	212.800
17.7250	218.900
17.7500	213.300
17.8000	177.200
17.9000	57.7000
18.0000	27.3000
19.0000	17.8000
20.0000	13.9000

where P is the volume fraction occupied by pores, and A is a multiplier which depends on pore shape and thermal conductivity. Following the analysis of Ref. G.1, A may be written as

$$A = 3* \epsilon *((K-K_p)/(K_p+2*K)) \qquad \text{(G.1b)}$$

where K is nominal fuel thermal conductivity, K_p is the thermal conductivity of the pore material and ϵ is a "shape" factor (unity for spherical pores) to be determined empirically. Fitting thermal conductivity measured on irradiated U-Fs fuel with low conductivity pores ($K_p = 0$) [G.2] to Eq. (G.1) suggests a value for ϵ of about 1.67.

If total porosity, P, is divided between sodium-filled, P_s, and gas-filled, P_g, then C_f of Eq. (G.1) may be re-written as:

$$C_f = 1 - A_s*P_s - A_g*P_g$$

and, $A_s = 2.5*3*\epsilon*(1-r)/(r+2)$

$$A_g = 3*\epsilon*P_g/2 \qquad \text{(G.2)}$$

where "r" is the ratio of thermal conductivity of sodium to fuel (nominal). Eq. (G.2) was used to calculate the burnup correction to thermal conductivity used in all the reported analyses. For these calculations, ϵ was assumed equal to the fitted value of 1.67 and the average amounts of gas-filled and sodium-filled porosity assumed for each test pin is reported in Table F.1 consistent with fuel characteristics reported in Table 2.2. (For higher burnup ternary fuel pins, a radial distribution of porosity was also assumed-see Eq. (G.3) below.)

Typical values of computed thermal conductivity are reported in Table 2.2. Computed magnitudes of the burnup correction are consistent with bounding estimates from Ref. 2.4.

G.3 In-Pin Radial Distributions of Constituents Assumed in Test Analysis

As was discussed in Sect. 2, direct measurements of the radial distribution of the relative distribution of fuel constituents have been made for ternary fuel at burnups tested in M5-M7 and exhibit significant nonuniformity [2.2 and G.3]. Porosity distributions were not directly measured, but microphotographs give qualitative indication of an increasing porosity with pin radius in higher burnup pins. Measured isotope distributions in 5 and 10 at.% burnup pins, when integrated, yield the expected initial pin loadings as modified by burnup level, provided a modest density decrease with radius is assumed [G.4]. Since the particular mix of constituents affects fuel melting points and thermal conductivity, "best estimates" of radial distributions for uranium, plutonium, and zirconium and porosity, were included in thermal analyses. These distributions were assumed to apply at all axial heights and are consistent with both measured distributions and analysis of total isotope inventory.

In ternary fuel of burnup greater than 5 at.% fuel mass density is assumed to decrease with relative radius, R according to a factor, $EXP(-(0.5R)^2)$, which multiplies the fuel's average smear density. Porosity increases with radius accordingly. (Average values of fuel porosity used in the analyses were given in Table F.1.)

Isotopic distributions of uranium and plutonium as a function of relative radius, R, were input by weight fraction, W, according to a quadratic function:

$$W = A + B*R + C*R*R \tag{G.3}$$

Coefficients A, B, and C are given in Table G.2. Zirconium distribution is calculated on the basis of the weight distribution of uranium, plutonium and zirconium summing to unity at every radial location.

Table G.2 Radial Distribution Coefficients of U and Pu in IFR Ternary Test Fuel

Test Fuel:		0.8 at.%	1.9 at.%	5.3 at.%	9.8 at.%
Uranium:					
	A	0.710	0.613	0.873	0.841
(Eq.	B	0.0	0.646	-0.481	-0.345
G.3)	C	0.0 (uniform)	-0.662	0.288	0.233
Plutonium:					
	A	0.190	0.185	0.139	0.099
(Eq.	B	0.0	-0.018	0.211	0.373
G.3)	C	0.0 (uniform)	-0.004	-0.184	-0.292

In general, the assumed constituent nonuniformity exerted minimal influence on the key (mainly thermal) calculations of pre-failure axial expansion, gross amounts of fuel melting, and cladding failure threshold. Assuming uniform distributions of constituents and whole-pin averages in these calculations should then be adequate for most purposes.

References

G.1. T. H. Bauer, "Effects of Porosity on Thermal Conductivity with Application to Sodium-Bonded, Metal Reactor Fuel," ANL-RDP-115, p. 1.40 (1984).

G.2. R. A. di Novi,"Effect of Burnup, Swelling, and Irradiation Temperature on Thermal Diffusivity and Conductivity of Uranium-Fissium Alloy," Argonne National Laboratory Report, ANL-7886 (1972).

G.3. R. G. Pahl, "IFR Fuels Performance and Fabrication Progress Reports, March, October, and December 1987," (1987).

G.4. T. H. Bauer, Argonne National Laboratory, unpublished information, (February 1988).